



UNIVERSITÀ DEGLI STUDI ROMA TRE

Dipartimento di Matematica e Fisica

Doctoral program in Physics - Final Dissertation

X-ray Polarization of Accreting Weakly Magnetized Neutron Stars

Candidate:
Andrea Gnarini

Supervisor:
Prof. Giorgio Matt

Co-Supervisor:
Dr. Francesco Ursini

Ph. D. XXXVI cycle

X-ray Polarization of Accreting Weakly Magnetized Neutron Stars

Ph. D. Thesis, Università degli Studi Roma Tre

Email: *andrea.gnarini@uniroma3.it*

Copyright © 2024 Andrea Gnarini – v.2.0, April 2024

SEE YOU SPACE COWBOY...

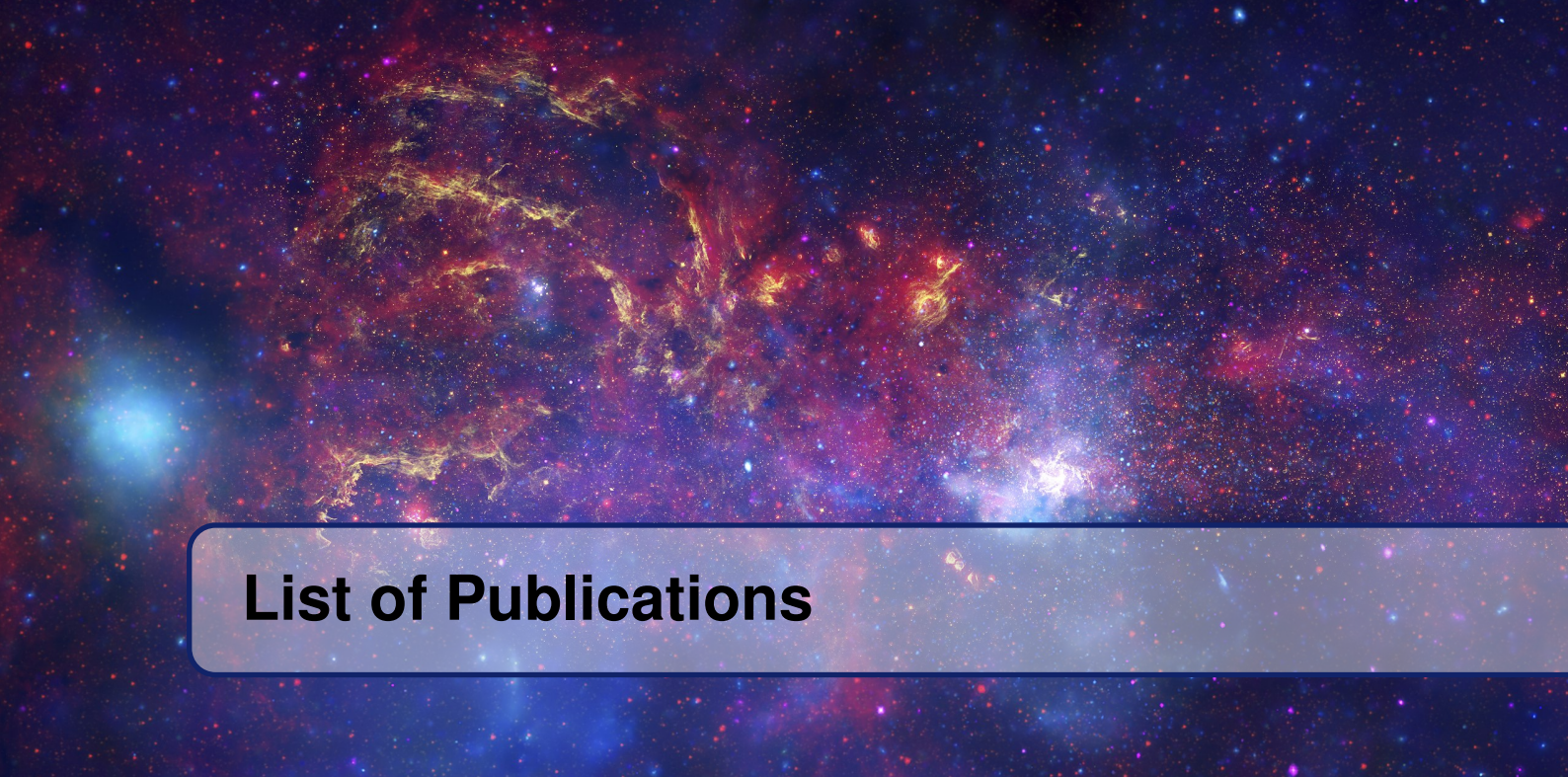


Abstract

X-ray Binaries hosting Neutron Stars (NS-LMXBs) are a fundamental laboratory to study radiation processes in strong gravity regime. The central NS accretes matter via Roche-lobe overflow from a companion star, typically a solar mass star or an evolved white dwarf. These sources are amongst the brightest in X-rays, with spectra well described by a soft thermal emission and a hard Comptonization component. However, the physical origin of these components is still matter of debate. The thermal emission is related either to the accretion disk or to the NS surface, whereas the Comptonized component originates in a hot electron plasma surrounding the NS. In addition to the primary continuum, reflection of X-ray photons above by accretion disk is detected in several NS-LMXBs, although not in all of them.

The launch of the NASA and Italian Space Agency *Imaging X-ray Polarimetry Explorer (IXPE)* on 2021 December 9 has opened a new window in X-ray astronomy, providing for the first time space-, time-, and energy-resolved polarimetric observations. X-ray polarimetry is crucial to constrain the geometry of the accreting system and the involved physical processes, left unconstrained by spectroscopy alone.

This work presents the first spectro-polarimetric results obtained from *IXPE* observations of NS-LMXBs. Several NS-LMXBs were observed by *IXPE* during the first two-year observational campaign. Significant polarization has been detected in most of the observed sources, with intriguing and unexpected results. The observed polarization properties obtained from *IXPE* observations are also compared with numerical simulations performed with the Monte Carlo radiative transfer code `MONK` to constrain the geometry of the accreting systems. `MONK` is a General Relativistic Monte Carlo code able to compute the polarization of the Comptonized radiation. It was originally developed to study accreting black holes and has been adapted here to NS-LMXBs by adding the option of seed photons from the NS surface. The polarization properties strongly depend on the geometry of the accreting system and the Comptonizing region. Different coronal shapes result in significantly different X-ray polarization degree and angle, which can therefore be used to constrain the geometry of the systems. Moreover, the polarization degree also increases with the inclination of the system. *IXPE* observations seem to exclude the accretion disk as the main contribution to the polarization, which can instead be explained as the combination of Comptonization in a boundary or spreading layer plus reflection. The spreading layer-like geometries exhibit a quite low polarization in the 2–8 keV range (compared to typical slab-like geometries), but highly polarized reflected photons contribute significantly to the polarization even if their fraction to the total flux is relatively small.



List of Publications

Part of this work has been presented in the following papers:

Published

Polarization properties of weakly magnetized neutron stars in low-mass X-ray binaries

Authors: **A. Gnarini**, F. Ursini, G. Matt, S. Bianchi, F. Capitanio, M. Cocchi, R. Farinelli and W. Zhang
Monthly Notices of the Royal Astronomical Society, Volume 514-2 (2022), DOI: 10.1093/mnras/stac1523

Polarization properties of the weakly magnetized neutron star X-ray binary GS 1826–238 in the high soft state

Authors: F. Capitanio, S. Fabiani, **A. Gnarini**, ... and the *IXPE* Collaboration
The Astrophysical Journal, Volume 943, id.129 (2023), DOI: 10.3847/1538-4357/acae88

Accretion geometry of the neutron star low mass X-ray binary Cyg X–2 from X-ray polarization measurements

Authors: R. Farinelli, ..., **A. Gnarini**, ... and the *IXPE* Collaboration
Monthly Notices of the Royal Astronomical Society, Volume 519-3 (2023), DOI: 10.1093/mnras/stac3726

Discovery of strongly variable X-ray polarization in the neutron star low-mass X-ray binary transient XTE J1701–462

Authors: M. Cocchi, **A. Gnarini**, ... and the *IXPE* Collaboration
Astronomy & Astrophysics, Volume 674, id.L10 (2023), DOI: 10.1051/0004-6361/202346541

X-ray polarimetry and spectroscopy of the neutron star low-mass X-ray binary GX 9+9: an in-depth study with IXPE and NuSTAR

Authors: F. Ursini, R. Farinelli, **A. Gnarini**, ... and the *IXPE* Collaboration
Astronomy & Astrophysics, Volume 676, id.A20 (2023), DOI: 10.1051/0004-6361/202346541

First detection of X-ray polarization from the accreting neutron star 4U 1820–303

Authors: A. Di Marco, ..., **A. Gnarini**, ... and the *IXPE* Collaboration

The Astrophysical Journal Letters, Volume 953, id.L22 (2023), DOI: 10.3847/2041-8213/acec6e

Highly Significant Detection of X-Ray Polarization from the Brightest Accreting Neutron Star Sco X-1

Authors: F. La Monaca, ..., **A. Gnarini**, ... and the *IXPE* Collaboration

The Astrophysical Journal Letters, Volume 960, id.L11 (2024), DOI: 10.3847/2041-8213/ad132d

X-Ray Polarized View on the Accretion Geometry in the X-Ray Binary Circinus X–1

Authors: J. Rankin, ..., **A. Gnarini**, ... and the *IXPE* Collaboration

The Astrophysical Journal Letters, Volume 961, id.L8 (2024), DOI: 10.3847/2041-8213/ad1832

Polarized Light from Accreting Low Mass X-Ray Binaries

Authors: F. Capitanio, **A. Gnarini**, S. Fabiani, F. Ursini, R. Farinelli, M. Cocchi, N. Rodriguez Cavero and L. Marra

Astronomy Reports, Volume 67, Suppl. 2 (2024) DOI: 10.1134/S1063772923140044

X-Ray Polarimetry of the Dipping Accreting Neutron Star 4U 1624–49

Authors: M. L. Saade, P. Kaaret, **A. Gnarini**, ... and the *IXPE* Collaboration

The Astrophysical Journal Letters, Volume 963, id.133 (2024), DOI: 10.3847/1538-4357/ad235a

Discovery of a variable energy-dependent X-ray polarization in the accreting neutron star GX 5–1

Authors: S. Fabiani, ..., **A. Gnarini**, ... and the *IXPE* Collaboration

Astronomy & Astrophysics, Volume 684, id.137 (2024), DOI: 10.1051/0004-6361/202347374

Submitted/Accepted

Polarization Properties of Neutron Star Low-Mass X-ray Binaries with IXPE Observations

Authors: **A. Gnarini**, F. Capitanio, M. Cocchi, S. Fabiani, R. Farinelli and F. Ursini

Accepted for publication in Memorie della Società Astronomica Italiana, 2024

Discovery of a strong rotation of the X-ray polarization angle in the galactic burster GX 13+1

Authors: A. Bobrikova, ..., **A. Gnarini**, ... and the *IXPE* Collaboration

Submitted to Astronomy & Astrophysics, 2024

In Preparation

Constraining the geometry of the dipping atoll 4U 1624–49 with X-ray spectroscopy and polarimetry

Authors: **A. Gnarini**, M. L. Saade, F. Ursini, S. Bianchi, P. Kaaret, G. Matt, F. Capitanio, and W. Zhang



Contents

List of Publications	vii
Introduction	1

I

Part One

1	Neutron Stars	5
1.1	A Brief History of Neutron Stars	5
1.2	Physics of Neutron Stars	8
1.3	Internal Structure	10
1.4	Global Structure	12
2	X-Ray Binaries	15
2.1	Accretion	15
2.1.1	Roche Lobe Overflow	16
2.1.2	Accretion Disk Structure	18
2.1.3	Energy Release	21
2.1.4	Boundary Layer	22
2.2	Neutron Stars X-ray Binaries	23
2.3	Physical processes	26
2.3.1	Compton Scattering	26
2.3.2	Photoelectric Absorption	27
2.3.3	Reflection	28
3	Numerical Setup & Simulations	35
3.1	MONK	35
3.1.1	Ray-tracing in the Kerr Spacetime	37

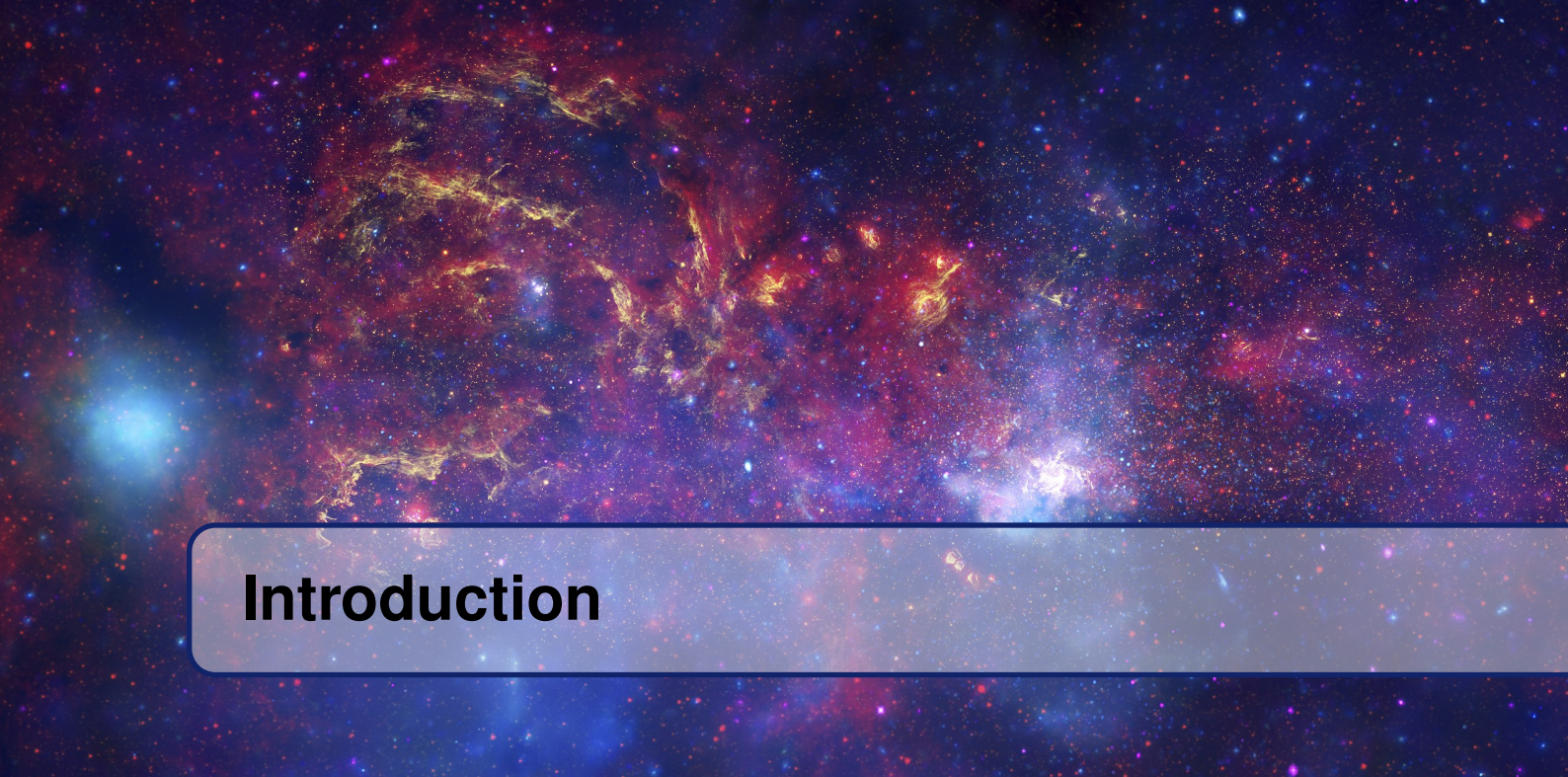
3.1.2	Propagation of the Polarization Vector	38
3.1.3	Comptonization	41
3.2	Numerical Setup	43
3.3	Slab Geometry	45
3.4	Spherical Geometry	46
3.5	Torus Geometry	47
3.6	Wedge Geometry	48
3.7	Boundary/Spreading Layer Geometry	49

II

Part Two

4	Spectro-Polarimetric Observations	53
4.1	X-ray Polarimetry	53
4.2	IXPE	55
4.2.1	Data Reduction	55
4.3	GS 1826–238	56
4.3.1	Observations	57
4.3.2	Spectro-Polarimetric Analysis	58
4.4	GX 9+9	60
4.4.1	Observations	60
4.4.2	Spectro-Polarimetric Analysis	61
4.5	4U 1820–303	64
4.5.1	Observations	65
4.5.2	Radio Observation	66
4.5.3	Spectro-Polarimetric Analysis	67
4.6	4U 1624–49	70
4.6.1	Observations	71
4.6.2	Spectro-Polarimetric Analysis	72
4.7	Cygnus X–2	75
4.7.1	Observations	75
4.7.2	Spectro-Polarimetric Analysis	77
4.8	XTE J1701–462	80
4.8.1	Observations	81
4.8.2	Spectro-Polarimetric Analysis	83
4.9	GX 5–1	87
4.9.1	Observations	88
4.9.2	Radio Observations	89
4.9.3	Spectro-Polarimetric Analysis	90
4.10	Scorpius X–1	94
4.10.1	Observations	94
4.10.2	Polarimetric Analysis	95
4.11	Circinus X–1	96
4.11.1	Observations	97
4.11.2	Polarimetric Analysis	98

5	Results	99
5.1	Comparison Between Different Geometries	99
5.2	Comparison Between Observations	102
5.2.1	Atoll-Sources	102
5.2.2	Z-sources	107
6	Conclusions	113
6.1	Future Perspectives	114
	Appendices	117
A	Polarization Properties	117
A.1	Stokes Parameters	117
B	X-ray Observatories	121
B.1	NuSTAR	121
B.1.1	Data Reduction	121
B.2	NICER	122
B.2.1	Data Reduction	122
B.3	INTEGRAL	122
B.3.1	Data Reduction	123
C	XSPEC	125
C.1	Spectral Fitting	125
C.2	Useful Models	126
C.2.1	Bbodyrad	126
C.2.2	CompTT	127
C.2.3	Comptb	127
C.2.4	Diskbb	128
C.2.5	ThComp	128
C.2.6	Relxill	128
C.2.7	TBAbs	129
C.2.8	Polconst	129
C.2.9	Pollin	129
	References	151



Introduction

Accreting, weakly magnetized Neutron Stars in Low-mass X-ray binaries (NS-LMXBs) are a fundamental laboratory to study radiation processes in the strong gravity regime. Neutron stars are the endpoints of the evolution of massive stars ($8M_{\odot} \lesssim M \lesssim 25M_{\odot}$), the remnants of the supernova explosion which follows the core collapse and marks the death of the progenitor. With a mass of the order of the solar mass and a radius of only 10–15 km, NSs are the most compact stellar objects with a surface in the present universe, reaching densities higher than those of atomic nuclei. The existence of NS was first proposed by [Baade and Zwicky \(1934\)](#), less than two years after the discovery of the neutron by [Chadwick \(1932\)](#). Until the end of the 1960s, NSs were thought to be too faint to be detectable. However, [Pacini \(1967\)](#) showed that if the NSs were spinning and had large magnetic fields, they would emit electromagnetic radiation that could have been detected. Indeed, the first NS was discovered in the same year (PSR B1919+21; [Hewish et al. 1968](#)): the observed pulsar exhibits strictly periodic pulses with an extremely regular 1.33730121 s period. NSs are endowed with extremely strong magnetic fields (up to $10^{14} - 10^{15}$ G in magnetars). The magnetic field evolution is coupled to that of the surface temperature. NSs are born very hot ($T \approx 10^{11}$) and cool down as they age, dissipating part of their magnetic fields and transferring energy between poloidal and toroidal magnetic field components. Weakly magnetized NSs in X-ray binaries are therefore old system with typical lifetime of the order of billions of years, with typical magnetic fields of $10^8 - 10^{10}$ G ([Geppert and Urpin, 1994](#)). When a NS is formed in a binary system, it may start accreting matter from the companion star via Roche-lobe overflow through the inner Lagrangian point. The accreting matter forms an accretion disk due to its high angular momentum before reaching the NS surface. The accretion disc emits radiation due to viscous dissipation. Typically, approximately 10% of the rest-mass energy of the accreting matter is emitted, mostly in the X-ray energy range. X-ray binaries are amongst the brightest sources in the X-ray sky, with luminosities ranging in the $10^{36} - 10^{38}$ erg/s interval. The brightest non-transient source of X-rays in the sky (aside from the Sun) is indeed Sco X-1, the first NS-LMXBs and extrasolar X-ray source discovered in 1962 ([Giacconi et al., 1962](#)).

According to their joint timing and spectral properties in the X-ray band and following their tracks in the Hard-color/Soft-color diagrams (CCD), NS-LMXBs are traditionally divided into two broad categories: the high soft state Z-sources and the Atoll-sources. The position in the CCD is also correlated with the mass accretion rate, which is close to the Eddington limit in Z-sources. The X-ray emission of NS-LMXBs is generally well described by a soft thermal component plus a hard Comptonized emission, but their physical origin is still uncertain. The soft component could be related either to the accretion disc emission or to the NS surface radiation, whereas the hard component may originate by Compton scattering of

soft photons in the hot electron plasma surrounding the NS and near the accretion flow. Furthermore, several detections of the Fe $K\alpha$ emission line at ~ 6 keV strongly suggest that Compton reflection by a colder medium (such as the outer accretion disc itself) is a further spectral component to be taken into account. Although X-ray spectroscopy can provide crucial information on the physical parameters of the emitting regions (i.e. the soft photon temperature, the plasma optical depth or the inclination of the system from the reflection features), it is not able to unequivocally disentangle among different broad-band models. X-ray polarimetry is the key to distinguish between different scenarios, which can otherwise equally well describe the spectral and temporal observed properties of NS-LMXBs. The X-ray polarized radiation strongly depends on the geometry of the accreting system and the Comptonizing region. Both the polarization degree and angle result to be different in value and energy dependence between different geometrical configurations, which can therefore be distinguished. In particular, the polarization degree increases with increasing deviation from spherical symmetry.

For the first time, thanks to the NASA and Italian Space Agency (ASI) *Imaging X-ray Polarimetry Explorer* (*IXPE*; Weisskopf et al. 2016, 2022) mission, it is possible to measure the polarimetric properties of the X-ray radiation (in the 2–8 keV energy band) coming from NS-LMXBs. *IXPE* was successfully launched on 2021 December 9 and in its first two years has observed all major classes of X-ray sources covering a wide range of luminosities, including several NS-LMXBs (both Atoll- and Z-sources). *IXPE* has detected significant polarization in most of the observed NS-LMXBs. Interestingly, surprising large polarization has been observed in some sources, up to 4 – 5% in the whole *IXPE* band and up to $\sim 10\%$ at high energy, which is quite difficult to explain with standard geometries. Z-sources seems to be the most polarized NS-LMXBs in the 2–8 keV band, with a strong dependence of the PD on the position along the CCD: on the horizontal branch, the radiation is more polarized ($\sim 4 - 5\%$) and starts to decrease as the sources move along the normal and flaring branches ($\sim 1 - 2\%$). The direction of the polarization seems to be consistent with that of the radio jet (i.e. perpendicular to the accretion disc). This result suggests that most of the observed polarization may originate in the spreading layer around the NS and roughly perpendicular to the disc plane or from reflection off the disc of the soft photons (or a combination of these two contributions).

The work is organized as follows:

- in Chapter 1, the general properties of the NSs are reviewed, including their classification and the general relativistic structure equations;
- in Chapter 2, after introducing the properties of accretion, NS-LMXBs are characterized along with a detailed description of the main physical processes involved;
- in Chapter 3, the main characteristic of the general relativistic Monte Carlo radiative transfer code *MONK* are described, together with the spectro-polarimetric results obtained for different geometries of the Comptonizing region;
- in Chapter 4, the observations of several NS-LMXBs made by *IXPE* are reported, with detailed spectro-polarimetric analyses;
- in Chapter 5, the results of the different *IXPE* observations are compared with each other and with numerical simulations in order to study the general properties of the polarized X-ray radiation and understand the geometry of the accreting system.

Part One

1	Neutron Stars	5
1.1	A Brief History of Neutron Stars	5
1.2	Physics of Neutron Stars	8
1.3	Internal Structure	10
1.4	Global Structure	12
2	X-Ray Binaries	15
2.1	Accretion	15
2.1.1	Roche Lobe Overflow	16
2.1.2	Accretion Disk Structure	18
2.1.3	Energy Release	21
2.1.4	Boundary Layer	22
2.2	Neutron Stars X-ray Binaries	23
2.3	Physical processes	26
2.3.1	Compton Scattering	26
2.3.2	Photoelectric Absorption	27
2.3.3	Reflection	28
3	Numerical Setup & Simulations	35
3.1	MONK	35
3.1.1	Ray-tracing in the Kerr Spacetime	37
3.1.2	Propagation of the Polarization Vector	38
3.1.3	Comptonization	41
3.2	Numerical Setup	43
3.3	Slab Geometry	45
3.4	Spherical Geometry	46
3.5	Torus Geometry	47
3.6	Wedge Geometry	48
3.7	Boundary/Spreading Layer Geometry	49



1. Neutron Stars

Neutron stars are born after the gravitational core-collapse Supernova of a star with quite high mass $8 M_{\odot} \lesssim M \lesssim 25 M_{\odot}$. Massive stars can proceed past the He-burning phase and arrive to synthesize elements of the iron group, unlike solar mass stars. When the core is made mainly of Fe and Ni, no exothermic nuclear reactions can take place and the high temperature causes photodisintegration of nuclei and neutrino production and emission. With no pressure support, the core collapses under its own gravity, the density starts to increase and, at $\rho \gtrsim 10^{14} \text{ g cm}^{-3}$, the nuclei are completely broken up and matter is mainly composed of neutrons. If the star has sufficiently high mass, the degeneracy pressure of neutrons can stop the collapse and trigger a shock that propagating outward blows up the star envelope (*Supernova event*). After the shock reaches the surface, it produces a splash of radiation in all bands of the electromagnetic spectrum (EM). In addition, the core collapse itself should be accompanied by a powerful outburst of neutrino emission and, possibly, of gravitational radiation. Supernova explosions are accompanied by enormous energy release, a few times 10^{53} erg in total, mostly in the form of neutrinos. About 1% of the total energy transforms into the kinetic energy of the ejected explosion, and only a minor part ($\sim 10^{49}$ erg) becomes electromagnetic radiation; a smaller part can also be emitted in the form of gravitational waves. A gravitational collapse of a degenerate stellar core occurs on time scales of 0.1 s. If the shock wave produced by the core bounce is successful in ejecting the outer layers, it should result in the appearance of a proto-neutron star with internal temperature $T \sim 10^{11}$ K (see e.g. [Yakovlev et al., 2005](#)). This proto-NS is hot, opaque to neutrinos and larger than an ordinary NS. It lives for about one minute and then transforms into an ordinary NS that is transparent to neutrinos. Current estimates of the supernova explosion rate in the Milky Way are uncertain and give one event per 60–1000 years. The total number of neutron stars in the Galaxy is estimated as $10^8 - 10^9$ but only a very limited fraction of these can be observed.

1.1 A Brief History of Neutron Stars

The existence of astrophysical objects supported by the neutron degenerate gas pressure, in analogy to the case of white dwarfs which are supported by electron degenerate gas pressure, was first proposed in the 1930s by [Baade and Zwicky \(1934\)](#) and then confirmed later on with the discovery of Pulsars ([Hewish et al., 1968](#)). Before the discovery of the neutron by [Chadwick \(1932\)](#), Landau improvised the concept of NSs in a discussion with Bohr and Rosenfeld in March 1931 ([Rosenfeld, 1974](#); [Yakovlev et al., 2013](#)) :

I recall when the news on the neutron discovery reached Copenhagen, we had a lively discussion on the same evening about the prospects opened by this discovery. In the course of it Landau improvised the conception of neutron stars – “*unheimliche Sterne*”, weird stars, which would be invisible and unknown to us unless by colliding with visible stars they would originate explosions, which might be supernovae. Somewhat later, he published a paper with Ivanenko in which he again mentioned neutron stars as systems to which quantum mechanics would not be applicable.

Landau was able to derive the maximum mass of white dwarfs independently of Chandrasekhar (1931) and speculated on the possible existence of more compact stars than white dwarfs, with matter close to nuclear density. However, the only solution which Landau could propose violates quantum mechanics, since it was a problem to construct atomic nuclei without neutrons because the Heisenberg principle forbids to localize the electrons within the nuclei. The theoretical prediction of NSs was made by Baade and Zwicky (1934a) proposing an explanation of the energy release in supernova explosions:

With all reserve we advance the view that supernovae represent the transitions from ordinary stars to neutron stars, which in their final stages consist of extremely closely packed neutrons.

In the forthcoming publication, Baade and Zwicky (1934b) delve deeper into the concept of NSs:

[NSs] may possess a very small radius and an extremely high density. As neutrons can be packed much more closely than ordinary nuclei and electrons, the “gravitational packing” energy in a cold neutron star may become very large, and, under certain circumstances, may far exceed the ordinary nuclear packing fractions.

Afterwards, Gamow and Landau separately proposed that the core of any (normal) star could potentially host a NS. This hypothesis implied a gradual “*accretion*” of stellar material onto its core, with the release of gravitational energy during the accretion process potentially providing the stellar energy. However, very soon the idea was almost forgotten when Bethe and Critchfield (1938) showed that the energy of stars is provided by thermonuclear reactions.

The most crucial ingredient of NSs is the equation of state (EOS) of dense matter in its interior. The dependence of pressure P on the mass density ρ (or the associated energy density $\mathcal{E} = \rho c^2$) and on the temperature T of matter must be specified. Since NSs are mainly composed of strongly degenerate fermions, the temperature dependence can be neglected and the EOS can be considered at $T = 0$. Tolman (1939) and independently Oppenheimer and Volkoff (1939) derived the equation of hydrostatic equilibrium for a spherically symmetric star in the framework of General Relativity, the so-called Tolman-Oppenheimer-Volkoff (TOV) equation. Tolman (1939) was able to obtain some exact solutions of the TOV equation. Even if these solutions do not correspond to any realistic EOS of the NS matter, they allow to understand the existence of a maximum mass of NSs. Oppenheimer and Volkoff (1939) solved NS models for the simplest EOS considering a NS made of a non-interacting strongly degenerate relativistic gas of neutrons and found the maximum (gravitational) mass for a stable static NS, $M_{\max} \approx 0.71 M_{\odot}$ (Oppenheimer-Volkoff mass limit).

In the 1960s, motivated by the attempts to discover NSs, the first studies on the thermal emission from cooling NSs were proposed (Tsuruta and Cameron 1966; see also Yakovlev et al. 1999), emphasizing the strong dependence of the cooling rate on neutrino emission processes and pointing out that this dependence can be used to explore the EOS of dense matter by comparing theoretical cooling models with observations of thermal radiation from NSs. A standard NS with surface temperature of $\sim 10^6$ K emits soft X-rays that can not be detected by ground-based facilities. The first X-ray detectors were launched on rockets and balloons at the beginning of the 1960s. The first cosmic X-ray source of non-solar origin detected was Sco X-1 (Giacconi et al., 1962), discovered with rocket experiments, followed by

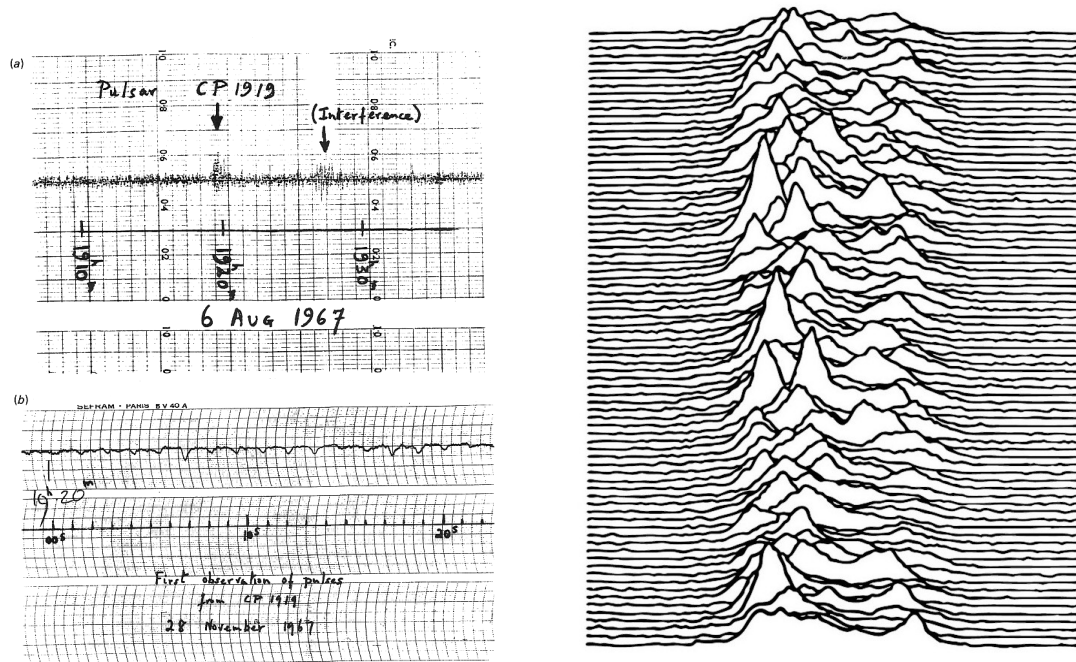


Figure 1.1: The first ever detection of a pulsar CP 1919 obtained by Jocelyn Bell on 1967 August 6 (Hewish et al., 1968). *Right Panel*: successive pulses of CP 1919 occurring every 1.337 s superimposed vertically (Mitton, 1977, also famous worldwide for being the cover of “Unknown Pleasures” by Joy Division).

other several X-ray sources (Giacconi et al., 1972). Located in the constellation Scorpius at a distance of approximately 2.8 kpc, Sco X–1 stands out as the brightest observable X-ray source in the sky. In 1967, by studying the X-ray and Optical observations of Sco X–1, Shklovsky (1967) concluded that the radiation comes from a NS accreting matter from a companion star, so the first NS-LMXBs was discovered. The discovery sparked significant interest in NSs. However, initial attempts to establish a clear link between the NSs and newly discovered compact X-ray sources failed. In particular, Bowyer et al. (1964) estimated the size of the X-ray source in the Crab Nebula obtaining a size much larger than expected for a NS ($\approx 10^{13}$ km). Ironically, the Crab Nebula turned out to be an exception: the Nebula indeed hosted a NS, the famous Crab pulsar, hidden within a supernova remnant with the active pulsar at its center, driving expansion and radiation.

On 1967 August 6, Jocelyn Bell - a graduate student supervised by Antony Hewish - discovered a weak variable radio source (Hewish et al., 1968) with the new radio telescope in Cambridge. This telescope differed from the other ones by a good temporal resolution in order to study scintillations of radio sources while their radiation passes through inhomogeneities of the solar wind in interplanetary space. Although scintillations from ordinary radio sources are stronger during the day, when the telescope is pointed closer to the Sun, a new weak variable source was detected during the night. The observations also indicated that the source had emitted strictly periodic pulses with a perfectly stable period of 1.3373012 s (Figure 1.1). This led to the speculation that these signals were artificially produced, perhaps by space satellites or even by an extraterrestrial civilization (the so-called “little green men”, LGM). It took several weeks to realize that the rapidly pulsating source, a pulsar now called PSR B1919+21, was located far from the solar system. By the beginning of February 1968, three further pulsars (PSR B1133+16, PSR B0834+06, and PSR B0950+08) were identified. In the last ten months of 1968, more than 100 pulsars were detected and discovered. In 1974 Hewish was awarded the Nobel Prize for the discovery of pulsars, but “in some circles, controversy still lingers over the decision of the Swedish Academy not to include Ms Bell in the award” (Will, 1994). The discovery of the Crab pulsar provided a crucial hint that the discovered sources were indeed rotating magnetized NSs instead of oscillating white dwarfs or NSs (Gold,

1968): its measured pulsation period appeared to be very short $P = 33$ ms (Comella et al., 1969) and the white dwarfs could not sustain such a rapid rotation, as they would be destroyed by centrifugal forces. Pacini (1967) demonstrated that a rapidly rotating NS with a strong dipole magnetic field could efficiently transform its rotational energy into radiation, suggesting that the rotational energy loss is the same as produced by a rotating magnetic dipole in vacuum. Therefore, pulsars are spinning NSs with magnetic moments inclined with respect to the spin axes. Radio emission is produced in the magnetosphere outside the star and is beamed along the magnetic axis. The beamed radiation rotates with the star, and a pulsar is detected if its beam crosses the Earth. The rotational energy and momentum are carried away by the released EM radiation, causing regular slow spin-down of the pulsar (increasing the pulse period).

1.2 Physics of Neutron Stars

Soon after the observational discovery by Hewish et al. (1968), NSs were identified as radio pulsars (PSRs), which exhibit regular pulsations in the radio band. Although the existence of several different types of NS sources has been confirmed by observations, the number of detected radio PSRs is by far the largest. The energy that sustains pulsar emission is supplied by their fast rotation via the braking operated by their intense magnetic field, which is usually assumed to be dipolar. A rotating dipole emits electromagnetic energy according to the Larmor formula:

$$\dot{E}_{\text{rad}} = -\frac{2}{3c^3} |\ddot{\mathbf{m}}|^2 = -\frac{B_{\text{pol}}^2 R_{\text{NS}}^6 \Omega^4 \sin^2 \xi}{6c^3} \quad (1.1)$$

where \mathbf{m} is the magnetic dipole moment, B_{pol} is the magnetic field strength at the magnetic pole, ξ is the angle between the dipole axis and the star spin axis, R_{NS} is the stellar radius and $\Omega = 2\pi/P$ the star angular frequency. The spin period P of PSRs (typically in the range $\approx 0.01 - 1$ s) is measured from the pulsations they show in the radio band. By equating \dot{E}_{rad} given by equation (1.1) with the rotational energy losses $\dot{E}_{\text{rot}} = I\Omega\dot{\Omega}$ it results

$$\frac{\dot{\Omega}}{\Omega^3} = -\frac{B_{\text{pol}}^2 R_{\text{NS}} \sin^2 \xi}{6Ic^3}, \quad (1.2)$$

where I is the stellar moment of inertia and, as it can be seen from the minus sign at the right-hand side, the rotational motion of the star slows down. Solving the previous equation for B_{pol} and considering a typical NS with mass $M_{\text{NS}} = 1.4 M_{\odot}$ and radius $R_{\text{NS}} = 10$ km (and so $I \approx 10^{45}$ g cm²), the intensity of the dipolar magnetic field, assuming that all rotational loss \dot{E}_{rot} is converted into radiation power \dot{E}_{rad} is

$$B_{\text{pol}} = \sqrt{\frac{6Ic^3}{4\pi^2 R_{\text{NS}}^6 \sin^2 \xi} P\dot{P}} \approx 3.2 \times 10^{19} \sqrt{P\dot{P}} \text{ G} \quad (1.3)$$

with \dot{P} the spin-down rate, typically $\approx 10^{-16} - 10^{-12}$ s s⁻¹.

Integrating equation (1.2) over time, starting from star birth $t = 0$ up to current time $t = t_c$, one has

$$\frac{1}{\Omega^2(t_c)} = \frac{2B_{\text{pol}}^2 R_{\text{NS}}^6 \sin^2 \xi}{6Ic^3} t_c, \quad (1.4)$$

where the magnetic field has been considered as constant and, since the star slows down, it has been assumed $\Omega(0) \gg \Omega(t_c)$. Then, solving for t_c , one obtains

$$t_c = \frac{1}{2} \frac{P}{\dot{P}}, \quad (1.5)$$

that is called the *characteristic age* of the star. Actually, t_c is a good approximation of the real star age (which can be evaluated through different methods, e.g. from the kinematics or the cooling properties

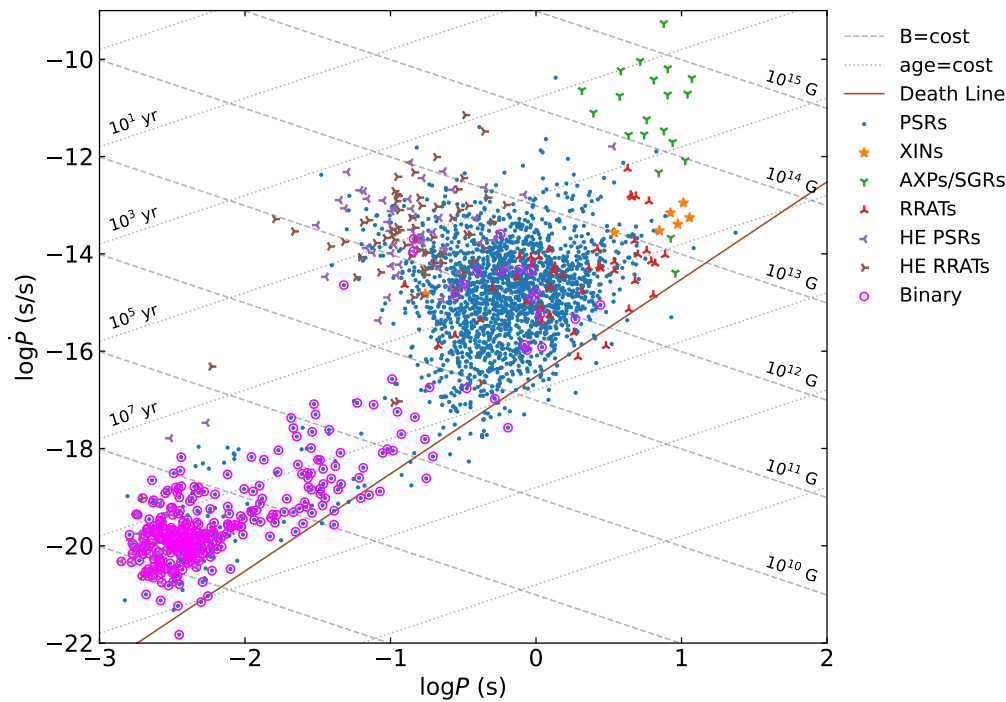


Figure 1.2: Neutron stars population in the $P - \dot{P}$ diagram. The labels refer to the observational properties of the NS: rotation powered pulsars (PSRs), X-ray Dim Isolated NSs (XINs), Anomalous X-ray pulsars (AXPs), Rotating Radio Transients (RRATs) and Magnetars (AXPs/SGRs). The High Energy (HE) label is assigned to PSRs or RRATs with pulsed emission from radio to higher frequencies and energies. Magenta circles indicate the NS in binary system. The dashed lines represent constant magnetic field while the dotted ones the constant characteristic age. The brown line correspond to the Death line.

of the source) if indeed the spin period of the star at birth is much smaller than that today. P and \dot{P} play a fundamental role in characterizing the properties of NSs and the Galactic NS population is usually represented in the $P - \dot{P}$ diagram, shown in Figure 1.2. Data are taken from the Australian Telescope National Facility Catalogue¹ (ATNF Catalogue, [Manchester et al., 2005](#)).

Rotation powered PSRs are the most abundant population and fill the central region of the plot with typical periods of 0.1–1 s and magnetic fields of $\approx 10^{12}$ G. Most of them are noted for their pulsed radio activity, although they are also visible in other bands, i.e. X- and γ -rays. *Millisecond PSRs* are placed in the bottom-left corner at small values of P and \dot{P} , with low magnetic fields $\approx 10^8$ G. Their fast rotation originates in the spin-up by accretion from a companion star in binary systems (*recycled pulsars*, see e.g. [Patruno and Watts, 2021](#)). The *X-ray Dim Isolated NSs* (XDINs) are a very small class of isolated, middle-aged objects exhibiting a very soft, purely thermal X-ray spectrum with typical temperatures of 0.05–0.1 keV and a very large X-ray-to-optical flux ratio, without radio emission. So far, only seven of these NS have been discovered, also known as *Magnificent Seven* (see e.g. [Turolla, 2009](#)). *Magnetars*, observationally identified as *Anomalous X-ray pulsars* (AXPs) and *Soft Gamma Repeaters* (SGRs), are found in the upper right corner with a very strong spin-down magnetic field ($\gtrsim 10^{13}$ G) and a young age. They are bright in the X-rays, with transient activity such as high-energy bursts and outbursts powered by the fast dissipation of the strong magnetic field (see e.g. [Turolla et al., 2015](#); [Kaspi and Beloborodov, 2017](#)). *Rotating Radio Transients* (RRATs) are isolated NSs that emit short and bright radio bursts of 2–30 ms duration in an irregular way, without direct observations of the rotational period. The available estimates were inferred from the time intervals between radio bursts ([McLaughlin et al., 2006](#); [Mereghetti, 2011](#)).

¹<https://www.atnf.csiro.au/research/pulsar/psrcat/expert.html>

1.3 Internal Structure

A NS can be divided into different layered regions as shown in Figure 1.3 (Haensel et al., 2007):

- The outer region (*atmosphere*) is a thin plasma layer where the spectrum of thermal electromagnetic NS radiation is formed, mainly composed of heavy elements (Fe, Ni) and possibly H and He coming from accreted interstellar medium. The atmosphere layer is very thin due to the strong gravity of the neutron star, but can be optically thick. The spectrum, beaming and polarization of emerging radiation can be determined theoretically by solving the radiation transfer problem in atmospheric layers. The thickness of the atmosphere varies from about ten centimeters in a hot NS (with an effective surface temperature $T_s \sim 3 \times 10^6$ K) to a few millimeters in a cold one ($T_s \sim 3 \times 10^5$ K). Very cold or ultra-magnetized NSs may have a solid or liquid surface.
- The *envelope* (or *ocean*) is about 100 m thick and is made up of a Coulomb liquid of ions and electrons with relatively low density ($\rho \lesssim 10^9$ g cm⁻³). It is the region with the largest temperature and pressure gradients, while the density decreases smoothly. Together with the atmosphere, it represents only a very small fraction of the total mass.
- The outer part of the *crust* is mainly composed by a Coulomb lattice of Fe nuclei, free neutrons and ultra-relativistic degenerate electrons. The nuclei are increasingly rich in neutrons as the density increases ($\rho \geq 10^9 - 10^{10}$ g cm⁻³, up to $\approx 10^{14}$ g cm⁻³) as a result of electron capture. The transition between the crust and the envelope takes place at a density below which the matter is in a liquid state. Free degenerate neutrons, electrons and heavy nuclei make up the *inner crust*. The thickness of the entire crust is about 1 km.
- The next layer is the *mantle* in which the nuclei are condensed in a superfluid. Due to the high energy given by the Coulomb interaction, the nuclei are deformed into cylindrical or planar forms (*nuclear pasta*). The existence of the mantle is strictly correlated to the stability of nuclei and its very existence is hence debated.
- The *outer core* has extremely high densities ($0.5\rho_0 \lesssim \rho \lesssim 2\rho_0$, where ρ_0 is the normal nuclear density) at which matter consists in a plasma of protons, neutrons and leptons (*npe μ -matter*). The thickness of the outer core is generally of the order of a few kilometers and makes up the bulk of the NS mass.
- The central part (*inner core*) has a very high density and exists only for stars with $M \gtrsim 1.5 M_\odot$. The inner core composition is still not well understood. Classically, it is described as a superfluid of baryons, most of which are neutrons. Neutrons degeneracy pressure can maintain the star against gravity. The presence of heavy particles, mainly Λ^- and Σ^+ hyperons, is also possible (*npe $\mu\Lambda\Sigma$ -matter*). But there is the possibility to have instead exotic state matter hyperons, like the formation of Bose-Einstein condensates of K or π mesons or a quark-gluon plasma.

For a cold non-accreting NS, complete thermodynamic equilibrium can be assumed with respect to all interactions at zero temperature. For a given baryon density n_B , charge neutrality and β -equilibrium, the ground state is the one that minimize the total energy density. The β -equilibrium corresponds to the chemical equilibrium reached between *direct* and *inverse β -decay*:

$$\begin{cases} n \rightarrow e^- + p + \bar{\nu}_e \\ e^- + p \rightarrow n + \nu_e . \end{cases}$$

Only degenerate neutrons can provide the pressure to sustain the star against gravity. However, the inverse β -decay may occur only if protons and electrons are completely degenerate because in this case their energy, which corresponds to the Fermi energy, can compensate for the proton-neutron mass defect $Q = m_n - m_p \approx 2.5 m_e \approx 1.3$ MeV. Complete degeneracy is reached in the limit of temperature going to

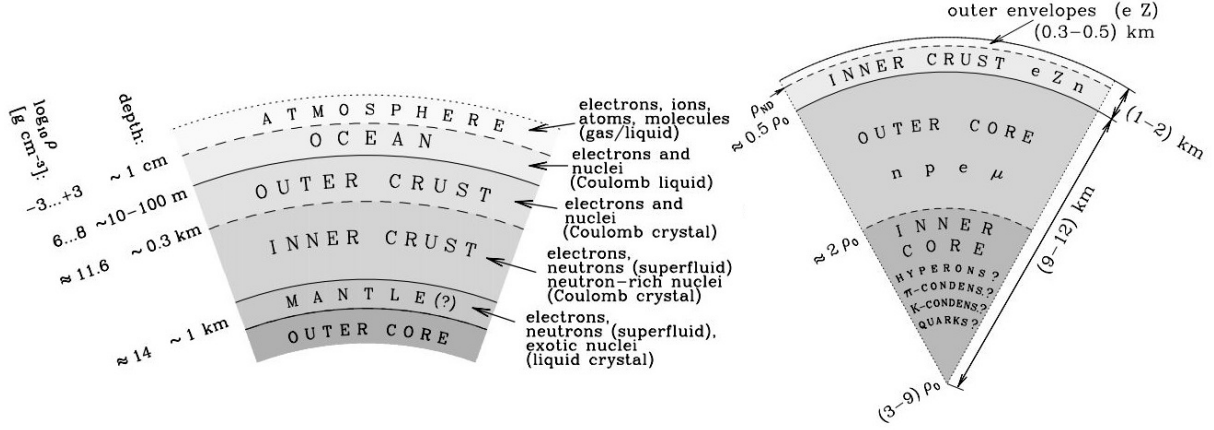


Figure 1.3: Schematic representation of a NS structure (Haensel et al., 2007).

zero and the Fermi-Dirac distribution function at thermodynamic equilibrium becomes

$$f(T) = \frac{1}{1 + e^{(E-\mu)/T}} \xrightarrow{T \rightarrow 0} \Theta(E_F - E)$$

where μ is the chemical potential and $\Theta(E_F - E)$ is the Heaviside step function. The Fermi energy is also defined as $E_F = \mu(T \rightarrow 0) = mc^2 \sqrt{1 + x_F^2}$, with x_F being the adimensional Fermi momentum as a function of the number density n

$$x_F \equiv \frac{p_F}{mc} = \frac{h}{mc} \left(\frac{3n}{8\pi} \right)^{\frac{1}{3}}. \quad (1.6)$$

and where $c = 2.99 \times 10^8$ m/s is the speed of light and $h = 4.135 \times 10^{-15}$ eV s is the Planck constant.

In NSs we can always assume complete degeneracy for all species because the temperature is much lower than the Fermi temperature defined as $T_F = k_B E_F \approx 10^{12}$ K. Furthermore, the density is so high that degenerate electrons also become relativistic ($x_{F,e} \gg 1$) while neutrons and protons remain non-relativistic ($x_{F,n}, x_{F,p} \ll 1$). Finally, the β -equilibrium can be expressed using the Saha equation for the chemical potentials equilibrium, neglecting the contribution of neutrino ($\mu_\nu = \mu_{\bar{\nu}} = 0$):

$$\mu_e + \mu_p = \mu_n. \quad (1.7)$$

At zero temperature, chemical potentials are given by Fermi energies so that equation (1.7) reads

$$m_e c^2 \sqrt{1 + x_e^2} + m_p c^2 \sqrt{1 + x_p^2} = m_n c^2 \sqrt{1 + x_n^2} \quad (1.8)$$

and combining with charge neutrality condition, we can obtain the neutron to proton ratio R in the NS

$$R = \frac{n_n}{n_p} = x_n^3 \left[\frac{4(1 + x_n^2)}{x_n^4 + 4Qx_n^2/m_n + 4(Q^2 - m_e^2)/m_n^2} \right]^{3/2} \quad (1.9)$$

which can be related to mass density as

$$\rho = m_n n_n \left(1 + \frac{n_p}{n_n} \right) = m_n \frac{8\pi}{3} \left(\frac{m_n c}{h} \right)^3 x_n^3 \left(1 + \frac{1}{R} \right). \quad (1.10)$$

Taking this relation to the high density limit, one sees that the ratios between the number densities of the particles go as $n_n : n_p : n_e = 8 : 1 : 1$. This relation can be used as a rule-of-thumb for the whole NS; in particular, the presence of charged particles is crucial for the generation of magnetic fields.

The macroscopic properties of NSs strictly depend on the details of the dense-matter EOS. For a given EOS describing the structure of the core and the crust of the NS, a maximum predicted NS mass and the corresponding radius are associated. The EOS models can be divided in *soft*, *moderate* and *stiff* with respect to the compressibility of the matter. A small maximum mass is associated with stiff models, whereas the opposite occurs for soft models. The maximum mass can provide a comparison with the observations, as the heaviest known NS mass $M = 2.14_{-0.09}^{+0.10} M_{\odot}$ (Cromartie et al., 2020) is bigger than what many EOS predicted. Furthermore, assuming that the isotropic pressure on the surface is zero, a prediction of the NS radius can be derived. Knowing the mass-radius relation precisely would put strict constraints on the EOS itself. However, it is extremely difficult to measure with any precision the mass and especially the radius of a NS (see Haensel et al., 2007, and references therein for more details)

1.4 Global Structure

Spherical symmetry can be assumed for the matter distribution in neutron stars with high accuracy. Deformations could be induced by very fast rotation ($P \lesssim 1$ ms) or extremely strong fields, $B \gtrsim 10^{18}$ G (Haskell et al., 2006). However, the present values of P and B , as derived from observations, are outside these ranges. The equilibrium configuration of the neutron star crust is the result of the competition between pressure, electromagnetic and elastic stresses and the gravitational pull. The global structure can be derived from Einstein's equations (Einstein, 1915)

$$R_{\mu\nu} - \frac{1}{2}Rg_{\mu\nu} = 8\pi T_{\mu\nu} \quad (1.11)$$

where $R_{\mu\nu}$ is the Ricci curvature tensor coming from the contraction of the Riemann curvature tensor, $R = g^{\mu\nu}R_{\mu\nu}$ is the Ricci scalar and $g_{\mu\nu}$ is the spacetime metric. The stress-energy tensor $T_{\mu\nu}$ takes into account pressure, electromagnetic and elastic stresses. Using spherical coordinated (r, θ, φ) , it is possible to write the most general form of a non-rotating, spherically symmetric spacetime (Misner et al., 1973) as

$$ds^2 = -e^{2\Phi(r)} dt^2 + e^{2\lambda(r)} dr^2 + r^2(d\theta^2 + \sin^2\theta d\varphi^2). \quad (1.12)$$

The presence of matter for $r < R_*$, where R_* is the stellar radius, modifies the metric (*interior Schwarzschild solution*). Describing matter as a perfect fluid of energy density ρ , isotropic pressure P and 4-velocity u^μ , the function λ in the metric coefficient can be computed as

$$\lambda(r) = -\frac{1}{2} \ln \left[1 - \frac{2m(r)}{r^2} \right]$$

while the lapse function $e^{2\Phi(r)}$ is determined by

$$\frac{d\Phi(r)}{dr} = \frac{m(r)}{r^2} \left(1 + \frac{4\pi r^3 P}{m(r)} \right) \left(1 - \frac{2m(r)}{r} \right)^{-1} \quad (1.13)$$

with the boundary condition at the stellar radius $e^{2\Phi(R_*)} = 1 - 2M/R_*$ where $M \equiv m(R_*)$ is the total gravitational mass of the central object. We define the enclosed gravitational mass within a radius r as

$$m(r) = 4\pi \int_0^r \rho(\tilde{r}) \tilde{r}^2 d\tilde{r}$$

where ρ is the mass-energy density. In the empty space surrounding a spherically symmetric distribution of matter, i.e. $P = \rho = 0$, the *exterior* Schwarzschild solution is recovered. The total radius of the star is determined by the condition $P(R) = 0$. The hydrostatic equilibrium condition in this configuration is described by the Tolman-Oppenheimer-Volkoff equation (Tolman, 1939; Oppenheimer and Volkoff, 1939) and the pressure profile $P(r)$ is

$$\frac{dP(r)}{dr} = -(\rho + P) \frac{d\Phi(r)}{dr}. \quad (1.14)$$

The TOV equation completely determines the structure of a spherically symmetric body of isotropic material in equilibrium. We can recover the Newtonian limit simply by setting the exponential terms $e^\lambda = e^\Phi = 1$.

For a rotating object such as a NS, the spherical symmetry is no longer valid. The spacetime outside a NS can be modelled, at the first order, using the Kerr metric (Kerr, 1963). Using Boyer-Lindquist coordinate (t, r, θ, ϕ) , the Kerr metric line element can be written as (Bardeen et al., 1972):

$$ds^2 = -\left(1 - \frac{2Mr}{\Sigma^2}\right) dt^2 - \frac{4Mra \sin^2 \theta}{\Sigma^2} d\phi dt + \frac{\Sigma^2}{\Delta} dr^2 + \Sigma^2 d\theta^2 + \left(r^2 + a^2 + \frac{2Mra^2 \sin^2 \theta}{\Sigma^2}\right) \sin^2 \theta d\phi^2, \quad (1.15)$$

where M is the mass of the central object, $a = J/M$ is the angular momentum per unit mass ($0 \leq a \leq M$) and Δ and Σ^2 are defined as:

$$\begin{aligned} \Delta &\equiv r^2 - 2Mr + a^2, \\ \Sigma^2 &\equiv r^2 + a^2 \cos^2 \theta. \end{aligned} \quad (1.16)$$

Hartle and Thorne (1968) derived the actual spacetime metric that describes the exterior of a slowly and rigidly rotating, stationary and axially symmetric body as a solution of Einstein's equations (1.11). In the limit $r \rightarrow \infty$, the Kerr metric reduces to Minkowski's metric in polar coordinates, i.e. is asymptotically flat, while for $a \rightarrow 0$ (with $M \neq 0$) the Schwarzschild metric is recovered.

Being stationary and axisymmetric, the Kerr metric admits two Killing vector fields for t and ϕ associated to two conserved quantities for particles motion

$$E \equiv -g_{t\mu} u^\mu = -p_t \quad (1.17)$$

$$L \equiv g_{\phi\mu} u^\mu = p_\phi \quad (1.18)$$

where u^μ is the particle four-velocity, p^μ the four-momentum and E and L are respectively the conserved energy and angular momentum at infinity (Misner et al., 1973). Along with these two quantities and the particle rest mass μ , the equation of motion in Kerr spacetime can be uniquely determined using the Carter constant (Carter, 1968)

$$Q = p_\theta + \cos^2 \theta [a^2(\mu^2 - p_r^2) + p_\phi^2 \sin^{-2} \theta]. \quad (1.19)$$

For equatorial orbits, the Carter constant must vanish ($Q = 0$). The equation of motion for particles or photons can be derived by minimizing the action, which is equivalent to the Euler-Lagrange equations:

$$\frac{d}{ds} \left(\frac{\partial \mathcal{L}}{\partial \dot{x}^\mu} \right) - \frac{\partial \mathcal{L}}{\partial x^\mu} = 0 \quad \text{with} \quad \mathcal{L} = g_{\mu\nu} \frac{dx^\mu}{ds} \frac{dx^\nu}{ds}. \quad (1.20)$$

Using the conserved quantities for equatorial orbits, the particles motion is described by

$$r^3 \left(\frac{dr}{d\tau} \right)^2 = [r(r^2 + a^2) + 2Ma^2] E^2 - 4aLME - (r - 2M)L^2 - r\Delta. \quad (1.21)$$

However, there is a difference between Schwarzschild and Kerr spacetime: while in the former case, each L corresponds to only one value of E , in Kerr E depends on a and not on a^2 , i.e. it has a sign. This implies that the scenario of a prograde (concordant) or retrograde (discordant) orbit around the BH or NS is different. The radius of the innermost marginally stable circular orbit r_{ms} can be determined from the effective potential V_{eff} . In particular, the derivative of V_{eff} with respect to r has to be null evaluated at $r = r_{ms}$ leading to the following equation (Misner et al., 1973)

$$r_{ms}^2 - 6Mr_{ms} + 8aM^{1/2}r_{ms}^{1/2} - 3a^2 = 0 \quad (1.22)$$

and its solution will be

$$r_{\text{ms}} = M \left\{ 3 + Z_2 - \left[(3 - Z_1)(3 + Z_1 + 2Z_2) \right]^{1/2} \right\} \quad (1.23)$$

where Z_1 and Z_2 are defined as:

$$Z_1 = 1 + \left(1 - \frac{a^2}{M^2} \right)^{1/3} \left[\left(1 + \frac{a}{M} \right)^{1/3} + \left(1 - \frac{a}{M} \right)^{1/3} \right] \quad \text{and} \quad Z_2 = \left(3 \frac{a^2}{M^2} + Z_1^2 \right)^{1/2}.$$

For different values of the spin, the innermost stable circular orbit varies:

- $a = 0$ (Static BH): the circular motion becomes unstable at distances $r < 6M$;
- $0 < a/M \ll 1$ (Slowly rotating BH): the region of stable motion shifts closer towards the event horizon, $r_{\text{ms}} \approx 6M - 4\sqrt{6}aM/3$;
- $a = 1$ (Extreme-spin BH): in this limit case, the innermost stable circular orbit coincides with the gravitational radius of BH for co-rotating orbits, $r_{\text{ms}} = M$, while it broadens up to $r_{\text{ms}} = 9M$ for counter-rotating orbits.



2. X-Ray Binaries

Accretion plays a crucial role in several fields of astrophysics. Most celestial objects (such as galaxies, stars and planets) are formed by accretion processes at different scales. By definition, accretion represents the gradual accumulation of matter onto an object under the effects of gravity. The extraction of gravitational potential energy from matter accreting onto a gravitating body is now known to be the main source of power in several types of close binary systems. Therefore, accretion is a natural and very powerful mechanism for producing high-energy radiation and powering the most luminous objects in the Universe.

2.1 Accretion

As matter comes closer to a gravitational body, such as a compact object, it releases gravitational potential energy, which turns the accreting object into a highly powerful source of energy, e.g. for binary systems, active galactic nuclei or quasars. Taking into account a body of mass M and radius R , the gravitational potential energy released by the accretion of a mass m onto its surface is

$$\Delta E_{\text{acc}} = \frac{GMm}{R} . \quad (2.1)$$

If the central body accretes matter continuously at a rate \dot{M} , in the time interval Δt it will liberates the energy

$$\Delta E_{\text{grav}} = \frac{GM\dot{M}\Delta t}{R} . \quad (2.2)$$

If the energy is radiated away at the same rate at which it liberated, the luminosity due to the accretion process is

$$L_{\text{acc}} = \frac{GM\dot{M}}{R} = \eta\dot{M}c^2 \quad (2.3)$$

where η is the accretion efficiency. For a fixed mass accretion rate, the accretion luminosity L_{acc} increases with the compactness M/R of the accreting object. The efficiency of the accretion mainly depends on the specific energy at the inner edge of the accretion disk r_{in} , assuming that the torque there is negligible

$$\eta = 1 - \sqrt{1 - \frac{2M}{3r_{\text{in}}}} . \quad (2.4)$$

The efficiency will be smaller for inner edge far from the innermost stable circular orbit, ranging from $\approx 6\%$ for non-rotating BHs to $\approx 42\%$ for maximum spinning BHs. For a solar mass NS with a typical radius of $R_{\text{NS}} \sim 10$ km, assuming that the accretion flow stops onto the NS surface, the typical efficiency is

$$\eta_{\text{NS}} \sim \frac{GM_{\text{NS}}}{R_{\text{NS}}} \approx 15\% . \quad (2.5)$$

Therefore, despite its extra compactness, a stellar mass BH may not be more efficient in the conversion of gravitational potential energy to radiation than a NS of similar mass (Frank et al., 1992).

In binary systems with a central compact object, matter coming from the companion star and accreting onto the central object can generate large luminosities. However, if the accretion of matter becomes too important, the radiation pressure will limit the accretion rate and consequently the observed luminosity. Considering steady spherical symmetric accretion and assuming that the accreting matter is mainly made up of fully ionized hydrogen, the radiation exerts a force mainly on the free electrons through Thomson scattering, since the scattering cross section for protons is a factor $(m_e/m_p)^2$ smaller. If there is a population of elements other than hydrogen that have retained some bound electrons, the effective cross section resulting from the absorption of photons in spectral lines can considerably exceed the Thomson cross section σ_T . The outward radial force on each electron corresponds to the rate at which the electron absorbs momentum from the radiant energy flux. Protons are dragged with the electron because of the attractive electrostatic Coulomb force. The net effect is that radiation pushes the electron-proton pairs against the total gravitational force acting on each pair at a radial distance r from the center. The limiting luminosity for which the two forces compensate for each other is

$$\frac{GMm_p}{D^2} = \frac{L_{\text{Edd}}\sigma_T}{4\pi D^2 c} \quad \rightarrow \quad L_{\text{Edd}} = \frac{4\pi GMm_p c}{\sigma_T} \approx 1.26 \times 10^{38} \left(\frac{M}{M_\odot} \right) \text{ erg s}^{-1} \quad (2.6)$$

where L_{Edd} is the Eddington luminosity. At higher luminosities, the outward radiation pressure would exceed the inward gravitational attraction and accretion would be halted. For accretion-powered objects, the Eddington limit implies a limit on the steady accretion rate. The mass accretion rate corresponding to the Eddington luminosity is

$$\dot{M}_{\text{Edd}} \approx 1.5 \times 10^{-8} \left(\frac{R}{10 \text{ km}} \right) \frac{M_\odot}{\text{yr}} . \quad (2.7)$$

Any additional mass is blown off by radiation pressure. However, it should be noted that the previous derivation assumes a steady and spherically symmetric accretion flow mainly composed of fully ionized hydrogen. For different geometries of the accretion flow and in realistic situations, the previous Eddington limit relation provides only a ‘‘crude’’ estimate.

2.1.1 Roche Lobe Overflow

In an interacting binary system, one of the main processes for the transfer of matter between the two objects is the so-called *Roche lobe overflow*. During their evolutionary lifetimes, if one of the stars increases its size (or their binary separation shrinks) to the point where the gravitational pull of the companion can strip off the outer layers of its envelope, the matter starts flowing between the two objects. Let us consider a test particle moving in the gravitational field of a binary system, composed of the *donor* star with mass M_2 and the compact object with mass M_1 , both rotating around the center of mass. The orbit of a test particle in the gravitational potential due to the two massive stars orbiting each other under the influence of their gravitational attractions can be assumed to be circular, as the test particle does not perturb the orbits of the two stars (Frank et al., 1992). This is usually a good approximation for binary systems, as tidal effects tend to circularize originally eccentric orbits on timescales shorter than the average time over which mass transfer occurs. Moreover, the two massive stars are assumed to be ‘‘centrally condensed’’ and can be considered as point-like masses. The motion of the gas particles (which

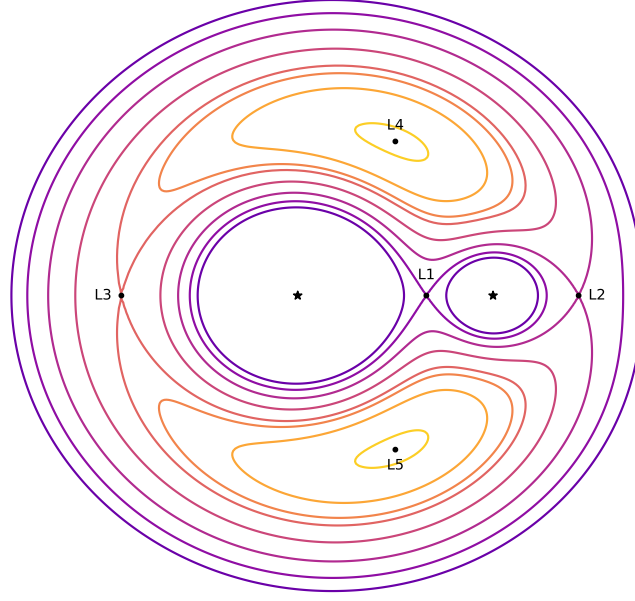


Figure 2.1: Deprojected equipotential surfaces of the Roche potential ϕ_R on the plane orthogonal to the angular velocity ω . The *Lagrange* points L_1 , L_2 , L_3 , L_4 and L_5 are defined by $\nabla\phi_R = 0$. The point L_1 is known as the *saddle* point and it is crossed by matter in motion from the donor towards the accretor.

belong to the donor star) is governed by the Euler equation

$$\frac{\partial \mathbf{v}}{\partial t} + (\mathbf{v} \cdot \nabla) \mathbf{v} = -\frac{\nabla P}{\rho} - 2\boldsymbol{\omega} \times \mathbf{v} - \boldsymbol{\omega} \times (\boldsymbol{\omega} \times \mathbf{r}) - \nabla\phi_G \quad (2.8)$$

where the left hand side represents the total derivative of the fluid velocity \mathbf{v} and the right hand side contains the pressure gradient, the Coriolis and Centrifugal terms and the gradient of the gravitation potential ϕ_G of the system. The angular velocity of the binary system $\boldsymbol{\omega}$ can be computed from Kepler's law in terms of a unit vector \hat{e}_n as

$$\boldsymbol{\omega} = \sqrt{\frac{GM}{a^3}} \hat{e}_n, \quad (2.9)$$

where a is the binary separation, i.e. the distance between the centres of mass of the two masses.

Since the centrifugal force admits a potential, we can define the total *Roche* potential as

$$\phi_R = \phi_G + \phi_C = -\frac{GM_1}{|\mathbf{r} - \mathbf{r}_1|} - \frac{GM_2}{|\mathbf{r} - \mathbf{r}_2|} - \frac{1}{2}(\boldsymbol{\omega} \times \mathbf{r})^2 \quad (2.10)$$

where \mathbf{r}_1 and \mathbf{r}_2 are the position vectors of the centres of the two stars. The locus of points in which that potential is constant is called *equipotential surface* and for this case it corresponds to the surface on which the gravitational force exerted by the two masses on the test mass is balanced by the centrifugal force (see Figure 2.1). The points defined by $\nabla\phi_R = 0$ are called *Lagrange points*. The shape of the equipotentials is entirely governed by the mass ratio $q = M_2/M_1$, while the overall scale depends on the binary separation a .

In order to understand how the mass transfer is triggered, let us consider the donor star, which is evolving slowly so that its surface can be seen, to a first approximation, to be at rest. The Euler equation for a particle on the star surface, since for the previous assumption the Coriolis contribution vanishes, reads as follows

$$-\frac{1}{\rho} \nabla P - \nabla\phi_R = 0 \quad (2.11)$$

and since the surface of the star is in hydrostatic equilibrium

$$\nabla P = 0 \quad (2.12)$$

the star surface turns out to be an equipotential surface. Until the surface of the donor star is smaller than its Roche lobe, there is no flow of matter related to gravitational attraction of the compact star and so the binary system is detached and mass transfer could only proceed through winds. Let us assume that for some reason, possibly related to stellar evolution, the donor star expands to the point where its surface entirely fills its Roche lobe. Any perturbation around the inner Lagrange point (L1; Figure 2.1) will push matter into the Roche lobe of the compact star, starting the accretion mechanism. When mass transfer begins, the parameters q and a of the system will vary: as M_1 increases accreting matter while M_2 decreases, the mass ratio q will change over time; because of the redistribution of the angular momentum within the system, the binary separation a and the period P will also be altered during the mass transfer process.

Since the Roche geometry is determined by a and q , it is important to verify the effect of their variations with time, checking whether the Roche lobe of the donor star will shrink or swell. In particular, in the former case, the Roche lobe-overflow process will be self-sustaining for some time. Each lobe is characterized by an average radius defined as the radius of a sphere that has the same volume as the lobe. Due to the complicated form of the Roche potential (Equation 2.10), numerical calculations are required to compute the lobes radii; a good fit for all values of q is given by the approximate analytical formula (Eggleton, 1983):

$$R_2 = a \cdot \frac{0.49 q^{2/3}}{0.6 q^{2/3} + \ln(1 + q^{1/3})} = a \cdot f(q). \quad (2.13)$$

The variation of the lobe size over time can be written as

$$\frac{dR_2}{R_2} = \frac{da}{a} + \frac{df(q)}{f(q)} \approx \frac{da}{a} \quad (2.14)$$

where the approximation holds as $f(q)$ depends weakly on q . Therefore, when the orbital separation decreases, the radius of the Roche lobe decreases at the same time until it reaches or becomes smaller than the radius of the donor star itself. In this case, the Roche lobe overflow regime can take place and for a sufficiently long time. By combining the angular momentum conservation with the third Kepler law:

$$M_1 a_1^2 \omega + M_2 a_2^2 \omega = \text{constant} \quad \text{and} \quad 4\pi^2 a^3 = G(M_1 + M_2) P_{\text{orb}} \quad (2.15)$$

where a_1 and a_2 are the distances of the two stars from the center of mass and P_{orb} is the orbital binary period, the binary separation variation over time can be written as

$$\frac{da}{a} = \frac{2}{3} \frac{dP_{\text{orb}}}{P_{\text{orb}}} = \frac{2(q-1)}{q+1} \frac{dq}{q}. \quad (2.16)$$

Since dq is always negative as M_2 is losing mass in favor of M_1 , for $q \gtrsim 1$ (i.e. the accreting object has a smaller mass than the donor one), the Roche lobe of the donor star shrinks while the star increases its volume while the binary system loses angular momentum and therefore the mass transfer will continue for a sufficiently long time.

2.1.2 Accretion Disk Structure

As a consequence of the Roche lobe overflow process, the transferring material has rather high specific angular momentum, so that it cannot accrete directly onto the mass-capturing star. The components of particles stream velocity in a non-rotating frame along and perpendicular to the line of centers are

$$v_{\perp} \sim b_1 \omega \sim 100 \left(\frac{M_1}{M_{\odot}} \right)^{1/3} (1+q)^{1/3} \left(\frac{P}{1 \text{ day}} \right)^{-1/3} \text{ km/s} \quad \text{and} \quad v_{\parallel} \lesssim c_s \approx 10 \sqrt{\frac{T}{10^4 \text{ K}}} \text{ km/s} \quad (2.17)$$

where b_1 is the distance of L_1 with respect to the center of M_1 and c_s is the speed of sound in the envelope of the donor star, since the gas is pushed through L_1 by pressure forces. Therefore, as the gas emerges through L_1 , its stream will be almost orthogonal to the line of centers forming a disk around the compact object (see [Frank et al., 1992](#), for more details).

The steady-state structure of the disk is governed by the equation of (magneto)hydrodynamics, since the characteristic macroscopic length of the disk (i.e. its thickness) is much greater than the mean free path of collisions of microscopic particles. This model was introduced by [Shakura and Sunyaev \(1973\)](#) with several assumptions that are common to most models that describe accretion disks:

- the donor star in the binary system has negligible gravitational influence on the disk;
- the self-gravitation of the disk is not important;
- the disk is axisymmetric ($\partial_\phi = 0$) and in stationary state ($\partial_t = 0$);
- the disk is thin, i.e. $h(r) \ll r$;
- particles move around the compact object on Keplerian circular orbits;
- the disk is radiatively efficient, i.e. radiative cooling is the only cooling mechanism.

This model was upgraded right after by [Novikov and Thorne \(1973\)](#) including General Relativity assuming the Kerr spacetime metric and introducing a very convenient formalism of splitting all the relations into Newtonian limits times GR corrections (see also [Sądowski et al., 2011](#); [Abramowicz and Fragile, 2013](#)).

The first fundamental equation is the *rest mass conservation*

$$\nabla_\mu(\rho u^\mu) = 0 \quad (2.18)$$

where ρ is the rest mass density and u^μ the four-velocity. The second fundamental equation that describes the fluid dynamics is

$$\nabla_\mu T_\nu^\mu = 0 \quad (2.19)$$

where the stress-energy tensor is defined as:

$$T_\nu^\mu = u^\mu u_\nu (P + \epsilon) + P g_\nu^\mu - t_\nu^\mu + u^\mu q_\nu + u_\nu q^\mu \quad (2.20)$$

where P is the total pressure, ϵ is the gas internal energy, q^μ is the radiative energy flux. The viscous stress tensor t_ν^μ is then given by

$$t_\nu^\mu = \nu \rho \sigma_\nu^\mu \quad (2.21)$$

with ν the kinematic viscosity coefficient and σ_ν^μ the shear tensor of the velocity field. Assuming that the internal energy density of the gas is much smaller than the gravitational binding energy, we can neglect the contribution of ϵ . When the viscosity results directly from magneto-rotational instability ([Abramowicz and Fragile, 2013](#)), the stress-energy tensor is

$$T_\nu^\mu = u^\mu u_\nu (P + \epsilon + b^2) + (P + b^2/2) g_\nu^\mu - b^\mu b_\nu + u^\mu q_\nu + u_\nu q^\mu \quad (2.22)$$

where the fluid-frame magnetic field b^μ is related to the reference-frame magnetic field B^μ :

$$b^\mu = \frac{1}{u^t} B^\nu (u^\mu u_\nu + \delta_\nu^\mu) . \quad (2.23)$$

These general relations are used to build all relativistic hydrodynamical models of accretion disks. For stationary, axisymmetric accretion flow in the non-relativistic limit, these two equations become the Navier-Stokes equations. Integrating over r and z the mass conservation (Eq. 2.18), the mass accretion rate \dot{M} is

$$\dot{M} = -2\pi r \Sigma V \quad (2.24)$$

where the disk surface density Σ and the fluid radial velocity measured in the local rest frame are introduced as

$$\Sigma \equiv \int_{-h}^{+h} \rho dz \quad (2.25)$$

$$V \equiv \frac{1}{\Sigma} \int_{-h}^{+h} \rho u_r dz . \quad (2.26)$$

Considering the ϕ -component of Eq. 2.19, the general form of the *angular momentum conservation* is

$$\nabla_{\mu}(T_{\nu}^{\mu}\xi^{\nu}) = 0 \quad (2.27)$$

where $\xi^{\mu} = \partial_{\phi}$ is the Killing vector along ϕ associated to axial symmetry of the Kerr metric. Integrating Eq. 2.27 over r and z , assuming that the only non-vanishing component of the stress-energy tensor is $t_{\phi r}$, the final angular momentum conservation can be written as

$$\frac{\dot{M}}{2\pi}(L - L_{\text{in}}) = -2hr^2 t_{\phi r} \quad (2.28)$$

where $L = \Omega r^2$ is the angular momentum per unit mass, Ω is angular velocity of the fluid and L_{in} is the angular momentum at the inner edge of the disk, assuming vanishing torque at the inner boundary.

Evaluating now the t -component of Eq. 2.19, the general form of the *energy conservation equation*

$$\nabla_{\mu}(T_{\nu}^{\mu}\eta^{\nu}) = 0 \quad (2.29)$$

where η^{ν} is the Killing vector related to time symmetry of the Kerr metric. After integration over z (similarly to Landau, 1932), the energy balance equation can be obtained as

$$\Sigma T \left[u^t \frac{\partial S}{\partial t} + u^r \frac{\partial S}{\partial r} \right] = Q_{\text{vis}} - Q_{\text{rad}} \quad (2.30)$$

where S is the entropy per unit mass and on the right hand side the local viscous heat generation rate Q_{vis} and the radiative cooling rate are defined as (Abramowicz et al., 1996)

$$Q_{\text{vis}} = T^{\mu\nu} \sigma_{\mu\nu} \approx 2T^{r\phi} \sigma_{r\phi} \quad \text{and} \quad Q_{\text{rad}} = \frac{32\sigma T^4}{3\Sigma\kappa} \quad (2.31)$$

where σ is the Stefan-Boltzmann constant and κ is the opacity.

After vertical integration, the *vertical hydrostatic equilibrium* (i.e. the θ -component of Eq. 2.19) can be derived assuming that the pressure gradient is balanced by the vertical component of the gravitational force

$$\frac{dP}{dz} = \rho g = P_0 \frac{Mz}{r^3} \quad (2.32)$$

which has the same form as in the Newtonian case but with different tidal gravitation acceleration g .

In accretion disks, the angular momentum is therefore transported by viscosity. Let us consider a parallel shear flow where the upper layer moves at a higher velocity and momentum is transferred from the top to the bottom. This leads to deceleration of the upper layer and acceleration of the bottom layer. Viscosity plays a role in reducing shear and promoting the formation of uniform layers. The horizontal viscous force exerted on the unit surface of the interface plane is

$$t_{xy} = \eta \frac{\partial v_x}{\partial y} \quad (2.33)$$

where on the right hand side there are $\eta = \rho\nu$ is the coefficient of dynamical viscosity and the velocity gradient along the normal direction. In the accretion disk case, we do not deal with parallel layers but

with differentially rotating annuli, with rotational velocity increasing in Keplerian flows inward. As a consequence, viscosity will transfer the angular momentum from the inner annulus to the outer one. This results in the loss of angular momentum by matter, causing it to move inward. If the accretion disk is truncated at a specific outer radius and there is no external force acting on it, the outermost annuli will receive all of the transported angular momentum and move outward towards infinity. The viscous force per unit area acting in the azimuthal direction of the interface plane between differentially rotating annuli is

$$t_{r\phi} = \eta \left(\frac{\partial v_\phi}{\partial r} - \frac{v_\phi}{r} \right) = \eta r \frac{\partial \Omega}{\partial r}. \quad (2.34)$$

As the nature of the viscous processes in accretion disks was not well understood at the outset, [Shakura and Sunyaev \(1973\)](#) proposed a sophisticated and plausible framework for accounting for viscosity effects, assuming that the origin of viscosity is somehow linked to turbulence within the gas-dynamical flow. The kinematic viscosity coefficient can be assumed to be

$$\nu \approx v_{\text{turb}} l_{\text{turb}} \quad (2.35)$$

where v_{turb} and l_{turb} are respectively the typical turbulent motion velocity and length scale. Assuming that the velocity of turbulent elements cannot exceed the speed of sound c_s and that their typical size cannot be larger than the thickness of the disk h , one gets

$$v \lesssim c_s h. \quad (2.36)$$

Using the vertical equilibrium equation (Eq. 2.32) and comparing it with the stress tensor in the azimuthal direction (Eq. 2.34)

$$t_{r\phi} \approx -\rho \nu \Omega \quad \text{and} \quad c_s h = \frac{c_s^2}{\Omega} \approx \frac{P}{\rho \Omega} \quad (2.37)$$

one can find that

$$|t_{r\phi}| < P \quad \longrightarrow \quad t_{r\phi} = -\alpha P \quad (2.38)$$

where an adimensional viscosity parameter $\alpha \leq 1$ has been introduced (the so-called α -prescription, [Shakura and Sunyaev, 1973](#)).

2.1.3 Energy Release

The viscous dissipation of energy possessed by fluid particles occurs within the disk and the heating is radiated locally. The standard geometrically thin and optically thick accretion disk implies that photons scatter many times before being emitted from the disk surface, so particles and photons continuously transfer kinetic energies. As a consequence, each element of the disk surface radiates as a blackbody with temperature $T(R)$ related to the dissipation rate

$$\sigma T^4(R) = D(R) = \frac{3GM_* \dot{M}}{8\pi R^3} \left[1 - \left(\frac{R_*}{R} \right)^{1/2} \right] \quad (2.39)$$

where M_* and R_* are respectively the mass and radius of the accretion object. Thus, the (local) blackbody spectrum emitted by each element of the disk surface is

$$I_\nu = \frac{2h\nu^3}{c^2} \frac{1}{e^{h\nu/kT(R)} - 1}. \quad (2.40)$$

Considering an observer distant D from the system whose line of sight angle with respect to the normal of the disk plane is i , the observed flux is

$$F_\nu = \frac{2\pi \cos i}{D^2} \int_{R_*}^{R_{\text{out}}} I_\nu R dR = \frac{4\pi h\nu^3 \cos i}{c^2 D^2} \int_{R_*}^{R_{\text{out}}} \frac{R dR}{e^{h\nu/kT(R)} - 1} \quad (2.41)$$

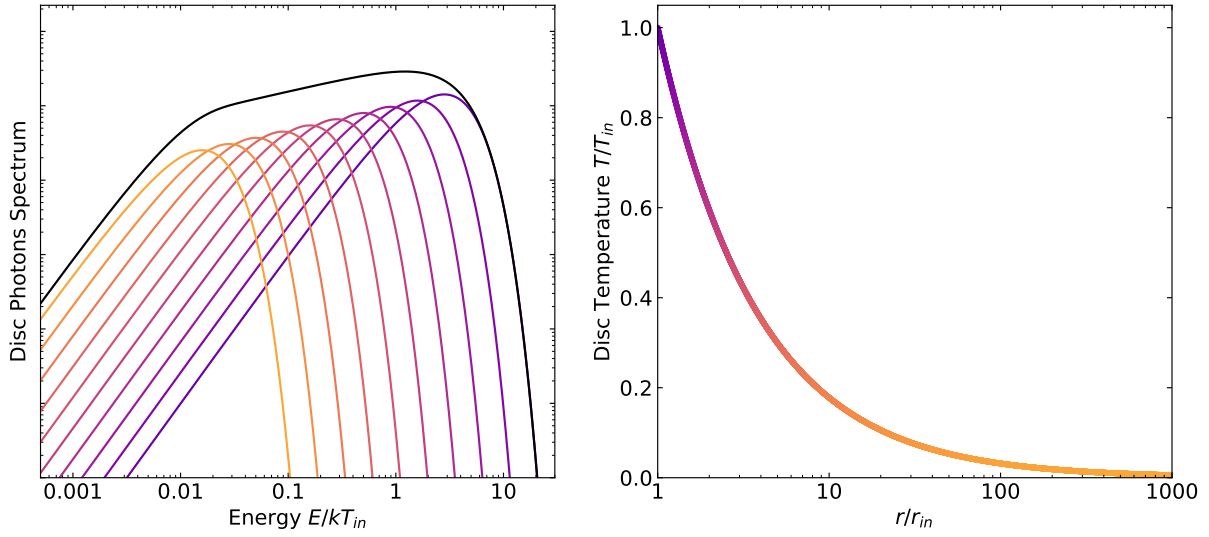


Figure 2.2: Accretion disk spectrum (left panel) with a radial temperature profile $T \propto r^{-3/4}$ (right panel). The disk has been divided into ten annular regions, whose blackbody spectra are represented with different colors, from the hotter inner region in purple to the colder outer region in orange.

which is independent of the disk viscosity and it is roughly a superposition of many subsequent blackbody spectra at slightly different temperatures (Figure 2.2, see also Frank et al. 1992). For $h\nu \ll kT(R_{\text{out}})$, each local spectrum assumes the Rayleigh-Jeans form, while for $h\nu \gg kT(R_*)$ each Planck function takes the Wien form

$$\begin{cases} B_\nu(T) \propto \nu^2 T & \text{for } h\nu \ll kT(R_{\text{out}}) \\ B_\nu(T) \propto \frac{2h\nu^3}{c^2} e^{-h\nu/kT} & \text{for } h\nu \gg kT(R_*) \end{cases} \quad (2.42)$$

For intermediate frequencies $kT(R_{\text{out}}) \ll h\nu \ll kT(R_*)$, the integrated spectrum is a “stretched-out” blackbody, $F_\nu \propto \nu^{1/3}$. The total luminosity emitted by the whole disk is

$$L_{\text{disk}} = 2 \int_{R_*}^{R_{\text{out}}} D(R) 2\pi R dR = \frac{3GM\dot{M}}{2} \int_{R_*}^{R_{\text{out}}} \left[1 - \left(\frac{R_*}{R} \right)^{1/2} \right] \frac{dR}{R^2} = \frac{GM\dot{M}}{2R_*} = \frac{1}{2} L_{\text{acc}} \quad (2.43)$$

where $R_{\text{out}} \rightarrow \infty$ is assumed. Half of the available energy is radiated as matter moves slowly spiraling towards the central object.

2.1.4 Boundary Layer

If the central object is a NS, the accretion disk could extend all the way down to the star surface. In a realistic situation, since the NS rotates slower than the accretion disk, the disk material begins to decrease the velocity from its Keplerian value Ω_{Kep} to the angular velocity of the NS surface Ω_{NS} in a *boundary layer* of radial extension b (Figure 2.3). For a thin disk, $b \ll R_{\text{NS}}$ and thus the velocity is very close to the Keplerian value at $R_{\text{NS}} + b$ (where $d\Omega/dr = 0$) and then starts to decrease towards the NS, but if b is instead comparable to R_{NS} , there is no more a boundary layer and the disk will become thick (Frank et al., 1992). For strong magnetized NSs (e.g. Pulsars), the inner regions of the disk could be disrupted by the magnetic field and the accretion flow will be redirected onto the magnetic poles.

The luminosity radiated by the boundary layer can be easily derived from the specific energy difference between the Keplerian velocity at R_* and a particle with angular velocity Ω_* on the star, including also the stress contribution on the “edge” on the star surface (see Frank et al., 1992)

$$L_{\text{BL}} = \frac{GM\dot{M}}{2R_*} \left[1 - \frac{\Omega_*}{\Omega_K} \right]^2 \quad (2.44)$$

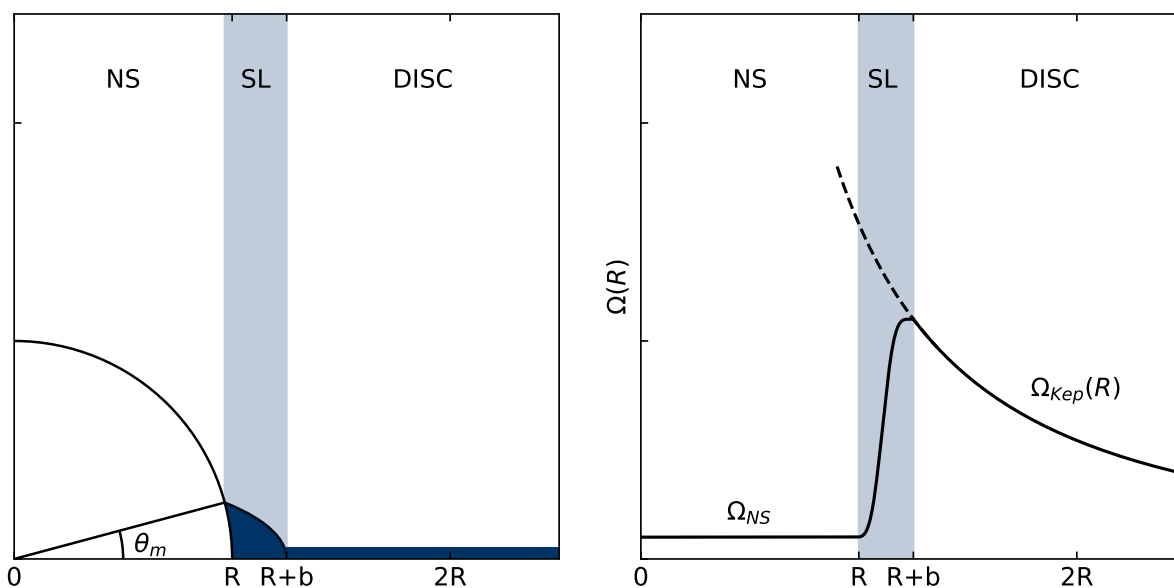


Figure 2.3: *Left panel:* Schematic representation of the boundary/spreading layer between the accretion disk and the NS surface, extending up to a latitude θ_m . *Right panel:* Radial dependence of the NS, spreading layer and disk velocity. The velocity decreases from its Keplerian value Ω_{Kep} to the angular velocity of the NS surface Ω_{NS} in the boundary layer (Inogamov and Sunyaev, 1999; Popham and Sunyaev, 2001).

and L_{BL} will reduce to half L_{acc} for $\Omega_* \ll \Omega_K$ as expected. The luminosity radiated by the boundary layer is emitted through a region of radial extent H on the two faces of the disk. If the accretion rate is high enough, the boundary layer will be optically thick and radiate roughly as a blackbody. With the knowledge of the emitted luminosity, the characteristic boundary layer blackbody temperature is

$$4\pi R_* H \sigma T_{BL}^4 = \frac{GM\dot{M}}{2R_*} \left[1 - \frac{\Omega_*}{\Omega_K} \right]^2 \quad \rightarrow \quad T_{BL} \sim \left(\frac{R_*}{H} \right)^{1/4} T_* \quad (2.45)$$

where T_* is the characteristic blackbody temperature of the disk.

The region of the accretion disk where the gas begins to decelerate is the *boundary layer*, while the *spreading layer* is considered as the gas approaches the NS surface and extends to high latitudes (Inogamov and Sunyaev, 1999; Suleimanov and Poutanen, 2006). For low mass accretion rates, the hot inner flow smoothly joins the optically thin boundary layer and the NS surface provides soft seed photons to the observed spectra (Done et al., 2007). When the accretion rate increases, the temperature of the NS increases and the disk eventually moves inward, with the hot inner flow collapsing into a thin disk. The boundary thus becomes optically thick to electron scatterings, but not completely thermalized into a blackbody (Popham and Sunyaev, 2001).

2.2 Neutron Stars X-ray Binaries

Compact objects in binary systems regularly accrete mass from the companion star and X-ray binary systems are often classified based on the different ways of mass transfer and the type of the donor star:

- In *high-mass X-ray binaries* (HMXBs), the donor star is an early-type massive star (typically a O or B star) with strong high-velocity stellar winds, which constantly transfer mass towards the compact object (Hoyle and Lyttleton, 1939; Bondi and Hoyle, 1944; Bondi, 1952). If the star is already close to its Roche lobe limit, the wind will be particularly focused along the binary axis (Friend and Castor, 1982).

- In the *Be binaries*, the donor is a fast rotating Be star (characterized by a spectrum with hydrogen emission lines) with an equatorial circumstellar gas disk (Porter and Rivinius, 2003).
- In *low-mass X-ray binaries* (LMXBs), the donor is a main sequence, evolved star or a white dwarf (typically lower than $\sim 1 M_{\odot}$) and the central object is surrounded by an accretion disk fed by Roche-lobe overflow passing through the inner Lagrange point L_1 . The accreted matter could eventually hit the stellar surface and generate EM radiation primarily in X-ray wavelengths. The accretion disk also emits radiations by viscous dissipation and both of these emissions are powered by the gravitational potential energy release (see Section 2.1).

Weakly magnetized NS-LMXBs are traditionally classified into a few broad categories according to their joint timing and spectral properties in the “classic” X-ray band (1–10 keV) and following their tracks in the Hard-color/Soft-color diagrams (CCDs) or hardness-intensity diagrams (HIDs, Hasinger and van der Klis, 1989; van der Klis, 1989; van der Klis, 2006):

- High Soft State Z-sources ($> 10^{38}$ erg/s)
- High Soft State Bright Atoll sources ($10^{37} - 10^{38}$ erg/s)
- Low Hard State Atoll sources ($\sim 10^{36}$ erg/s)

Z-sources trace out a Z-shaped tracks in the CCDs and HIDs on timescales of hours to a day, consisting of three branches (Hasinger and van der Klis, 1989; Church et al., 2006): the *Horizontal Branch* (HB), the *Normal Branch* (NB) and the *Flaring Branch* (FB). The luminosities and the accretion rate increase while the sources move from the HB to the FB (van der Klis, 2006; Migliari and Fender, 2006). Z-sources can be further divided into two subgroups: Cyg X–2-like sources (e.g. Cyg X–2, GX 5–1, GX 340+0) displaying the full Z-track with full HB, NB and FB but with weak flaring; on the other hand, in Sco X–1-like sources (e.g. Sco X–1, GX 17+2, GX 349+2) there is hardly any HB, but flaring is strong and frequent with large increases in X-ray intensity (Church et al., 2012). From the spectral point of view, the Z-sources are characterized by parameters that remain relatively stable during the motion along the Z-track (Di Salvo et al., 2000; Farinelli et al., 2009). The most noticeable transient feature is instead a hard X-ray excess above 30 keV, which occurs along the HB and appears to be correlated with radio jet emission (D’Amico et al., 2001; Di Salvo et al., 2002; Iaria et al., 2004; Farinelli et al., 2005; Paizis et al., 2006; Migliari and Fender, 2006). Atoll-sources cover a wide range in luminosities, from 0.1% L_{Edd} up to about 50% L_{Edd} (van der Klis, 2006), accreting at relatively low rates (compared to Z-sources; Migliari and Fender 2006). Many of these sources frequently exhibit X-ray bursts. At high luminosities (or accretion rate), Atoll-sources trace out a well-defined curved *banana branch* in the CCDs or HIDs, along which sources move back and forth on timescales of hours to day, sometimes showing also secular motion not affecting the variability. The banana branch is further divided into the *upper banana*, the *lower banana* and the *lower left banana* based on timing properties (i.e. low-frequency noise and kHz quasi-periodic oscillations; van der Klis et al. 1990). The harder regions of the CCD patterns are traced out at lower luminosities and the motion is often much slower (from days to weeks), forming isolated patches in the CCD or HIDs (the *island state*; Hasinger and van der Klis 1989). In this state, the motion of the source does not often follow a well-defined track, since the secular motion and the branch motion have similar timescales. The majority of persistent NS-LMXBs are generally observed in the High Soft State (HSS), with only a few Atolls observed persistently in the Low Hard State (LHS), but most transients and some persistent sources can easily perform state transitions from one state to the other, e.g. XTE J1701–462 (Lin et al. 2009a; more details in Section 4.8) or GS 1826–238 (Sánchez-Fernández et al. 2020; more details in Section 4.3). The timing and spectral properties of weakly magnetized NS-LMXBs are very similar to those observed in BH-LMXBs (see Muñoz-Darias et al., 2014; Motta et al., 2017).

The X-ray emission of NS-LMXBs is generally modelled with two main spectral components: a soft thermal emission produced by the relatively cold and optically thick accretion disk and a harder component related to the inverse Compton scattering of these soft photons by the hot electron plasma in the corona or

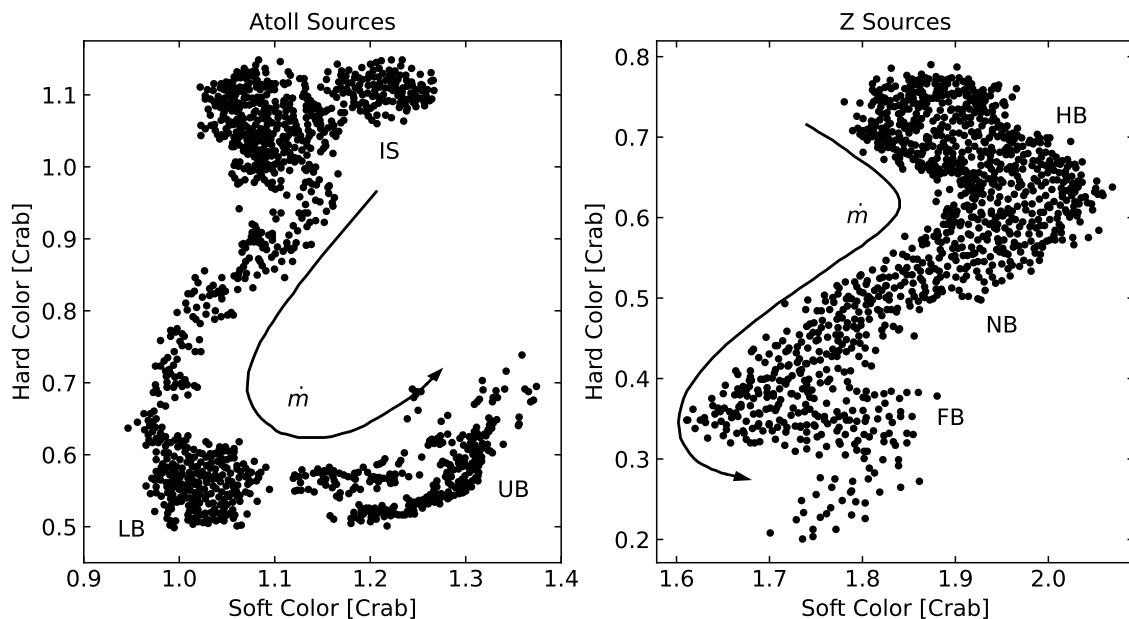


Figure 2.4: Typical CCD of Atoll (*left panel*) and Z-sources (*right panel*). For both types of NS-LMXBs the expected direction of increasing mass accretion rate \dot{m} is indicated (Migliari and Fender, 2006). For Atolls, the sources pass through the island state (IS) towards the lower (LB) and upper banana branches (UB). Z-sources move along three branches: the horizontal (HB), the normal (NB) and the flaring branch (FB).

in the spreading layer close to the NS (*eastern model*, Mitsuda et al., 1984, 1989). The opposite occurs in the *western model* (White et al., 1988): the hotter, NS population is directly detected and modelled by pure blackbody while the cold, disk photons are Compton-upscattered by the electron corona. These two models are largely degenerate spectroscopically; however, frequency-resolved spectra of a sample of Atoll- and Z-sources show lower kHz quasi-periodic oscillations with the same spectral shapes of the boundary layer (i.e. Comptonized) component (Gilfanov et al., 2003; Revnivtsev and Gilfanov, 2006; Revnivtsev et al., 2013). Since the most rapid variability is associated with the boundary layer rather than the disk, this strongly points in favor of an Eastern-like scenario (see also review by Done et al., 2007). However, it is reasonable to think that both soft seed photon populations get scattered in the corona (Cocchi et al., 2011). Moreover, the frequent observation of a Fe emission line at ~ 6 keV, especially in Z-sources, strongly suggests that Compton reflection by a colder medium (such as the outer accretion disk itself) is a further spectral component that needs to be taken into account (D’Ài et al., 2009; Ludlam et al., 2019; Iaria et al., 2020; Ludlam et al., 2022; Saavedra et al., 2023). The overall spectra of Z-sources and bright Atolls are very soft, compared to hard state sources with an high-energy cut-off above ~ 100 keV (Barret et al., 2000; Barret and Olive, 2002). However, an additional strong component above 30–40 keV (*transient hard tail*) was occasionally detected in some sources in the soft state. The first detection was in the Sco X–1 spectrum, with a hard component dominating the spectrum above 40 keV (Peterson and Jacobson, 1966). The observations of these transient hard tails in the spectra of Z-sources are strictly correlated with the HB positions in the CCD (D’Amico et al., 2001; Di Salvo et al., 2002; Farinelli et al., 2005) and with the radio emission (Paizis et al., 2006; Migliari and Fender, 2006; Migliari et al., 2007). Hard states are associated with weak radio emission, which increases in the intermediate state (along the HB) when the accretion rate is higher and then is quenched in the soft state (Fender and Hendry, 2000; Paizis et al., 2006; Fender et al., 2007), corresponding to the NB and FB of the Z-track and accretion rates very close to the critical (Eddington) values. Hard tails may possibly be produced by scattering in a jet-like outflow (Reig and Kylafis, 2016).

2.3 Physical processes

The accretion disk, the corona and the boundary layer constitute a fairly complex system in which important interactions could take place. The main processes involved in the interaction between high-energy photons and atoms or electrons are Compton scattering, photoelectric absorption, and electron-positron pair production (Rybicki and Lightman, 1979; Bradt, 2008; Longair, 2011).

2.3.1 Compton Scattering

In the non-relativistic limit ($h\nu \ll m_e c^2$), photons are scattered elastically in a random direction by free charge particles and the EM frequency does not change after the interaction (*Thomson scattering*; Rybicki and Lightman 1979). In this low-energy limit, the electric field \mathbf{E} of the incident radiation accelerates the electron, which in turn re-emits a photon at the same frequency as the incident EM wave, according to the Larmor formula (Eq. 1.1). As the electric field must always be perpendicular to the propagation direction, its component in the scattering plane is reduced by a factor $\cos \theta$. The average scattering cross section for unpolarized EM radiation is

$$\frac{d\sigma_T}{d\Omega} = \frac{1 + \cos^2 \theta}{2} r_0^2 \quad (2.46)$$

where r_0 is the classical electron radius

$$r_0 = \frac{e^2}{4\pi\epsilon_0 m_e c^2} = 2.81794 \times 10^{-15} \text{ m} . \quad (2.47)$$

The integrated Thomson cross section can be derived from Eq. 2.46 as

$$\sigma_T = \int_0^{2\pi} d\phi \int_{-1}^1 d(\cos \theta) \frac{d\sigma_T}{d\Omega} = \frac{8\pi}{3} r_0^2 = 6.65246 \times 10^{-29} \text{ m}^2 . \quad (2.48)$$

If photon energy is comparable or greater with respect to the electron rest mass energy, non-classical effects have to be considered. In this case, the momentum transferred from the photon to the electron can not be neglected and the scattering becomes inelastic, resulting in a decrease in energy and an increase in the wavelength of the photon (*Compton scattering*). When the energy and momentum conservation during the scattering are combined, the shift in wavelength and energy can be easily derived.

$$\lambda_f - \lambda = \frac{h}{m_e c} (1 - \cos \theta) \quad \text{and} \quad E_f = \frac{E}{1 + \frac{E}{m_e c^2} (1 - \cos \theta)} \quad (2.49)$$

and the energy variation depends only on the scattering angle θ (Rybicki and Lightman, 1979). Compton scattering results in being not isotropic, so the probability that a photon will be scattered is higher when θ is close to 0. The fully relativistic angular distribution of the scattering and the differential cross section has been derived by Klein and Nishina (1929), assuming free electrons at rest, as

$$\frac{d\sigma_{\text{KN}}}{d\Omega} = \frac{r_0^2}{2} \frac{E_f^2}{E^2} \left[\frac{E}{E_f} + \frac{E_f}{E} - \sin^2 \theta \right] \quad (2.50)$$

and, in the non-relativistic regime, $E \ll m_e c^2$ and $E_f \rightarrow E$, so the Thomson cross section (Eq. 2.46) is recovered. The net effect is to reduce the cross section from its classical value as the photon energy becomes large. The probability of a photon being scattered in a specific direction θ is

$$\sigma_{\text{KN}} = \int_0^\pi \frac{d\sigma_{\text{KN}}}{d\Omega}(\theta) 2\pi \sin \theta d\theta = \frac{3}{4} \sigma_T \left[\frac{1+x}{x^3} \left(\frac{2x(1+x)}{1+2x} - \ln(1+2x) \right) + \frac{1}{2x} \ln(1+2x) - \frac{1+3x}{(1+2x)^2} \right] \quad (2.51)$$

where $x = h\nu/(m_e c^2)$.

Photons that interact via Compton scattering with electrons not at rest in the reference frame of the observer may also gain energy, contrary to the results of Eqs. 2.49 (*inverse Compton scattering*; Rybicki and Lightman 1979). The average relative energy gained by the photon during a single scattering is

$$\frac{\Delta E}{E} = \frac{P_C}{\sigma c U_{\text{rad}}} = \frac{4}{3} \gamma^2 \beta^2 \quad (2.52)$$

where $E = h\nu$ is the energy of the photon, P_C is the power emitted by Compton scattering by an electron with Lorentz factor γ

$$P_C = \frac{4}{3} \sigma c U_{\text{rad}} \gamma^2 \beta^2 \quad (2.53)$$

and U_{rad} is the radiation energy density before the scattering. As a consequence, low-energy photons are converted into high-energy photons by a factor γ^2 . Therefore, inverse Compton scattering is a very efficient process to create very high-energy photons.

When a population of cold photons interact with a region of free electrons with sufficient optical depth, the inverse Compton scattering modifies the photon spectrum. On average, the incoming photons are scattered to higher energies if they are less energetic than the electron population. On the other hand, photons are scattered to lower energies if they are more energetic than free photons. The average energy variation of the photons per collision is (Ghisellini, 2013)

$$\frac{\Delta E}{E} = \frac{4kT_e - h\nu}{m_e c^2} \quad (2.54)$$

where T_e is the temperature of electron population, assuming a quasi-thermal Maxwellian distribution of electrons.

The average number of scatterings is strictly related to the optical depth of the electron plasma

$$\tau = n_e \sigma_T l \quad (2.55)$$

where n_e is the electron density and l the typical size of the electron distribution. The probability that a photon can cross the electron plasma without scattering is $e^{-\tau}$. When $\tau < 1$, most of the photons do not interact with electrons and pass directly through the plasma. If $\tau > 1$, the photons are scattered τ^2 times on average before leaving the plasma and the mean free path is $\lambda = l/\tau$. The importance of inverse Compton scattering is described by the Compton parameter y , which represents the average energy gain of photons when crossing the electron distribution. If $y > 1$ the Comptonized spectrum has more energy than the seed photon spectrum and the Comptonization is important, while for $y \ll 1$ the photon spectrum is not modified (Pozdnyakov et al., 1983; Zdziarski, 1988; Ghisellini, 2013). The final Comptonization spectrum is a power-law spectrum with a high-energy cut-off and the spectral shape depends mainly on the temperature and the optical depth of the plasma. When the temperature or the optical depth increases, the spectral slope becomes harder and the spectral index of the power-law decreases. If $\tau \gg 1$, the equilibrium between photons and electrons is reached and the temperature will be the same. Since photons are conserved, the spectrum has a Wien shape

$$F_\nu \propto \nu^2 e^{-\nu} \quad (2.56)$$

which is harder than a blackbody at low frequencies.

2.3.2 Photoelectric Absorption

X-ray photons may also be absorbed by particles in the interstellar medium between the source and the observer (e.g. interstellar dust or material in molecular clouds) or from the companion star and the accretion disk. This is the dominant process for low photon energies, below 1–10 keV. The *photoelectric absorption* consists in the absorption of a photon by an atom and the release of a bound electron. When an

incident photon interacts with an atom, it transfers all of its energy to the atom. If the energy of the photon exceeds the energy level E_l , an electron is emitted from that level. The remaining energy is manifested as the kinetic energy of the ejected electron:

$$E_e = h\nu - E_l. \quad (2.57)$$

As the energy of a photon increases, its likelihood of ejecting more tightly bound electrons from the nucleus also increases. The probability of absorbing photons depends on the energy. Low-energy X-rays have a higher likelihood of being absorbed compared to high-energy X-rays. This is because the cross section for photoelectric absorption decreases approximately as ν^{-3} . Furthermore, the absorption cross section is strongly influenced by the atomic number Z of the elements. Consequently, the contribution of heavier elements to the overall absorption cross section is more significant at X-ray energies, although they are less abundant than hydrogen. The photoelectric absorption cross section for photons with energy $E_l \ll h\nu \ll m_e c^2$ for the emission of electrons from the K-shells of an atom is (Karzas and Latter, 1961; Rybicki and Lightman, 1979)

$$\sigma_K = 4\sqrt{2}\sigma_T\alpha^4 Z^5 \left(\frac{m_e c^2}{h\nu}\right)^{7/2} \quad (2.58)$$

where $\alpha = e^2/2\epsilon_0 hc$ is the fine structure constant. The photoelectric absorption cross section is then summed up over all the different elements, weighted by their cosmic abundances

$$\sigma_{\text{tot}}(E) = \frac{1}{n_H} \sum_i n_i \sigma_i(E) \quad (2.59)$$

where n_H is the abundance of hydrogen, the most abundant element. When the energy of the photon corresponds to the ionization state of the absorbing element, the probability of absorbing it dramatically increases. This results in an *absorption edge* in the spectrum.

2.3.3 Reflection

In addition to thermal emission, the X-ray photons coming from the NS or from the boundary layer may also be reflected by the disk itself (Fabian et al., 1989). Reflection occurs when photons interact with electrons in the surrounding material, leading to various physical phenomena. In X-ray binary systems, reflection becomes particularly important when the accreting compact object emits a strong X-ray continuum. The continuum radiation can illuminate the surrounding material in the disk, causing X-ray photons to scatter or be absorbed and subsequently re-emitted. The interaction probability depends on the energy of the photon and the composition and ionization state of the matter. The reflection spectrum depends on the incident radiation spectrum (Fabian et al., 2000).

In the accretion disk, incident photons may undergo photoelectric absorption or Compton scattering depending on their energy. Soft X-ray photons ($E_\gamma \lesssim 15$ keV) are mainly absorbed in the cold medium and reprocessed at higher energies, whereas hard X-ray photons are rarely absorbed and are predominantly Compton scattered at lower energies until they are emitted from the system or photoabsorbed. These effects lead to the characteristic *Compton hump* in the spectrum at ~ 30 keV. Additionally, there is an emission line spectrum resulting from the fluorescent $K\alpha$ lines of the most abundant metals (Figure 2.5, *left panel*). After that X-ray photons undergo photoelectric absorption by the material in the accretion disk, they can be re-emitted via Auger de-excitation or through the emission of a fluorescent line. Following the K-shell photoabsorption by a high-energy photon, the inner shell electron of an atom is removed and electron cascades from higher shells will fill the vacancy. The emitting photon may also be absorbed by another electron in the atom, leading to its release from the atom (the so-called *Auger electron*). These effects after photoelectric absorption lead to the emission of fluorescent lines at precise energies that correspond to the energy level differences within the ion.

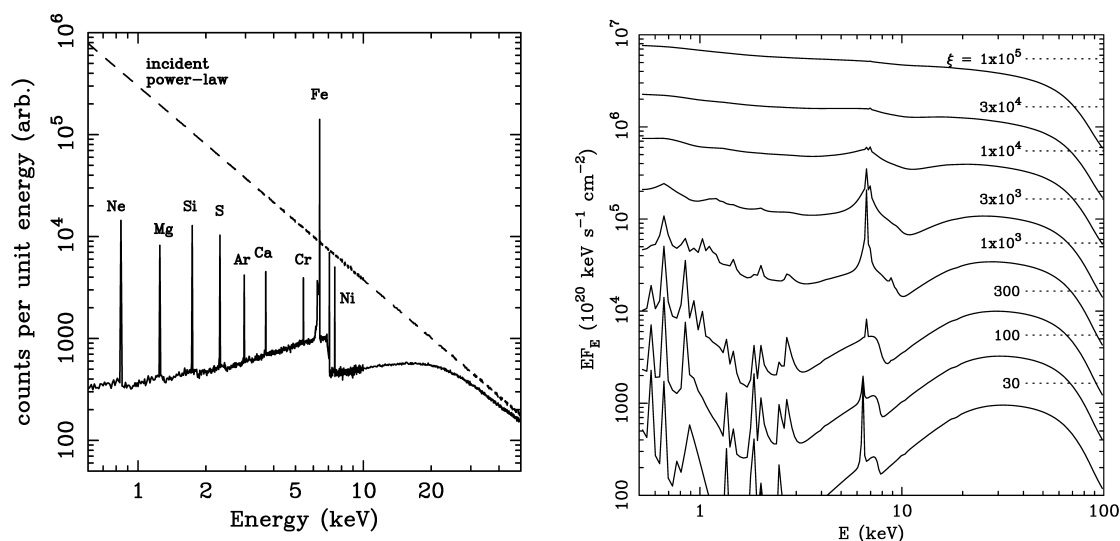


Figure 2.5: *Left panel*: X-ray reflection spectrum obtained for an incident power-law spectrum (dashed line) on a cold gas with cosmic abundances (Reynolds, 1997). *Right panel*: X-ray reflection spectrum from ionized matter for different values of the ionization parameter ξ (Fabian et al., 2000).

Due to the iron abundance and the large absorption cross section for K-shell electrons, the strongest X-ray emission line expected from accretion disks around a BH or a NS is the $K\alpha$ line of iron (Matt et al., 1997). This line appears when an X-ray photon at 7.1 keV is absorbed, allowing the transition from the L- to the K-shell, emitting a doublet line centered at 6.4 keV (for neutral iron), which could not be resolved by the last generation of X-ray telescopes but could now be observed for the first time now by *X-Ray Imaging and Spectroscopy Mission (XRISM)*, a JAXA X-ray space telescope in partnership with NASA launched on 2023 September 6). The emission line depends on both the abundances and the ionization states of the different species. In particular, atomic abundances will have an impact on the intensities of the different fluorescent lines, whereas ionization states regulate the energies and intensities of the lines (Fabian et al., 1989). The ionization parameter is defined as

$$\xi(r) = \frac{4\pi F(r)}{n_e} \quad (2.60)$$

where $F(r)$ is the incident flux per unit area and n_e is the electron density (Reynolds and Nowak, 2003). For weakly ionized disks ($\xi < 100 \text{ erg cm s}^{-1}$), the iron line is expected at 6.4 keV with a weak iron absorption edge at 7.1 keV and the spectrum shows strong absorption features below 10 keV and weak Compton scattering of the continuum. As ionization increases ($100 \lesssim \xi \lesssim 500 \text{ erg cm s}^{-1}$), the iron is more ionized (predominantly Fe XVII-Fe XXIII, with a vacancy in their L-shells) reducing the intensity of the $K\alpha$ line. For high ionization ($500 \lesssim \xi \lesssim 5000 \text{ erg cm s}^{-1}$), all low-Z elements are completely ionized to allow the Auger effect, while Fe XXV and Fe XXVI emit lines respectively at 6.67 and 6.97 keV with the corresponding absorption edges increased to 8.85 and 9.28 keV. In the fully ionized regime ($\xi > 5000 \text{ erg cm s}^{-1}$), the disk is too ionized to show any atomic signature. No iron lines or edges are then visible (see Figure 2.5; Fabian et al. 2000).

Radiation is emitted in a narrow spectral line at the specific energy in the local rest frame corresponding to the energy gaps between different levels (see Figure 2.6, left panel). The observed energy can be shifted depending on the emitting location in the disk and the line profile has to be integrated over the entire accretion disk. Each contribution is weighted by the projected area of the disk as seen by the observer and the final line is then extended over a range of different energies. For a static observer at infinity, the line will be Doppler shifted due to the disk rotation. If the disk is observed almost edge-on (at high inclination), the emission line shape becomes a double-peak profile symmetric about the rest-frame energy of the line,

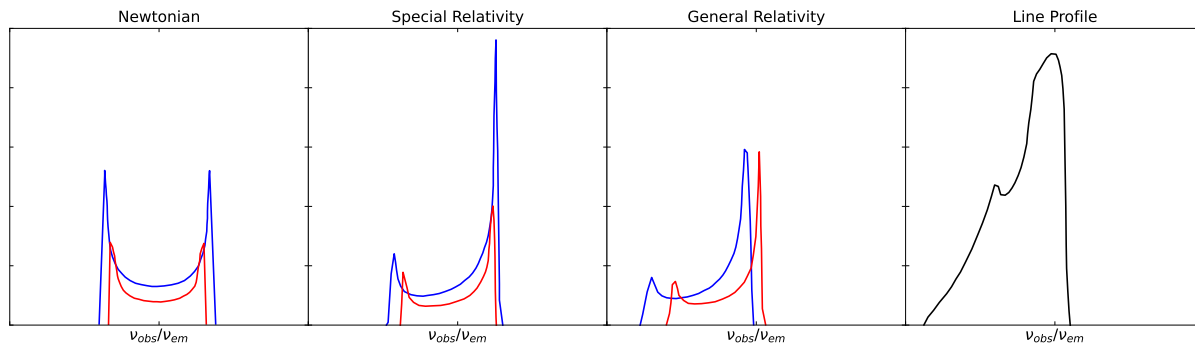


Figure 2.6: Effects produced by special and general relativity on the line profile. The profile of the broad iron line (*right panel*) is caused by the interplay of Doppler and transverse-Doppler shifts, relativistic beaming and gravitational redshifting. The *left panel* shows the symmetric double peaked profiles from two narrow annuli on a non-relativistic disk. In the second panel, the effects of transverse Doppler shifting and relativistic beaming (Special Relativity effects) have been included, while in the third panel the gravitational redshift is added. The two lines indicate the emission from two different regions of the disk and the broadest corresponds to the inner radius (Fabian et al., 2000).

consequently to the redshift and blueshift effect for the material rotating with respect to the observer. If the matter orbits very close to the BH or NS, the Doppler enhancement of the flux becomes important and the blue peak will have more flux than the red one (*Doppler boosting*). However, special relativistic effects must be taken into account since the velocity of the disk is quite high, e.g. at the innermost stable circular orbit the velocity is about half the speed of light. The emission is then further redshifted due to time dilation with respect to the observer at rest at infinity (*transverse Doppler shift* and is beamed in the direction of motion. The net effect on the line profile is to make it asymmetric and shifted about the rest-frame energy of the emission (see Figure 2.6, middle panels). In addition, general relativistic effects are not negligible (Cunningham, 1975). The strong gravitational field around the BH or NS induces the gravitational redshift of the emission and the line profile is shifted to lower energy as the matter of the accretion disk moves closer to the central object (see Figure 2.6, right panel). All these combined effects lead to the observed relativistically broadened line profile (Fabian et al., 1989; Laor, 1991; Matt et al., 1993). The line profile strongly depends on the extension of the disk (i.e. the inner and outer radii), on the inclination and on the spin parameters of the BH. The higher the inclination, the broader the emission line profile, which also extends at higher energies (Figure 2.7). Furthermore, the radial dependence of the line emissivity can influence the final shape of the line (Fabian et al., 1989). Therefore, the overall line profile can be used as a sensitive diagnostic to determine the inclination of the system, as well as the location of the line emission region.

If the geometry configuration of the matter on which the photons are reflected is not spherical (as the accretion disk), a certain amount of linear polarization of the reflected radiation is expected (Matt, 1993). For an optically thick atmosphere above the disk, externally illuminated by a central point-like source, the radiative transfer equation for a plane-parallel layer can be written as (Chandrasekhar, 1960; Matt, 1993)

$$\mu \frac{d\mathbf{I}(\tau, \mu, \phi)}{d\tau} = \mathbf{I}(\tau, \mu, \phi) - \frac{3\lambda}{16\pi} \int_{-1}^{+1} \int_0^{2\pi} \mathbf{S}(\mu, \phi, \mu', \phi') \mathbf{I}(\tau, \mu', \phi') d\mu' d\phi' - \mathbf{F}(\tau, \mu, \phi) \quad (2.61)$$

where $\mathbf{I} = (I_l, I_r, I_U, I_V)$ is the intensity of radiation, $\mathbf{F} = (F_l, F_r, F_U, F_V)$ is the source function and $\mathbf{S}(\mu, \phi, \mu', \phi')$ is the Rayleigh phase matrix. The directions in the meridian plane and perpendicular to it are referred to as l and r , while U and V denote the Stokes parameters. τ is the optical depth along the normal direction ($\tau = 0$ at the upper bound), μ is the cosine of the angle between the direction of the photon and the normal axis, ϕ is the azimuthal angle and $\lambda(E)$ is defined as

$$\lambda(E) = \frac{\sigma_{sc}(E)}{\sigma_{sc}(E) + \sigma_{ph}(E)} \quad (2.62)$$

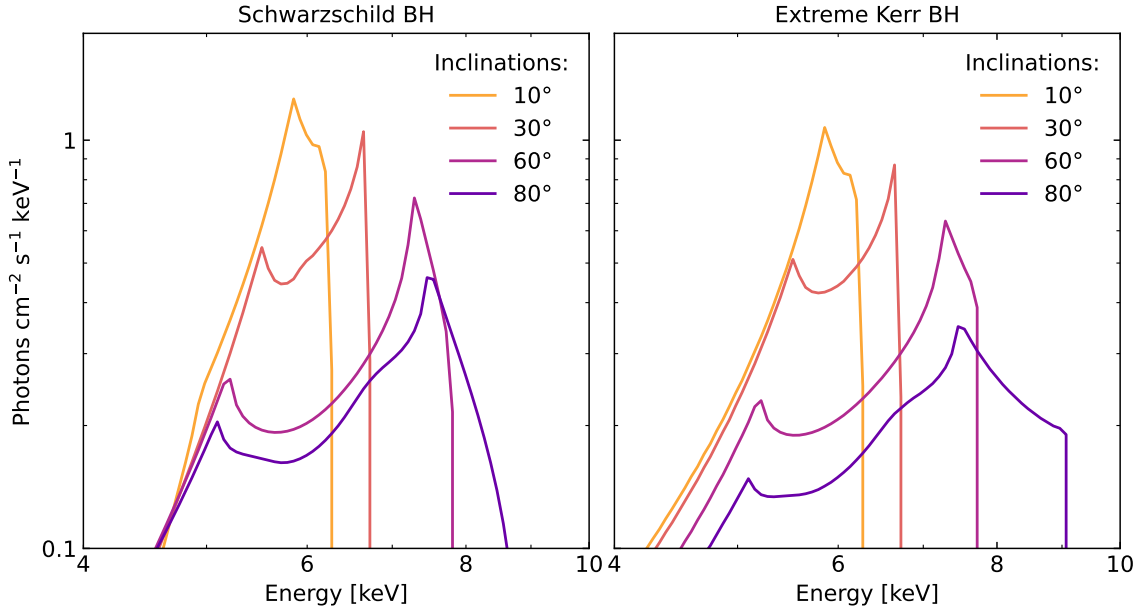


Figure 2.7: Comparison of relativistic iron line profiles for different inclinations (10° , 30° , 60° and 80°) and between an accretion disk around a Schwarzschild BH (narrower line) and a near-extremal Kerr BH (broader line; [Fabian et al. 2000](#)). The disk extends from the innermost stable orbit up to $30 R_G$.

with σ_{sc} and σ_{ph} being the scattering and photoelectric absorption cross-sections respectively. The polarization is then calculated as

$$\delta = \frac{\sqrt{(I_l - I_r)^2 + I_U^2 + I_V^2}}{I_l + I_r} \quad \text{and} \quad \psi = \frac{1}{2} \arctan\left(\frac{I_U}{I_r - I_l}\right). \quad (2.63)$$

Following [Sunyaev and Titarchuk \(1985\)](#), the intensity can be written as the sum of the intensity of the radiation scattered k times

$$\mathbf{I} = \sum_{k=0}^{\infty} \mathbf{I}^k. \quad (2.64)$$

Therefore, the radiative transfer equation for \mathbf{I}^k is

$$\mu \frac{d\mathbf{I}^k(\tau, \mu)}{d\tau} = \mathbf{I}^k(\tau, \mu, \phi) - \frac{3\lambda}{8} \int_{-1}^{+1} \mathbf{S}(\mu, \mu') \mathbf{I}^{k-1}(\tau, \mu') d\mu'. \quad k \geq 1. \quad (2.65)$$

where the ϕ dependence is neglected consider axial symmetry, which is reasonable for the accretion disk. For this configuration, the Rayleigh phase matrix is ([Chandrasekhar, 1960](#))

$$\mathbf{S} = \begin{pmatrix} 2(1 - \mu^2)(1 - \mu'^2) + \mu^2 \mu'^2 & \mu^2 \\ \mu'^2 & 1 \end{pmatrix}. \quad (2.66)$$

Since \mathbf{I}^k is proportional to λ^k , in the energy band where the photoelectric absorption dominates over scattering, only a few terms in Equation 2.64 contribute significantly.

If an external radiation flux \mathbf{F} illuminates the disk with an angle θ_0 with respect to the normal direction with an initial polarization $P_i = (F_r - F_l)/(F_r + F_l)$, after one scattering, the resulting polarization is ([Matt, 1993](#))

$$P^1(\mu, \mu_0) = \frac{(1 - \mu^2)(3\mu_0^2 - 1) + 3P_i(1 - \mu^2)(1 - \mu_0^2)}{2(1 - \mu^2)(1 - \mu_0^2) + (1 + \mu^2)(1 + \mu_0^2) + P_i(3\mu^2 - 1)(1 - \mu_0^2)}. \quad (2.67)$$

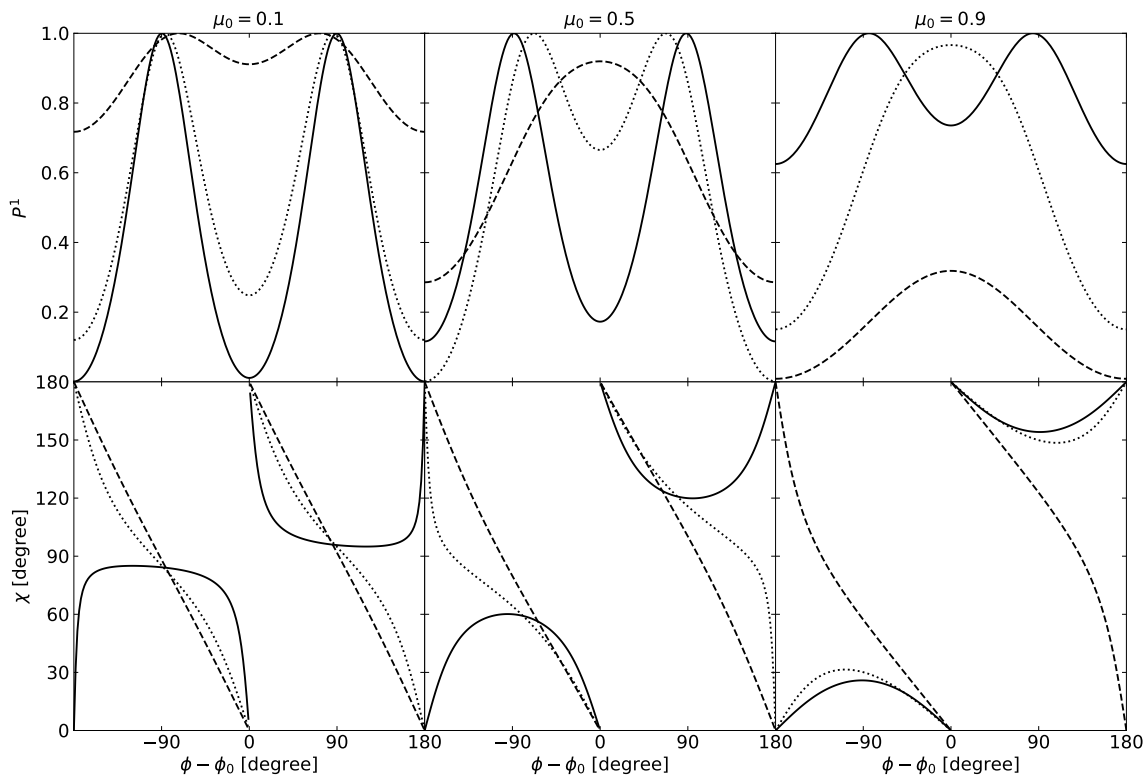


Figure 2.8: Polarization degree (*upper panels*) and angle (*lower panels*) of the once-scattered radiation as a function of the azimuthal angle, for an unpolarized incident radiation with different choices of μ and μ_0 (Matt, 1993).

If P_i (or μ_0) is equal to 1, P^1 does not depend on μ_0 (or P_i) and is given by $(1 - \mu^2)/(1 + \mu^2)$. If there is no axial symmetry for the incident radiation, the results also depend on $\phi - \phi_0$ (see Figure 2.8 in Matt 1993), where ϕ and ϕ_0 are the azimuthal coordinates of the reflected and incident photons, respectively, and, in this case, the third Stokes parameter is no longer null.

For accretion disks around a black hole or a weakly magnetized neutron star, the relativistic effects on the radiative transfer could be important. Considering a standard accretion disk, with inner and outer radii R_{in} and R_{out} and inclination i illuminated by a source of (unpolarized) photons idealized as a point, located at height h above the disk plane on its symmetry axis, the reprocessing of the primary photons occurs on a scale size sufficiently small to neglect the relativistic effects within the matter inside the accretion disk rotating with Keplerian velocity. Therefore, the kinematic and relativistic corrections are applied only to incident and emerging radiation, producing noticeable changes in the polarization properties. The first effect is the rotation of the polarization plane along the photon orbit (Connors et al., 1980; Chen and Eardley, 1991), particularly relevant for low inclination angles (Laor, 1991). The second (more relevant) factor is the symmetry breaking between the half of the disk where the matter goes away from the observer (*redshift*) and the half where the matter approaches the observer (*blueshift*). Due to Doppler boosting, the *blue*-half results to be brighter than the *red* one. Both these effects lead to polarization angles different from 0° (i.e. along the accretion disk plane) or 90° (i.e. along the symmetry axis), contrary to the non-relativistic case. Doppler boosting leads to a polarization angle between 90° and 180° (Matt, 1993). At very high inclinations, the polarization degree is smaller compared to the results without relativistic effects, since light deflection due to the central compact object enhances the contribution of low-polarized photons emitted from the far region of the accretion disk, with respect to the observer (Matt et al., 1992; Matt and Perola, 1992). At lower inclinations, Doppler boosting leads to higher values of the polarization degree, in particular when $\phi_{\text{em}} \sim 0^\circ$, where the emitted photons are highly polarized.

The polarization degree of the reflected radiation strongly depends on the geometrical parameters

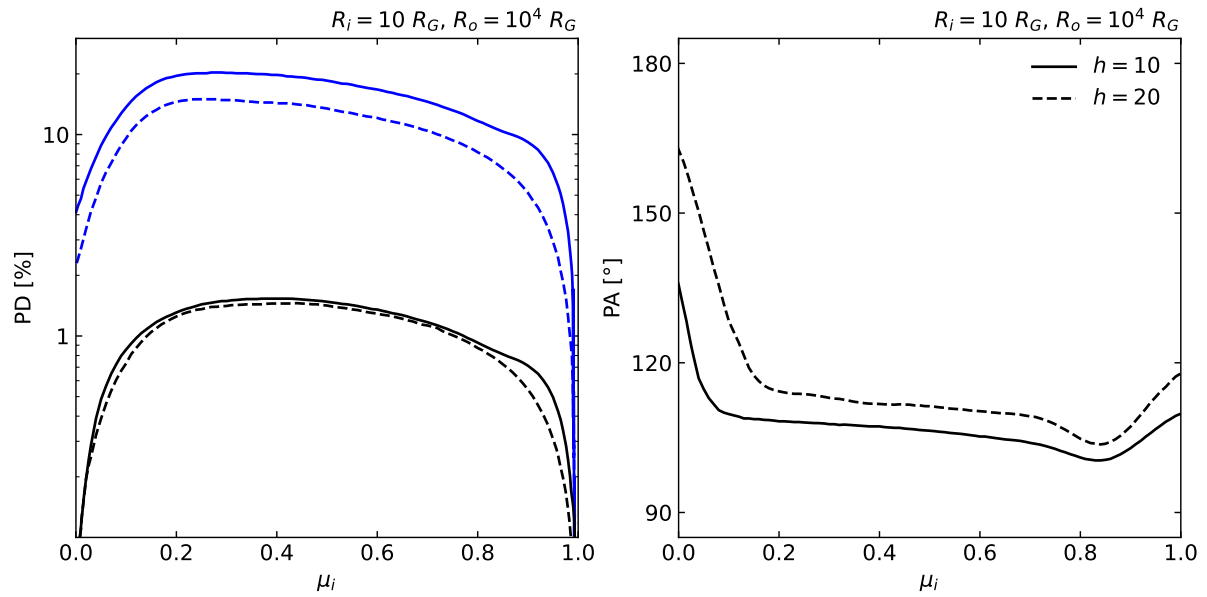


Figure 2.9: Polarization degree (*left*) and angle (*right*) of the reflected radiation (blue curves) and of the total radiation (black curves) as a function of the inclination μ_i , considering an accretion disk with $R_{\text{in}} = 10 R_G$ and $R_{\text{out}} = 10^4 R_G$. The central unpolarized source illuminating the disk is located at height $h = 10$ (solid lines) or 20 (dashed line). See [Matt \(1993\)](#) for more details.

of the disk, increasing with the inclination and the outer radius (up to $\sim 30\%$ for an edge-on disk, [Matt 1993](#)). When kinematic and relativistic effects are included, the expected polarization is higher, except at very high inclinations. The polarization angle rotates depending on the inclination, ranging between 90° and 180° (see Figure 2.9). These results have been confirmed by more recent Monte Carlo numerical simulations ([Podgorný et al., 2022](#)), showing that reflection can locally induce large polarization despite multiple scatterings and other depolarization factors.

3. Numerical Setup & Simulations

The polarization properties of the X-ray radiation coming from NS-LMXBs can be studied for the first time thanks to the NASA/ASI *Imaging X-ray Polarimetry Explorer* (*IXPE*; [Weisskopf et al. 2016, 2022](#); more details in Section 4.2). Combining spectral and polarimetric observations is crucial to constrain several different physical parameters of the NS and the accreting system, in particular to try to understand the configuration and dimensions of the Comptonizing region. Numerical simulations are required to compare *IXPE* observations with theoretical models. The Monte Carlo radiative transfer code `MONK` ([Zhang et al., 2019](#)), adapted for NS-LMXBs, is able to compute the X-ray polarized radiation coming from the accreting system for specific coronal geometries including all special and general relativistic effects.

3.1 MONK

`MONK` is a general relativistic Monte Carlo radiative transfer code capable of computing the spectral and polarization properties of Comptonized radiation coming from the corona in a BH or NS X-ray Binary or AGN, along with direct radiation from the standard accretion disk ([Zhang et al., 2019](#)). The code has been adapted for NS-LMXBs by also including ray-tracing and scattering of photons emitted from the NS surface ([Gnarini et al., 2022](#)).

To account for disk and NS emissivities, the *superphotons* scheme by [Dolence et al. \(2009\)](#) is followed. A superphoton is a package of several identical photons parameterised by: four-position x^μ , wave vector k^μ and polarization vector f^μ , which need to be propagated along the geodesics, its energy at infinity E_∞ , weight w and polarization degree δ . The weight $w \gg 1$ is a pure number that represents the ratio of photons to superphotons, i.e. $dN = w dN_s$ (where N_s is the number of superphotons and N the number of “ordinary” photons). The weight has the physical meaning of the photon generation rate per unit time in observer frame far from the source. Compared to ordinary photons, a superphoton can also “split” into multiple superphotons. A simple blackbody spectrum with kT_{NS} is assumed to model the unpolarized NS surface emission of superphotons. Taking into account an optically thick accretion disk on the equatorial plane, the flux density defined as follows is a relativistic invariant ([Kulkarni et al., 2011](#); [Schnittman and Krolik, 2013](#)):

$$F_\nu = I_\nu \frac{1}{u^t} \cos \theta_{\text{em}} dS d\Omega \quad (3.1)$$

where I_ν is the specific intensity, $1/u^t$ is the factor to transform time from the disk fluid rest frame to a

distant observer's frame, θ_{em} is the polar emission angle with respect to the disk norm in the disk fluid rest frame, dS is the proper area and $d\Omega$ is the solid angle. The number of photons emitted per unit time in the distant observer's frame is also an invariant

$$\dot{N} = \int \frac{F_\nu}{h\nu} d\nu. \quad (3.2)$$

Considering the Kerr spacetime in Boyer-Lindquist coordinate (Eq. 1.15), for photons emitted from an annulus in the equatorial plane of the disk

$$\frac{1}{u^t} = \sqrt{1 - \frac{2}{r} + \frac{4\Omega a}{r} - \Omega^2 \left(r^2 + a^2 + \frac{2a^2}{r} \right)} \quad (3.3)$$

where Ω is the angular velocity of the disk fluid, which for a Keplerian disk is

$$\Omega = \frac{1}{r^{3/2} + a} \quad (3.4)$$

and the proper area is (Wilkins and Fabian, 2012)

$$dS = \frac{2\pi\rho\Gamma}{\sqrt{\Delta}} \sqrt{r^2 + a^2 + \frac{2a^2r}{\rho^2}} dr \quad (3.5)$$

where Γ is the Lorentzian factor of disk fluid as measured by a zero angular momentum observer. The velocity along the ϕ direction as measured by a stationary observer is

$$v_\phi = \frac{(\Omega - \omega)A}{r^2 \sqrt{\Delta}} \quad (3.6)$$

where ω is the frame-dragging angular velocity, hence the Lorentzian factor

$$\Gamma = \frac{1}{\sqrt{1 - v_\phi^2}}. \quad (3.7)$$

The Novikov-Thorne emissivity profile with zero torque at the inner edge of the disk is considered (Novikov and Thorne, 1973), while the local spectrum is the color-corrected blackbody with a color correction factor of f_{col} and an effective temperature of T_{eff} (Shakura and Sunyaev, 1973)

$$I_\nu = f_{\text{limb}} \frac{1}{f_{\text{col}}^4} \frac{2h\nu^3}{c^2} \frac{1}{e^{h\nu/k_B f_{\text{limb}} T_{\text{eff}}} - 1}, \quad (3.8)$$

where f_{limb} is the limb-darkening factor and the number of photons emitted per unit time is

$$\dot{N} = \frac{4\zeta(3)k_B^3}{c^2 h^3} \frac{f_{\text{limb}} \cos \theta_{\text{em}} dS d\Omega T_{\text{eff}}^3}{f_{\text{col}} u^t} \quad (3.9)$$

with ζ being the Riemann zeta function. So, from each annulus, N_s photons are sampled, each with weight $w = \dot{N}/N_s$ into the solid angle $d\Omega$. The energies of the sampled photons at infinity follow the Planckian distribution with a temperature of $g f_{\text{col}} T_{\text{eff}}$, where $g = -1/k_\mu U^\mu$ is the redshift factor and U^μ is the disk particle four-velocity. To sample the Planckian distribution, the rejection method is used (see Pozdnyakov et al., 1983).

If the polarization option is switched off, the disk emission is assumed to be isotropic in the local frame, and the seed superphotons emitted by the disk are unpolarized. Otherwise, the disk atmosphere is modelled as a semi-infinite plane atmosphere (Chandrasekhar, 1960), as in Dovčiak et al. (2008) and Li

et al. (2009) to compute the polarization properties and the angular distribution of the seed superphotons. In this case, the polarization angle is perpendicular to the meridian plane, i.e. the plane containing both the symmetry axis and the line of sight to the observer, and the polarization degree increases monotonically with the polar emission angle. Given the emission angle, the intensity and polarization degree of the radiation can be calculated using Chandrasekhar H -functions (Chandrasekhar, 1960).

The energy and polarization spectra can be reconstructed by counting superphotons arriving at infinity. For an observer at inclination i , the luminosity density at energy E (in counts per unit time per energy interval) is

$$L_E = \frac{4\pi \sum_k w_k}{\Delta E \Delta \Omega} \quad (3.10)$$

where ΔE is the energy bin width, $\Delta \Omega = 2\pi[\cos(i - \Delta i/2) - \cos(i + \Delta i/2)]$ is the solid angle subtended by the inclination bin Δi and the sum is performed over all superphotons with $\theta_\infty \in (i - \Delta i/2, i + \Delta i/2]$ and $E_\infty \in (E - \Delta E/2, E + \Delta E/2]$, with E_∞ and θ_∞ the energy and polar angle of the superphotons at infinity, respectively. As Compton scattering only induces linear polarization (see Section 2.3.1), the Stokes parameter V is always null. For the other two Stokes parameters:

$$\begin{aligned} Q_E &= \frac{4\pi \sum_k w_k \delta_k \cos 2\psi_k}{\Delta E \Delta \Omega} \\ U_E &= \frac{4\pi \sum_k w_k \delta_k \sin 2\psi_k}{\Delta E \Delta \Omega} \end{aligned} \quad (3.11)$$

where ψ is the polarization angle measured at infinity in a comoving frame attached to the observer, while the x - and y -axes are identified as ∂_θ and ∂_ϕ , respectively. The polarization degree and angle are then, as customary, defined as

$$\text{PD} = \sqrt{q_E^2 + u_E^2} \quad \text{and} \quad \text{PA} = \frac{1}{2} \arctan\left(\frac{q_E}{u_E}\right) \quad (3.12)$$

where $q_E = Q_E/I_E$ and $u_E = U_E/I_E$ are the normalized Q and U Stokes parameters at energy E . In `MONK`, the polarization is defined parallel to the accretion disk plane if the polarization angle is 90° and parallel to the symmetry axis (i.e. orthogonal to the accretion disk) if the polarization angle is 0° or 180° .

3.1.1 Ray-tracing in the Kerr Spacetime

In `MONK` two independent methods of ray-tracing photons along null geodesics are implemented: the first is to integrate the geodesic equation directly, while the second is to consider the separability of the Hamilton-Jacobi equation and then integrate the equations of motion for r and θ (Zhang et al., 2019). The two methods give consistent results.

The propagation of photon is described by

$$\frac{dx^\mu}{d\lambda} = k^\mu \quad (3.13)$$

where λ is the affine parameter, which is normalised in order to have $k_t = -1$. The propagation of k^μ is then given by the geodesic equation

$$\frac{dx^\mu}{d\lambda} = -\Gamma_{\nu\sigma}^\mu k^\nu k^\sigma \quad (3.14)$$

where $\Gamma_{\nu\sigma}^\mu$ are the Christoffel symbols.

In Kerr spacetime, the Hamilton-Jacobi equation is separable (Carter, 1968). As a result, the following two integrals of r and $\mu \equiv \cos \theta$ are related (Chandrasekhar, 1983)

$$I = s_r \int \frac{dr}{\sqrt{R(r)}} = s_\mu \int \frac{d\mu}{\sqrt{M(\mu)}} \quad (3.15)$$

where $s_r, s_\mu = \pm 1$, set in such a way that the integrals are always positive. For massless particles

$$R(r) = r^4 + (a^2 - l^2 + Q)r^2 + 2[Q + (l - a)^2]r - a^2Q \quad (3.16)$$

$$M(\mu) = Q + (a^2 - l^2 - Q)\mu^2 - a^2\mu^4. \quad (3.17)$$

Considering a superphoton at x_0^μ with wave vector k_0^μ and setting $I = 0$, the photon trajectory along the geodesic can be evaluated in the following way: for each step, $I \rightarrow I + dI$ and the Equation 3.15 is solved for r and μ . At any step, one can solve for k^μ given $l \equiv L_z/E_\infty$, Q and the signs of k^r and k^θ following [Carter \(1968\)](#). The affine parameter can be obtained by

$$\lambda = \int \frac{r^2 dr}{\sqrt{R(r)}} + a^2 \int \frac{\mu^2 d\mu}{\sqrt{M(\mu)}}. \quad (3.18)$$

For axisymmetric configuration and not considering variability properties, the evaluation of t and ϕ is not considered. The integrals in Equation 3.18 are computed by making use of Carlson's elliptical functions, following ([Rauch and Blandford, 1994](#); [Li et al., 2005](#); [Dexter and Agol, 2009](#)). To perform the ray-tracing, the `sim5` package ([Bursa, 2017, 2018](#)) has been used. Emitted photons propagating in Kerr spacetime affected by the presence of the BH or NS experience GR effects. Once photons leave the atmosphere, their energies are modified by the gravitational redshift and Doppler effects and the polarization vector can be rotated due to aberration and light-bending effects ([Connors and Stark, 1977](#); [Connors et al., 1980](#)).

3.1.2 Propagation of the Polarization Vector

The polarization state of linearly polarized photons can be described by the invariant scalar polarization degree δ and a real vector $f^\mu \equiv A^\mu/A$ where A^μ is the wave amplitude vector ([Misner et al., 1973](#)). The polarization vector is orthonormal to the photon wave vector:

$$\begin{aligned} f^\mu f_\mu &= 1 \\ k^\mu f_\mu &= 0 \end{aligned} \quad (3.19)$$

and is parallel transported along null geodesics

$$k^\mu \nabla_\mu f^\nu = 0. \quad (3.20)$$

The parallel transport of the polarization vector along the curved trajectory results in a rotation of the polarization vector with respect to its initial direction. Therefore, the expected polarization fraction and angle will be modified with respect to those at the emission. The change of the polarization angle Ψ is defined as the angle by which a vector parallel transported along the light geodesic rotates with respect to some chosen frame. For the local frame that is comoving with the disk fluid, the x -axis is in the $-\partial_\theta$ -direction in the plane defined by the normal of the disk n^μ and the momentum p_e^μ of the emitted photon perpendicular to it, while the y -axis lies in the plane of the disk, along the $-\partial_\phi$ -direction. At infinity, the static frame is attached to the sky of the observer with x - and y -axes, respectively, identified with the two impact parameters α , defined as positive in the $-\partial_\theta$ -direction, and β , defined as positive in the ∂_ϕ -direction. The rotation of the polarization angle is then given by ([Connors et al., 1980](#))

$$\Psi = \arctan \frac{Y}{X} \quad (3.21)$$

where

$$\begin{aligned} X &= -(\alpha - a \sin \theta_o)\kappa_1 - \beta\kappa_2 \\ Y &= (\alpha - a \sin \theta_o)\kappa_2 - \beta\kappa_1 \end{aligned} \quad (3.22)$$

with a defined positive when the BH or the NS rotates counter-clockwise. The angle θ_o is the observer's inclination, while κ_1 and κ_2 are components of the complex Penrose-Walker constant of parallel transport along null geodesics (Walker and Penrose, 1970)

$$\begin{aligned}\kappa_1 &= arp_e^\theta f^t - r[a p_e^t - (r^2 + a^2) p_e^\phi] f^\theta - r(r^2 + a^2) p_e^\theta f^\phi \\ \kappa_2 &= -rp_e^2 f^t + r[p_e^t - ap_e^\phi] f^r + arp_e^r f^\phi\end{aligned}\quad (3.23)$$

where the polarization vector f^μ is then

$$f^\mu = \frac{n^\mu - \mu_e (g p_e^\mu - U^\mu)}{\sqrt{1 - \mu_e^2}} \quad (3.24)$$

The previous equations (3.21, 3.22) also show that a further rotation, the so-called gravitational Faraday rotation, occurs only if the central BH or NS is rotating with specific angular momentum $a \neq 0$ (see Ishihara et al., 1988).

Since the Penrose-Walker constant κ_{pw} is conserved along null geodesics, instead of propagating f^μ using Equation 3.20, MONK keep record step by step of κ_{pw} . Only when a photon interacts with an electron via Compton scattering, the code solves the parallel transport for f^μ computing the polarization and the wave vector after the interaction, and subsequently re-evaluate κ_{pw} as Connors et al. (1980)

$$\kappa_{pw} = \kappa_2 - i\kappa_1 \quad (3.25)$$

However, with Equations 3.19 and 3.20, given κ_{pw} , one can only determine f^μ up to an addition of multiple of k^μ , as these equations are gauge invariant under the transformation

$$f^\mu \rightarrow f^\mu + \tilde{\alpha} k^\mu \quad (3.26)$$

where $\tilde{\alpha}$ is an arbitrary real number. By selecting $f^t = 0$, the other three vector components of f^μ can be derived from Equations 3.19 and 3.20.

Given δ and κ_{pw} , to evaluate the Stokes parameters (I, Q, U, V) at infinity, the procedure by Li et al. (2009) is followed. The Stokes parameter I represents the total intensity of the radiation, while Q and U are related to the linear polarization. V represents the circular polarization and is null for linear polarization (Appendix A). An arbitrary radiation field can be decomposed into different components: an unpolarized one, with Stokes parameters

$$\{(1 - \delta)I, 0, 0, 0\}, \quad (3.27)$$

and a completely polarized component with Stokes parameters

$$\{\delta I, Q, U, V\}, \quad (3.28)$$

where δ is the polarization degree. Since the photons emitted by the disk or corona are linearly polarized ($V = 0$), the Stokes parameters will be:

$$\begin{aligned}I_p &\equiv \delta I \\ Q &= I_p \cos 2\psi \\ U &= I_p \sin 2\psi\end{aligned}\quad (3.29)$$

or equivalently

$$Q + iU = I_p e^{2i\psi}. \quad (3.30)$$

The *superposition theorem* states that when multiple independent light beams are combined, the Stokes parameters for the resulting combined radiation are obtained by adding up the Stokes parameters of each individual stream (Chandrasekhar, 1960).

For the polarized component, a beam of perfectly polarized radiation emitted by an infinitesimal surface element is considered. This beam is received by an observer along an infinitesimal solid angle element $d\Omega_{\text{obs}}$. The Stokes parameters of the beam are

$$\{I_{\text{p,obs}}, Q_{\text{obs}}, U_{\text{obs}}, 0\}. \quad (3.31)$$

Summing over the radiation received from all the infinitesimal elements using the superposition theorem

$$\langle I_{\text{p,obs}} \rangle = \frac{1}{\Delta\Omega_{\text{obs}}} \int I_{\text{p,obs}} d\Omega_{\text{obs}} \quad (3.32)$$

and

$$\langle Q_{\text{obs}} \rangle + i\langle U_{\text{obs}} \rangle = \frac{1}{\Delta\Omega_{\text{obs}}} \int I_{\text{p,obs}} e^{2i\psi_{\text{obs}}} d\Omega_{\text{obs}} \quad (3.33)$$

where the Stokes parameters are averaged over solid angle, and $\Delta\Omega_{\text{obs}}$ is the total solid angle subtended by the source on the sky. Although each infinitesimal element may produce perfectly polarized light, the radiation observed by the observer may still become partially polarized as a result of averaging. This occurs because the individual light-rays may have different values of ψ_{obs} at the observer. Considering radiation emitted from the accretion disk or from the corona, even if all emitted beams have the same polarization in their emitting regions, geodesic propagation can cause a change in ψ along each null geodesic and cause a reduction in the observed polarization degree. However, any unpolarized radiation emitted by the disk or by the NS will remain unpolarized to the observer. As a result, geodesic propagation and averaging can only reduce the polarization degree (Connors et al., 1980; Li et al., 2009). The intensity of this unpolarized component is

$$\langle I_{\text{u,obs}} \rangle = \frac{1}{\Delta\Omega_{\text{obs}}} \int I_{\text{u,obs}} d\Omega_{\text{obs}}, \quad (3.34)$$

where $I_{\text{u,obs}} \equiv I_{\text{obs}} - I_{\text{p,obs}}$. By combining Equations (3.32) and (3.34), the total intensity can be computed

$$\langle I_{\text{u,obs}} \rangle + \langle I_{\text{p,obs}} \rangle = \frac{1}{\Delta\Omega_{\text{obs}}} \int (I_{\text{u,obs}} + I_{\text{p,obs}}) d\Omega_{\text{obs}} = \frac{1}{\Delta\Omega_{\text{obs}}} \int I_{\text{obs}} d\Omega_{\text{obs}} = \langle I_{\text{obs}} \rangle \quad (3.35)$$

and is found to be conserved. Since $I_{E_{\text{loc}}}/E_{\text{loc}}^3$ (where E_{loc} is the photon energy measured by a local observer) is invariant along the null geodesic (Misner et al., 1973), Equation (3.33) can be rewritten as (Connors et al., 1980):

$$\langle Q_{\text{obs}} \rangle + i\langle U_{\text{obs}} \rangle = \frac{1}{\Delta\Omega_{\text{obs}}} \int g^3 P_{\text{em}} I_{\text{em}} e^{2i\psi_{\text{obs}}} d\Omega_{\text{obs}}, \quad (3.36)$$

where P_{em} is the degree of polarization of the radiation at the time that radiation is emitted from the disk surface or the corona, g is the redshift factor of the photon (Li et al., 2005). In the same way, the total intensity can be written as

$$\langle I_{\text{obs}} \rangle = \frac{1}{\Delta\Omega_{\text{obs}}} \int g^3 I_{\text{em}} d\Omega_{\text{obs}}. \quad (3.37)$$

The observed average polarization degree is then computed by

$$\langle P \rangle = \frac{1}{\langle I_{\text{obs}} \rangle} \sqrt{\langle Q_{\text{obs}} \rangle^2 + \langle U_{\text{obs}} \rangle^2} \quad (3.38)$$

while the observed average polarization angle is determined by

$$\sin 2\langle \psi \rangle = \frac{\langle U_{\text{obs}} \rangle}{\sqrt{\langle Q_{\text{obs}} \rangle^2 + \langle U_{\text{obs}} \rangle^2}} \quad \text{and} \quad \cos 2\langle \psi \rangle = \frac{\langle Q_{\text{obs}} \rangle}{\sqrt{\langle Q_{\text{obs}} \rangle^2 + \langle U_{\text{obs}} \rangle^2}}. \quad (3.39)$$

The solution of this equation is

$$\langle \psi \rangle = \langle \psi \rangle_{\text{pr}} + n\pi \quad (3.40)$$

where n is any integer number, while the primitive angle $\langle \psi \rangle_{\text{pr}}$ defined in the $[0, \pi]$ range is

$$\langle \psi \rangle_{\text{pr}} = \begin{cases} \frac{1}{2} \arccos \xi_Q & \text{when } \langle U_{\text{obs}} \rangle > 0; 0 < \langle \psi \rangle_{\text{pr}} < \frac{\pi}{2} \\ \pi - \frac{1}{2} \arccos \xi_Q & \text{when } \langle U_{\text{obs}} \rangle < 0; \frac{\pi}{2} < \langle \psi \rangle_{\text{pr}} < \pi \end{cases}, \quad (3.41)$$

where

$$\xi_Q \equiv \frac{\langle Q_{\text{obs}} \rangle}{\sqrt{\langle Q_{\text{obs}} \rangle^2 + \langle U_{\text{obs}} \rangle^2}}. \quad (3.42)$$

3.1.3 Comptonization

As superphotons propagate inside the corona, for each step, the covariant scattering optical depth is evaluated as [Younsi et al. \(2012\)](#):

$$\tau_\nu = - \int_{\lambda_0}^{\lambda_1} \alpha_{0,\nu}(\lambda) k_\alpha U^\alpha|_\lambda d\lambda \quad (3.43)$$

where λ_0 and λ_1 are the affine parameters of the superphoton at the beginning and the end of the step, and $\alpha_{0,\nu}$ is the scattering coefficient in the fluid rest frame. The superphoton energy in the fluid frame is $E_0 = -k_\mu U^\mu E_\infty$. The scattering coefficient of the superphoton with respect to a population of electrons can be evaluated as ([Pozdnyakov et al., 1983](#)):

$$\alpha_{0,\nu} = \int \frac{dN_e}{d^3p} (1 - \mu_e \beta_e) \sigma(x) d^3p, \quad (3.44)$$

where $\frac{dN_e}{d^3p}$ is the electron velocity distribution, $\mu_e = \cos \theta_e$ while θ_e is the angle between the momenta of the photon and the electron, $\beta_e \equiv v_e/c$ is the electron velocity, γ_e is the Lorentz factor of the electron, $\sigma(x)$ is the scattering cross section and $x = \gamma_e x_0 (1 - \mu_e \beta_e)$ is the dimensionless photon energy in the electron rest frame, with $x_0 \equiv E/(m_e c^2)$ and m_e is the electron rest mass.

In the electron rest frame, the differential scattering cross section is ([Berestetskii et al., 1971](#); [Connors et al., 1980](#)):

$$\frac{d\sigma}{d\Omega} = \frac{r_0^2}{2} \left(\frac{x'}{x} \right)^2 \left[\frac{x}{x'} + \frac{x'}{x} - \sin^2 \theta' - \sin^2 \theta' (X_s \cos 2\phi' + Y_s \sin 2\phi') \right] \quad (3.45)$$

where r_0 is the classical electron radius, x' is photon energy after scattering, and θ' and ϕ' are the polar and azimuthal angles of the photon wave vector after scattering. The coordinate system is defined with the z -axis aligned with the photon wave vector, whereas the x - and y -axes are defined by two orthonormal unit vectors in the plane perpendicular to the photon wave vector. For a superphoton with polarization degree δ and polarization angle ψ :

$$X_s = \delta \cos 2\psi \quad \text{and} \quad Y_s = \delta \sin 2\psi. \quad (3.46)$$

By integrating Equation (3.45), the total Klein-Nishina cross section is obtained:

$$\sigma(x) = \pi r_0^2 \frac{1}{x} \left[\left(1 - \frac{2}{x} - \frac{2}{x^2} \right) \ln(1 + 2x) + \frac{1}{2} + \frac{4}{x} - \frac{1}{2(1 + 2x)^2} \right] \quad (3.47)$$

which is independent of the polarization degree. For thermal electrons with temperature T_e , the electron velocity distribution is the Maxwell-Jüttner distribution:

$$\frac{dN_e}{d\gamma_e} \propto \frac{\gamma_e^2 \beta_3}{\theta_T K_2(1/\theta_T)} e^{-\gamma_e/\theta_T} \quad (3.48)$$

where $\theta_T \equiv k_B T_e / m_e c^2$ is the dimensionless electron temperature and K_2 is the modified Bessel function of order 2.

The optical depth τ in the case of a thermal electron can be derived using Equations 3.44, 3.47 and 3.48, with the scattering probability being $P = 1 - e^{-\tau}$. For optically thin coronae, a bias factor $b \gg 1$ is introduced, following [Pozdnyakov et al. \(1983\)](#) and [Dolence et al. \(2009\)](#) to enhance the statistics at high energy, so that the scattering probability will become $P = 1 - e^{-b\tau}$, and after the scattering the superphoton “splits” into two superphotons with appropriate weights. The condition for scattering is $\epsilon \leq P$, where ϵ is a random number sampled by a uniform distribution between 0 and 1.

If the superphoton is scattered, first the momentum of the scattering electron is sampled and the probability density to find an electron with momentum $\mathbf{p}_e = [\gamma_e m_e, \gamma_e m_e \mathbf{v}]$:

$$P(\mathbf{p}_e) \propto \frac{dN_e}{d^3p} (1 - \mu_e \beta_e) \sigma_{\text{KN}}. \quad (3.49)$$

The probability density distribution is sampled through rejection method, following [Pozdnyakov et al. \(1983\)](#) and [Canfield et al. \(1987\)](#).

Once the four-velocity of the scattering electron is sampled, the energy, the wave and the polarization vector of the photon in the electron rest frame are derived with a generic Lorentz transformation. As required by the gauge choice, α is set in such a way that the polarization vector in the electron rest frame satisfies $f'_e = 0$. Taking into account a set of Cartesian coordinates in which the z - and x - axes are aligned with the wave and the polarization vector, the differential cross section for the photon to be scattered into a solid angle $d\Omega'$ centering at the polar angle θ' and azimuthal angle ϕ' is

$$\frac{d\sigma}{d\Sigma'} = \frac{r_0^2}{2} \left(\frac{x'}{x} \right)^2 \left[\frac{x}{x'} + \frac{x'}{x} - \sin^2 \theta' - \delta \sin^2 \theta' \cos 2\phi' \right] \quad (3.50)$$

where x' is the dimensionless photon energy after scattering and is related with θ' by the Compton recoil relation:

$$x' = \frac{x}{1 + x(1 - \cos \theta')}. \quad (3.51)$$

The integrated probability density of x' will be

$$p(x') = \frac{1}{\sigma_{\text{KN}}} \frac{\pi r_0^2}{x^2} \left[\frac{x}{x'} + \frac{x'}{x} - \sin^2 \theta' \right], \quad (3.52)$$

which is independent on the polarization degree. The scattering polar angle θ' is found by the Compton recoil relation (3.51), after sampling x' following ([Kahn, 1954](#)). The probability density distribution of the scattering azimuthal angle ϕ' is

$$p(\phi' | x'; \delta) = \frac{p(x', \phi'; \delta)}{p(x')} = \frac{1}{2\pi} - \frac{\delta \sin^2 \theta' \cos 2\phi'}{2\pi \left(\frac{x}{x'} + \frac{x'}{x} - \sin^2 \theta' \right)}. \quad (3.53)$$

The photon wave vector in the electron rest frame after scattering \mathbf{k}'_e can be found knowing θ' and ϕ' . Considering a new coordinate system with the z -axis aligned with \mathbf{k}'_e and

$$\mathbf{e}'_{\perp} = \frac{\mathbf{k}_e \times \mathbf{k}'_e}{\sqrt{|\mathbf{k}_e \times \mathbf{k}'_e|}} \quad \text{and} \quad \mathbf{e}_{\parallel} = \mathbf{k}'_e \times \mathbf{e}'_{\perp}, \quad (3.54)$$

the two normalised Stokes parameters of the scattered photon will be ([Connors et al., 1980](#))

$$\begin{aligned} \frac{Q'}{I} &= \frac{1}{N} [\sin^2 \theta' - \delta(1 + \cos^2 \theta') \cos 2\phi'] \\ \frac{U'}{I} &= \frac{2}{N} \delta \cos \theta' \sin 2\phi', \end{aligned} \quad (3.55)$$

where

$$N = \frac{x'}{x} + \frac{x}{x'} - \sin^2 \theta' - \delta \sin^2 \theta' \cos 2\phi'. \quad (3.56)$$

As customary, the polarization degree and angle after scattering will be

$$\delta' = \frac{\sqrt{Q'^2 + U'^2}}{I'} \quad \text{and} \quad \psi' = \frac{1}{2} \arctan\left(\frac{U'}{Q'}\right) \quad (3.57)$$

and the polarization vector is then $\mathbf{f}'_e = \cos \psi' \mathbf{e}'_{\parallel} + \sin \psi' \mathbf{e}'_{\perp}$. The energy, wave and polarization vectors after scattering in the Boyer-Lindquist frame can be obtained from x' , \mathbf{k}'_e and \mathbf{f}'_e by a series of transformations including rotation, generic Lorentz boost, and tetrad transform. Finally, the Walker-Penrose constant of the superphoton can be evaluated after scattering following Equation (3.25).

3.2 Numerical Setup

MONK have been already tested for BH X-ray binaries and AGNs (Zhang et al., 2019; Ursini et al., 2022), with excellent agreement with previous numerical codes (e.g. GRMONTY; Dolence et al. 2009) and observed spectra. The spectra produced by the new version of MONK adapted including the NS photons reproduce very well those of observations and the most used theoretical models for NS-LMXBs (e.g. Mitsuda et al. 1984; Makishima et al. 1986; Titarchuk 1994; Zdziarski et al. 1996; Życki et al. 1999; Farinelli et al. 2008; Zdziarski et al. 2020). MONK requires several different input parameters (Zhang et al., 2019; Gnarini et al., 2022): the physical parameters of the NS (i.e. mass, radius, spin period); the accretion rate and the disk parameters; the optical depth τ , the temperature kT_e and the geometrical parameters of the Comptonizing region.

For all simulations, a standard NS with $M = 1.4 M_{\odot}$ and $R = 12$ km has been assumed. Since photons propagate along null geodesics in Kerr space-time, the spin parameter a for the metric is required. The General Relativistic effects on the polarization depend on the value of the spin parameter (Connors and Stark, 1977; Connors et al., 1980; Ishihara et al., 1988). For typical NS-LMXBs, the NS period ranges between 2–10 ms (see also Patruno et al. 2017 for a statistical analysis of the spin distributions of NS-LMXBs). Therefore, the NS period P is fixed at 3 ms in analogy to the one derived from QPOs by Wijnands et al. (1998) for Cyg X–2. For a standard NS, the spin parameter a can be derived by adopting $a = 0.47/P(\text{ms}) \approx 0.16$ (see Braje et al. 2000). With this choice of P and a , the General Relativistic effects are almost maximized for typical NS-LMXB systems. In principle, one could also use the effects of Special and General Relativity to measure the spin parameter a of some observed NS-LMXBs, but it is very challenging with the current technology available.

To derive general polarization properties for standard NS-LMXBs, the temperature of the NS is set to 1.6 keV, which corresponds to 1.3 keV for the observer. This value is consistent with several best-fit models found for different NS-LMXB observations (see Revnivtsev and Gilfanov 2006; Farinelli et al. 2008; Iaria et al. 2020). When MONK simulations are performed for a specific source (see also Sections 5.2.1 and 5.2.2), the temperature of the NS can be derived from the best-fit value obtained from the spectral analysis (e.g. Chapter 4) and considering the gravitational redshift correction

$$kT_{\text{best-fit}} = kT_{\text{NS}} \sqrt{1 - \frac{2GM_{\text{NS}}}{R_{\text{NS}}c^2}}. \quad (3.58)$$

The accretion rate \dot{M} and the inner disk radius R_{in} depend on the spectral state of the NS-LMXB. The disk can extend down to the boundary layer or NS surface or can be truncated at an arbitrary radius. If the magnetic field is high enough, the disk can not extend all the way to the NS surface because of the magnetic field that stops the accreting plasma at a position where the magnetic pressure and the plasma pressure become of the same order. Then, the accreted matter starts flowing towards the NS following

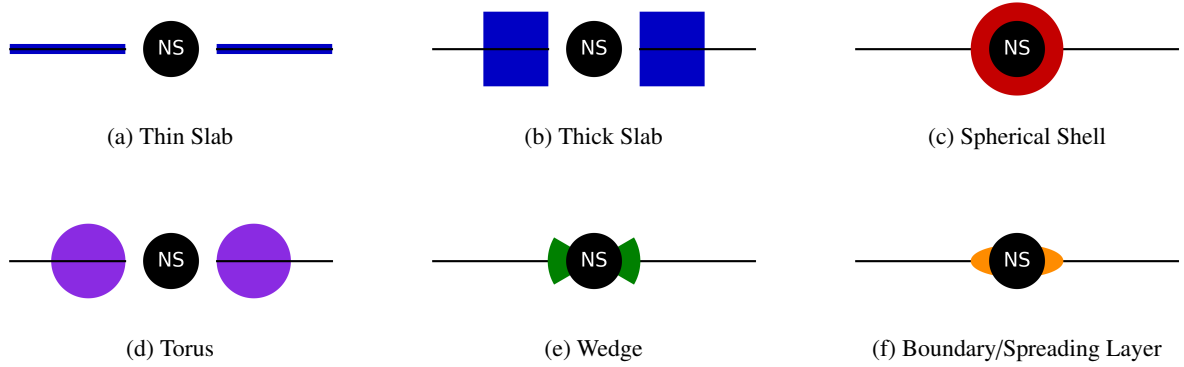


Figure 3.1: Schematic representation of the different geometries of the Comptonizing region used in `MONK` simulations.

magnetic field lines. Depending on the spectral states of the NS-LMXB, typical values for the accretion rate have been considered (Paizis et al., 2006) in terms of the Eddington accretion rate \dot{M}_{Edd} as

$$\dot{M} = \frac{4\pi G m_p M}{c \sigma_T} \dot{m} = \dot{M}_{\text{Edd}} \dot{m} \approx 1.3987 \cdot 10^{17} \left(\frac{M}{M_{\odot}} \right) \dot{m} \quad (3.59)$$

where \dot{m} is the adimensional accretion rate. Soft state NS-LXMBs are characterized by a high mass accretion rate very close to the critical (Eddington) values (Farinelli et al., 2008, 2009) while, for NS-LMXBs in the Hard state the mass accretion rate is relatively low (Falanga et al., 2006). The accretion rate mainly affects the disk contribution to the total flux: for lower accretion rates, the accretion disk is colder and therefore it dominates the emission at lower energies ($\lesssim 0.5 - 1$ keV, depending on the specific geometry) and the spectrum in the 2–8 keV is mainly due to the Comptonized NS photons; as the accretion rate grows, the disk contribution becomes more and more relevant (dominating up to 3–4 keV) and its flux is also closer to the NS contribution when the disk is not the main component.

Also the color correction factor f_{col} varies with the spectral state (e.g. Merloni et al. 2000), however slight differences will not qualitatively affect the results. The color correction factor is then set to $f_{\text{col}} = 1.8$ for both the spectral states and the different geometries (Shimura and Takahara, 1995). The physical parameters of the Comptonizing region (i.e. the electron plasma temperature kT_e and the optical depth τ) are fixed according to the spectral state of the NS-LMXB. In the soft state, the Comptonizing region is characterized by lower temperatures and a more opaque plasma ($kT_e \sim 3$ keV and $\tau \sim 8 - 10$). On the contrary, hard-state NS-LMXBs show much hotter and more transparent plasma ($kT_e \sim 25$ keV and $\tau \sim 1 - 2$; Farinelli et al. 2009; Cocchi et al. 2010, 2011; Sánchez-Fernández et al. 2020). These values for optical depth refer to a spherical Comptonizing region for which τ is defined radially. However, the optical depth for a slab geometry is defined in `MONK` as $\tau = n_e \sigma_T h$, where h is the half-thickness of the slab (Zhang et al. 2019, see also Titarchuk 1994; Poutanen et al. 1996a for the same definition). Therefore, to obtain a similar spectral shape, the value of τ must be a factor of 2 smaller than the radial one for a geometrically thick slab or a factor of 4 smaller for a geometrically thin slab (see Ursini et al. 2022 for more details).

Since the entire sample of NS-LMXBs observed by *IXPE* during the first two years of operations includes only NS-LMXBs in Soft state, detailed `MONK` simulations have been produced only considering these kinds of sources. Therefore, the temperature of the Comptonizing region was fixed at 3 keV for all geometries, while the optical depth τ of the electron plasma was set to 8 – 10 depending on its definition for each specific configuration. Some general examples of `MONK` simulations for Hard state NS-LMXBs are reported in Gnarini et al. (2022) for a thick slab and a spherical shell configuration. In particular, for Hard state NS-LMXBs the expected polarization is slightly higher than typical Soft state NS-LMXBs,

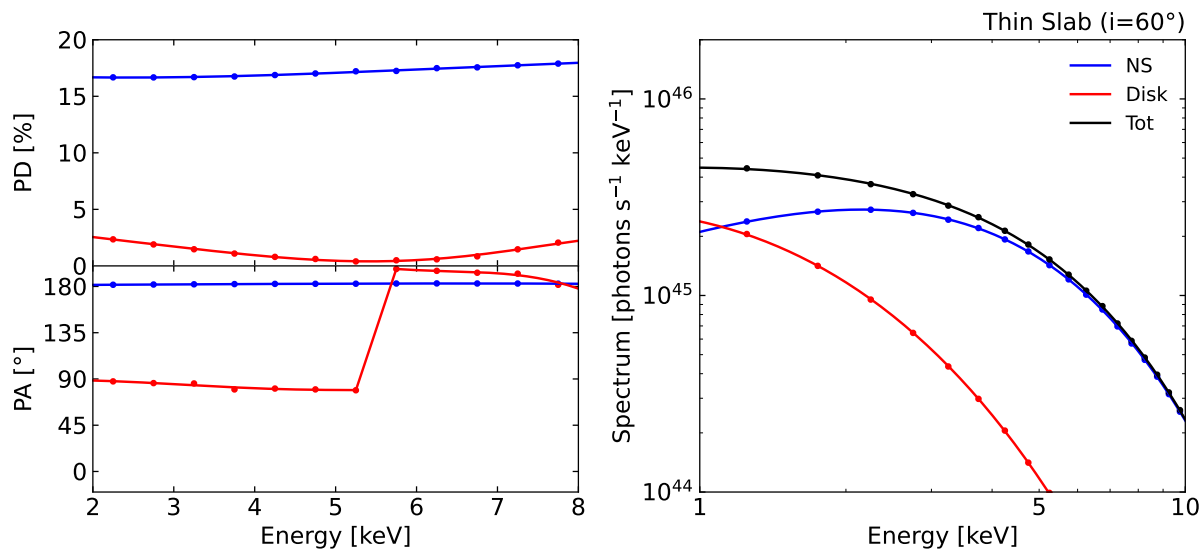


Figure 3.2: Polarization degree and angle (*left panels*) and spectrum (*right panel*) of NS and disk photons (respectively, blue and red lines) as a function of energy considering a geometrically thin slab Comptonizing region. Each contribution includes the direct radiation directly observed. The system is observed at 60° inclination. The PA in MONK is measured from the projection of the rotation axis onto the sky plane.

mainly because the emission in the 2–8 keV energy range is due to only the Comptonized NS photons, as the disk photons, which are expected to be polarized orthogonally to the Comptonized NS photons, are only a small fraction of the total flux.

3.3 Slab Geometry

The slab configuration is assumed to cover part or all of the disk, starting from the inner disk radius R_{in} , and to co-rotate with the Keplerian disk (Zhang et al., 2019). The vertical thickness H and the radial extension ΔR of the corona can vary in order to reproduce a (geometrically) thin slab covering all the disk (Figure 3.1a) or a thicker slab that covers part of the disk and the NS surface (Figure 3.1b, see also Gnarini et al. 2022).

The results for the polarization degree and angle of the two different components (i.e. the NS and the disk seed photons) are shown in Figure 3.2 for a thin slab configuration. For this geometry, the accretion disk is completely covered by a geometrically thin slab and only a few disk photons are directly observed without being Compton scattered. The NS component includes the direct emission from the NS surface along with the NS seed photons scattered in the Comptonizing region. The main contribution seems to come from the NS photons that hit the slab from above and are scattered toward the observer, in a similar way to the reflection of soft photons off the accretion disk surface. As for reflected photons (e.g. Matt 1993; Poutanen et al. 1996b), the scattered NS photons are highly polarized (15 – 20%) orthogonally to the meridian plane. The disk photons are less polarized and contribute significantly to the polarization only at low energies ($\lesssim 1 - 2$ keV). The predicted PD for the disk contribution is consistent with the classical results for a semi-infinite plane parallel atmosphere (Chandrasekhar, 1960) in the low-energy part of the spectrum ($E \lesssim 5$ keV), where unscattered and few-scattered components dominate the total disk emission. The multi-scattered photons that travelled the most through the slab become dominant at higher energies and as a consequence the PD increases and the PA flips by $\approx 90^\circ$ (Tamborra et al., 2018).

The results for the polarization degree and angle of the two different components (i.e. the NS and the disk seed photons) are shown in Figure 3.3 for a geometrically thick slab configuration. As before, the NS component includes the direct photons emitted from the NS surface, together with the NS photons

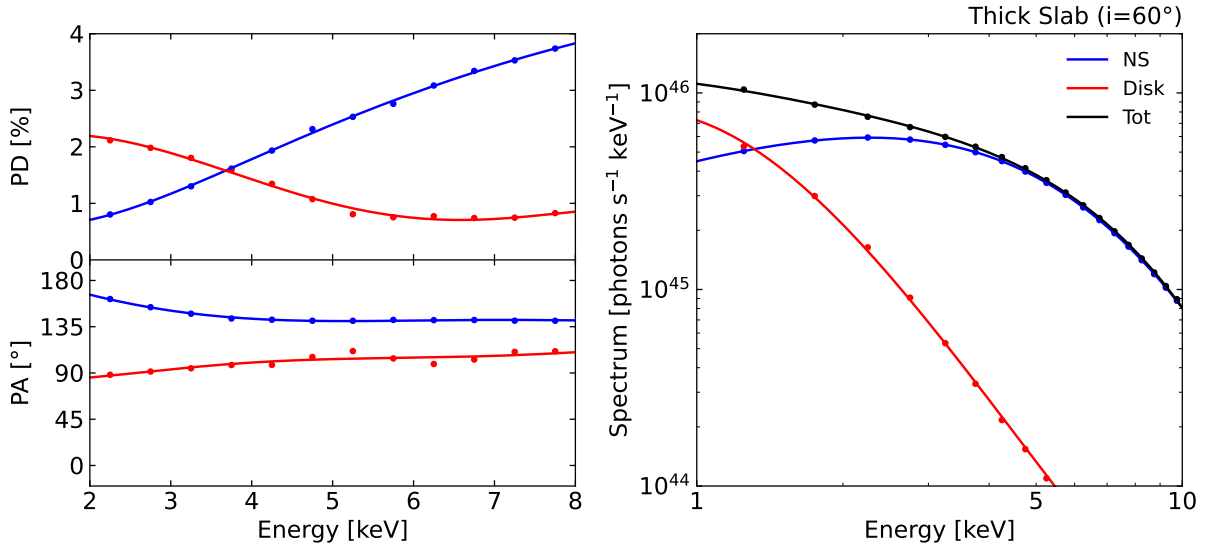


Figure 3.3: Polarization degree and angle (*left panels*) and spectrum (*right panel*) of NS and disk photons (respectively, blue and red lines) as a function of energy considering a geometrically thick slab Comptonizing region. Each contribution includes the direct radiation directly observed. The system is observed at 60° inclination. The PA in MONK is measured from the projection of the rotation axis onto the sky plane.

scattered in the Comptonizing region. Similarly, the disk component is made of the disk photons directly detected and those scattered in the corona. As the thickness of the thick slab is comparable to the NS radius, most of the NS seed photons will hit the corona and eventually get scattered towards the observer, with a significant fraction hitting instead the underlying disk. The scattered NS hot photons are expected to be the dominant contribution for energy $\gtrsim 2 - 3$ keV, with a polarization degree reaching values up to 4–5% (for high inclinations). The polarization angle of the scattered NS photons is almost perpendicular to the disk plane. The misalignment is due to special and general relativistic effects. At lower energies, the total flux is dominated by direct disk emission and the polarization is close to the classical result (Chandrasekhar, 1960), if the disk seed photons are assumed to be polarized. When unpolarized seed photons are considered, the disk radiation directly observed will not contribute to the polarization signal and the expected polarization degree will be lower. The scattered disk photons contribute significantly to the disk polarization at energies $\gtrsim 2 - 3$ keV, as can be noted from the polarization degree and angle. The rotation of the polarization angle of the disk component is related to the scattered disk photons, along with special and general relativistic effects.

3.4 Spherical Geometry

The spherical shell configuration (Figure 3.1c) is characterized simply by the outer R_{out} and inner radii R_{in} , which can be assumed to be very close to the surface of the NS. Depending on the radial extension of the shell, the disk could be partially covered by the corona itself, which will therefore intercept mostly the high-energy photons emitted by the inner region of the disk (Gnarini et al., 2022). These photons will be Compton scattered by the electron plasma in the shell towards the observer or towards the NS or the disk (and then get absorbed). The spherical shell configuration is assumed to be stationary (Zhang et al., 2019). This is a quite reasonable assumption for a spherically symmetric configuration; the rotation of the electron plasma could indeed break the symmetry of the system and increase the polarization but it can be verified that the PD is always quite small (in particular it is always below 0.5% for the NS contribution; Figure 5.1)

The results for the polarization degree and angle of the two different components (i.e. the NS and

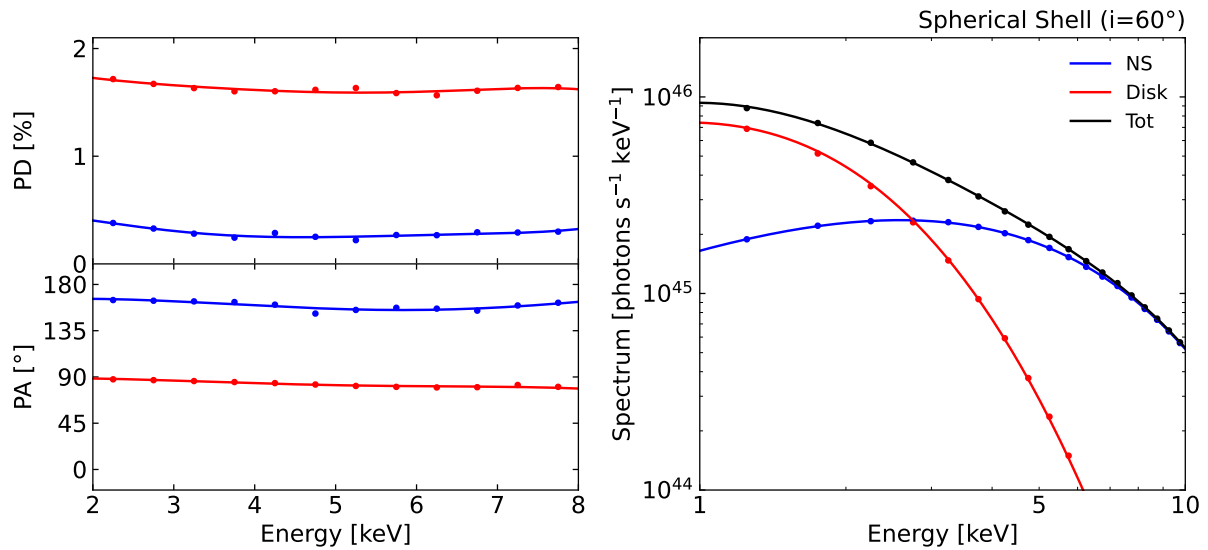


Figure 3.4: Polarization degree and angle (*left panels*) and spectrum (*right panel*) of NS and disk photons (respectively, blue and red lines) as a function of energy considering a spherical shell Comptonizing region. Each contribution includes the direct radiation directly observed. The system is observed at 60° inclination. The PA in MONK is measured from the projection of the rotation axis onto the sky plane.

the disk) are shown in Figure 3.4. The disk component includes the direct emission of the disk and the disk seed photons scattered in the Comptonizing region. Most of the NS seed photons are scattered in the spherical shell corona surrounding the surface of the NS. However, the NS component also includes the NS photons passing through the corona without being scattered. As the shell extends from the NS surface up to the inner disk radius, only a small fraction of the disk photons are Comptonized in the spherical shell and their contribution to the total flux is quite small. The flux is dominated by the direct disk emission for low energies ($\lesssim 3 - 4$ keV) and by the scattered NS photons for higher energies. Since both the NS and the Comptonizing region are spherically symmetric, the polarization related to the scattered NS photons should be zero. The non-zero results are simply artifacts of the finite statistic (due to the fact that the polarization degree can assume only positive values) and give an idea of the uncertainty in the simulation. As a sanity check, it has been verified that the Stokes parameters Q and U oscillate around zero (Gnarini et al., 2022). The only contribution to the polarization is due to disk photons directly observed at infinity, since only a small fraction is Comptonized inside the spherical shell. Therefore, the polarization significantly depends on the intrinsic polarization of the disk photons: if the disk photons are polarized, the resulting polarization is the same as Chandrasekhar (1960) at low energies and starts to decrease as the NS contribution becomes more significant at higher energies; if the disk photons are unpolarized, neither the disk nor the NS components are polarized and the total polarization is zero.

3.5 Torus Geometry

The torus configuration (Figure 3.1d) is characterized by the radial distance of the center D_c and the radius R_c of the circular section. Depending on the position and the radial extension, the torus can cover part of the disk (very similar to the thick slab configuration; Gnarini et al. 2022) and the electron plasma is assumed to co-rotate with the Keplerian disk. The optical depth τ is defined radially starting from the center of the circular section. This geometry represents a puffed-up inner region of the disk as Comptonizing region of the NS and disk photons.

The results for the polarization degree and angle of the two different components (i.e. the NS and the disk) are shown in Figure 3.5. The NS component includes the direct photons emitted from the NS surface

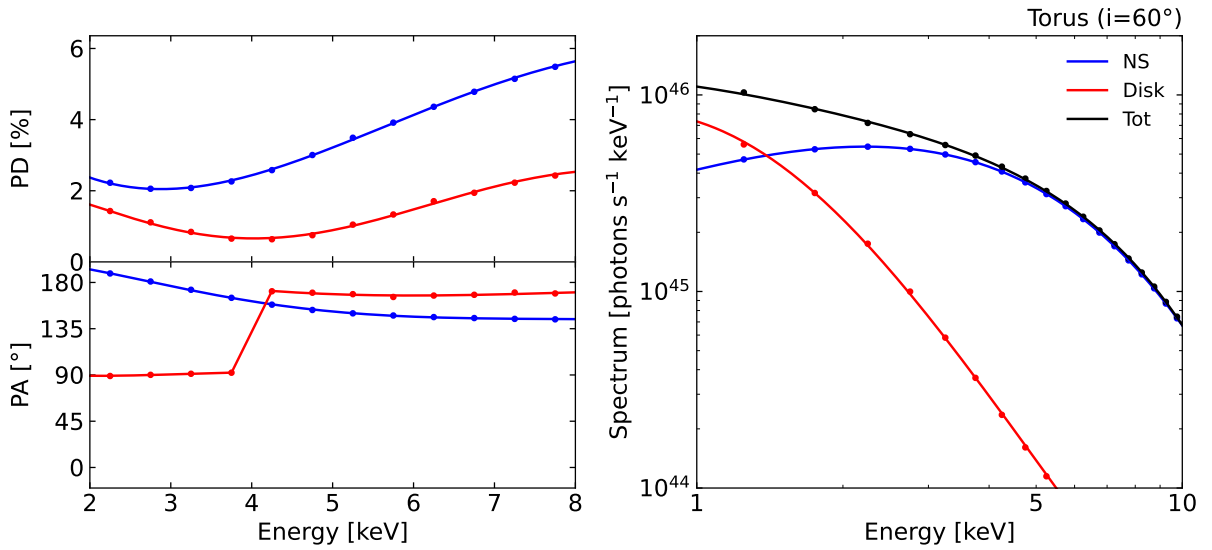


Figure 3.5: Polarization degree and angle (*left panels*) and spectrum (*right panel*) of NS and disk photons (respectively, blue and red lines) as a function of energy considering a toroidal Comptonizing region. Each contribution includes the direct radiation directly observed. The system is observed at 60° inclination. The PA in `MONK` is measured from the projection of the rotation axis onto the sky plane.

along with Comptonized radiation. The disk component consists of the disk photons directly detected and those scattered in the corona. Similarly to the thick slab configuration, as the radius of the torus section is comparable to the NS radius, most of the NS seed photons pass through the Comptonizing region and eventually get scattered towards the observer, with a significant fraction absorbed by the underlying disk. The scattered NS photons are the main contribution to the total flux in the high-energy part of the spectrum, with a quite high polarization degree increasing with energy. The polarization angle of the scattered NS photons is almost perpendicular to the disk plane. The small misalignment and the rotation with energy are due to special and general relativistic effects. At lower energies, the total flux is dominated by the direct disk emission. If the disk seed photons are considered to be polarized, the total polarization is close to the classical results [Chandrasekhar \(1960\)](#). Multi-scattered disk photons contribute to the disk polarization for energies above 4–5 keV, resulting in an increase of the polarization degree and a rotation of the polarization angle.

3.6 Wedge Geometry

The wedge configuration (Figure 3.1e) is built to roughly mimic the equatorial boundary layer ([Popham and Sunyaev 2001](#); see also [Poutanen et al. 2018](#)) and corresponds to a spherical shell without the polar caps. This geometry is characterized by the outer R_{out} and inner radii R_{in} , along with the maximum opening angle θ_m (measured from the accretion disk plane). In particular, the wedge radially extends from the NS surface up to the inner edge of the accretion disk. For this geometry, the electron plasma rotates with Keplerian velocity and its optical depth is measured in the radial direction from the NS surface.

The results for the polarization degree and angle of the two different components (i.e. the NS and the disk) are shown in Figure 3.6. The disk component includes the direct emission directly detected by the observer, along with disk photons scattered in the corona. Similarly to the spherical shell configuration, the direct disk emission is the dominant contribution to the total flux at low energies ($\lesssim 3 - 4$ keV), while the scattered NS photons contribute significantly at higher energies. The fraction of the disk photons passing through the corona and getting scattered increases the polarization degree of the disk at higher energies. At lower energies, the polarization of the disk strongly depends on the choice of the intrinsic polarization:

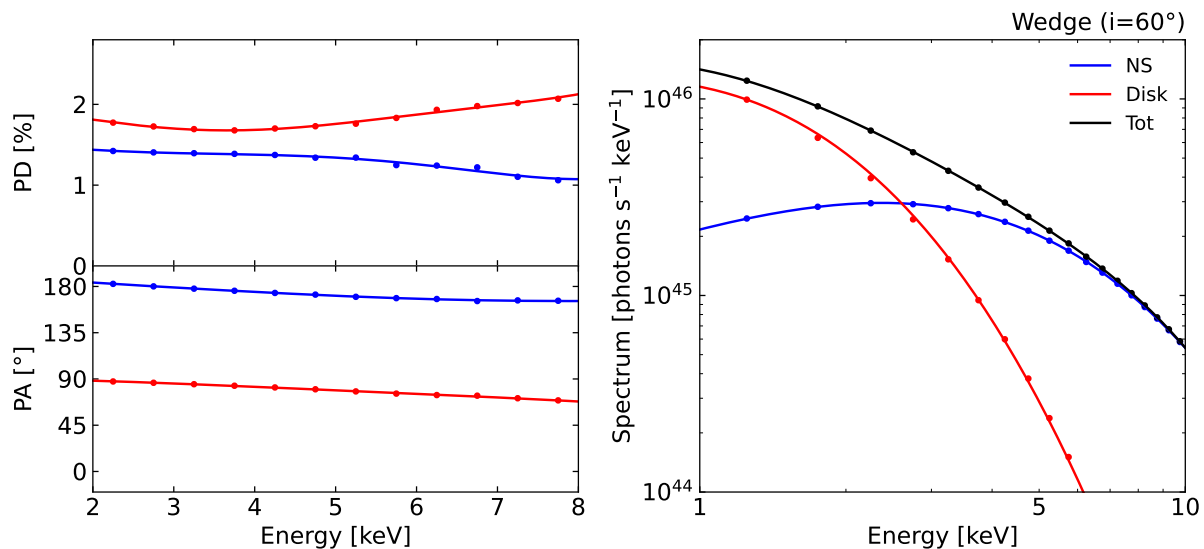


Figure 3.6: Polarization degree and angle (*left panels*) and spectrum (*right panel*) of NS and disk photons (respectively, blue and red lines) as a function of energy considering a wedge configuration of the Comptonizing region. Each contribution includes the direct radiation directly observed. The system is observed at 60° inclination. The PA in MONK is measured from the projection of the rotation axis onto the sky plane.

if the disk photons are polarized, the total polarization is similar to the classical [Chandrasekhar \(1960\)](#) results, while the disk photons are less polarized when intrinsic polarization is not considered. As the wedge is a quite symmetric configuration, the resulting polarization expected from the Compton scattering of soft seed photons is low (between 1–2%). To the first approximation, the wedge is almost perpendicular to the disk plane. Therefore, the polarization angle is expected to be rotated by 90° with respect to that of the polarized radiation emerging from the electron-scattering dominated disk atmosphere ([Chandrasekhar, 1960](#)).

3.7 Boundary/Spreading Layer Geometry

In order to have a better description of the polarization properties of the radiation emitted by the equatorial boundary layer, an additional ellipsoidal shell has been built around the NS equator (Figure 3.1f). The elliptical shell is characterized by a semi-major axis that coincides with the inner disk radius and covers part of the surface of the NS up to the maximum opening angle θ_m (measured from the accretion disk plane). As the accretion rate increases, the radial and latitudinal extension of the spreading layer can vary: at low accretion rates, the inner edge of the disk is located further from the NS surface and the spreading layer extends mainly radially, with lower maximum opening angle (i.e. the boundary layer configuration); at higher accretion rate, the latitudinal extension θ_m increases and the spreading layer covers a larger region of the NS surface (up to the entire NS surface when the accretion rate is close to the Eddington limit [Inogamov and Sunyaev 1999](#); [Popham and Sunyaev 2001](#)). The latitude dependence of the rotation velocity of the boundary layer plasma is required to compute the maximum opening angle θ_m . To study the polarimetric properties of a “general” spreading layer-like configuration, the maximum opening angle θ_m is set to 45°. The dependence of the PD and PA for different θ_m is studied in Section 5.1 and also applied for some Z-sources (Section 5.2.2). In the standard boundary/spreading layer models, the accreting matter rapidly decelerates its rotation inside the boundary layer from the Keplerian disk velocity to the rotational velocity of the NS (Section 2.1.4; [Inogamov and Sunyaev 1999](#)). However, in MONK simulations (up to now) the electron plasma is assumed to rotate with Keplerian velocity. This is however a reasonable assumption: the rotational velocity “breaks” the symmetry of the system, creating

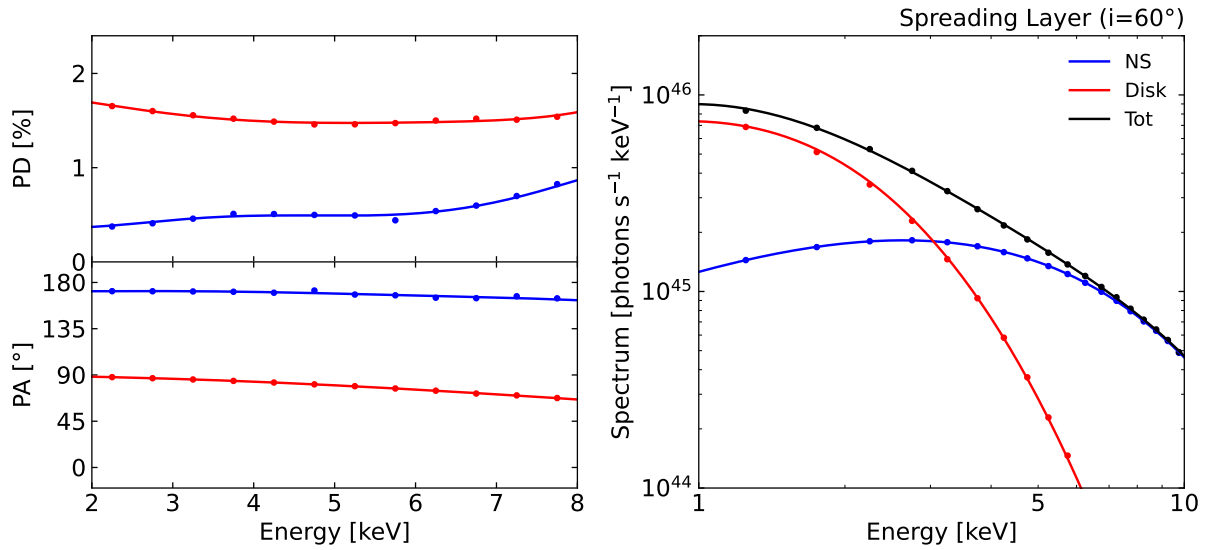


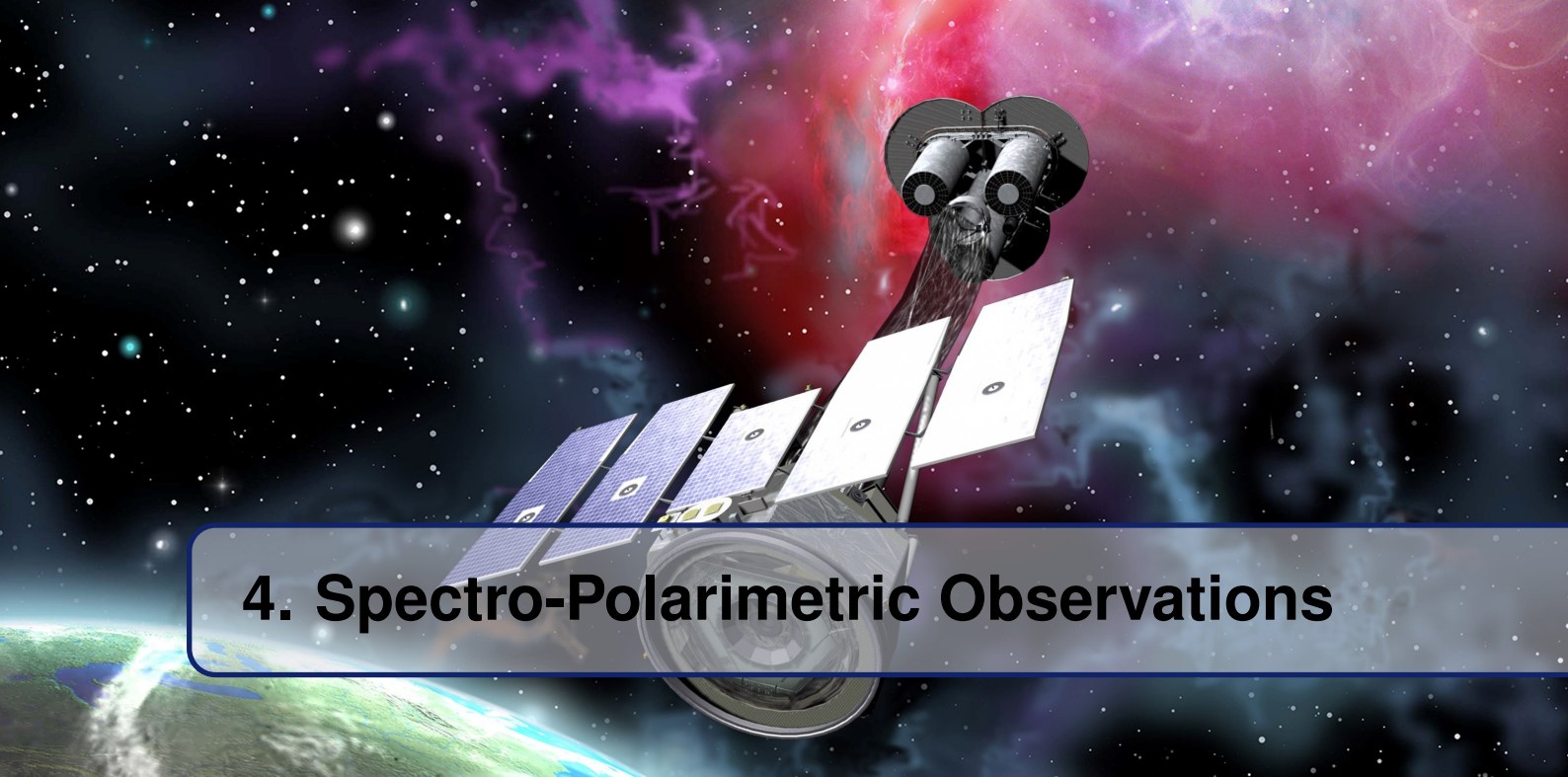
Figure 3.7: Polarization degree and angle (*left panels*) and spectrum (*right panel*) of NS and disk photons (respectively, blue and red lines) as a function of energy considering a spreading layer-like geometry of the Comptonizing region. Each contribution includes the direct radiation directly observed. The system is observed at 60° inclination. The PA in MONK is measured from the projection of the rotation axis onto the sky plane.

a preferential direction for emitted photons; not accounting for the drop from the Keplerian to the NS rotational velocity, this effect is maximized having only the Keplerian velocity. Therefore, the resulting polarization is a kind of upper limit obtainable for this shape of the Comptonizing region. For this class of geometries, the optical depth of the electron plasma is measured in the radial direction from the NS surface.

The results for the polarization degree and angle of the two different components (i.e. the NS and the disk) are represented in Figure 3.7. The disk component includes the photons emitted from the accretion disk and directly detected by the observer without any Compton scattering, along with the Comptonized disk radiation. The NS direct and scattered photons contribute significantly to the emission at higher energies ($\gtrsim 3 - 4$ keV) and result to be low-polarized ($\lesssim 1\%$) with direction perpendicular to the accretion disk plane, as the spreading layer is at zero order approximation perpendicular to the meridian plane. The direct disk emission dominates at lower energies, with polarization vector along the meridian plane (if polarized; Chandrasekhar 1960). Only a few photons from the disk will be scattered as the spreading layer extends between the NS and the inner edge of the accretion disk. The expected polarization is very similar to that of the wedge configuration, as expected since these two types of geometries are built in order to approximate the boundary/spreading layer geometry.

Part Two

4	Spectro-Polarimetric Observations	53
4.1	X-ray Polarimetry	53
4.2	IXPE	55
4.2.1	Data Reduction	55
4.3	GS 1826–238	56
4.3.1	Observations	57
4.3.2	Spectro-Polarimetric Analysis	58
4.4	GX 9+9	60
4.4.1	Observations	60
4.4.2	Spectro-Polarimetric Analysis	61
4.5	4U 1820–303	64
4.5.1	Observations	65
4.5.2	Radio Observation	66
4.5.3	Spectro-Polarimetric Analysis	67
4.6	4U 1624–49	70
4.6.1	Observations	71
4.6.2	Spectro-Polarimetric Analysis	72
4.7	Cygnus X–2	75
4.7.1	Observations	75
4.7.2	Spectro-Polarimetric Analysis	77
4.8	XTE J1701–462	80
4.8.1	Observations	81
4.8.2	Spectro-Polarimetric Analysis	83
4.9	GX 5–1	87
4.9.1	Observations	88
4.9.2	Radio Observations	89
4.9.3	Spectro-Polarimetric Analysis	90
4.10	Scorpius X–1	94
4.10.1	Observations	94
4.10.2	Polarimetric Analysis	95
4.11	Circinus X–1	96
4.11.1	Observations	97
4.11.2	Polarimetric Analysis	98
5	Results	99
5.1	Comparison Between Different Geometries	99
5.2	Comparison Between Observations	102
5.2.1	Atoll-Sources	102
5.2.2	Z-sources	107
6	Conclusions	113
6.1	Future Perspectives	114



4. Spectro-Polarimetric Observations

The exact nature of the X-ray emitting regions in NS-LMXBs remains elusive, since the models are spectroscopically degenerate. X-ray polarimetry can significantly constrain the geometry of the accreting system together with its physical properties. X-ray polarimetric studies are now a reality thanks to the *Imaging X-ray Polarimetry Explorer* (*IXPE*; Weisskopf et al. 2016, 2022). During the first two-year observational campaign, *IXPE* observed all major classes of galactic and extragalactic X-ray sources, providing space, energy and time-resolved polarimetry (Weisskopf et al., 2022). Among all these X-ray sources, several NS-LMXBs were observed by *IXPE*: four soft state Atoll-sources (GS 1826–238, GX 9+9, 4U 1820–303 and 4U 1624–49) and three Z-sources (Cyg X–2, XTE J1701–462, GX 5–1). In this chapter, the *IXPE* observations of NS-LMXBs are re-analyzed using the same procedure for all the sources. In particular, all the data from *IXPE* and other X-ray facilities have been reduced using all the standard tools and the latest calibration files available. The joint spectro-polarimetric analysis is performed considering the same physical model to fit the observed spectra. This choice was made to allow for a direct comparison between the various sources using the same spectral model, differently from the *IXPE* discovery papers. Very recently, *IXPE* also observed two more Z-sources (Cir X–1 and Sco X–1) for which only the polarimetric analysis is reported.

4.1 X-ray Polarimetry

X-ray polarimetry can be a powerful tool for studying the physics and geometry of different classes of astrophysical sources, adding information that can be used to remove degeneracies in models. A polarimeter is a detector capable of analyzing different angular directions and detecting photons with respect to these directions. Any linear polarimeter is capable of measuring the azimuthal modulation of some physical quantity $N(\phi)$, around some specific direction of polarization ϕ_0 in the xy -polarization plane (see the review by Fabiani 2018 for more details). If the radiation is not polarized, every angular direction has the same probability; thus the number of photons detected, as a function of the angular directions, is the same and the detector response is flat (Figure 4.1, *left panel*). If the radiation is polarized, one angular direction will be more probable and a $\cos^2 \phi$ modulation arises (Figure 4.1, *right panel*). This modulation depends on the dipole interaction between the photon and the interacting electron of an atom in the sensitive volume of the polarimeter. The modulation function is defined as

$$N(\phi) = A_P + B_P \cos^2(\phi - \phi_0) \quad (4.1)$$

where A_P is the flat term and B_P is the modulated term. The modulated fraction of the detector response is given by the modulation factor μ defined for 100% polarized radiation

$$\mu = \frac{N_{100\%}^{\max} - N_{100\%}^{\min}}{N_{100\%}^{\max} + N_{100\%}^{\min}} = \frac{B_{100\%}}{2A_{100\%} + B_{100\%}} \quad (4.2)$$

where $N_{100\%}^{\max}$ and $N_{100\%}^{\min}$ are the maximum and minimum number of photons detected in the angular bins of the modulation histogram for 100% polarized radiation. Once μ is known for the instrument, the polarization degree of a source can be derived from the measured value of modulation amplitude

$$PD = \frac{1}{\mu} \frac{B_P}{2A_P + B_P} . \quad (4.3)$$

It is more convenient to define the Stokes parameter for each photon i_k , q_k and u_k in the instrument-defined direction ϕ_k . The linearity of the Stokes parameters (see also Appendix A) allows to compute the Stokes parameters of N events per energy band over the exposure time T :

$$\begin{aligned} I_N &= \frac{1}{T} \sum_{k=1}^N i_k = \frac{1}{T} \sum_{k=1}^N 1 \\ Q_N &= \frac{1}{T} \sum_{k=1}^N q_k = \frac{1}{T} \sum_{k=1}^N 2 \cos(2\phi_k) \\ U_N &= \frac{1}{T} \sum_{k=1}^N u_k = \frac{1}{T} \sum_{k=1}^N 2 \sin(2\phi_k) . \end{aligned} \quad (4.4)$$

The measured PD and PA for realistic detectors may be determined as

$$\begin{aligned} PD &= \frac{1}{\mu} \frac{\sqrt{Q_N^2 + U_N^2}}{I_N} \\ PA &= \frac{1}{2} \arctan\left(\frac{U_N}{Q_N}\right) \end{aligned} \quad (4.5)$$

with some uncertainty in the measurement, which is a combination of both statistical and instrumental errors, calculated from μ (playing a major role in the description of quality of a polarimetric instrument). The event-by-event calculation of Stokes parameters does not provide expected values identical to those obtained by fitting the modulation function: the obtained values are proportional, with the constant of proportionality being the number of bins in the modulation curve. However, the two approaches are completely equivalent since the observable quantities are the PD and PA, which are invariant for proportional Stokes parameters (Muleri, 2022).

The detectability of a source can be estimated by means of the *Minimum Detectable Polarization* (MDP), which is defined as the minimum polarization that can be detected at a confidence level of 99% (Weisskopf et al., 2010; Strohmayer and Kallman, 2013)

$$MDP(99\%) = \frac{4.29}{\mu R} \sqrt{\frac{R+B}{T}} \quad (4.6)$$

where R is the count rate of the source, B is the background count rate and T is the net observation time. A signal with a modulation corresponding to a polarization lower than the MDP is compatible with a statistical fluctuation for an unpolarized source and, therefore, no positive detection of polarization can be claimed.

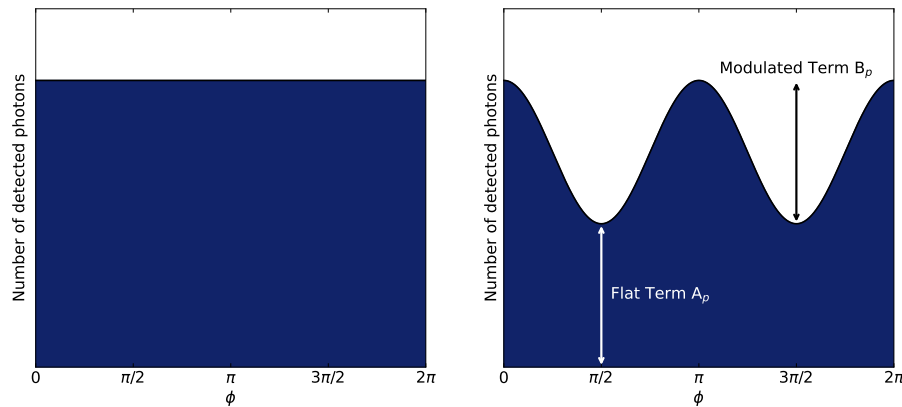


Figure 4.1: Detector response of a polarimeter to unpolarized radiation (flat, *left panel*) and to polarized radiation (modulated, *right panel*).

4.2 IXPE

IXPE (Weisskopf et al., 2016, 2022) is a joint NASA-Italian Space Agency (ASI) Small Explorer Mission selected in early 2017 and launched on 2021 December 9 on a SpaceX Falcon 9 from NASA's Kennedy Space Center (LC-39A) in Florida, with a 2-year baseline mission. Compared to the previous X-ray polarimetric mission on OSO-8, *IXPE* needs about two orders of magnitude less exposure time to reach the same sensitivity. It provides imaging capability with $\leq 30''$ angular resolution over $11'$ field of view, together with $1\text{--}2\ \mu\text{s}$ timing accuracy and a moderate spectral resolution typical of proportional counters. Figure 4.2 (*left panel*) shows a schematic of the *IXPE* observatory and its key payload elements. The payload consists of three identical X-ray telescopes with identical mirror modules and identical polarization-sensitive imaging detector units (DUs) at their focus. Inside each DU there is the *gas-pixel detector* (GPD; Figure 4.2, *right panel*) that images the photoelectron tracks produced by X-rays absorbed in the special fill gas (Costa et al., 2001). The initial emission direction of the photoelectron determines the polarization of the source, whereas the initial interaction point and the total charge in the track provide the location and energy of the absorbed X-ray, respectively. Once constructed and environmentally tested, each DU went through a comprehensive calibration to characterize the response to both polarized and unpolarized radiation and to measure the spectral, spatial, and timing performance. The DUs were also integrated into the detector service units (DSUs) and illuminated with X-ray sources (with known polarization and position angle) to test the operation of the instrument in the flight configuration. To also enable in-flight calibration monitoring, each DU is equipped with a filter and calibration wheel assembly that contain various radioactive sources that can be rotated in front of the GPD to provide for monitoring gain, energy resolution, spurious modulation and the modulation factor (Muleri et al., 2018; Ferrazzoli et al., 2020; Rankin et al., 2022). Data from the detectors are handled by the DSU, located under the S/C top deck.

4.2.1 Data Reduction

Data reduction and analysis of *IXPE* observations have been performed using the *IXPE* collaboration software tool *IXPEOBSSIM* software v.30.5.2 (Baldini et al., 2022) and the HEASOFT tools v.6.32 (Nasa High Energy Astrophysics Science Archive Research Center, 2014), with the latest calibration files (CALDB v.20230526). The *IXPEOBSSIM* tools include *xppicorr* to locally apply energy calibration with in-flight calibration sources, *xpselect* to filter data and *xpbin* to apply different binning algorithms for generating images and spectra. The rebinning and the spectro-polarimetric analysis were performed using HEASOFT *FTOOLS* including *XSPEC*. The normalized Stokes parameters Q/I and U/I , as well as their uncertainties, are calculated using the PCUBE binning algorithm of *IXPEOBSSIM*, which assumes that

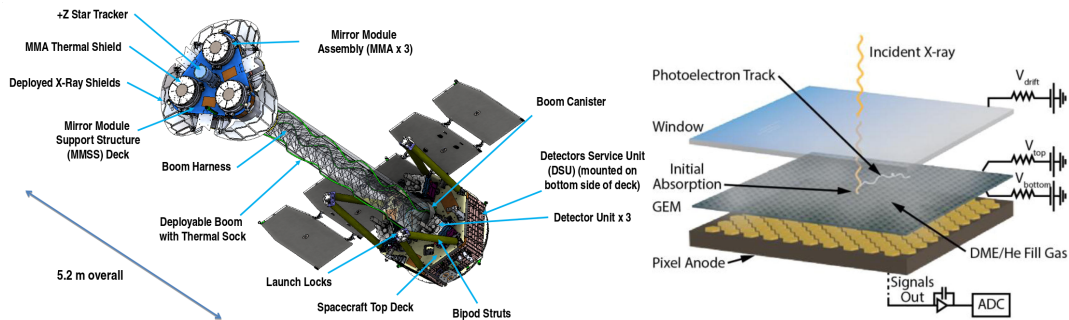


Figure 4.2: Schematic of the *IXPE* Observatory (Weisskopf et al., 2016, 2022) and the polarization-sensitive gas-pixel detectors (Costa et al., 2001).

they are not correlated and that PD and PA are independent (Kislat et al., 2015). The results of the polarimetric analysis obtained with both *xSPEC* and the *IXPEOBSSIM* tools *PCUBE* have been compared: while *xSPEC* requires the definition of a spectro-polarimetric model, *IXPEOBSSIM* allows a model independent analysis that computes the polarization only on the basis of detected photons. The uncertainties from the *xSPEC* analysis are computed with the `error` command for one parameter of interest. It is worth noting that the PD and PA are not independent. The contours representing the 68.27%, 95.45% and 99.73% confidence levels of the joint measurement of the PD and PA are a more appropriate method to represent the uncertainties. With *IXPEOBSSIM* such contours are derived as described in Weisskopf et al. (2010); Strohmayer and Kallman (2013); Muleri (2022) by using the parameters obtained by the *PCUBE* algorithm itself. In *xSPEC* the contours are obtained using the `steppar` command for two parameters of interest. The upper limits to the PD are based upon its error in one dimension, without regard to the value of the PA. Therefore, they are computed using a χ^2 with one degree of freedom.

The source and background regions were selected from the image of each DU. The source is located in a circular region, where the extraction radii have been calculated through an iterative process that leads to the maximization of the signal-to-noise ratio (SNR) in the 2–8 keV energy band, similar to the approach described in (Piconcelli et al. 2004, see also Marinucci et al. 2022; Ursini et al. 2023b). The background is always extracted from an annular region with internal and external radii of 180'' and 240'', respectively. Following the prescription by (Di Marco et al., 2023b) for bright sources, the background has not been subtracted. In fact, background subtraction does not significantly alter the results, especially the polarimetric measurements. Data analysis with *IXPEOBSSIM* is performed following the unweighted method: equal weights are assigned to each photo-electron track, regardless of its shape. The weighted analysis method presented in Di Marco et al. (2022) was applied for data analysis with *xSPEC*, using the parameter `stokes=Neff` in `xSELECT`. Since the modulation factor is significantly affected by weights, a weighting scheme using the photo-electron track ellipticity is considered, providing the best sensitivity and reducing the spurious modulation. A constant energy binning of 0.2 keV was used for the Q and U Stokes spectra, along with an SNR greater than 3 in each spectral channel for the intensity spectra.

4.3 GS 1826–238

GS 1826–238 is a well-known accreting NS-LMXB discovered by *Ginga* in 1988 (Makino, 1988). It was classified as an Atoll source in the hard spectral state until 2016 (Cocchi et al., 2011; Sánchez-Fernández et al., 2020), after which GS 1826–238 underwent a major transition to the high soft state. The peculiarity of this source was the presence of extremely regular X-ray bursts over a range of several years (Cocchi et al., 2000; Zamfir et al., 2012). For this reason, it is also known as “*clocked burster*”.

Source	Satellite	Obs. ID	Start Date (UT)	Net Exp. (ks)
GS 1826–238	<i>IXPE</i>	01002801	2022-03-29 07:14:28	85.0
	NICER	5050310101	2022-03-28 02:32:40	7.2
	NICER	5050310102	2022-03-29 00:20:20	9.5
	NICER	5050310103	2022-03-30 01:17:00	6.4
	NICER	5050310104	2022-03-31 00:20:00	1.2
	<i>INTEGRAL</i>	19700050001	2022-03-28 17:23:38	139/108.4

Table 4.1: Log of simultaneous observations of the Atoll-source GS 1826–238 (Capitanio et al., 2023).

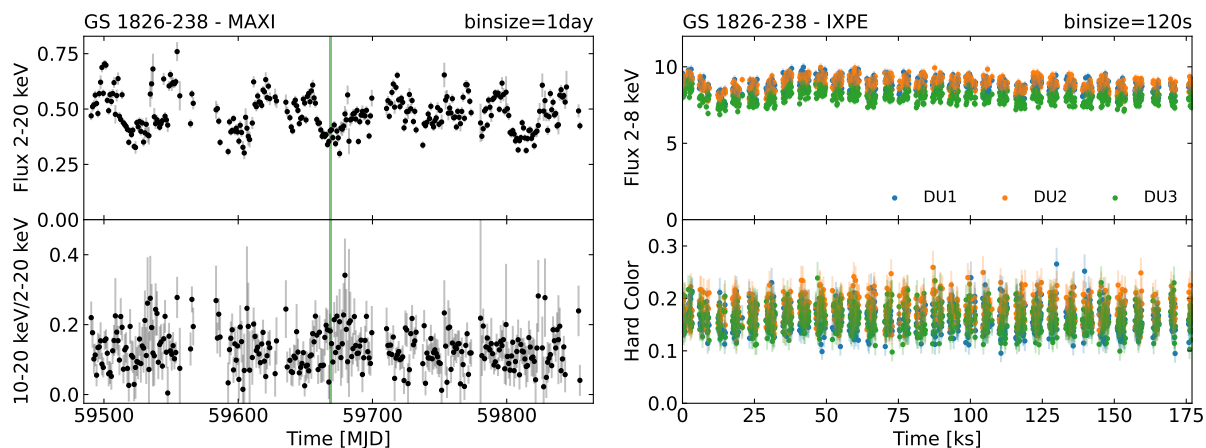


Figure 4.3: *Left panel*: GS 1826–238 MAXI 2–20 keV light curve in units of photons $\text{cm}^{-2} \text{s}^{-1}$ (top) and hardness ratio (10–20 keV/2–20 keV, bottom) as a function of time in MJD. The green line correspond to the *IXPE* observation. Flux variations among the light curve are mostly due to the MAXI spurious modulation (Mihara et al., 2022). *Right panel*: GS 1826–238 *IXPE* 2–8 keV light curve in units of cps (top) and Hard Color (5–8 keV/3–5 keV, bottom) as a function of the observational time (see also Capitanio et al. 2023). Each bin corresponds to 120 s.

4.3.1 Observations

The observation of GS 1826–238 with *IXPE* (Capitanio et al., 2023) was carried out from 2022 March 29 07:14:28 UT to 2022 March 31 09:20:06 UT (see Table 4.1), for a total net exposure time of 85 ks after taking into account Earth occultations. *IXPE* data were extracted as described in Section 4.2.1, considering 120'' source extraction radius. NICER (Gendreau et al. 2016, see also Appendix B.2) performed four observations of GS 1826–238 with continuous exposure between 2022 March 28 02:32:40 UT and 2022 March 31 00:43:00 UT. The source moves along the CCD/HID but remains at quite constant hard color. The four NICER spectra are summed up before the spectro-polarimetric analysis (see Table 4.1). Data have been extracted and reduced following the procedure described in the Appendix B.2.1. *INTEGRAL* (Winkler et al. 2003, see also Appendix B.3) observed the source from 2022-03-28 17:25 to 2022-03-30 23:43:32 UT for a total of 139 ks for JEM-X1 and 108.4 ks for JEM-X2. *INTEGRAL* data has been reduced following the procedure described in the Appendix B.3.1. A systematic error of 1.5% was added in quadrature for spectral analysis. Only JEM-X data were used for spectral extraction because IBIS, the γ -ray energy detector (Lebrun et al., 2003), did not detect the source (and therefore the high-energy tail) with an upper limit of 3σ on the flux of $\sim 10^{-11} \text{ erg cm}^{-2} \text{ s}^{-1}$ in the 28–40 keV range.

The left panel of Figure 4.3 reports the 2–20 keV MAXI (Matsuoka et al., 2009) light curve of GS 1826–238, along with the hardness ratio (10–20 keV/2–20 keV) that spans one year from 2021 September 28. After the major state transition to HSS (MJD ~ 57500), the large and periodic ($P \sim 72$ days) flux variations correspond to only slight variations in the hardness ratio, probably due to a spurious

Model	Parameter	Best-fit
TBabs	n_H (10^{22} cm^{-2})	$0.52^{+0.02}_{-0.02}$
diskbb	kT_{in} (keV)	$0.91^{+0.04}_{-0.05}$
	R_{in} (km)	$11.93^{+0.98}_{-0.69}$
bbodyrad	kT (keV)	$1.32^{+0.11}_{-0.12}$
	R_{bb} (km)	$6.75^{+1.59}_{-1.06}$
thcomp	kT_e (keV)	[2.8]
	τ	$6.44^{+1.05}_{-0.95}$
$\chi^2/\text{d.o.f.}$		200.9/151
$F_{\text{disk}}/F_{\text{tot}}$ (2–8 keV)		54.7%
$F_{\text{comp}}/F_{\text{tot}}$ (2–8 keV)		45.3%
F_{tot} ($\text{erg s}^{-1} \text{ cm}^{-2}$)		3.97×10^{-9}

Notes. A 7 kpc distance is assumed to compute the inner radius R_{in} and R_{bb} from normalizations.

Table 4.2: Best-fit Spectral Parameters obtained from the NICER and *INTEGRAL* data. The errors are at the 90% confidence level for a single parameter.

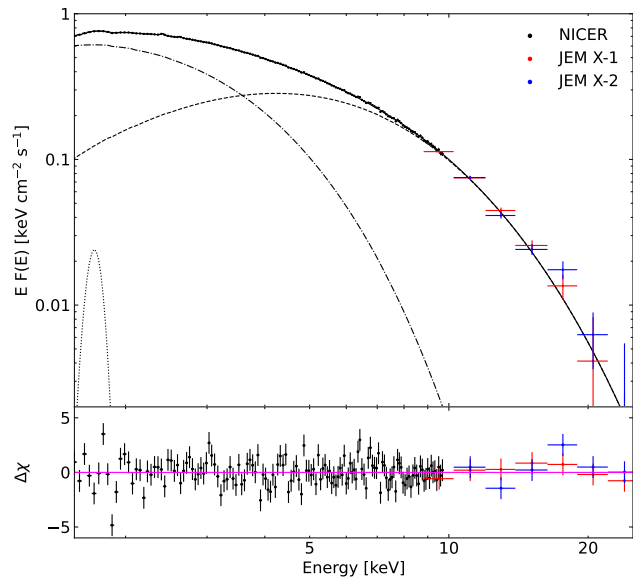


Figure 4.4: Best-fit of the *NuSTAR* and *INTEGRAL* deconvolved spectra GS 1826–238. The model includes `diskbb` (dashed dotted line), `thcomp*bbodyrad` (dashed line) and `gaussian` (dotted line) with residuals in units of σ . The spectral parameters are given in Table 4.2.

oscillation in the MAXI light curves (Mihara et al., 2022). The *IXPE* observation time, coordinated with NICER and *INTEGRAL*, is highlighted by the green line. The *IXPE* light curve and the hard color (5–8 keV/3–5 keV) are substantially constant within all observation (Figure 4.3, right panel). However, due to an improper correction of the telescope vignetting caused by the off-axis pointing during the *IXPE* pointing of GS 1826–238, the *IXPE* spectra were not compatible with NICER+JEM-X spectra. Due to the brightness of the source, the induced systematic effect is highly significant in the energy spectrum¹. On the other hand, since the Stokes parameters Q/I and U/I are normalized quantities of photon counts, their derivation is not influenced by different changes in efficiency over energy for single DU and PD and PA are not affected (Capitanio et al., 2023; Farinelli et al., 2023).

4.3.2 Spectro-Polarimetric Analysis

The model used for the fitting procedure is a multicolor disk blackbody component `diskbb` (Mitsuda et al. 1984, see also Appendix C.2.4) and a harder boundary layer/corona emission (e.g. Popham and Sunyaev 2001; Revnivtsev et al. 2013). Comptonized emission is modelled using the convolution model `thcomp` (Zdziarski et al. 2020, see Appendix C.2.5 for more details) applied to a simple blackbody (`bbodyrad`, see also Appendix C.2.1). The covering factor f of `thcomp` represents the fraction of Comptonized seed photons. When f is close to 1, all photons from the boundary layer `bbodyrad` are Comptonized. Both components are modified by interstellar absorption using `TBabs` (Appendix C.2.7), with `vern` cross-section (Verner et al., 1996) and `wilm` abundances (Wilms et al., 2000). No reflection component or iron line was observed in the spectra. The spectral parameters obtained from the fitting procedure are reported in Table 4.2 and the corresponding spectrum with the best-fit model is shown in Figure 4.4. To improve the quality of the fit, the covering factor and the electron temperature are fixed. The features in the residuals are due to NICER instrumental issues (Miller et al., 2018; Strohmayer et al., 2018). To deal with these residuals, some `gaussian` components and an absorption edge have been added. The first `gaussian` component peaks at 1.71 ± 0.04 keV and with line width 0.06 ± 0.01 keV, while the other

¹<https://heasarc.gsfc.nasa.gov/FTP/ixpe/data/obs/01/01002801/README>

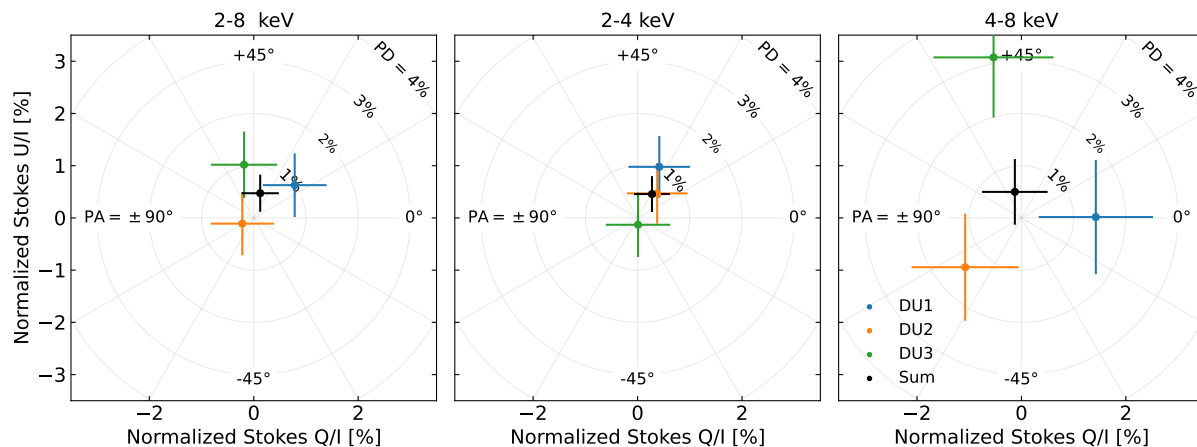


Figure 4.5: Stokes parameters of GS 1826–238 in the 2–8 keV, 2–4 keV and 4–8 keV energy bands for DU1 (blue), DU2 (orange), DU3 (green) and by summing all the events of the three DUs (black) (Capitanio et al., 2023).

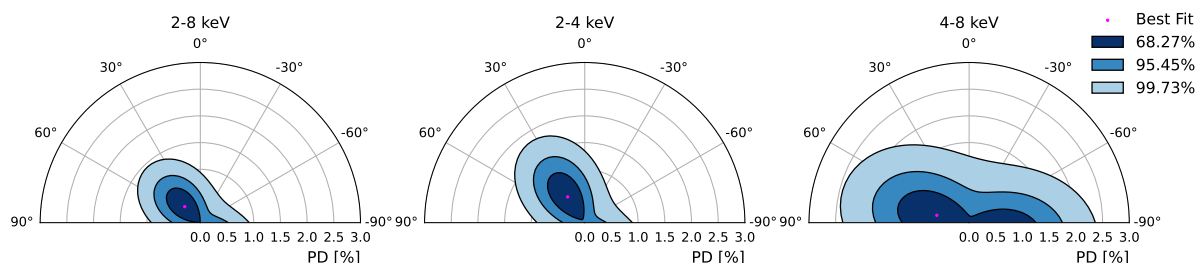


Figure 4.6: Polarization contours for GS 1826–238 in the 2–8 keV, 2–4 keV and 4–8 keV energy bands obtained with *xSPEC* by summing the events from the three DUs. Contours correspond to the 68.27%, 95.45% and 99.73% confidence levels derived using a χ^2 with two degrees of freedom (see also Capitanio et al. 2023).

two narrow components are respectively at 2.41 ± 0.02 keV and 2.66 ± 0.03 keV. The spectral parameters remain consistent within the errors. The spectrum of GS 1826–238 is consistent with typical spectra for a weakly magnetized NS-LMXB in the soft state, with low temperature and highly opaque electron plasma (see e.g. Paizis et al. 2006). Assuming a distance to the source of 7 kpc, the normalization of `diskbb` corresponds to an inner disk radius of $\sim 12 \sqrt{\cos i}$ km. The size of the seed photon-emitting region can be estimated from the best-fit normalization of `bbodyrad`, assuming that all seed photons are Comptonized and computing the flux and the emission area (see also in 't Zand et al. 1999). The estimated seed photon region size is equivalent to a spherical radius of ~ 7 km. This result is consistent with the seed photons originating in a region smaller than the entire NS, such as the boundary layer.

The Stokes parameters of GS 1826–238 observed by *IXPE* in the 2–8 keV, 2–4 keV and 4–8 keV energy bands obtained with *IXPEOBSSIM* are reported in Figure 4.5. No detection of polarization can be claimed, with no significant variation over time. Only upper limits can be found in each energy range both from *IXPEOBSSIM* (as described in Baldini et al. 2022) and from *xSPEC*. The resulting 1σ upper limits from *IXPEOBSSIM* (0.84%, 0.85%, and 0.94% in the 2–8, 2–4, and 4–8 keV range, respectively; see Capitanio et al. 2023) are somewhat larger than the estimates using a Bayesian approach presented by Maier et al. (2014), but are consistent with the corresponding limits from *xSPEC* (0.69%, 0.91%, and 1.48%, respectively). The *xSPEC* 3σ upper limits (99.73% confidence level) are 1.48%, 1.76%, and 2.45%, while the Bayesian approach gives rather consistent limits of 1.41%, 1.44%, and 2.37%. In any case, the PA is unconstrained in the three energy bands. The spectro-polarimetric fit is performed by applying a constant polarization

Source	Satellite	Obs. ID	Start Date (UT)	Net Exp. (ks)
GX 9+9	<i>IXPE</i>	01002401	2022-10-09 11:33:38	92.5
	<i>NuSTAR</i>	30801021002	2022-10-09 10:21:09	39.4

Table 4.3: Log of simultaneous observations of the bright Atoll-sources GX 9+9 (Ursini et al., 2023a).

through `polconst` (Appendix C.2.8) to the best-fit model found from NICER+JEM-X data. To derive the polarization parameters (PD and PA), all spectral parameters of `TBabs`, `diskbb` and `thcomp*bodyrad` were fixed to the best-fit value. At both low and high energies, the *IXPE* data differ significantly with respect to the best-fit model. This is probably related to calibration issues, already observed in other sources (Taverna et al., 2022; Krawczynski et al., 2022; Marinucci et al., 2022), and to improper correction of *IXPE* vignetting due to off-axis pointing. To correct for these deviations, a gain shift correction is applied to the response files of the *IXPE*/*I* spectra with the `gain fit` command in `xSPEC`. The gain parameters of the *Q* and *U* spectra are then linked to those of the *I* spectra for each DU. The energy shift was calculated using the relation $E' = E/\alpha - \beta$, where α is the gain slope and β the offset. The resulting slope is 1.067 ± 0.003 , 1.135 ± 0.003 , 1.055 ± 0.003 keV⁻¹ for the three DUs respectively, while the offset in each of them is -0.135 ± 0.064 , -0.087 ± 0.009 , -0.049 ± 0.010 keV. Figure 4.6 reports the contours of the PD and PA of the *IXPE* observation respectively in the 2–4, 4–8 and 2–8 keV energy bands and are consistent with those obtained with `IXPEOBSIM` (Capitani et al., 2023). As expected, the PD is compatible with null polarization and the PA is unconstrained even at a 1σ confidence level.

4.4 GX 9+9

GX 9+9, also known as 4U 1728-16, is a NS-LMXB discovered during a sounding rocket observation of the Galactic center (Bradt et al., 1968). It has been classified as a bright Atoll source (Hasinger and van der Klis, 1989), whose light curve shows a 4.2 h modulation in both the optical and the X-ray bands (Hertz and Wood, 1988; Schaefer, 1990). Its distance is not well known, the estimates range between 5 kpc (Christian and Swank, 1997) and 10 kpc (Savolainen et al., 2009). This source has been consistently observed in a bright soft state (Gladstone et al., 2007; Savolainen et al., 2009; Iaria et al., 2020). The average X-ray flux in the 2–20 keV band is ~ 200 mCrab (Iaria et al., 2020), and the X-ray spectrum is well represented by a two-component emission model plus reflection (Kong et al., 2006; Savolainen et al., 2009; Iaria et al., 2020). From the relativistic reflection component, the inclination has been estimated to be 40° – 50° , consistent with the upper limit of 70° indicated by the lack of X-ray eclipses (Schaefer, 1990; Savolainen et al., 2009).

4.4.1 Observations

IXPE observed GX 9+9 (Ursini et al., 2023a) between 2022 October 9 11:33:38 UT and October 11 13:19:10 UT for a net exposure time of 92.5 ks (Obs. ID 30801021002, see Table 4.3). Science data were extracted as described in Section 4.2.1 considering $120''$ source extraction radius. GX 9+9 was also observed by *NuSTAR* from 2022 October 9 10:21:09 UT to October 10 14:51:09 UT, with a net exposure of 38.5 ks, simultaneously with the first half of the *IXPE* exposure. The cleaned and calibrated data have been extracted following the procedure described in the Appendix B.1.1. For both detectors, the background was extracted from a circular region with $60''$ radius while the source radius is $120''$, found by following the signal-to-noise ratio maximization procedure (Piconcelli et al., 2004). Since the background starts dominating above 30 keV, the data are considered to be in the 3–30 keV range. GX 9+9 exhibits complex long-term X-ray variability (Kotze and Charles, 2010), however the MAXI light curve shows a quite constant baseline and small amplitude variations from 2009 (~ 56000 MJD; Asai et al.

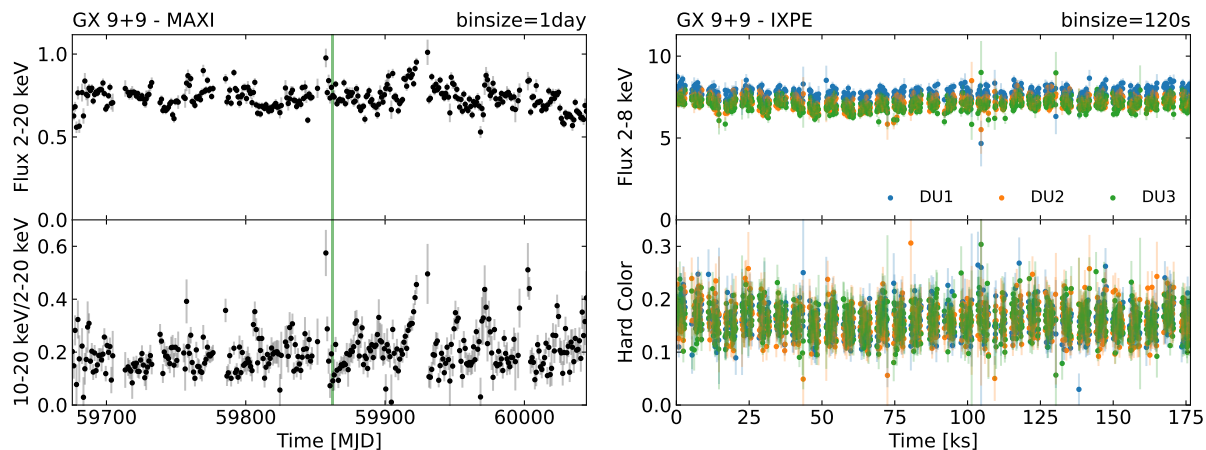


Figure 4.7: *Left panel*: GX 9+9 MAXI 2–20 keV light curve in units of photons $\text{cm}^{-2} \text{s}^{-1}$ (top) and hardness ratio (10–20 keV/2–20 keV, bottom) as a function of time in MJD. The green line correspond to the *IXPE* observation. *Right panel*: GX 9+9 *IXPE* 2–8 keV light curve in units of cps (top) and Hard Color (5–8 keV/3–5 keV, bottom) as a function of the observational time (see also Ursini et al. 2023a). Each bin corresponds to 120 s.

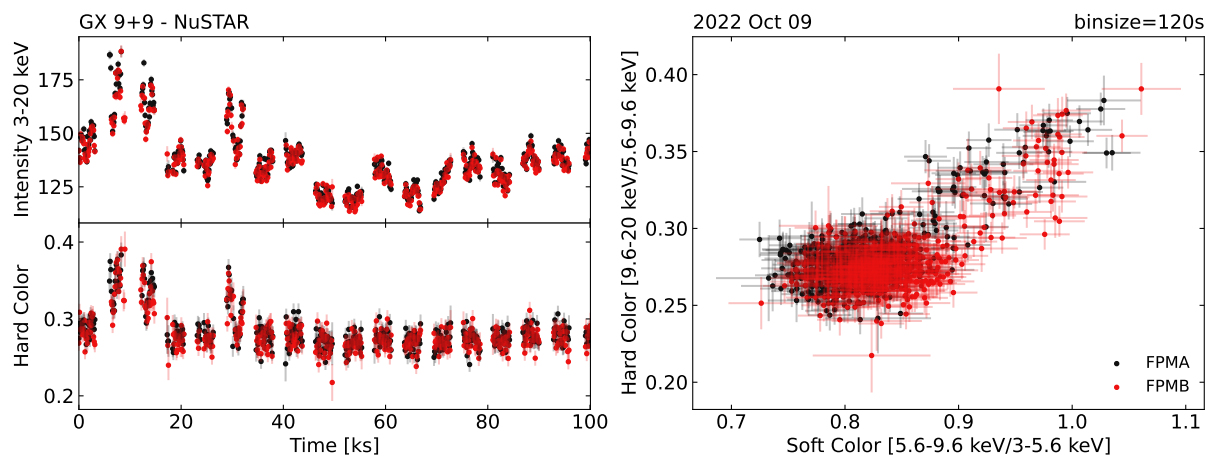


Figure 4.8: GX 9+9 *NuSTAR* 3–20 keV light curves in units of cps and Hard color (9.6–20 keV/5.6–9.6 keV) as a function of time (*left panel*) and Soft color (5.6–9.6 keV/3–5.6 keV, *right*). Red and black points correspond to the two *NuSTAR* detector, FPMA and FPMB respectively. Each bin corresponds to 120 s.

2022). The daily MAXI light curve is shown in Figure 4.7 (*left panel*) spanning one year. The X-ray flux is quite stable, whereas the hardness ratio shows variations on timescales of roughly 1–2 months. The *IXPE* observation, coordinated with *NuSTAR*, is highlighted with the green line. The *IXPE* light curve and the hard color are substantially constant within all observations (Figure 4.7, *right panel*). *NuSTAR* light curve and CCD (Hard color: 9.6–20 keV/5.6–9.6 keV, Soft color: 5.6–9.6 keV/3–5.6 keV) are shown in Figure 4.8. Flux variations can be observed for a short interval at the beginning of the *NuSTAR* exposure. However, the variation in HR is not dramatic and no flarings are detected. Therefore, the average spectrum over the entire observation is considered for spectral analysis.

4.4.2 Spectro-Polarimetric Analysis

The simple `diskbb+thcomp*bbodyrad` model does not provide a good fit to the observed data, leaving significant residuals, especially in the 6–7 keV range (Ursini et al., 2023a). To remove the residuals, the relativistic smeared reflection component is needed to fit the broadband spectrum. The observed residuals do not show any presence of an obvious Compton hump, so that reflection should be produced by a softer

Model	Parameter	Best-fit
TBabs	n_H (10^{22} cm $^{-2}$)	[0.3]
diskbb	kT_{in} (keV)	$1.05^{+0.02}_{-0.02}$
	R_{in} (km)	$9.09^{+0.71}_{-0.14}$
bbodyrad	kT (keV)	$1.58^{+0.05}_{-0.04}$
	R_{bb} (km)	$5.07^{+0.16}_{-0.26}$
thcomp	kT_e (keV)	$3.46^{+0.33}_{-0.21}$
	τ	$4.96^{+0.37}_{-0.36}$
	f	[1]
relxillNS	i ($^\circ$)	$32.16^{+15.83}_{-12.09}$
	R_{in} (ISCO)	$7.13^{+7.07}_{-4.81}$
	kT_{bb} (keV)	$= kT$
	$\log \xi$	$3.32^{+0.07}_{-0.12}$
	N_r (10^{-4})	$3.40^{+0.74}_{-0.55}$
$\chi^2/\text{d.o.f.}$		690.4/661
$F_{\text{disk}}/F_{\text{tot}}$ (2–8 keV)		52.8%
$F_{\text{comp}}/F_{\text{tot}}$ (2–8 keV)		42.5%
$F_{\text{refl}}/F_{\text{tot}}$ (2–8 keV)		4.7%
F_{tot} (erg s $^{-1}$ cm $^{-2}$)		4.04×10^{-9}

Notes. A 7.5 kpc distance is assumed to compute the inner radius R_{in} and R_{bb} from normalizations.

Table 4.4: Best-fit Spectral Parameters obtained from the *NuSTAR* and *IXPE* data. The errors are at the 90% confidence level for a single parameter.

illuminating spectrum than the typical non-thermal (power-law) continuum assumed in standard reflection models. Reflection is employed using `relxillNS` (García et al., 2022), a flavor of `relxill` (García et al., 2014; Dauser et al., 2014) in which the primary continuum illuminating the disk is a single temperature blackbody spectrum, corresponding to the NS surface or spreading layer emission. This model assumes an incident illuminating spectrum at 45° on the surface of the disk (García et al., 2022). Some `relxillNS` parameters, which the fit does not constrain, are fixed at reasonable values: the emissivity index $q_{\text{em}} = 2$ (see e.g. Wilkins 2018), the iron abundance $A_{\text{Fe}} = 1$ and the number density $\log n_e = 18$ (e.g. Ludlam et al. 2022). The adopted number density is consistent with the inner region of a standard accretion disk (see García et al. 2016 and references therein). The fit is not sensitive to this parameter, as its effect on X-ray reflection is significant only at lower energies (Ballantyne, 2004; García et al., 2016). The dimensionless spin a can be derived from the NS period (in ms) as $a = 0.47/P$ (Braje et al., 2000) and, analogously to the one derived from QPOs by Wijnands et al. (1998) for Cyg X–2, the spin is fixed at 0.1 (see also Patruno et al. 2017). The inclination i , the inner disk radius R_{in} (in units of ISCO) and the ionization parameter ξ are left free to vary. The blackbody temperature is also tied to that of the seed photon spectrum of `bbodyrad`. The covering factor f of `thcomp` is always > 0.96 and is then fixed at 1. The best-fitting parameters are reported in Table 4.4 and are quite typical for a NS-LMXB in the soft state (see also Figure 4.9). Considering a 7.5 kpc distance to the source, the normalization of `diskbb` corresponds to an inner disk radius of $\sim 10 \sqrt{\cos i}$ km. Assuming that all seed photons are Comptonized and computing the flux

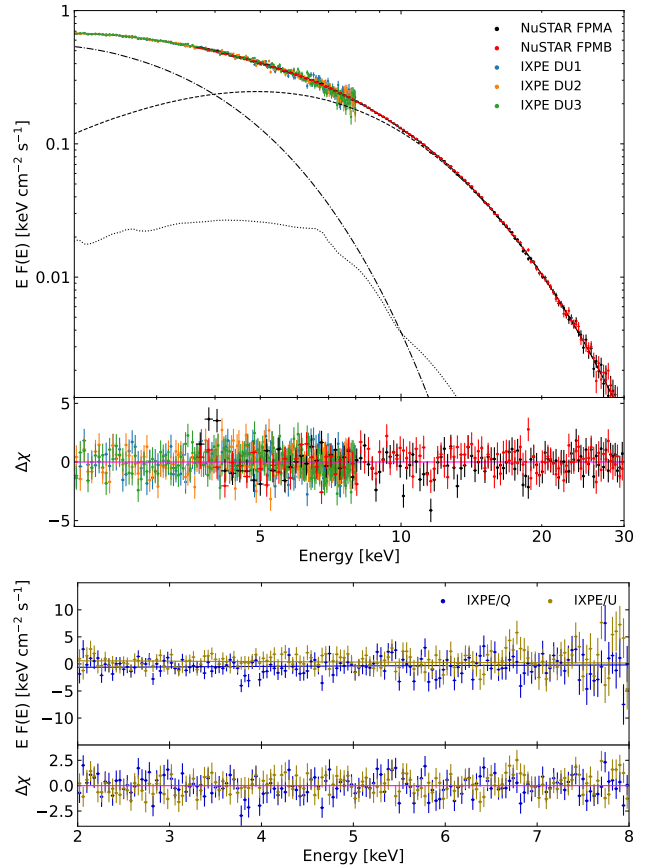


Figure 4.9: Best-fit of the *NuSTAR* and *IXPE* deconvolved I spectra (top panel) with Stokes Q and U spectra (lower panel) of GX 9+9. The model includes `diskbb` (dashed dotted line), `thcomp*bbodyrad` (dashed line) and `relxillNS` (dotted line) with residuals in units of σ . The spectral parameters are given in Table 4.4.

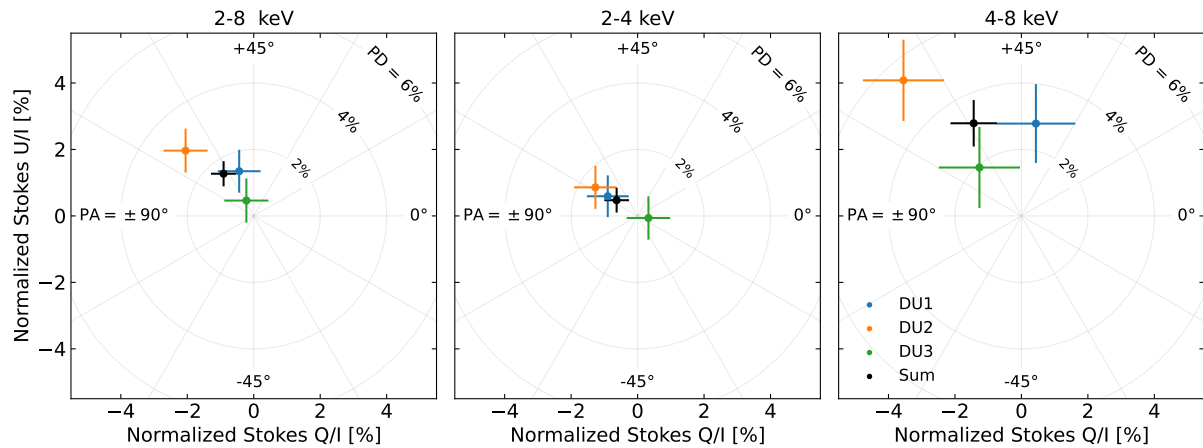


Figure 4.10: Stokes parameters of GX 9+9 in the 2–8 keV, 2–4 keV and 4–8 keV energy bands for DU1 (blue), DU2 (orange), DU3 (green) and by summing all the events of the three DUs (black).

and emission area, the size of the emitting region can be estimated from the best-fit normalization of `tbodyrad` (see also in [Zand et al. 1999](#)). The seed photon emitting region size results to be equivalent to a spherical radius of 5 km. This result is consistent with the soft photons originating in a region smaller than the entire NS, such as the boundary layer.

The Stokes parameters of GX 9+9 observed by *IXPE* in the 2–8 keV, 2–4 keV and 4–8 keV energy bands obtained with `IXPEOBSSIM` are reported in Figure 4.10. Significant polarization is detected in the 2–8 keV band with PD of $1.6\% \pm 0.4\%$ and an increasing trend of polarization with energies, up to $3.1\% \pm 0.7\%$ in the 4–8 keV energy range. This results are well consistent within the errors with those obtained with `XSPEC` (Figure 4.11). Between 2–4 keV, the polarization is compatible with null polarization at 3σ confidence level. The joint spectro-polarimetric fit is performed using the baseline model obtained only from *NuSTAR* and *IXPE* data (`diskbb+thcomp*tbodyrad+relxillNS`) and applying to each component a constant polarization through `polconst`. The reflection component modelled by `relxillNS` includes the fluorescent iron line, which should be unpolarized (its contribution to the photon flux is only $\sim 10\%$ in the 6–7 keV range). Some significant residuals are found at both low and high energies in the *IXPE* spectra, which can be corrected by applying a gain shift to the response files of the *IXPE* spectra with the `gain_fit` command in `XSPEC`. The resulting slope is 0.984 ± 0.003 , 0.982 ± 0.003 , 0.986 ± 0.003 keV^{-1} for the three DUs respectively, while the offset in each one is -0.031 ± 0.012 , -0.022 ± 0.013 , -0.021 ± 0.013 keV. All spectral parameters are fixed to their best-fit value. The *IXPE* band-pass does not allow to obtain tight constraints on the PD and PA of each component (especially for the Comptonized and reflected radiation because these two are quite degenerate peaking at similar energies and having similar spectral shapes), so some assumptions based on theoretical and observational expectations are required.

As a first test, only one of the three spectral components is assumed to be polarized, with the other two having null PD. Assuming a polarized disk only, the fit results to be acceptable ($\chi^2/\text{d.o.f.} = 1490.7/1569$, $800.3/894$ for the subset of Stokes Q and U spectra) with $2.1\% \pm 0.8\%$ PD and $70.3^\circ \pm 11.6^\circ$, but the assumption is not consistent with the observed PD increasing with energy. Actually, the opposite is expected from the disk contribution to the total flux ([Ursini et al., 2023a](#)). Considering the case where either `thcomp*tbodyrad` or `relxillNS` are the only polarized component, the fit improves ($\chi^2/\text{d.o.f.} = 1475.1/1569$, $784.7/894$ for the subset of Stokes Q and U spectra) for both cases. The model provides a good fit of both the flux and the Stokes Q and U spectra, without strong residuals. The PA obtained in the two cases is very similar ($66.5^\circ \pm 8.3^\circ$ for only polarized `thcomp*tbodyrad` and $67.3^\circ \pm 8.5^\circ$ for only polarized `relxillNS`) while the reflection-dominated scenario requires a very large PD of $33.2\% \pm 9.7$, compared to $3.8\% \pm 1.1$ of only `thcomp*tbodyrad` polarization, because the reflection component is subdominant with respect to Comptonized radiation, contributing to roughly 7% of the 4–8

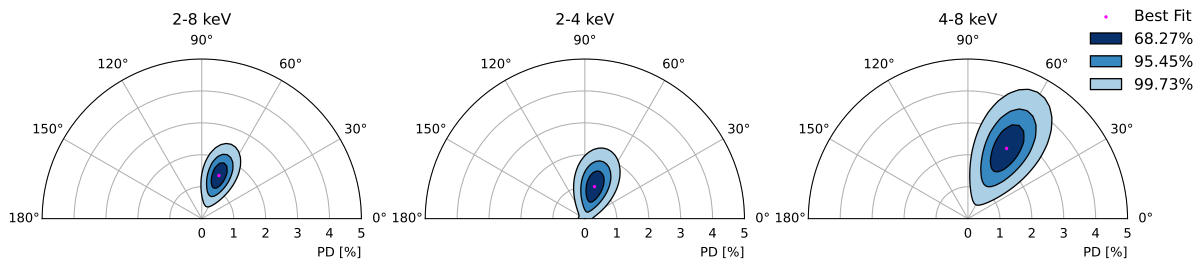


Figure 4.11: Polarization contours for GX 9+9 in the 2–8 keV, 2–4 keV and 4–8 keV energy bands obtained with `xSPEC` by summing the events from the three DUs. Contours correspond to the 68.27%, 95.45% and 99.73% confidence levels derived using a χ^2 with two degrees of freedom.

keV flux. Due to the similarity of GX 9+9 spectral shape to other bright NS-LMXBs in the soft state, following [Farinelli et al. \(2023\)](#) and considering that the reflection component has a PA perpendicular to the disk surface ([Matt, 1993](#); [Poutanen et al., 1996b](#); [Schnittman and Krolik, 2009](#)), the PA of the reflected radiation should be the same as that of the Comptonized component. This configuration is consistent with the geometry of a spreading layer, since the vertical height is significantly higher than its radial extension ($H \gg \Delta R$). To try to estimate the polarization of the reflected radiation, the PD of the Comptonized component is fixed at 1% (a reasonable value for wedge or spreading layer-like geometries, see Sections 3.6 and 3.7) and the PD of the disk at a conservative value of 1% at the inferred source inclination. The resulting PD of the reflection component is $22.8\% \pm 13.8\%$ with a PA of $63.6^\circ \pm 10.7^\circ$ (the same of the Comptonized component) and $139.2^\circ \pm 41.7^\circ$ for the disk (at 90% confidence level). Even if the disk PA is not tightly constrained, it is consistent with being perpendicular to the Comptonized and reflection PA. As a consequence, the PA of the disk can be fixed to be perpendicular to the other two components. Leaving the PD of the disk free to vary, an upper limit of 2.8% can be found (at 90% confidence level on a single parameter), with a PD of the reflection of $26.0\% \pm 18.8\%$ with $66.3^\circ \pm 8.3^\circ$ PA. A similar procedure can be done by leaving free to vary the PD of both the disk and Comptonized components and assuming that the reflection has a fixed PD of 10% (see e.g. [Matt 1993](#)). In this case, the PD of the disk is not constrained ($< 2.3\%$ at 90% confidence level) and the PD of the Comptonized component results in $3.6\% \pm 1.8\%$ with PA of $66.4^\circ \pm 8.4^\circ$.

4.5 4U 1820–303

4U 1820–303 is an ultracompact NS-LMXB accreting matter via Roche lobe overflow from a He white dwarf. It is located at 0.66 arcsec from the center of the globular cluster NGC 6624 ([Rappaport et al., 1987](#); [Shaposhnikov and Titarchuk, 2004](#)) at a distance of $d = 8.0 \pm 0.1$ kpc estimated from GAIA EDR3 ([Baumgardt and Vasiliev, 2021](#)). It was the first identified source of type-I X-ray bursts ([Grindlay et al., 1976](#)). 4U 1820–303 has an orbital period of 685 s ([Stella et al., 1987](#)) and the intrinsic luminosity shows variability along a super orbital ~ 170 days period ([Zdziarski et al., 2007](#)). 4U 1820–303 shows X-ray type-I bursts mainly around the flux minima, proving that the observed variability is related to changes in the intrinsic accretion rate. This is also supported by the strong correlations between the observed flux variations with the source spectral state (in a way typical of Atoll-type NS binaries) and the kHz frequency of quasi-periodic oscillations ([Smale et al., 1997](#)). 4U 1820–303 is also a known radio emitter (e.g. [Migliari et al. 2004](#); [Díaz Trigo et al. 2017](#)). At low X-ray fluxes, the radio spectrum is typically relatively flat, consistent with a compact radio jet, while at higher X-ray fluxes ([Russell et al., 2021](#)), the radio spectrum becomes steep, consistent with either a quenching of compact jet emission or emission from a transient jet ejecta ([Russell et al., 2021](#)). Assuming a uniform and ordered magnetic field, linear

Source	Satellite	Obs. ID	Start Date (UT)	Net Exp. (ks)
4U 1820–303	<i>IXPE</i>	02002301	2022-10-11 13:53:22	16.4
	<i>IXPE</i>	02002302	2023-04-15 01:33:24	86.1
	<i>NuSTAR</i>	90802327002	2022-10-12 14:31:09	16.5
	<i>NuSTAR</i>	90902308002	2023-04-15 00:01:09	16.8
	<i>NuSTAR</i>	90902308004	2023-04-16 14:36:09	15.2
	NICER	5050300117	2022-10-11 01:29:00	1.7
	NICER	6689020101	2023-04-15 01:13:11	10.3
	NICER	6689020102	2023-04-16 00:30:05	13.7

Table 4.5: Log of simultaneous observations of the Atoll-sources 4U 1820–303 (Di Marco et al., 2023a).

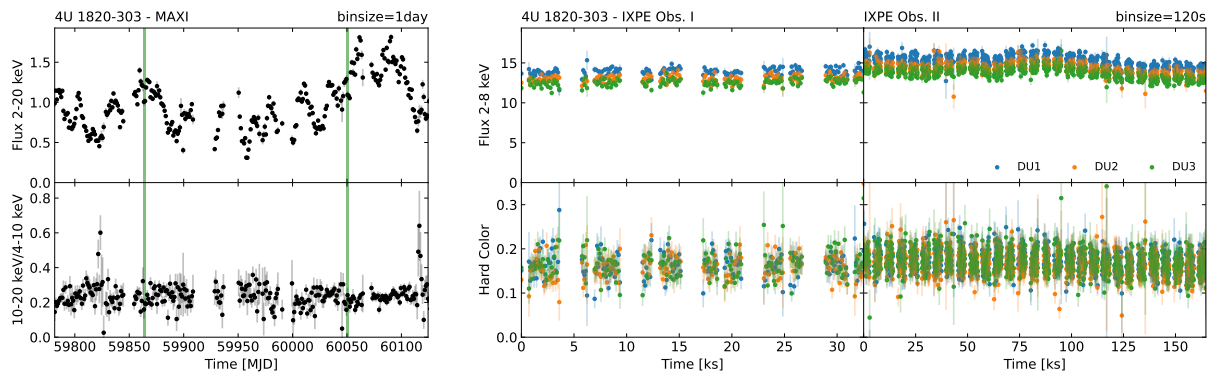


Figure 4.12: *Left panel:* 4U 1820–303 MAXI 2–20 keV light curve in units of photons $\text{cm}^{-2} \text{s}^{-1}$ (*top*) and hardness ratio (10–20 keV/2–20 keV, *bottom*) as a function of time in MJD. The green line corresponds to the *IXPE* observations. *Right panel:* 4U 1820–303 *IXPE* 2–8 keV light curves in units of cps (*top*) and Hard Color (5–8 keV/3–5 keV, *bottom*) as a function of observational time (see also Di Marco et al. 2023a). Each bin corresponds to 120 s.

polarization from a compact (self-absorbed) radio jet is expected to have a maximum degree of $\sim 10\%$ while the optically thin ejecta can exhibit values up to $\sim 70\%$ (see Longair 2011 for more details); however, due to disorder in the magnetic fields, lower values are typically observed (see e.g. Curran et al. 2014).

4.5.1 Observations

IXPE observed 4U 1820–303 in two different periods: on 2022 October 11 from 13:53: UT to 22:55: UT for a total exposure of 16 ks per DU and from 2023 April 15 01:33: to April 16 23:17: UT for a total exposure of 86 ks per DU (Di Marco et al., 2023a). The sequence ID and the exposure time of the *IXPE* observation used are given in Table 4.5. Science data were extracted as described in Section 4.2.1 with $120''$ source extraction radius. Background subtraction was not applied due to the high count rate of the source (≥ 2 counts s^{-1} per DU, see Di Marco et al. 2023b). During both *IXPE* observations, *NuSTAR* performed coordinated observations, the first from 2022 October 12 14:31:09 UT to October 13 02:41:09 UT with a total net exposure of 16.9 ks and the other two on 2023 April 15 from 00:01:09 to 16:01:09 and on April 16 from 14:36:09 to 01:26:09 with a total exposure of 16.8 ks and 15.2 ks, respectively. The sequence IDs and exposure times of the *NuSTAR* observations used are given in Table 4.5. The cleaned and calibrated data were extracted following the procedure described in the Appendix B.1.1. For both detectors, the background was extracted from a circular region with $60''$ radius while the source

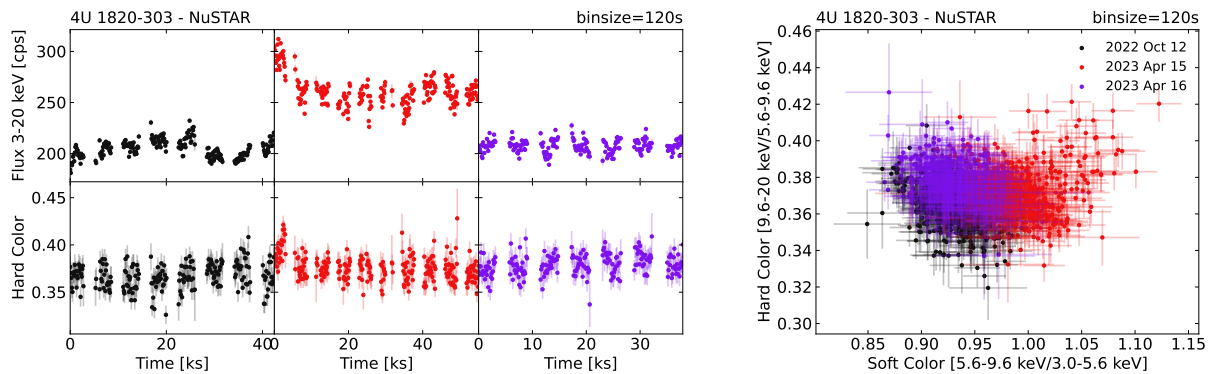


Figure 4.13: 4U 1820–303 *NuSTAR* 3–20 keV light curves in units of cps and Hard color (9.6–20 keV/5.6–9.6 keV) as a function of time (*left panel*) and Soft color (5.6–9.6 keV/3–5.6 keV, *right panel*). Red and black points correspond to the two *NuSTAR* detector, FPMA and FPMB respectively. Each bin corresponds to 120 s.

radius is $120''$, found by following the signal-to-noise ratio maximization procedure (Piconcelli et al., 2004). Since the background starts dominating above 30 keV, the data are considered in the 3–30 keV range. Contemporaneous observations of 4U 1820–303 were also made with NICER. During the first observation, NICER observed the source for a total exposure of 1.7 ks from 2022 October 11 01:31:19 to 09:21:33 UT. Then, NICER reobserved the 4U 1820–303 on 2023 April 15 from 02:49:15 to 23:12:10 and on April 16 from 00:34:26 to 22:50:54 for a total exposure time of 10.3 ks and 13.7 ks, respectively. The sequence IDs and exposure times of the NICER observations used are given in Table 4.5. Data have been extracted and reduced following the procedure described in the Appendix B.2.1. The daily MAXI light curve is shown in Figure 4.12 (*left panel*) spanning one year. *IXPE* observations (highlighted with the green line) were performed near the maximum of the flux along the superorbital period. The *IXPE* light curves and the hard color are substantially constant during the two pointings (Figure 4.12, *right panel*). The light curves and the CCD for the three *NuSTAR* observations are shown in Figure 4.13. The fluxes are very similar for the first and third observations, whereas during the second, the flux is higher as the source moves along the upper banana branch. The HR is substantially constant within all observations. Therefore, the average spectrum over the entire observation is considered for spectral analysis.

4.5.2 Radio Observation

4U 1820–303 was observed with the Australia Telescope Compact Array (ATCA) on 2021 April 15 from 12:49:40 to 21:51:20 UT. During this observation, ATCA was in a relatively compact H214 configuration², recording data at two central frequencies (5.5 and 9 GHz) with 2 GHz bandwidth at each frequency. The nearby source B1817–254 was used for gain calibration and to calibrate the polarization angle, following the standard procedures with the Common Astronomy Software Applications for Radio Astronomy (*CASA* v.5.1.2; CASA Team et al. 2022) `atcapolhelpers.py` task `qufromgain`³. While 4U 1820–303 was detected in both frequency bands, the radio counterpart was relatively faint, with a measured flux density of $100 \pm 12 \mu\text{Jy}$ at 5.5 GHz and $80 \pm 10 \mu\text{Jy}$ at 9 GHz. This corresponds to a radio spectral index of -0.45 ± 0.30 (Di Marco et al., 2023a). The X-ray brightness, state, and radio spectral index at the time of the observations suggest that the radio emission originates from either a quenched compact jet or a transient ejecta (see also Russell et al. 2021). Imaging the field in both Stokes Q and U , no significant linear polarization was detected with 60% upper limit at 5.5 GHz and 70% at 9GHz at 3σ .

²https://www.narrabri.atnf.csiro.au/operations/array_configurations/configurations.html

³<https://github.com/radio-astro>

Model	Parameter	Best-fit	
TBfeo	n_H (10^{21} cm^{-2})	$1.82^{+0.02}_{-0.01}$	
	A_O	$1.35^{+0.03}_{-0.04}$	
	A_{Fe}	$0.49^{+0.08}_{-0.09}$	
diskbb	kT_{in} (keV)	$0.62^{+0.01}_{-0.02}$	
	R_{in} (km)	$24.67^{+1.23}_{-0.92}$	
bbodyrad	kT (keV)	$0.86^{+0.01}_{-0.01}$	
	R_{bb} (km)	$21.81^{+2.24}_{-0.43}$	
thcomp	kT_e (keV)	$2.98^{+0.03}_{-0.02}$	
	τ_{NuSTAR}	$10.70^{+0.16}_{-0.15}$	
relxillNS	i ($^\circ$)	$32.89^{+3.06}_{-3.68}$	
	R_{in} (ISCO)	< 1.85	
	kT_{bb} (keV)	$2.99^{+0.19}_{-0.17}$	
	$\log \xi$	$2.90^{+0.17}_{-0.07}$	
	$\log N$ (cm^{-3})	[16]	
	A_{Fe}	[0.5]	
	N_r (10^{-3})	$1.08^{+0.12}_{-0.11}$	
	expabs	E_c	$= kT$
	powerlaw	α	[2.6]
		N_{pl}	$0.23^{+0.04}_{-0.04}$
$\chi^2/\text{d.o.f.}$		1294.9/1242	

Notes. A 8 kpc distance is assumed to compute the inner radius R_{in} and R_{bb} from normalizations.

Table 4.6: Best-fit Spectral Parameters obtained from the *IXPE*, *NuSTAR* and *NICER* data. The errors are at the 90% confidence level for a single parameter.

4.5.3 Spectro-Polarimetric Analysis

For this source, the absorption column along the line of sight is modelled with TBfeo, with `vern` cross-section (Verner et al., 1996) and `wilm` abundances (Wilms et al., 2000). TBfeo is considered to take into account the over/under-abundances of oxygen and iron, since the oxygen K-edge (0.56 keV) and the iron L-edge (0.71 keV) are observed in the *NICER* spectra. The hydrogen column density n_H , the abundance of oxygen A_O and iron A_{Fe} are left free to vary. Using the *NuSTAR*, *NICER* and *IXPE* spectra, the simple baseline `diskbb+thcomp*bbodyrad` model is not able to provide a good fit, leaving significant residuals in the 5–7 keV range and for energies > 10 keV. To remove residuals in the broadband spectra, the relativistic reflection component is added to the baseline model, using `relxillNS` (García et al., 2022). The fit is not able to constrain some of the `relxillNS` parameters: the emissivity index is set at $q_{em} = 2.5$ while the electron number density is fixed to $\log n_e = 16$. The number density is consistent with the inner region of a standard accretion disk (see García et al. 2016 and references therein). The fit is not sensitive to these parameters, since its effect on reflection is relevant only at lower energies (Ballantyne, 2004; García et al., 2016). The dimensionless spin a can be derived from the NS period (in ms) as $a = 0.47/P$ (Braja et al., 2000). The spin is then fixed at 0.1, consistent with the value obtained for the measured NS period for Cyg X–2 (Wijnands et al. 1998; see also Patruno et al. 2017). As a first test, the blackbody

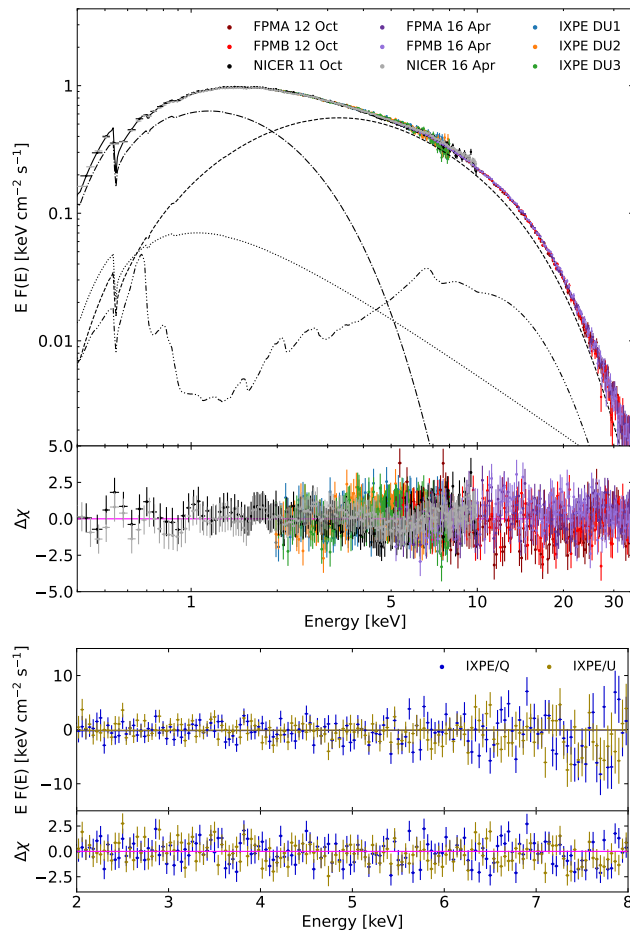


Figure 4.14: Best-fit of the *NuSTAR*, *NICER* and *IXPE* deconvolved spectra (*top panel*) with Stokes Q and U spectra (*lower panel*) of 4U 1820–303. The model includes `diskbb` (dashed dotted line), `thcomp*bbodyrad` (dashed line), `relxillNS` and `powerlaw` (dotted line) with residuals in units of σ . The spectral parameters are given in Table 4.6.

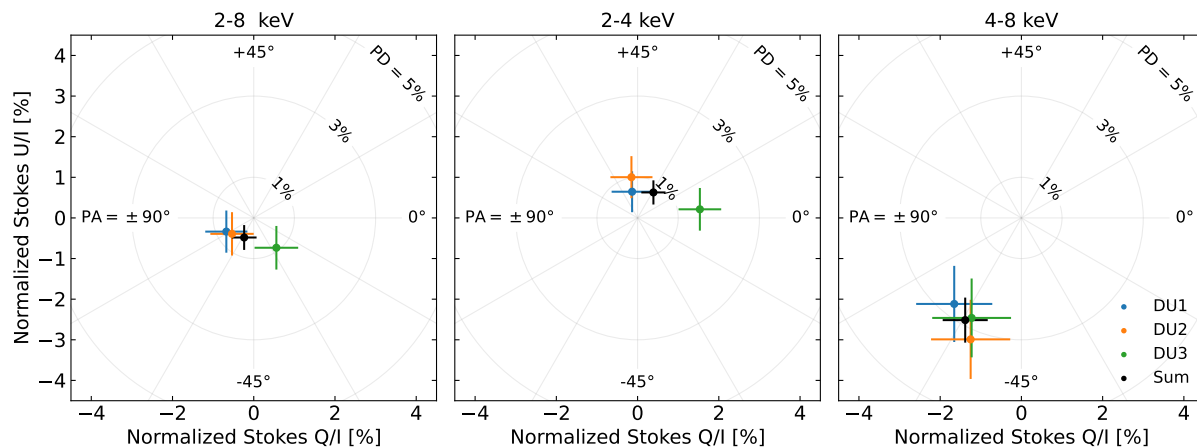


Figure 4.15: Stokes parameters of 4U 1820–303 in the 2–8 keV, 2–4 keV and 4–8 keV energy bands for DU1 (blue), DU2 (orange), DU3 (green) and by summing all the events of the three DUs (black).

temperature of the illuminating spectrum was tied to that of the seed photon spectrum of `bbodyrad`. However, with this assumption, the model was not able to provide a good fit. Therefore, the temperature of `relxillNS` is left free to vary. The covering factor f of `thcomp` is always > 0.98 and is then set to 1. Since the NICER and *NuSTAR* spectra seem to have some intercalibration issues that cannot be solved by only the normalization factor, the optical depth of the Comptonization spectrum τ in `thcomp` is free to vary for each observatory. However, the difference between the obtained optical depth is lower than 10% ($\tau_{\text{NICER Oct.}} = 10.77 \pm 0.19$ and $\tau_{\text{NICER Apr.}} = 11.18 \pm 0.18$). The inclination of the disk i , the inner disk radius R_{in} (in units of ISCO) and the ionization parameter ξ of `relxillNS` are left free to vary. The fit is able to estimate the inclination of the system and find an upper limit for the inner disk radius. To improve the fit at high energies, an additional hard tail is added to the model, represented by a power-law component (`powerlaw`) with a low-energy exponential roll-off (`expabs`). This power-law emission is assumed to originate from the seed distribution of the boundary/spreading layer, so the e-folding energy for the absorption of the exponential roll-off is set equal to the temperature of `bbodyrad`. The photon fluxes of the different components are reported in Table 4.7. Assuming a distance to the source of 8 kpc, the normalization of `diskbb` corresponds to an inner disk radius of $\sim 25 \sqrt{\cos i}$ km. The size of the seed photon-emitting region can be derived from the best-fit normalization of `bbodyrad`, assuming that all seed photons are Comptonized ($f = 1$) and computing the flux and the emission area (see also in [Zand et al. 1999](#)). The estimated seed photon emitting region size is equivalent to a spherical radius of ~ 22 km. This result is consistent with the seed photons originating in a boundary layer between the disk and the NS surface. The best-fit parameters are reported in Table 4.6 and are quite typical for a NS-LMXB in the soft state (see also Figure 4.14).

The Stokes parameters of 4U 1820–303 observed by *IXPE* in the 2–8 keV, 2–4 keV and 4–8 keV energy bands obtained with `IXPEOBSSIM` are reported in Figure 4.15. Although no detection of polarization is found in the whole *IXPE* energy range and in the low-energy part (2–4 keV), significant polarization is observed in the high-energy band (4–8 keV) with PD of $2.9\% \pm 0.6\%$ and PA of $120.7^\circ \pm 5.5^\circ$ (see also [Di Marco et al. 2023a](#)). The polarization signal increases with energy, up to $9.6\% \pm 2.4\%$ in the 7–8 keV energy bin (at 99.99% confidence level, see also [Di Marco et al. 2023a](#)). These results are consistent within the errors with those obtained with `XSPEC` (Figures 4.16 and 4.17). The polarization is compatible with null polarization at 3σ confidence level in the 2–4 keV range and in the whole *IXPE* band. The joint spectro-polarimetric fit is performed using the baseline model obtained from the *NuSTAR*, NICER and *IXPE* data and applying to each component a constant polarization through `polconst`. The reflection component modelled by `relxillNS` includes the fluorescent iron line, which should be unpolarized (its contribution to photon flux is only $\sim 10\%$ in the 6–7 keV range). Some significant residuals are found at

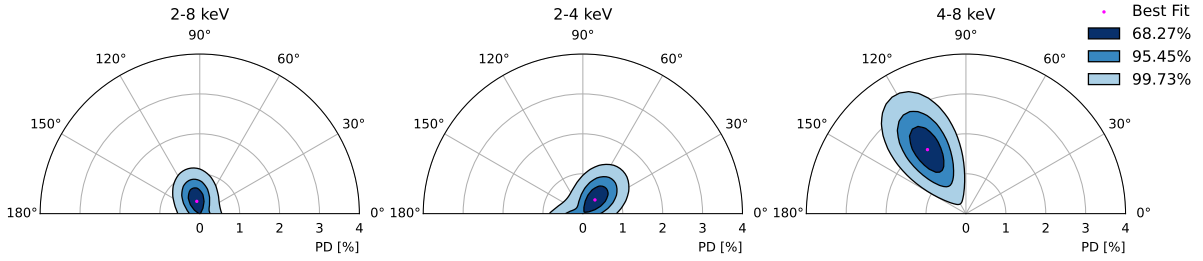


Figure 4.16: Polarization contours for 4U 1820–303 in the 2–8 keV, 2–4 keV and 4–8 keV energy bands obtained with *xSPEC* by summing the events of the three DUs. Contours correspond to the 68.27%, 95.45% and 99.73% confidence levels derived using a χ^2 with two degrees of freedom.

Energy	Photon Flux	Best-fit
2–8 keV		
	F_{tot} (erg s ⁻¹ cm ⁻²)	5.4×10^{-9}
	$F_{\text{diskbb}}/F_{\text{tot}}$	17.6%
	$F_{\text{thcomp*bb}}/F_{\text{tot}}$	76.1%
	$F_{\text{relxillNS}}/F_{\text{tot}}$	2.9%
	$F_{\text{powerlaw}}/F_{\text{tot}}$	3.4%
7–8 keV		
	F_{tot} (erg s ⁻¹ cm ⁻²)	5.6×10^{-10}
	$F_{\text{diskbb}}/F_{\text{tot}}$	0.2%
	$F_{\text{thcomp*bb}}/F_{\text{tot}}$	89.4%
	$F_{\text{relxillNS}}/F_{\text{tot}}$	8.1%
	$F_{\text{powerlaw}}/F_{\text{tot}}$	2.3%

Table 4.7: Unabsorbed energy flux in the 2–8 keV and 7–8 keV energy bands, with photon flux ratio for each spectral component.

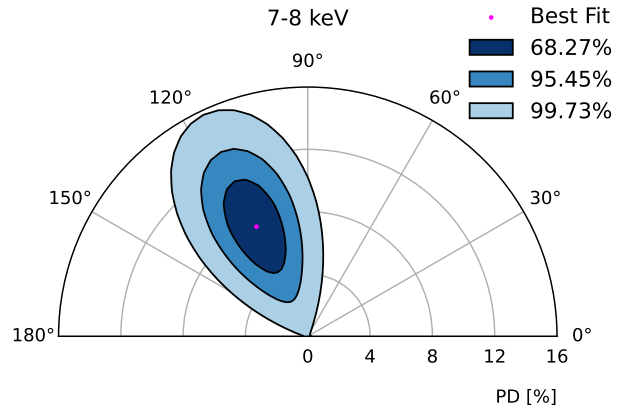


Figure 4.17: Polarization contours for 4U 1820–303 in the 7–8 keV energy band obtained with *xSPEC* by summing the events of the three DUs. Contours correspond to the 68.27%, 95.45% and 99.73% confidence levels derived using a χ^2 with two degrees of freedom.

both low and high energies in the *IXPE* spectra, which can be taken into account by applying a gain shift to the response files of the *IXPE* spectra with the `gain fit` command in *xSPEC*. The resulting slope of the gain shift is 0.982 ± 0.002 , 0.975 ± 0.003 , 0.982 ± 0.003 keV⁻¹ for the three DUs respectively, while the offset in each one is -0.046 ± 0.011 , 0.031 ± 0.010 , 0.019 ± 0.010 keV. All spectral parameters are fixed to their best-fit value. However, no tight constraints on the PD and PA of each component can be obtained, in particular for the Comptonized and reflected radiation because these two are quite degenerate, with similar spectral shapes. The fit is not able to constrain also the power-law component polarization, since its contribution to the 2–8 keV flux is very low. Therefore, the power-law component is considered together with the Comptonized radiation to compute the polarization. Some assumptions are required based on theoretical and observational expectations.

As a first test, only one component is assumed to be polarized, with the others having null polarization. Assuming a polarized disk only, the fit results to be acceptable ($\chi^2/\text{d.o.f.} = 1972.0/1733$, $986.7/894$ for the subset of Stokes *Q* and *U* spectra) but with only an upper limit of 2.3% for the PD. This assumption is not consistent with the observed polarization increasing with energy. Considering the case where either the Comptonized+power-law or reflection component is the only polarized one, the fit improves:

Source	Satellite	Obs. ID	Start Date (UT)	Net Exp. (ks)
4U 1624–49	<i>IXPE</i>	01001601	2023-08-19 09:51:25	198.9
	<i>NuSTAR</i>	90901327002	2023-08-20 18:36:09	41.0
	NICER	6203930102	2023-08-20 02:38:00	0.2
	NICER	6203930103	2023-08-21 00:15:40	1.8
	NICER	6203930104	2023-08-22 04:27:31	0.8
	NICER	6203930105	2023-08-23 00:22:26	0.7

Table 4.8: Log of simultaneous observations of the Atoll source 4U 1624–49.

$\chi^2/\text{d.o.f.} = 1970.0/1733$ (984.8/894 for the subset of Stokes Q and U spectra) is obtained for only `thcomp*bodyrad+expabs*powerlaw`, while $\chi^2/\text{d.o.f.} = 1962.4/1733$ (977.1/894 for the subset of Stokes Q and U spectra) is found considering reflection alone. These models are able to provide a good fit of both the flux and the Stokes parameters spectra without strong residuals. The PA obtained in these two cases is very similar and consistent within the errors ($109.3^\circ \pm 32.4^\circ$ for only Comptonized+power-law component and $116.8^\circ \pm 14.9^\circ$ for only reflection). The reflection-dominated scenario requires a very large PD ($18.7\% \pm 9.3\%$), compared to $0.6\% \pm 0.5\%$ obtained for the other case. Since the reflection component is characterized by a PA perpendicular to the disk surface (Matt, 1993; Poutanen et al., 1996b; Schnittman and Krolik, 2009), its direction should be the same as that of the Comptonized+power-law component (see also Farinelli et al. 2023). To estimate the polarization of the reflected radiation, the PD of the Comptonized+power-law component is fixed at 1%, a reasonable value for wedge or spreading layer geometries (see Sections 3.6 and 3.7), while the polarization of the disk is set to a conservative value of 2% at the inferred source inclination. Only an upper limit of 18.6% (at 90% confidence level) for the polarization of the reflected component can be obtained with the previous assumptions, with a PA of $117.4^\circ \pm 13.7^\circ$ (the same as the Comptonization+power-law). The PA of the disk is found to be consistent with being perpendicular to the Comptonized and reflection components, $33.4^\circ \pm 18.5^\circ$. As a consequence, the PA of the disk can be linked to be perpendicular to the other components. With this assumption and considering again the Comptonized+power-law component polarized at 1%, the disk PD results to be $3.9\% \pm 1.6\%$, while the PD of the reflection is $15.9\% \pm 10.8\%$ with $121.5^\circ \pm 11.5^\circ$. A similar procedure can be done by leaving free to vary the PD of both the disk and Comptonization+power-law components, with PA perpendicular to each other and a PD of the reflection fixed to 10% (see e.g. Matt 1993). The resulting PD of the disk is $3.7\% \pm 2.1\%$ and the PD of the Comptonized+power-law component results to be $1.1\% \pm 0.8\%$, with PA of $121.9^\circ \pm 12.7^\circ$. To take into account a possible energy dependence of PD and PA responsible for the spike of the PD in the 7–8 keV range, the spectro-polarimetric analysis can be performed applying `pollin` to each spectral component. The `diskbb` and `thcomp*bodyrad+expabs*powerlaw` polarization are assumed to be constant with energy, while only the PD of `relxillNS` is considered to vary linearly with energy, starting from PD= 0% at 1 keV. The PA of `relxillNS` is linked to that of the Comptonization+power-law component. The PD of the disk is found to be quite high for the inferred inclination ($4.2\% \pm 2.6\%$), while only an upper limit of 1.2% is obtained for the Comptonization+power-law PD, with PAs of the two components consistent with the previous cases with constant polarization. The PD of the reflected photons is found to increase with a slope of $6.6\%/keV \pm 3.5\%/keV$, reaching very high values in the 7–8 keV energy band.

4.6 4U 1624–49

4U 1624–49 is a persistent NS-LMXB, showing periodic 6–8 hour dips in its light curve (every ~ 21 hours; Watson et al. 1985). During dips, the flux in the 1–10 keV energy band decreases by 75% with

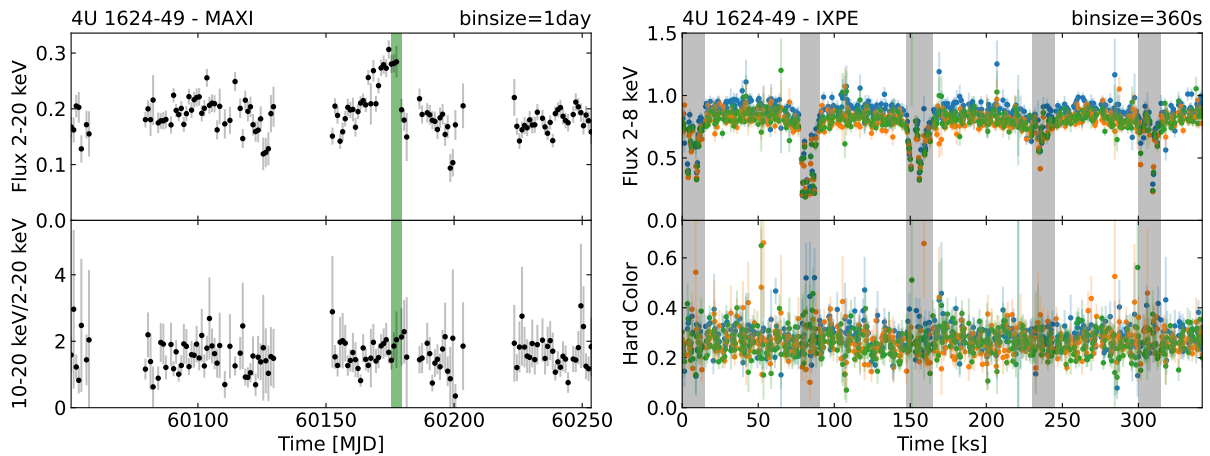


Figure 4.18: *Left panel:* 4U 1624–49 MAXI 2–20 keV light curve in units of photons $\text{cm}^{-2} \text{s}^{-1}$ (*top*) and hardness ratio (10–20 keV/2–20 keV, *bottom*) as a function of time in MJD. The green line corresponds to the *IXPE* observations. *Right panel:* 4U 1624–49 *IXPE* 2–8 keV light curves in units of cps (*top*) and Hard Color (5–8 keV/3–5 keV, *bottom*) as a function of observational time. The grey regions correspond to the dips. The time bin is 360 s.

respect to the persistent flux (Iaria et al., 2007). These dips are thought to be related to the obscuration of the central source by a thickened region of the outer accretion disk, where the incoming matter from the companion star first enters the accretion disk (White and Swank, 1982), due to its high inclination ($i > 60^\circ$; Frank et al. 1987). 4U 1624–49 is classified as an Atoll source in the banana state, similarly to GX 9+9 but with particularly high accretion rate ($0.5\text{--}0.8 L_{\text{Edd}}$; Lommen et al. 2005). Unlike many other NS-LMXBs, no QPOs have been detected (Smale et al., 2001; Lommen et al., 2005). When the source is not in the dip state, it shows flaring behavior up to 30% above its normal 2–10 keV flux level (Jones and Watson, 1989). The subset of NS-LMXBs that display dips in their light curves has been used to support the western model scenario, in which the corona extends above the accretion disk. The spectrum during the dips seems to arise from a thermal component (which may be completely obscured during the deepest part of the dipping) and from a Comptonization component, partially obscured during the dips. The obscuration of the thermal component is rapid and complete, suggesting that it originates in a very compact region, while the Comptonization component is obscured more gradual. From Chandra observation, Ca xx and Fe xxv/xxvi $K\alpha$ absorption lines were observed in the spectrum and they could be produced in a photoionized absorber between the coronal radius and the outer edge of the accretion disk (Iaria et al., 2007).

4.6.1 Observations

IXPE observations of 4U 1624–49 took place from 2023 August 19 09:51:25 UT to 2023 August 23 08:55:31 UT for a net exposure time of 198.9 ks (Obs. ID 02007301, see Table 4.8). Science data were extracted as described in Section 4.2.1 with a $120''$ source extraction radius. The background was not subtracted, following the prescription for bright sources reported in Di Marco et al. (2023b). 4U 1624–49 was also observed simultaneously by *NuSTAR* (Harrison et al. 2013, see also Appendix B.1) from 2023 August 20 18:36:09 UT to 2023 August 17 17:21:09 UT for 41.0 ks net exposure time (Obs. ID 90901327002, see also Table 4.8). The cleaned and calibrated data were extracted as described in the Appendix B.1.1. The spectra and light curves are reduced by selecting a circular region of $130''$ in radius centered on the source, following the maximization of the signal-to-noise ratio procedure (Piconcelli et al., 2004), and with a background region of $60''$ sufficiently far from the source. Since the background starts dominating above 20 keV, the spectra are considered only in the 3–20 keV energy band. NICER also observed 4U 1624–49 four times covering all the *IXPE* observation from 2023 August 20 02:38:00

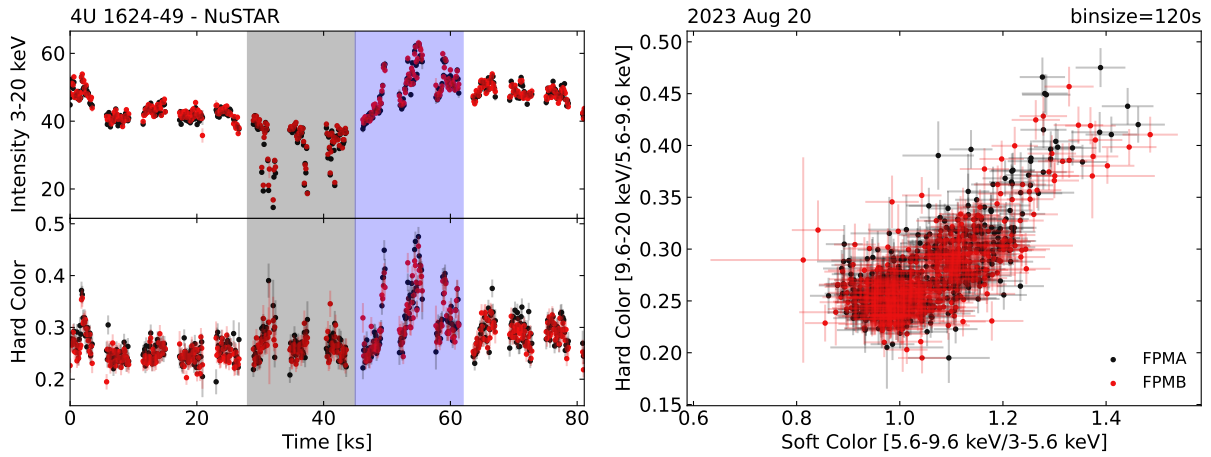


Figure 4.19: 4U 1624–49 *NuSTAR* 3–20 keV light curves in units of cps and Hard color (9.6–20 keV/5.6–9.6 keV) as a function of time (*left panel*) and Soft color (5.6–9.6 keV/3–5.6 keV, *right*). Red and black points correspond to the two *NuSTAR* detector, FPMA and FPMB respectively. The grey region highlights the dip, while the blue region shows the motion along the upper banana branch. Each bin corresponds to 120 s.

to 2023 August 23 05:26:20 UT (Obs. ID 6203930102, 6203930103, 6203930104, 6203930105) for a total net exposure of 3.5 ks. Data were extracted and reduced following the procedure described in the Appendix B.2.1.

The daily MAXI light curve is shown in Figure 4.18 (*left panel*). The green region corresponds to the *IXPE* observation. The X-ray flux and HR remain quite stable with time, except for some moments when it grows rapidly, possibly related to X-ray burst activity. During the *IXPE* observations, the 2–8 keV flux exhibits several dips in the light curve (Figure 4.18, *right panel*). The hard color remains quite constant throughout the whole observation. The *NuSTAR* light curve also shows a dip between 30 and 45 ks, immediately followed by an increase in flux and hard color (Figure 4.19, *left panels*). The CCD is also shown in Figure 4.19 (*right panel*) and the source appears to stay in the lower banana state during all the observation and moves along the upper banana branch when the flux and hard color increase (blue region). For the spectro-polarimetric analysis, only the non-dip part of the observation is taken into account.

4.6.2 Spectro-Polarimetric Analysis

The baseline model with a multicolor disk blackbody component `diskbb` and a Comptonized emission modelled with `thcomp` applied to `bbodyrad` does not provide a good fit to the observed data, leaving significant residuals between 5–10 keV. The relativistic smeared reflection component is needed to fit the observed spectra. The residuals do not show any presence of an obvious Compton hump, so that reflection should be related to a softer illuminating spectrum. Reflection is modelled using `relxillNS` (García et al., 2022), with some parameters fixed at reasonable values: the number density is set to $\log n_e = 18$ (e.g. Ludlam et al. 2022), consistently with the density in the inner region of a standard accretion disk (García et al., 2016). The fit is not sensitive to this parameter, as its effect on X-ray reflection is significant only at lower energies (Ballantyne, 2004; García et al., 2016). The dimensionless spin a is fixed at 0.1, similarly to the one derived from the NS period for Cyg X–2 (Wijnands et al., 1998; Braje et al., 2000). The emissivity is set to $q_{\text{em}} = 1.8$ (see also Ludlam et al. 2022). The iron abundance is left free to vary and is > 4 . Initially, the inclination of the disk i , the inner disk radius R_{in} (in units of ISCO) and the ionization parameter ξ are left free to vary. However, the fit is not able to constrain both the inclination and the inner disk radius, as they are degenerate. Therefore, the inner disk radius is fixed to $1.5 R_{\text{ISCO}}$, consistent with typical values obtained for NS-LMXBs (see e.g. Ludlam et al. 2022). The covering factor f of `thcomp` is always > 0.8 and is then fixed at the best-fit value. Since the *NuSTAR* and NICER spectra exhibit some absorption feature, an ionized absorber is added to the model with `CLOUDY` (Ferland et al.,

Model	Parameter	Best-fit
TBabs	n_H (10^{22} cm $^{-2}$)	$10.28^{+0.13}_{-0.22}$
CLOUDY	N_H (10^{22} cm $^{-2}$)	[10]
	ξ	$4.87^{+0.10}_{-0.09}$
diskbb	kT_{in} (keV)	$1.07^{+0.03}_{-0.03}$
	R_{in} (km)	$11.06^{+0.94}_{-1.02}$
bbbodyrad	kT (keV)	$1.17^{+0.04}_{-0.03}$
	R_{bb} (km)	$12.75^{+0.85}_{-0.88}$
thcomp	kT_e (keV)	$3.06^{+0.02}_{-0.02}$
	τ	$7.23^{+0.10}_{-0.09}$
relxillNS	i ($^\circ$)	> 60.4
	R_{in} (ISCO)	[1.5]
	kT_{bb} (keV)	$= kT$
	$\log \xi$	$2.49^{+0.25}_{-0.15}$
	N_r (10^{-3})	$1.62^{+0.91}_{-0.64}$
$\chi^2/\text{d.o.f.}$		681.9/714
$F_{\text{disk}}/F_{\text{tot}}$ (2–8 keV)		18.8%
$F_{\text{comp}}/F_{\text{tot}}$ (2–8 keV)		71.5%
$F_{\text{refl}}/F_{\text{tot}}$ (2–8 keV)		9.7%
F_{tot} (erg s $^{-1}$ cm $^{-2}$)		1.64×10^{-9}

Notes. A 15 kpc distance is assumed to compute the inner radius R_{in} and R_{bb} from normalizations.

Table 4.9: Best-fit Spectral Parameters obtained from the *IXPE*, *NuSTAR* and *NICER* data. The errors are at the 90% confidence level for a single parameter.

2017). The CLOUDY absorption table reproduces the absorption lines self-consistently through a slab with a constant density of 10^{12} cm $^{-3}$ and a turbulence velocity of 500 km s $^{-1}$, illuminated by the unabsorbed intrinsic best-fit SED. Modelling the absorption lines requires a highly ionized outflowing plasma, i.e. with ionization parameter $\xi \sim 4.87$ and column density $N_H = 10^{23}$ cm $^{-2}$. The best-fit parameters are reported in Table 4.9 and are quite typical for a NS-LMXB in the soft state (see also Figure 4.20). Assuming a 15 kpc distance to the source (Xiang et al., 2009), the normalization of `diskbb` corresponds to an inner disk radius of $\sim 11 \sqrt{\cos i}$ km. The inclination of the system results to be quite high, consistent with previous observations of the source.

The Stokes parameters of 4U 1624–49 observed by *IXPE* in the 2–8 keV, 2–4 keV and 4–8 keV energy ranges obtained with `IXPEOBSSIM` are reported in Figure 4.21. Significant polarization is detected in the 2–8 keV band, with a PD of $3.5\% \pm 0.7$ and an increasing trend of polarization with energies, up to $4.3\% \pm 1.0\%$ in the 4–8 keV energy range. The PA remains quite constant with energy. These results are well consistent within errors with those obtained with `XSPEC` (Figure 4.22). The polarization is well constrained at more than 3σ confidence level in the 2–8 keV and 4–8 keV energy ranges. The joint spectro-polarimetric fit of the *IXPE* data is performed considering the baseline model obtained with the *NuSTAR* and *NICER* data and applying a constant polarization to each component through `polconst`. Some significant residuals remain at both low and high energies in the *IXPE* spectra, which are probably related to calibration issues

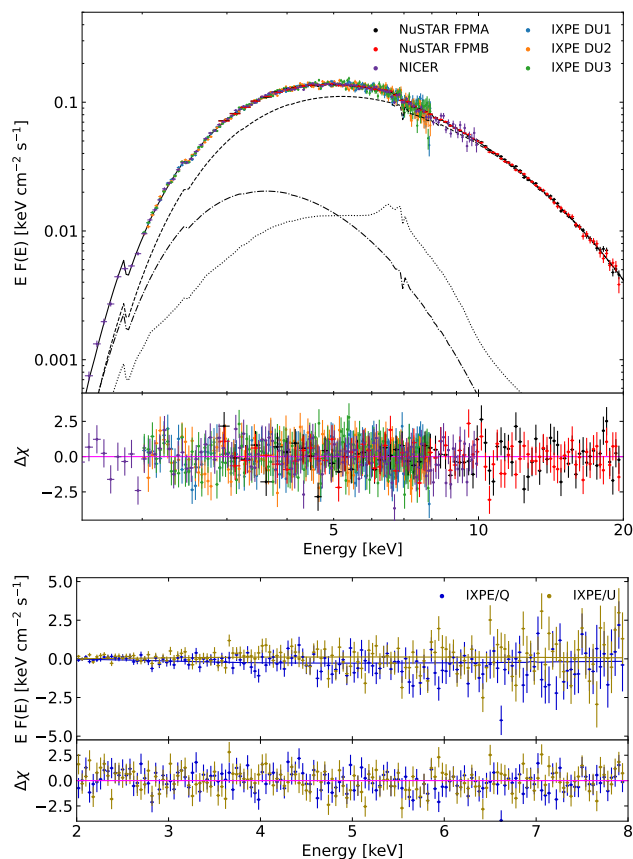


Figure 4.20: Best-fit of the *IXPE*, *NuSTAR* and *NICER* deconvolved spectra (*top panel*) with *IXPE* Stokes Q and U spectra (*lower panel*) of 4U 1624–49. The model includes `diskbb` (dashed dotted line), `thcomp*bbbodyrad` (dashed line) and `relxillNS` (dotted line) with residuals in units of σ . The spectral parameters are given in Table 4.9.

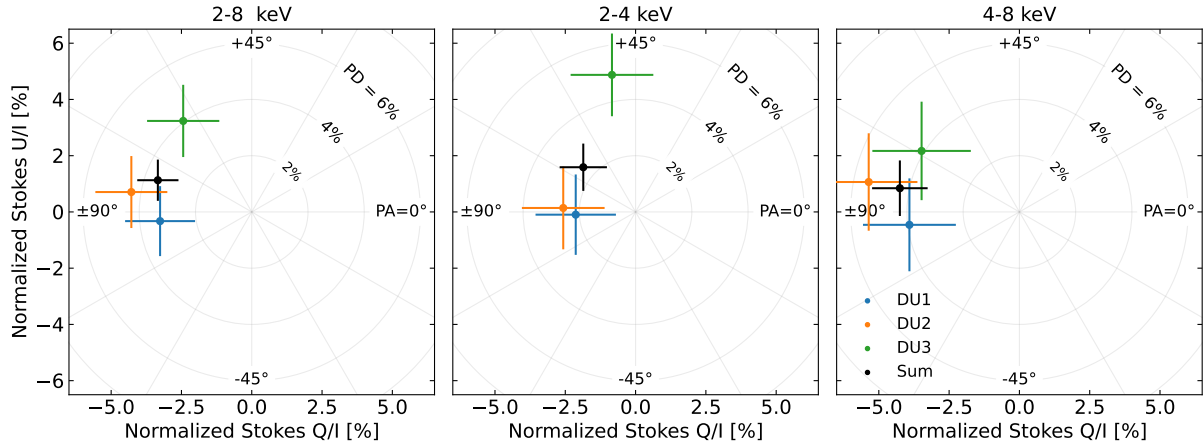


Figure 4.21: Stokes parameters of 4U 1624–49 in the 2–8 keV, 2–4 keV and 4–8 keV energy bands for DU1 (blue), DU2 (orange), DU3 (green) and by summing all the events of the three DUs (black).

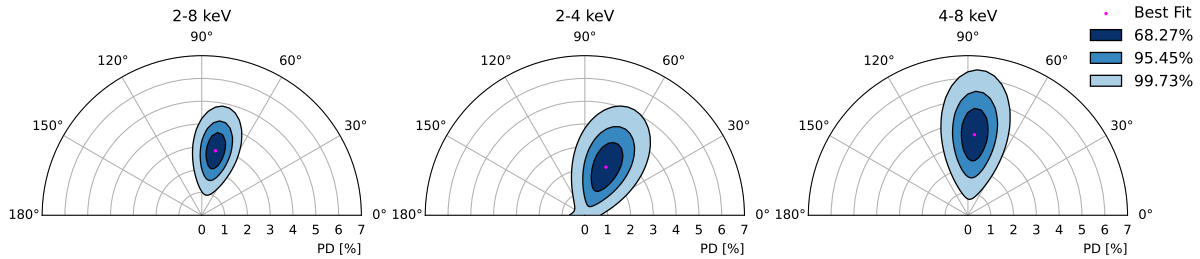


Figure 4.22: Polarization contours for 4U 1624–49 in the 2–8 keV, 2–4 keV and 4–8 keV energy bands obtained with *xSPEC* by summing the events from the three DUs. Contours correspond to the 68.27%, 95.45% and 99.73% confidence levels derived using a χ^2 with two degrees of freedom.

and can be corrected using the `gain fit` command in *xSPEC* to apply the gain shift to the *IXPE* spectra. The resulting slope is 0.976 ± 0.005 , 0.947 ± 0.005 , 0.942 ± 0.005 keV^{-1} for the three DUs respectively, while the offset in each DU is 0.093 ± 0.019 , 0.159 ± 0.018 , 0.153 ± 0.019 keV. All spectral parameters are fixed to their best-fit value. The overlap of the energy range between *IXPE* and *NuSTAR*+*NICER* is expected to minimize systematic effects on the derived polarimetric parameters. However, it is difficult to constrain the PD and PA for each spectral component, due to the *IXPE* band-pass. In particular, the Comptonized and reflected radiation are quite degenerate, peaking at similar energies and having similar spectral shapes. Some assumptions based on theoretical and observational expectations are required in order to estimate the contribution to the polarization of each spectral component.

As a first case, only one component is assumed to be polarized, with the others having null polarization. Taking into account only the disk component, the obtained PD is $13.5\% \pm 5.2\%$, with $71.4^\circ \pm 11.2^\circ$ PA. This result is quite high compared to the classical Chandrasekhar result for an inclination of $\sim 70^\circ$, which should be $\sim 3.5 - 4\%$. However, the contribution of the disk to the total flux in the 2–8 keV band is only $\sim 15\%$, so it requires large polarization to obtain the expected 3.5% PD as it is depolarized by the other two components. Moreover, this assumption is not consistent with the observed polarization increasing with energy. Taking instead into account the case where Comptonized or reflected radiation is the only polarized component, the fit improves ($\chi^2/\text{d.o.f.} = 1566.1/1616$, $884.2/894$ for the subset of Stokes *Q* and *U* spectra). These models are able to provide a good fit to both the flux and the Stokes parameters spectra without strong residuals. The PA obtained in these two cases is very similar and consistent within

Source	Satellite	Obs. ID	Start Date (UT)	Net Exp. (ks)
Cyg X-2	<i>IXPE</i>	01001601	2022-04-30 10:33:43	93.2
	<i>NuSTAR</i>	30801012002	2022-05-01 14:46:09	15.2
	NICER	5034150102	2022-04-30 02:07:20	3.6
	NICER	5034150103	2022-05-01 01:13:29	4.5
	<i>INTEGRAL</i>	19700060001	2022-04-30 21:43:29	54.5

Table 4.10: Log of simultaneous observations of the Z-sources Cyg X-2 (Farinelli et al., 2023).

the errors: $79.1^\circ \pm 8.6^\circ$ is found for `thcomp*bbbodyrad` only, while $78.7^\circ \pm 8.5^\circ$ is obtained for only `relxillNS`. The reflection-dominated scenario requires a very large PD of $21.6\% \pm 9.3\%$, compared to $3.9\% \pm 1.2\%$ obtained for Comptonization alone. As the reflection is characterized by a PA perpendicular to the disk plane (Matt, 1993; Poutanen et al., 1996b; Schnittman and Krolik, 2009), its direction should be the same as that of the Comptonized component associated with the spreading layer (Farinelli et al., 2023). By leaving free to vary the PD of all components and the PA of the disk and Comptonized radiation, the contribution to the polarization of each spectral component is difficult to constrain. To estimate the polarization of the reflected radiation, the PD of the disk is set to 3.5%, corresponding to the classical Chandrasekhar result for $i \sim 70^\circ$ (Chandrasekhar, 1960), while the PD of `thcomp*bbbodyrad` is fixed at 2%, a reasonable value for wedge or spreading layer-like geometries for the inferred inclination (see Sections 3.6 and 3.7). The resulting polarization of the reflected component is $19.7\% \pm 10.9\%$ with $82.3^\circ \pm 8.9^\circ$ PA (the same as Comptonization). The PA of the disk is poorly constrained, but is consistent with being perpendicular to the Comptonized and reflected components ($15.1^\circ \pm 41.8^\circ$). As a consequence, the PA of the disk can be assumed to be perpendicular to the other components. Assuming again a 2% polarization for `thcomp*bbbodyrad`, the reflection PD is $27.8\% \pm 21.2\%$ with $82.9^\circ \pm 8.8^\circ$, while the disk results to be (poorly constrained) polarized at $13.9\% \pm 12.1\%$. Also in this case, the disk is much more polarized than the classical Chandrasekhar result. A similar procedure can be performed by assuming 10% PD for the reflection (polarized perpendicular to the disk) and leaving the PD of both the disk and the Comptonization free to vary. The resulting PD of the Comptonized radiation is $4.6\% \pm 2.6\%$ with $82.8^\circ \pm 8.9^\circ$, while the disk is much more polarized ($12.9\% \pm 11.9\%$) but not very constrained.

4.7 Cygnus X-2

Cyg X-2 was first observed in X-rays in the 1960s (Byram et al., 1966) and was confirmed as NS-LMXBs when RXTE observed a Type-I X-ray burst with the source in a high-intensity state (Smale, 1998). It is classified as a Z-source from the tracks in the CCD and HID (Hasinger and van der Klis, 1989). From the spectral point of view, Z-sources are characterized by parameters that remain relatively stable during the motion along the Z-pattern (Di Salvo et al., 2000, 2001, 2002; Lavagetto et al., 2004; Farinelli et al., 2009; Bałucińska-Church et al., 2010). The most noticeable transient feature is instead a hard X-ray excess above 30 keV which occurs when the source is in the Horizontal Branch (HB) and appears to be correlated with episodic radio emission indicating the presence of a jet (D’Amico et al., 2001; Paizis et al., 2006; Farinelli et al., 2009). Joint observations of Cyg X-2 with *Swift*/XRT and the VLBI at 5 GHz have shown the presence of a sub-relativistic jet when the source was in the HB (Spencer et al., 2013) in the south-east direction, 141° east of north.

4.7.1 Observations

IXPE observations of Cyg X-2 (Farinelli et al., 2023) took place from 2022 April 30 10:33:42 UT to 2022 May 02 11:06:56 UT for about 93.2 ks of net exposure time (Obs. ID 01001601, see Table 4.10). *IXPE*

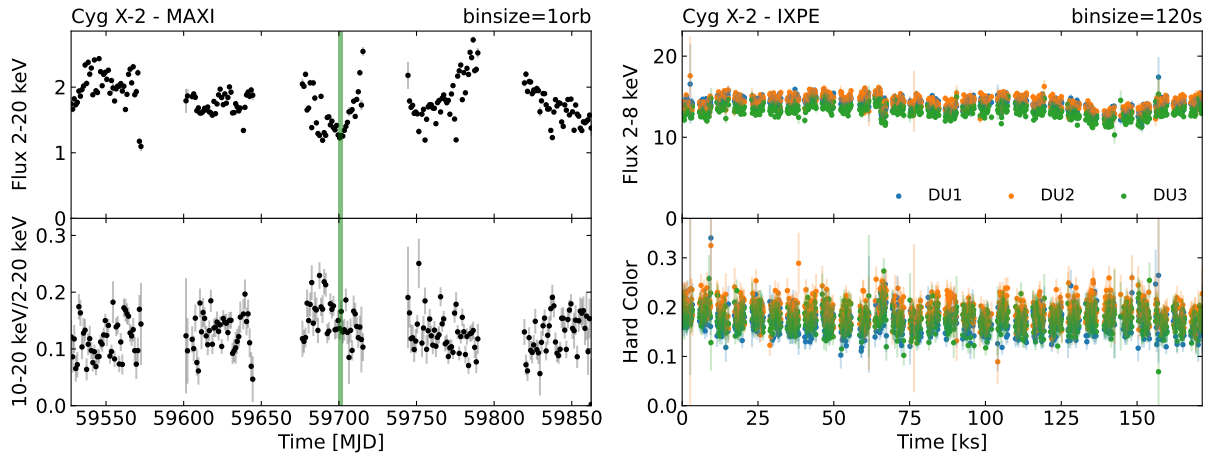


Figure 4.23: *Left panel*: Cyg X–2 MAXI 2–20 keV light curve in units of photons $\text{cm}^{-2} \text{s}^{-1}$ (top) and hardness ratio (10–20 keV/2–20 keV, bottom) as a function of time in MJD. The green line corresponds to the *IXPE* observation. *Right panel*: Cyg X–2 *IXPE* 2–8 keV light curve in units of cps (top) and Hard Color (5–8 keV/3–5 keV, bottom) as a function of observational time (see also Farinelli et al. 2023). Each bin corresponds to 120 s.

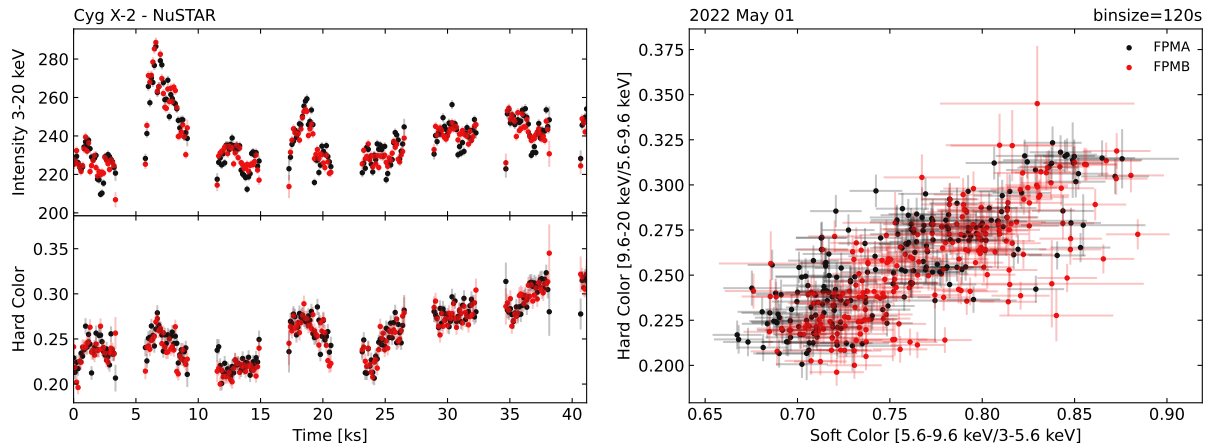


Figure 4.24: Cyg X–2 *NuSTAR* 3–20 keV light curves in units of cps and Hard color (9.6–20 keV/5.6–9.6 keV) as a function of time (*left panel*) and Soft color (5.6–9.6 keV/3–5.6 keV, *right*). Red and black points correspond to the two *NuSTAR* detector, FPMA and FPMB respectively. Each bin corresponds to 120 s.

data were extracted as described in Section 4.2.1 considering $120''$ source extraction radius. Cyg X–2 was also observed by *NuSTAR* (Harrison et al. 2013, see also Appendix B.1) from 2022 May 01 14:46:09 UT to 2022 May 03 17:45:33 UT for 15.2 ks of net exposure time (Obs. ID 30801012002, see also Table 4.10). The cleaned and calibrated data were extracted following the procedure described in the Appendix B.1.1. The spectra and light curves are obtained by selecting a circular region of $120''$ in radius centered on the source following the procedure to maximize the signal-to-noise ratio (Piconcelli et al., 2004) and a background region of $60''$ sufficiently far from the source. Since the background starts dominating above 30 keV, the data are considered in the 3–30 keV range. Two observations were also made by *NICER* on 2022 April 30 (Obs. ID 5034150102) and 2022 May 1 (Obs. ID 5034150103), with a net total exposure of 8.1 ks. The data have been extracted and reduced following the procedure described in the Appendix B.2.1. The presence of sharp changes in the effective area of the instrument due to the gold edges in the mirror coating is a known issue of the instrument and suggests performing spectral analysis starting from about 1–1.5 keV (Miller et al., 2018). *INTEGRAL* observed Cyg X–2 as a target-of-opportunity from 2022 April 30 21:43:28 UT to 2022 May 1 12:03:27 UT. The *JEM-X* and *IBIS* data have been

reduced following the procedure described in the Appendix B.3.1. A systematic error of 1.5% was added in quadrature for spectral analysis.

The daily MAXI light curve is shown in Figure 4.23 (*left panel*) spanning one year around *IXPE* observation. The X-ray flux is quite variable over time and was close to its minimum at the time of the observation (Farinelli et al., 2023). However, HR variations were less pronounced. This is consistent with the fact that spectral changes in *Z*-sources remain fairly moderate even when they track the full *Z* pattern in the CCD (e.g. Di Salvo et al. 2000; D’Amico et al. 2001). During the *IXPE* observation, the 2–8 keV flux and the hard color remain quite constant (Figure 4.23, *right panel*). However, due to an improper correction of the telescope vignetting caused by off-axis pointing during the *IXPE* observations of Cyg X–2, *IXPE* spectra were not compatible with the *NuSTAR* and NICER ones. Due to the brightness of the source, the induced systematic effect is highly significant in the energy spectrum⁴. On the other hand, since the Stokes parameters Q/I and U/I are normalized quantities of photon counts, their derivation is not influenced by different changes of efficiency over energy for the single DUs and the PD and PA are not affected too (Capitani et al., 2023; Farinelli et al., 2023). Taking into account the 3–20 keV energy range with *NuSTAR*, the source flux exhibits two peaks (between 5–10 ks and 17–20 ks, Figure 4.24) when the source moves along the FB, while it tracks out the NB during the rest of the observation. The average spectrum over the whole observation is considered for spectral analysis.

4.7.2 Spectro-Polarimetric Analysis

The simple `diskbb+thcomp*bbbodyrad` model does not provide a good fit to the observed data, leaving significant residuals in the 5–7 keV range. The observed residuals do not exhibit the presence of an obvious Compton hump, so that reflection off the disk should be related to a softer illuminating spectrum than the typical non-thermal (power-law) continuum assumed in standard reflection models. The relativistic smeared reflection component is required to remove the residuals in the fit, modelled with `relxillNS` (García et al., 2022). The fit is unable to constrain some of the parameters of `relxillNS`: the emissivity index $q_{\text{em}} = 1.8$, the iron abundance $A_{\text{Fe}} = 1.5$ and the number density $\log n_e = 18$ are set consistently with the results obtained by Ludlam et al. (2022). The number density is consistent with the inner region of a standard accretion disk (see García et al. 2016 and references therein). The fit is not sensitive to these parameters, since its effect on the reflection is relevant only at lower energies (Ballantyne, 2004; García et al., 2016). The dimensionless spin a can be derived from the NS period (in ms) as $a = 0.47/P$ (Braje et al., 2000). For Cyg X–2, the NS period was measured from QPOs by Wijnands et al. (1998) and therefore the spin is fixed to 0.1 (see also Patruno et al. 2017). The blackbody temperature of the illuminating spectrum is also tied to that of the seed photon spectrum of `bbbodyrad`. The covering factor f of `thcomp` is always > 0.99 and then is fixed to 1. Initially, the inclination of the disk i , the inner disk radius R_{in} (in units of ISCO) and the ionization parameter ξ of `relxillNS` are left free to vary. However, the fit is not able to constrain together the inclination and the inner disk radius since they are largely degenerate and a better fit can be found by fixing one of these two parameters. Taking into account the previously observed inclination (Ludlam et al., 2022), some residuals in the 5–7 keV range remain and the inner disk radius values are not well constrained, while assuming $R_{\text{in}} = 1.5 R_{\text{ISCO}}$ (quite similar to that estimated by Ludlam et al. 2022) the fit significantly improves ($\chi^2/\text{d.o.f.} = 349.7/359$, see Table 4.11). The best-fitting parameters are quite typical for a *Z*-source moving along the NB and FB, however the resulting inclination is found to be lower than the one previously obtained for Cyg X–2 (Ludlam et al., 2022). Assuming a distance to the source of 7 kpc, the normalization of `diskbb` corresponds to an inner disk radius of $\sim 9.85 \sqrt{\cos i}$ km. The size of the seed photon-emitting region can be estimated from the best-fit normalization of `bbbodyrad`, assuming that all seed photons are Comptonized ($f = 1$) and computing the flux and the emission area (see also in ’t Zand et al. 1999). The estimated seed photon region size is equivalent to a spherical radius of 7.4 km. This result is consistent with the seed photons originating in a region smaller than or similar to the entire NS, such as the boundary layer.

⁴<https://heasarc.gsfc.nasa.gov/FTP/ixpe/data/obs/01/01001601/README>

Model	Parameter	Best-fit
TBabs	n_H (10^{22} cm^{-2})	[0.12]
diskbb	kT_{in} (keV)	$1.13^{+0.05}_{-0.05}$
	R_{in} (km)	$9.85^{+0.57}_{-0.56}$
bbodyrad	kT (keV)	$1.36^{+0.04}_{-0.04}$
	R_{bb} (km)	$7.44^{+0.64}_{-0.67}$
thcomp	kT_e (keV)	$3.31^{+0.08}_{-0.11}$
	τ	$7.25^{+0.32}_{-0.42}$
	f	[1]
relxillNS	i ($^\circ$)	$33.58^{+5.23}_{-3.54}$
	R_{in} (ISCO)	[1.5]
	kT_{bb} (keV)	$= kT$
	$\log \xi$	$2.86^{+0.10}_{-0.11}$
	N_r (10^{-3})	$2.20^{+0.27}_{-0.19}$
$\chi^2/\text{d.o.f.}$		349.7/359
$F_{\text{disk}}/F_{\text{tot}}$ (2–8 keV)		51.9%
$F_{\text{comp}}/F_{\text{tot}}$ (2–8 keV)		35.8%
$F_{\text{refl}}/F_{\text{tot}}$ (2–8 keV)		12.3%
F_{tot} ($\text{erg s}^{-1} \text{ cm}^{-2}$)		7.53×10^{-9}

Notes. A 7 kpc distance is assumed to compute the inner radius R_{in} and R_{bb} from normalizations.

Table 4.11: Best-fit Spectral Parameters obtained from the *NuSTAR* and NICER data. The errors are at the 90% confidence level for a single parameter.

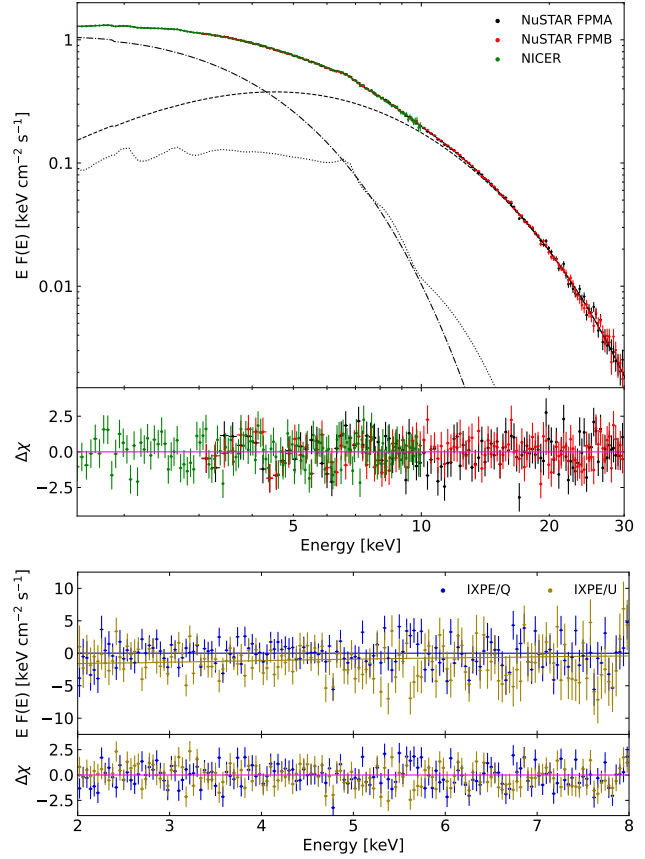


Figure 4.25: Best-fit of the *NuSTAR* and NICER deconvolved spectra (*top panel*) with *IXPE* Stokes Q and U spectra (*lower panel*) of Cyg X-2. The model includes `diskbb` (dashed dotted line), `thcomp*bbodyrad` (dashed line) and `relxillNS` (dotted line) with residuals in units of σ . The spectral parameters are given in Table 4.11.

The Stokes parameters of Cyg X-2 observed by *IXPE* in the 2–8 keV, 2–4 keV and 4–8 keV energy ranges obtained with `IXPEOBSSIM` are reported in Figure 4.26. Significant polarization is detected in the 2–8 keV band with a PD of $1.6\% \pm 0.3\%$ and an increasing trend of the polarization with energies, up to $2.5\% \pm 0.5\%$ in the 4–8 keV energy range. The PA seems to remain constant with energy. These results are well consistent within errors with those obtained with `xSPEC` (Figure 4.27). Between 2–4 keV, the polarization is just detected at 3σ . The joint spectro-polarimetric fit of the *IXPE* data is performed using the baseline model obtained only from *NuSTAR* and NICER (`diskbb+thcomp*bbodyrad+relxillNS`, Table 4.11) and applying a constant polarization to each component through `polconst`. The reflection component modelled by `relxillNS` includes the fluorescent iron line, which should be unpolarized (however, its contribution to the photon flux is only $\sim 10\%$ in the 6–7 keV range). Some significant residuals can be found at both low and high energies in the *IXPE* spectra, which are likely artifacts of calibration issues already observed in other sources (Taverna et al., 2022; Krawczynski et al., 2022; Marinucci et al., 2022) and to the improper correction of *IXPE* vignetting due to off-axis pointing. This problem can be taken into account by applying a gain shift to the response files of the *IXPE* spectra with the `gain fit` command in `xSPEC`. The resulting slope of the gain shift is 1.052 ± 0.002 , 1.128 ± 0.002 , $1.066 \pm 0.003 \text{ keV}^{-1}$ for the three DUs respectively, while the energy offset in each one is -0.064 ± 0.008 , -0.090 ± 0.007 , $-0.057 \pm 0.009 \text{ keV}$. All spectral parameters are fixed to their best-fit value. However, the *IXPE* band-pass does not allow to obtain tight constraints on the PD and PA for each spectral component,

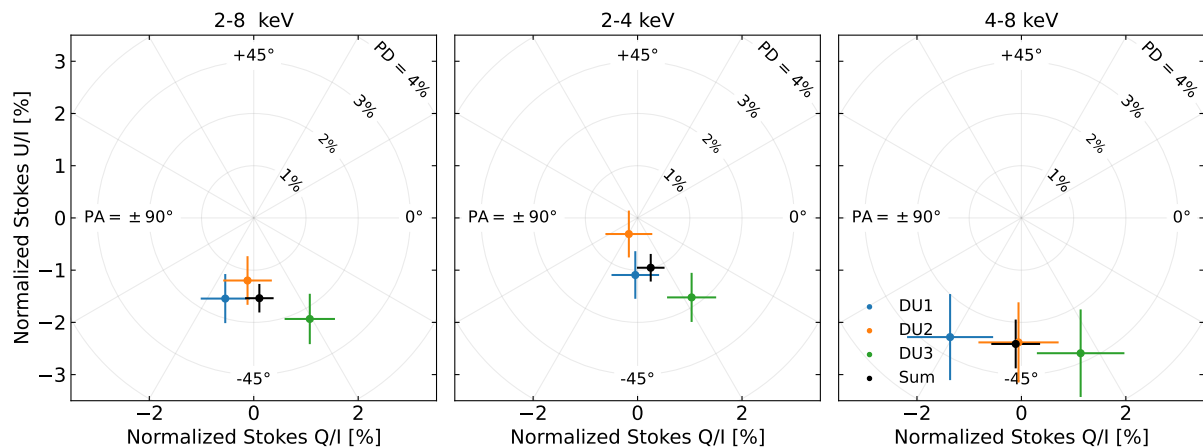


Figure 4.26: Stokes parameters of Cyg X-2 in the 2–8 keV, 2–4 keV and 4–8 keV energy bands for DU1 (blue), DU2 (orange), DU3 (green) and by summing all the events of the three DUs (black).

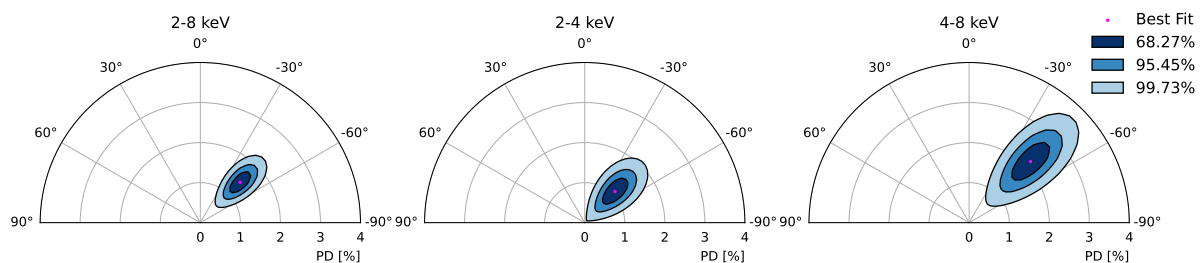


Figure 4.27: Polarization contours for Cyg X-2 in the 2–8 keV, 2–4 keV and 4–8 keV energy bands obtained with `xSPEC` by summing the events from the three DUs. The contours correspond to the 68.27%, 95.45% and 99.73% confidence levels derived using a χ^2 with two degrees of freedom.

in particular for the Comptonized and reflected radiation since these two are quite degenerate peaking at similar energies and having similar spectral shapes, and therefore some assumptions based on theoretical and observational expectation are required.

As a first test, only one component is assumed to be polarized, with the others having null polarization. Assuming a polarized disk only, the resulting PD is $2.0\% \pm 0.6\%$ with $135.7^\circ \pm 8.9^\circ$. The fit results to be acceptable ($\chi^2/\text{d.o.f.} = 1448.6/1306$, $954.6/894$ for the subset of Stokes Q and U spectra), but this assumption is not consistent with the observed polarization increasing with energy. Considering the case where either the Comptonized or reflection component is the only polarized one, the fit improves: $\chi^2/\text{d.o.f.} = 1442.2/1306$ ($948.2/894$ for the subset of Stokes Q and U spectra) is found for polarized `thcomp*bbbodyrad`, while $\chi^2/\text{d.o.f.} = 1432.1/1306$ ($938.1/894$ for the subset of Stokes Q and U spectra) is obtained for reflection only. These models provide a good fit of both the flux and the Stokes parameters spectra, without strong residuals. The PA in these two cases is very similar and consistent within errors ($135.3^\circ \pm 6.8^\circ$ for Comptonization alone and $135.4^\circ \pm 7.2^\circ$ for only reflection). The reflection-dominated scenario requires a larger PD of $11.5\% \pm 2.8\%$, compared to $4.2\% \pm 1.1\%$ found for the other case. Since the reflection component is characterized by a PA perpendicular to the disk surface (Matt, 1993; Poutanen et al., 1996b; Schnittman and Krolik, 2009), its direction should be the same as that of the Comptonized component (see also Farinelli et al. 2023). This configuration corresponds to the geometry of the spreading layer, since the vertical height is significantly greater than its radial extension ($H \gg \Delta R$). The soft component (i.e. the disk radiation) and the hard one (made up of Comptonization and reflection,

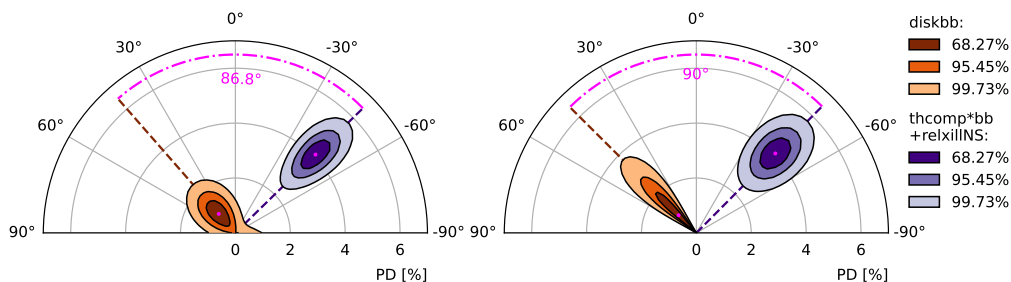


Figure 4.28: Polarization contours for Cyg X–2 in the 2–8 keV energy band obtained with `xSPEC`. The data have been fitted with two `polconst` models separately for the `diskbb` (orange) and `thcomp*bb+relxillNS` (purple) components. *Left panel*: the PD and PA of each component are left free to vary. *Right panel*: the PA of `diskbb` is assumed to differ from the PA of the hard component by 90° . The contours correspond to the 68.27%, 95.45% and 99.73% confidence levels.

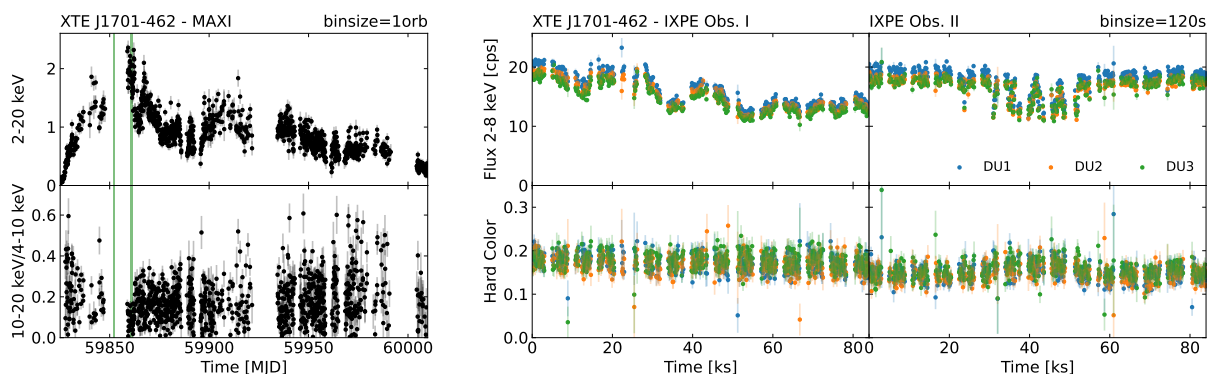
having a similar spectral shape and peaking at similar energies) are now considered separately to compute the polarization for each part of the spectrum. By leaving free to vary the PD and PA for the `diskbb` and the `thcomp*bb+relxillNS` models, the polarization contour plots are shown in Figure 4.28 (*left panel*). The Comptonization+reflection component is well constrained at a 99.9% confidence level, while the disk is consistent with zero. There is a clear hint that the PA of the disk is nearly perpendicular ($\sim 86.8^\circ$) to that of the hard component, which is theoretically expected. Therefore, the PA of `diskbb` is set to be perpendicular to that of the hard component. With this link, the best-fit value and the uncertainties of the hard component PD do not vary significantly, while only an upper limit is found for the disk polarization (Figure 4.28, *right panel*). Fixing the PD of the Comptonization at 1%, a reasonable value for wedge or spreading layer geometries (see Sections 3.6 and 3.7) and the disk polarization to a conservative value of 1% at the inferred source inclination, the reflection PD results to be $13.7\% \pm 3.1\%$, with a PA of $135.7^\circ \pm 10.1^\circ$ (the same of the Comptonized component). Even if the PA of the disk is not tightly constrained ($42.8^\circ \pm 37.1^\circ$), it is consistent with being perpendicular to the reflected and Comptonized components. As a consequence, the PA of the disk can be fixed to be perpendicular to the harder components. Leaving free to vary the PD of the disk, an upper limit of 2.9% can be found (at 99.73% confidence level for a single parameter), with a PD of the reflection of $15.8\% \pm 6.8\%$ with $135.2^\circ \pm 6.5^\circ$ PA (at 90% confidence level). A similar procedure can be done by leaving free to vary the PD of both the disk and Comptonized components and assuming that reflection has a fixed PD of 10% (see e.g. [Matt 1993](#)). With this assumption, only upper limits can be found for the polarization of the two components: the PD of `diskbb` is $< 1.4\%$, while for `thcomp*bb+relxillNS` the PD is $< 3.1\%$, with a PA of $135.3^\circ \pm 6.6^\circ$.

4.8 XTE J1701–462

After more than 15 years of quiescence since its first outburst ([Lin et al., 2009a,b](#)), the transient NS-LMXBs XTE J1701–462 has become bright again on 2022 September 6 ([Iwakiri et al., 2022](#); [Chandra, 2022](#)). Discovered at the beginning of its 2006 outburst the source was soon identified as the first transient Z-source ([Remillard et al., 2006](#); [Homan et al., 2006, 2007a,b](#)), also showing kHz QPO in the time domain of *RXTE* during its soft state ([Sanna et al., 2010](#)). A radio counterpart was identified by [Fender et al. \(2007\)](#), along with a large-scale jet-like structure, $\sim 2\text{--}3$ arcmin south of the source and possibly connected to unobserved activity from the past. Among its class, XTE J1701–462 is a unique object, as it is the

Source	Satellite	Obs. ID	Start Date (UT)	Net Exp. (ks)
XTE J1701–462 Obs. I	<i>IXPE</i>	01250601	2022-09-29 12:05:22	47.5
	NICER	5203390122	2022-09-29 00:51:09	0.5
XTE J1701–462 Obs. II	<i>IXPE</i>	01250701	2022-10-08 11:23:15	48.0
	<i>NuSTAR</i>	90801325002	2022-10-08 10:41:09	12.4
	<i>INTEGRAL</i>	19700120001	2022-10-08 21:56:36	58.2

Table 4.12: Log of simultaneous observations of the Z-sources XTE J1701–462 (Cocchi et al., 2023).

Figure 4.29: *Left panel*: XTE J1701–462 MAXI 2–20 keV light curve in units of photons cm⁻² s⁻¹ (top) and hardness ratio (10–20 keV/2–20 keV, bottom) as a function of time in MJD. The green line corresponds to the *IXPE* observations. *Right panel*: XTE J1701–462 *IXPE* 2–8 keV light curve in units of cps (top) and Hard Color (5–8 keV/3–5 keV, bottom) as a function of the observational time. Each bin corresponds to 120 s.

only known NS-LMXB to exhibit all the different spectral substates during its outburst evolution, from the Cyg X–2-like Z class up to the Sco X–1-like Z (see Kuulkers et al., 1994, for more details), down to the bright Atoll and finally to the island Atoll (Lin et al., 2009b). Furthermore, the source exhibited the typical transient hard tail that is usually observed in the HB of the Z-sources (Paizis et al., 2006). Then XTE J1701–462 evolved into a bright soft Atoll source in the Banana spectral state and finally transitioned into a low-hard Atoll Island state (Homan et al., 2007a).

4.8.1 Observations

IXPE observed XTE J1701–462 twice (Cocchi et al., 2023), during the first source visibility windows (expired on 2022 October 10) after the outburst observed by MAXI on 2022 September 6. Both observations had a nominal duration of 50 ks, with net (GTI filtered) time measurements of 47.7 ks (DU1, DU2) and 47.2 ks (DU3) for Obs. I and net 48.1 ks (DU1) and 48.0 ks (DU2, DU3) recorded in Obs. II (IDs 01250601 and 01250701, see Table 4.12). *NuSTAR* has observed XTE J1701–462 on 2022 October 8, from 10:41:09 to 22:56:09 UT. The sequence IDs and the exposure times are given in Table 4.12. Clean and calibrated data were extracted following the procedure described in the Appendix B.1.1. For both detectors, the background was extracted from a circular region with 60'' radius while the source radius is 120'', found by following the signal-to-noise ratio maximization procedure (Piconcelli et al., 2004). Since the background starts dominating above 20–25 keV, the data are considered in the 3–20 keV range. No Type-I X-ray bursts were detected in all light curves. During the first visibility window, NICER started monitoring the source daily on September 8 (17:09:58 UT), about two days after the MAXI transient alert, up to September 29 (21:10:40 UT). Then, a second set of NICER observations was carried out

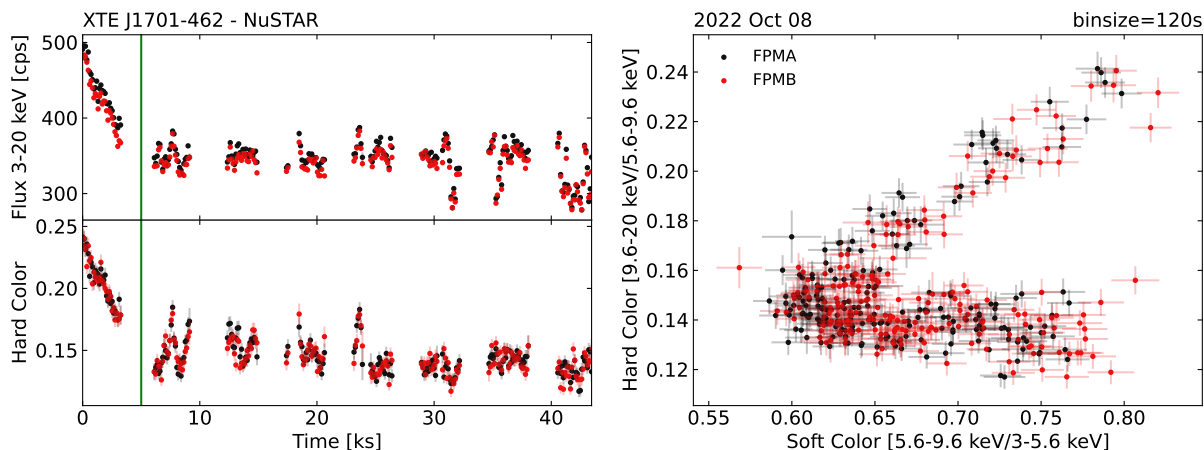


Figure 4.30: XTE J1701–462 *NuSTAR* 3–20 keV light curves in units of cps and Hard color (9.6–20 keV/5.6–9.6 keV) as a function of time (*left panel*) and Soft color (5.6–9.6 keV/3–5.6 keV, *right*). Red and black points correspond to the two *NuSTAR* detector, FPMA and FPMB respectively. Each bin corresponds to 120 s.

from October 7 (00:05:03 UT) to October 13 (12:54:00 UT). The sequence IDs and exposure times of the NICER observations are given in Table 4.12. The data have been extracted and reduced following the procedure described in the Appendix B.2.1. Due to its short duration, it is not possible to build a complete CCD or HID from the NICER observation. However, during the first *IXPE* observation of XTE J1701–462, the source moves between the upper and lower HB towards the NB (Cocchi et al., 2023). *INTEGRAL* observed the source from 2022 October 8 (21:00:00 UT) to 2022 October 10 (04:07:54 UT) for a total of 24.4 ks. Data have been reduced following the procedure described in the Appendix B.3.1. A systematic error of 1.5% was added in quadrature for spectral analysis. Only JEM-X data were used for the spectral analysis because IBIS, the γ -ray energy detector (Lebrun et al., 2003), did not detect the source with a 3σ upper limit on the flux of $\sim 8 \times 10^{-10}$ erg s $^{-1}$ cm $^{-2}$ in the 28–40 keV energy range, implying that the high energy tail was not present.

The daily MAXI light curve after this new outburst is shown in Figure 4.29 (*left panel*). The 2022 outburst looks different in shape and less luminous than the 2006 one (Cocchi et al., 2023). According to the MAXI light curve, the source returned in quiescence after ~ 200 days. *IXPE* light curves in the 2–8 keV energy band and the hard color (5–8 keV/3–5 keV) are shown in Figure 4.29 for each DU, with time bin of 120 s. While for the first observation the source flux decreases from 20–25 counts s $^{-1}$ to about 15 counts s $^{-1}$ (*left panel*), in the second one the flux remains more stable, except during the central part, in which the source exhibits very rapid variations in intensity (*right panel*). In Figure 4.30, the 3–20 keV *NuSTAR* light curve of XTE J1701–462 spanning all the observation is shown, considering 120 s time bin. The X-ray light curve clearly shows a reduction in intensity from a count rate of ~ 500 counts s $^{-1}$ at the beginning of the observation to ~ 350 counts s $^{-1}$ after ~ 5 ks. *IXPE* did not detect this drop in intensity, since its observations began shortly thereafter (green line in the left panels). The Hard Color (9.6–20 keV/5.6–9.6 keV) is shown in Figure 4.30 as a function of both the observational time (*bottom left panel*) and the Soft Color (5.6–9.6 keV/3–5.6 keV, *right panel*) for each FPM. The source clearly traces out part of the NB in the CCD, in correspondence with the drop in intensity at the beginning of the observations and then remains almost constant in Hard Color and intensity while it moves along the FB. Rapid variations in intensity in the middle of *IXPE* Obs. II are also detected in the last part of the *NuSTAR* observation and correspond to the motion along the FB towards the NB. Intensity reductions can create tracks in CCDs or HIDs similar to those of the FB found in Sco X–1-like sources (e.g. GX 349+2, GX 17+2, see Church et al., 2012), however these variability events can also be related to absorption dips in the outer disk for highly inclined Cyg X–2-like sources (Church et al., 2006; Bałucińska-Church et al., 2012). The *NuSTAR* observation has been divided into two different parts using good time intervals (GTIs)

Model	Parameter	Best-fit
TBabs	n_H (10^{22} cm^{-2})	$2.78^{+0.04}_{-0.04}$
diskbb	kT_{in} (keV)	$0.99^{+0.08}_{-0.06}$
	R_{in} (km)	$15.91^{+0.70}_{-0.94}$
bbodyrad	kT (keV)	$1.10^{+0.09}_{-0.06}$
	R_{bb} (km)	$22.48^{+3.61}_{-3.94}$
thcomp	kT_e (keV)	$2.61^{+0.04}_{-0.04}$
	τ	$8.56^{+0.29}_{-0.25}$
	f	[1]
relline	E_l (keV)	$6.72^{+0.08}_{-0.09}$
	i ($^\circ$)	$31.73^{+14.91}_{-5.52}$
	R_{in} (ISCO)	[2]
	N_r (10^{-3})	$4.77^{+1.27}_{-1.04}$
$\chi^2/\text{d.o.f.}$		575.40/559
$F_{\text{disk}}/F_{\text{tot}}$ (2–8 keV)		31.6%
$F_{\text{comp}}/F_{\text{tot}}$ (2–8 keV)		68.2%
$F_{\text{line}}/F_{\text{tot}}$ (2–8 keV)		0.2%
F_{tot} ($\text{erg s}^{-1} \text{ cm}^{-2}$)		1.63×10^{-8}

Notes. A 7.5 kpc distance is assumed to compute the inner radius R_{in} and R_{bb} from normalizations.

Table 4.13: Best-fit Spectral Parameters obtained from the NICER and *IXPE* data. The errors are at the 90% confidence level for a single parameter.

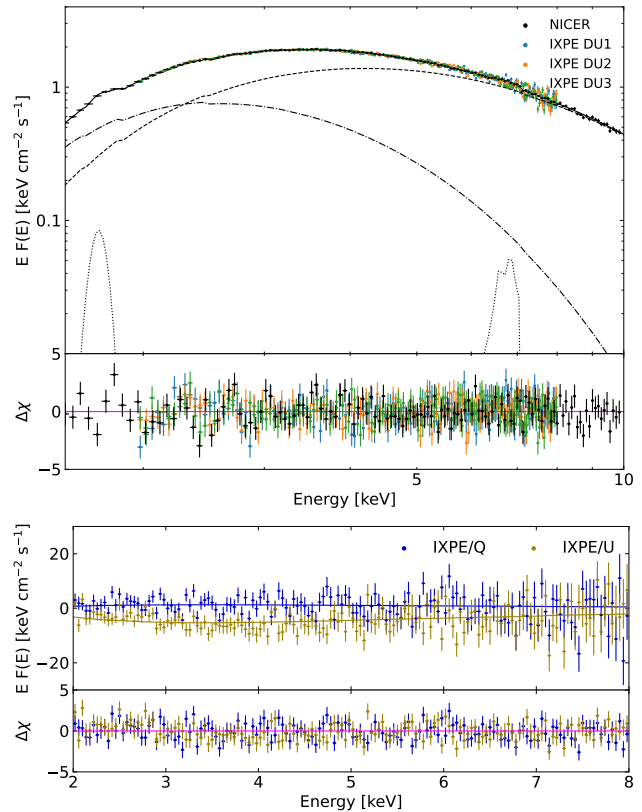


Figure 4.31: Best-fit of the NICER and *IXPE* deconvolved I spectra (top panel) with Stokes Q and U spectra (lower panel) of XTE J1701–462 (Obs. I). The model includes diskbb (dashed dotted line), thcomp*bbbodyrad (dashed line) and relline (dotted line) with residuals in units of σ . The spectral parameters are given in Table 4.13.

based on the light curves and the HID (Figure 4.30). For spectral analysis, only the second part of the *NuSTAR* observations simultaneous with *IXPE* ($t \gtrsim 5$ ks) is taken into account.

4.8.2 Spectro-Polarimetric Analysis

The best-fitting spectral parameters are presented in Tables 4.13 and 4.14, while the spectra and model residuals are shown in Figures 4.31 and 4.32, respectively for Obs. I and II. The best-fits are obtained by employing the following spectral model:

Obs. I: $\text{tbabs} * (\text{diskbb} + \text{thcomp} * \text{bbodyrad} + \text{relline} + \text{gaussian})$

Obs. II: $\text{tbabs} * (\text{diskbb} + \text{thcomp} * \text{bbodyrad} + \text{relxillNS})$

When XTE J1701–462 moves along the HB towards the NB during the Obs. I, the covering factor is always > 0.95 , i.e. all photons emitted from the boundary layer are Comptonized. To improve the fit statistic to better constrain the other parameters, the covering factor is then fixed to the best-fit value for this set of data ($f=1$). The NICER data of Obs. I shows evidence of an iron line between 6–7 keV which is modelled by adding to the continuum a relativistically broadened emission line (relline; Dauser et al. 2010, 2013). The emissivity index $q_{\text{em}} = 2$, the dimensionless spin $a = 0.1$ and the outer disk radius $R_{\text{out}} = 1000 R_g$ are fixed, since the fit is not very sensitive to these parameters (see also Ludlam et al. 2022). The relline model is not able to constrain the inner disk radius parameters and is then fixed to 1.5 in units of the innermost stable circular orbit (ISCO). The resulting line energy is 6.72 ± 0.09 keV, with a 0.03 keV equivalent width for a disk inclination of $\approx 32^\circ$ ($\chi^2/\text{d.o.f.} = 575.4/559$). The NICER spectrum

Model	Parameter	Best-fit
TBabs	n_H (10^{22} cm^{-2})	$1.78^{+0.15}_{-0.19}$
diskbb	kT_{in} (keV)	$1.05^{+0.01}_{-0.01}$
	R_{in} (km)	$12.02^{+0.37}_{-0.49}$
bbodyrad	kT (keV)	$1.26^{+0.01}_{-0.01}$
	R_{bb} (km)	$14.85^{+0.32}_{-0.24}$
thcomp	kT_e (keV)	$3.79^{+0.52}_{-0.38}$
	τ	$5.27^{+0.76}_{-0.79}$
	f	[0.2]
relxillNS	i ($^\circ$)	$22.58^{+6.76}_{-9.04}$
	R_{in} (ISCO)	[2]
	kT_{bb} (keV)	$= kT$
	$\log \xi$	$2.61^{+0.09}_{-0.10}$
	N_r (10^{-3})	$2.22^{+0.42}_{-0.44}$
$\chi^2/\text{d.o.f.}$		632.3/564
$F_{\text{disk}}/F_{\text{tot}}$ (2–8 keV)		31.6%
$F_{\text{comp}}/F_{\text{tot}}$ (2–8 keV)		65.4%
$F_{\text{refl}}/F_{\text{tot}}$ (2–8 keV)		3.0%
F_{tot} ($\text{erg s}^{-1} \text{ cm}^{-2}$)		1.18×10^{-8}

Notes. A 7.5 kpc distance is assumed to compute the inner radius R_{in} and R_{bb} from normalizations.

Table 4.14: Best-fit Spectral Parameters obtained from the *NuSTAR* and *IXPE* data. The errors are at the 90% confidence level for a single parameter.

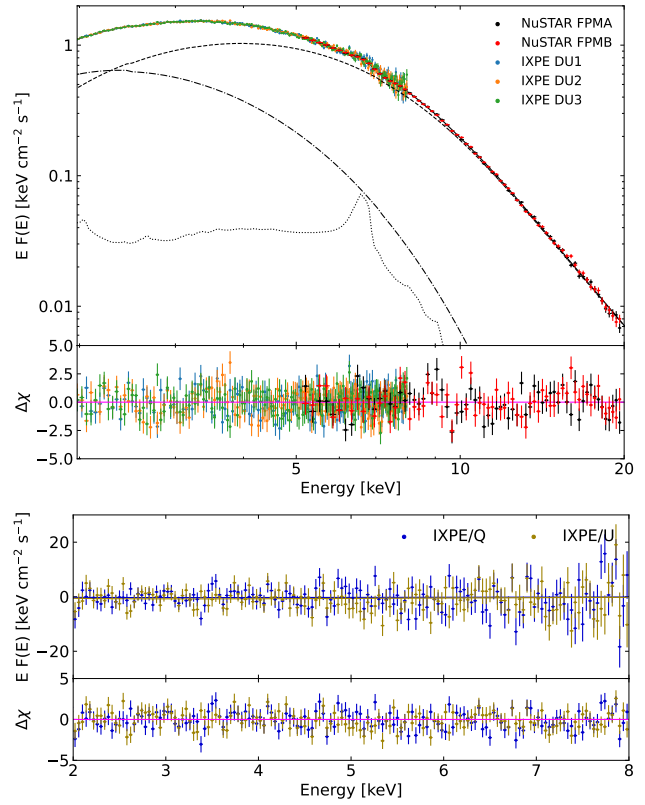


Figure 4.32: Best-fit of the *NuSTAR* and *IXPE* deconvolved I spectra (top panel) with Stokes Q and U spectra (lower panel) of XTE J1701–462 (Obs. II). The model includes diskbb (dashed dotted line), thcomp*bbodyrad (dashed line) and relxillNS (dotted line) with residuals in units of σ . The spectral parameters are given in Table 4.14.

also shows bad features in the residuals below 2 keV, related to instrumental issues (Miller et al., 2018; Strohmayer et al., 2018). Another gaussian component peaked at 1.73 ± 0.03 keV and with an equivalent width 6.51 ± 0.22 eV is added to model some of these features. The spectral parameters remain consistent within the errors. The model used for Obs. I does not provide a good fit to the *NuSTAR* data of Obs. II, leaving some residuals at higher energies. Compared to the first observation, relline is able to fit the emission line at 6.65 ± 0.06 keV, with an inclination of $\approx 30^\circ$ and an upper limit to the inner disk radius ($R_{\text{in}} < 4 R_{\text{ISCO}}$). To remove the residuals, the relativistic line profile is replaced by the complete reflection model relxillNS (García et al., 2022). The relxill model is able to calculate the relativistic reflection from the innermost regions of the accretion disk (García et al., 2014; Dauser et al., 2014). In particular, relxillNS assumes a single temperature blackbody spectrum as the primary continuum that illuminates the disk, physically related to the NS surface or the emission of the spreading layer. As for relline, the emissivity index $q_{\text{em}} = 2$, the dimensionless spin $a = 0.1$ and the outer radius $R_{\text{out}} = 1000 R_g$ are again fixed. The number density has been fixed at $\log n_e = 18 \text{ cm}^{-3}$, since the fit is not sensitive to this parameter because its effect is relevant only at lower energies (Ballantyne, 2004; García et al., 2016). The number density is consistent with the inner region of standard accretion disks (see García et al. 2016; Ludlam et al. 2022). The temperature of the seed photons is also tied to the blackbody temperature of bbodyrad. The fit is not able to constrain at the same time the inclination and the inner disk radius. Therefore, the inner disk radius has been fixed to the same value as relline in Obs. I ($R_{\text{in}} = 2 R_{\text{ISCO}}$). The resulting inclination is slightly lower than in the Obs. I, but it is consistent within errors. With respect to the first

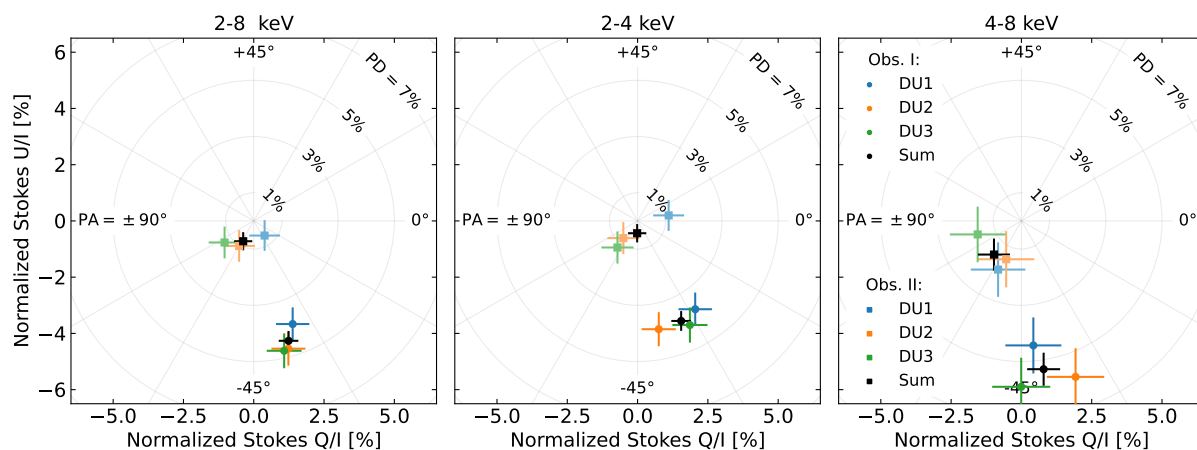


Figure 4.33: Stokes parameters of XTE J1701–462 in the 2–8 keV, 2–4 keV and 4–8 keV energy bands for DU1 (blue), DU2 (orange), DU3 (green) and by summing all the events of the three DUs (black) for both observations.

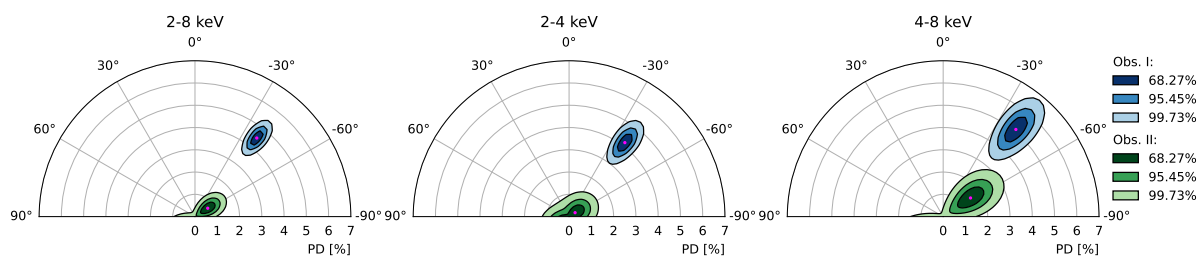


Figure 4.34: Polarization contours for XTE J1701–462 in the 2–8 keV, 2–4 keV and 4–8 keV energy bands obtained with *xSPEC* by summing the events from the three DUs for Obs. I (blue) and Obs. II (green). Contours correspond to the 68.27%, 95.45% and 99.73% confidence levels derived using a χ^2 with two degrees of freedom.

observation, the Comptonizing region seems to be hotter and less opaque in Obs. II, while the disk and the boundary layer are hotter in the NB and FB. The soft disk component dominates up to $\approx 2 - 2.2$ keV in Obs. I and up to ≈ 3.5 keV in Obs. II (see Figures 4.31 and 4.32) but its contribution to the total flux in the 2–8 keV energy band is the same in the two observations (Tables 4.13 and 4.14). The flux of the Comptonized radiation slightly decreases between the first and second observations, in favour of the reflection component (Table 4.14).

The Stokes parameters of XTE J1701–462 observed by *IXPE* in the 2–8 keV, 2–4 keV and 4–8 keV energy bands obtained with *IXPEOBSSIM* are reported in Figure 4.33. Polarimetric results show strong (model-independent) variability of linear PD between the two observations. During Obs. I, an average PD of $4.5\% \pm 0.3\%$ was found, with a slight increasing trend of polarization with energies, up to $5.4\% \pm 0.5\%$ in the 4–8 keV energy range, while in Obs. II (~ 10 days after Obs. I), the polarization signal in the 2–8 keV band could not be constrained with 99% upper limit of 1.6% (see also [Cocchi et al. 2023](#)). From the time-resolved CCD built with *NuSTAR*, *NICER* and *IXPE* data, during Obs. I XTE J1701–462 moved from a lower to an upper position of the HB, while in Obs. II the source is found to move along the NB. The polarization seems to be related to the position along the Z-track: in the HB, the X-ray radiation is more polarized and starts decreasing moving along the NB towards the FB. This is also consistent with the results obtained for Cyg X–2 (see Section 4.7), as the observed PD along the NB is slightly higher than the upper limit found for XTE J1701–462 in its NB. The PA does not show any variability along the Z-track. The results are well consistent within errors with those obtained with *xSPEC* (Figure 4.34). For

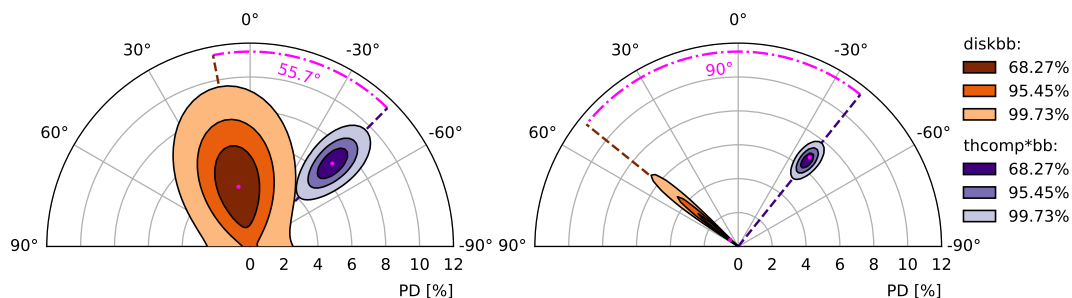


Figure 4.35: Polarization contours for XTE J1701–462 in the 2–8 keV energy range of Obs. I. The `polconst` polarimetric model is applied separately to the `diskbb` and `thcomp*bb` components. *Left panel*: the PD and PA of each component are left free to vary. *Right panel*: the PA of `diskbb` is assumed to differ from the PA of the hard component by 90° . Contours correspond to the 68.27%, 95.45% and 99.73% confidence levels derived using a χ^2 with two degrees of freedom.

Obs. I, the polarization is well constrained in each energy band considered, whereas it is unconstrained at 3σ confidence level during Obs. II. The joint spectro-polarimetric analysis of the two observations is performed using the baseline model obtained with NICER and *IXPE* for Obs. I and *NuSTAR* and *IXPE* for Obs. II and applying to each component a constant polarization through `polconst`. The reflection component modelled with `relline` and `relxillNS` includes the fluorescent iron line, which should be unpolarized. Some significant residuals can be found at both low and high energies in the *IXPE* spectra, which are likely artifacts of calibration issues and can be taken into account by applying a gain shift to the response files of the *IXPE* spectra with the `gain_fit` command in `xspec`. The resulting slope of the gain shift is 0.981 ± 0.003 , 0.970 ± 0.003 , 0.992 ± 0.003 keV $^{-1}$ for the three DUs respectively, while the energy offset in each one is -0.047 ± 0.011 , 0.027 ± 0.010 , -0.058 ± 0.010 keV for Obs. I and 0.951 ± 0.003 , 0.948 ± 0.003 , 0.962 ± 0.003 keV $^{-1}$ with offsets 0.142 ± 0.009 , 0.163 ± 0.010 , 0.144 ± 0.009 keV for Obs. II. All spectral parameters are fixed to their best-fit value. The overlap in the energy range between *IXPE* and *NuSTAR* or NICER is expected to minimize systematic effects on the derived polarimetric parameters. However, the *IXPE* band-pass does not allow to obtain tight constraints on the PD and PA for each spectral component, in particular for the Comptonized and reflected radiation since these two are quite degenerate peaking at similar energies and having similar spectral shapes, and therefore some assumptions based on theoretical and observational expectation are required.

For Obs. I, after assigning `polconst` to each spectral component, the polarization of Comptonized radiation is well constrained at a 99.9% confidence level ($6.9\% \pm 1.23\%$, with PA of $-44.8^\circ \pm 5.2^\circ$), while the polarization of the disk is not well constrained ($< 6.3\%$). The PA of the two components appears to differ by approximately $\sim 56^\circ$ (see Figure 4.35, *left panel*). However, it cannot be ruled out that the two PAs are perpendicular, due to uncertainty on the polarization of the disk. By fixing the PA of `diskbb` perpendicular to that of `thcomp*bb`, the polarization of the Comptonized component is again well constrained ($6.75\% \pm 1.03\%$, with PA of $-38.8^\circ \pm 2.7^\circ$), while the upper limit on the PD of the disk decreases ($< 3.3\%$, see Figure 4.35, *right panel*). In both cases, the high polarization seems to be related mainly to the hard Comptonized component (which may also include reflection, even if it is not directly distinguishable from the spectrum except for the iron line). In Obs. II, reflection is detected and is a further component to be taken into account in the spectro-polarimetric analysis. As a first test, only one component is considered to be polarized, with the others having null polarization. For a polarized disk only, the PA is unconstrained and only an upper limit of 2.1% is obtained for the PD ($\chi^2/\text{d.o.f.} = 1580.8/1465$, $948.4/894$ for the subset of Stokes Q and U). The fit improves considering

Source	Satellite	Obs. ID	Start Date (UT)	Net Exp. (ks)
GX 5–1 Obs. I	<i>IXPE</i>	02002799	2023-03-21 04:16:14	48.6
	<i>NuSTAR</i>	90902310002	2023-03-21 16:41:48	12.6
	<i>NICER</i>	6010230101	2023-03-21 03:41:20	9.1
	<i>NICER</i>	6010230102	2023-03-22 00:58:08	3.9
	<i>INTEGRAL</i>	20700060001	2023-03-21 03:58:07	40.1
GX 5–1 Obs. II	<i>IXPE</i>	02002799	2023-04-13 23:43:42	47.1
	<i>NuSTAR</i>	90902310004	2023-04-13 15:57:07	9.3
	<i>NuSTAR</i>	90902310006	2023-04-14 15:51:09	6.4
	<i>NICER</i>	6010230106	2023-04-14 00:24:46	8.2
	<i>INTEGRAL</i>	20700060002	2023-04-13 03:51:17	85.0

Table 4.15: Log of simultaneous observations of the Z-sources GX 5–1.

Comptonization or reflection as the main polarized component: $\chi^2/\text{d.o.f.} = 1572.3/1465$ ($939.8/894$ for the subset of Stokes Q and U) is obtained for polarized `thcomp*bbbodyrad` only, finding a PD of $1.2\% \pm 0.6\%$ with $-56.1^\circ \pm 16.2^\circ$ PA, while $\chi^2/\text{d.o.f.} = 1571.2/1465$ ($938.8/894$ for the subset of Stokes Q and U) with PD of $28.2\% \pm 14.3\%$ and PA of $-60.4^\circ \pm 15.2^\circ$. These models provide a good fit of both the flux and Stokes parameters spectra, without strong residuals. The PA is very similar and consistent within errors, whereas the reflection-dominated scenario requires a larger PD compared to the other case.

For the configuration of the spreading layer, since the vertical height is significantly greater than its radial extension ($H \gg \Delta R$), the PA of the Comptonized component should be the same as that of the reflection, since it is characterized by a PA perpendicular to the disk surface (Matt, 1993; Poutanen et al., 1996b; Schnittman and Krolik, 2009). When the PD and PA for the disk and the hard components are left free, only upper limits can be found for each component. Fixing the PD of the Comptonization at a reasonable value for a wedge or spreading layer geometry (i.e. 1%, see Sections 3.6 and 3.7), the disk polarization is still not well constrained with an upper limit on the PD ($< 4.8\%$ at 90% confidence level) and $33.95^\circ \pm 40.35^\circ$ PA, while the PD of the reflection results in $28.79\% \pm 21.11\%$ with $-57.38^\circ \pm 17.86^\circ$ PA, nearly perpendicular to the disk polarization (even if it is not tightly constrained). If the PA of the disk is fixed to be perpendicular to the harder components, the fit statistic and the best-fit parameters remain practically unchanged but with smaller uncertainties. A similar procedure can be done by leaving free to vary the PD of both the disk and Comptonized components and considering reflection with fixed PD of 10% (see e.g. Matt 1993). With this assumption, the polarization components are not well constrained and only upper limits can be found for both the disk and Comptonized radiation (at 99.73% confidence level for a single parameter), while the fit worsens compared to previous cases.

4.9 GX 5–1

GX 5–1 is a Galactic Z source (Kuulkers et al., 1994; Jonker et al., 2002) located near the Galactic Center. It is a radio source (Fender and Hendry, 2000) with radio emission most likely originating from a compact jet. The radio counterpart allowed for an accurate localization that, despite source confusion and optical obscuration near the Galactic Center, has led to the determination of a likely infra-red companion candidate (Jonker et al., 2000). Until the early 1990s, GX 5–1 X-ray data were probably contaminated by the Black Hole LMXB GRS 1758–258, located only $40'$ apart. The two sources have been resolved by (Sunyaev et al., 1991) and (Gilfanov et al., 1993), showing that GX 5–1 was $\sim 30 - 50$ times brighter than GRS 1758–258 below 20 keV. GX 5–1 has not shown any X-ray pulsations or X-ray bursts so far. An

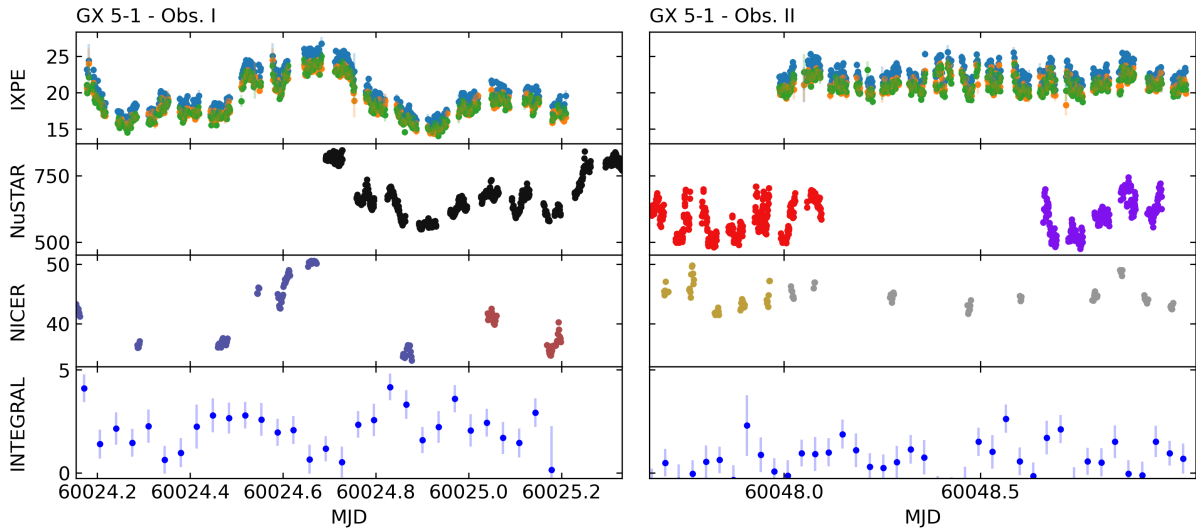


Figure 4.36: Light curves of *IXPE*, *NuSTAR*, *NICER* and *IBIS/ISGRI* during Obs. I (left panel) and Obs. II (right panel). The 2–8 keV *IXPE* light curves of the three DUs are shown in the top panels (DU1 blue, DU2 orange and DU3 green). The 3–20 keV *NuSTAR* light curves are represented in the second panels (black, red and purple colors correspond to the three *NuSTAR* observation). The 0.5–10 keV *NICER* light curves are plotted in the third panel (the different colors correspond to each *NICER* segment). The 28–40 keV *IBIS/ISGRI* light curves are shown in the lower panels. For *IXPE*, *NuSTAR* and *NICER* each bin correspond to 120 s.

X-ray halo due to single and multiple scattering (much less significant above 2.5 keV) of X-ray photons is present, as highlighted by the Chandra image (Smith et al., 2006; Clark, 2018). Such a halo arises because of the presence of multiple clouds along the line of sight.

4.9.1 Observations

IXPE observed GX 5–1 twice (within the same Obs. ID 02002799, see Table 4.15). The first observation segment (Obs. I) lasted from 2023 March 21 04:16:14 UT to March 22 05:02:52 UT, while the second observation segment (Obs. II) lasted from 2023 April 13 23:43:42 UT to April 15 00:37:32 UT with a nominal integration time of 50 ks each (Fabiani et al., 2024). Science data were extracted as described in Section 4.2.1 with 60'' source extraction radius, due to the presence of the X-ray halo. Background subtraction was not applied due to the high count rate of the source ($\sim 20 - 25$ counts s^{-1} per DU, see Di Marco et al. 2023b). GX 5–1 was also observed by *NuSTAR* on 2023 March 21 and twice between 2023 April 13–14 (see Table 4.15). The cleaned and calibrated data were extracted following the procedure described in the Appendix B.1.1. For both detectors, background and source spectra and light curves were extracted from a circular region with 60'' radius sufficiently far from each other. Since the background starts dominating above 30 keV, the data are considered in the 3–30 keV range. *NICER* performed a total of six observations of GX 5–1, four of which occurred between 2023 March 21–25 and the remaining two on 2023 April 13–14 (see Table 4.15). Only the first two observations (Obs. ID 6010230101, 6010230102) and the final one (Obs. ID 6010230106) were included in the spectro-polarimetric analysis, as they were the only ones that occurred simultaneously with the *IXPE* observations. Data have been extracted and reduced following the procedure described in the Appendix B.2.1. During the contemporary observation with *IXPE*, there were two significant increases in the count rate in the *NICER* data, up to double the typical value. These events were in coincidence with two solar flares (C class the first one peaking at about 60048.5389 MJD and M class the second one peaking at about 60048.6806 MJD) and they have been removed manually from the GTIs. Some relevant features are noticed below 4 keV in the energy spectrum. Due to the high count rate of the source, these residuals are assumed to arise from the ARF estimation and included some edges only in the *NICER* *xSPEC* spectral modelling. These edges account

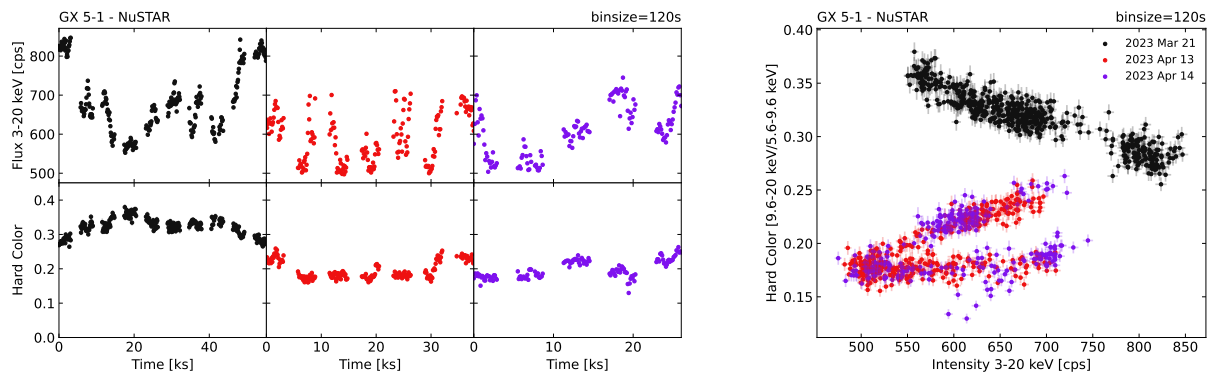


Figure 4.37: GX 5–1 *NuSTAR* 3–20 keV light curves in units of cps and Hard color (9.6–20 keV/5.6–9.6 keV) as a function of time (*left panel*) and Intensity (3–20 keV, *right panel*). The red and black points correspond to the two *NuSTAR* detector, FPMA and FPMB respectively. Each bin corresponds to 120 s.

for the Si and Au transmission of the windows and filters and, to some extent, for the dead layer of the silicon detector itself. Furthermore, the features at about 2.0–3.5 keV are also due to absorption features in the reflectivity due to the M edges of the gold in the concentrators⁵. The energy of these edges has been frozen to their best-fit values (see [Fabiani et al. 2024](#)). *INTEGRAL* observed the source from 2023 March 21 03:58:07 UT to March 22 04:28:46 and from 2023 April 13 03:51:17 to April 15 08:53:00 for a total of 125.1 ks. The equivalent on-axis exposures of the IBIS/ISGRI spectra are 40 and 85 ks. JEM-X and IBIS data have been reduced following the procedure described in the Appendix B.3.1. A systematic error of 1.5% was added in quadrature for the spectral analysis.

The *NuSTAR*, NICER and IBIS/ISGRI light curves contemporaneous to each *IXPE* observations are represented in Figure 4.36 as a function of time (in MJD). The time-resolved CCD and HID for all the observations show GX 5–1 moving along the Z-track from March 21 to April 15 ([Fabiani et al., 2024](#)). *NuSTAR* CCD and HID clearly highlight the Z-shape (Figure 4.37), also disentangling the NB with respect to the FB, due to the wide *NuSTAR* energy band from 3 to 20 keV. During *IXPE* Obs. I, the source was in the HB, whereas it was moving along the NB and FB during Obs. II. The *IXPE* CCD was also checked to confirm this behavior. From March 24 to 25 (about 3 days after the end of *IXPE* Obs. I), NICER detected GX 5–1 moving from the HB to the NB upper corner, corresponding to the ATCA observation.

4.9.2 Radio Observations

ATCA observed GX 5–1 on 2023 March 24 and April 14. On March 24, the telescope was on source between 2023-03-24 15:21:20 UT to 2023-03-25 01:55:50 UT, with the array in its 750C configuration⁶. Observations taken on April 14 ATCA were carried out between 11:32:00 UT and 17:57:40 UT, with the array in a relatively compact H214 configuration. For both observations, data were recorded simultaneously at central frequencies of 5.5 GHz and 9.0 GHz, with 2 GHz of bandwidth at each frequency. The nearby source B1817–254 was used for gain calibration and to calibrate the polarization angle using the *CASA* `atcapolhelpers.py` task `qufromgain`⁷. Calibration and imaging followed standard procedures within the Common Astronomy Software Applications for Radio Astronomy (*CASA*, version 5.1.2; [CASA Team et al. 2022](#)). For the 24 March observations, fitting for a point source in the image plane, GX 5–1 was detected at a flux density of $960 \pm 19 \mu\text{Jy}$ at 5.5 GHz and $810 \pm 11 \mu\text{Jy}$ at 9 GHz coincident with the previously reported radio position of GX 5–1 (e.g. [Berendsen et al. 2000](#); [Liu et al. 2007](#)). These detections correspond to a radio spectral index of -0.37 ± 0.09 . Without clear detection in the Stokes *Q*

⁵https://heasarc.gsfc.nasa.gov/docs/nicer/analysis_threads/arf-rmf/

⁶https://www.narrabri.atnf.csiro.au/operations/array_configurations/configurations.html

⁷<https://github.com/radio-astro>

Model	Parameter	Best-fit
TBabs	n_H (10^{22} cm^{-2})	$4.86^{+0.07}_{-0.05}$
diskbb	kT_{in} (keV)	$0.92^{+0.04}_{-0.09}$
	R_{in} (km)	$25.71^{+2.45}_{-1.30}$
bbodyrad	kT (keV)	$1.19^{+0.08}_{-0.09}$
	R_{bb} (km)	$22.19^{+4.10}_{-2.68}$
thcomp	kT_e (keV)	$2.94^{+0.04}_{-0.04}$
	τ	$9.10^{+0.34}_{-0.34}$
	f	[1]
expabs	E_{cut} (keV)	$= kT$
powerlaw	Γ	[2.5]
	N_{pl}	$0.31^{+0.05}_{-0.05}$
$\chi^2/\text{d.o.f.}$		537.5/435
$F_{\text{disk}}/F_{\text{tot}}$ (2–8 keV)		39.9%
$F_{\text{comp}}/F_{\text{tot}}$ (2–8 keV)		58.9%
$F_{\text{pl}}/F_{\text{tot}}$ (2–8 keV)		1.2%
F_{tot} ($\text{erg s}^{-1} \text{ cm}^{-2}$)		2.22×10^{-8}

Notes. A 7.6 kpc distance is assumed to compute the inner radius R_{in} and R_{bb} from normalizations.

Table 4.16: Best-fit Spectral Parameters obtained from the *NuSTAR*, NICER and *INTEGRAL* data. The errors are at the 90% confidence level for a single parameter.

or U images, their values were measured at the position of the peak source flux density (Stokes I). No significant linearly polarized (LP) emission was detected at either frequency, with 3σ upper limits of $58 \mu\text{Jy beam}^{-1}$ at 5.5 GHz and $48 \mu\text{Jy beam}^{-1}$ at 9 GHz, where $LP = \sqrt{Q^2 + U^2}$. This corresponds to a 3σ fractional linear polarization of $< 6.1\%$ at 5.5 GHz and $< 5.9\%$ at 9 GHz. Stacking the two frequencies to maximize the sensitivity also yields a non-detection of linearly polarized emission, with a 3σ upper-limit of $< 4.2\%$ (centred at 7.25 GHz). On April 14, following the same steps, GX 5–1 was detected at flux density of $750 \pm 50 \mu\text{Jy}$ and $620 \pm 40 \mu\text{Jy}$ at 5.5 and 9 GHz, respectively. These detections correspond to a radio spectral index of 0.4 ± 0.1 . The compact configuration coupled with a shorter exposure time resulted in a higher noise level in the images. At 5.5 GHz, no linearly polarised emission was detected from GX 5–1, with a 3σ upper limit of 12.5%, with only an upper limit on the linearly polarized emission of 20% at 9 GHz a 3σ .

4.9.3 Spectro-Polarimetric Analysis

The best-fitting spectral parameters are presented in Tables 4.16 and 4.17, while the spectra and model residuals are shown in Figures 4.38 and 4.39, respectively for Obs. I and II. The best-fit models obtained with the *NuSTAR*, NICER and IBIS/ISGRI spectra are

Obs. I: $\text{tbabs} * (\text{diskbb} + \text{thcomp} * \text{bbodyrad} + \text{expabs} * \text{powerlaw})$

Obs. II: $\text{tbabs} * (\text{diskbb} + \text{thcomp} * \text{bbodyrad})$

respectively. The normalization cross-calibration multiplicative factors for *NuSTAR* FPMA (fixed) and

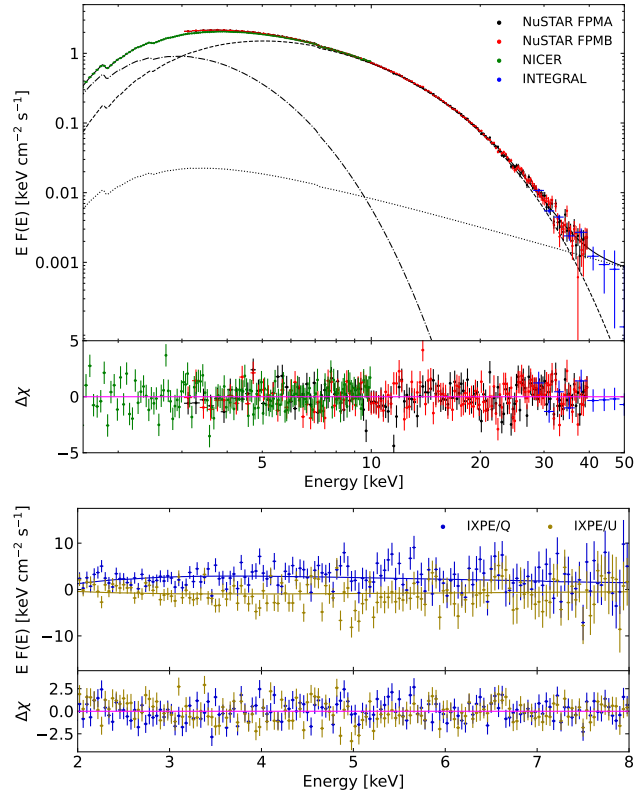


Figure 4.38: Best-fit of the *NuSTAR*, NICER and *INTEGRAL* deconvolved I spectra (top panel) with *IXPE* Stokes Q and U spectra (lower panel) of GX 5–1 (Obs. I). The model includes *diskbb* (dashed dotted line), *thcomp***bbodyrad* (dashed line) and *expabs***powerlaw* (dotted line), with residuals in units of σ . The spectral parameters are given in Table 4.16.

Model	Parameter	Best-fit
TBabs	n_H (10^{22} cm^{-2})	$4.74^{+0.02}_{-0.02}$
diskbb	kT_{in} (keV)	$1.27^{+0.02}_{-0.02}$
	R_{in} (km)	$17.61^{+0.42}_{-0.38}$
bbodyrad	kT (keV)	$1.71^{+0.03}_{-0.02}$
	R_{bb} (km)	$8.54^{+0.38}_{-0.42}$
thcomp	kT_e (keV)	$3.46^{+0.18}_{-0.17}$
	τ	> 12
	f (10^{-2})	$7.16\%^{+1.58}_{-1.29}$
expabs	E_{cut} (keV)	...
powerlaw	Γ	...
	N_{pl}	...
$\chi^2/\text{d.o.f.}$		454.1/378
$F_{\text{disk}}/F_{\text{tot}}$ (2–8 keV)		73.9%
$F_{\text{comp}}/F_{\text{tot}}$ (2–8 keV)		26.1%
$F_{\text{pl}}/F_{\text{tot}}$ (2–8 keV)		...
F_{tot} ($\text{erg s}^{-1} \text{ cm}^{-2}$)		2.39×10^{-8}

Notes. A 7.6 kpc distance is assumed to compute the inner radius R_{in} and R_{bb} from normalizations.

Table 4.17: Best-fit Spectral Parameters obtained from the *NuSTAR*, *NICER* and *INTEGRAL* data. The errors are at the 90% confidence level for a single parameter.

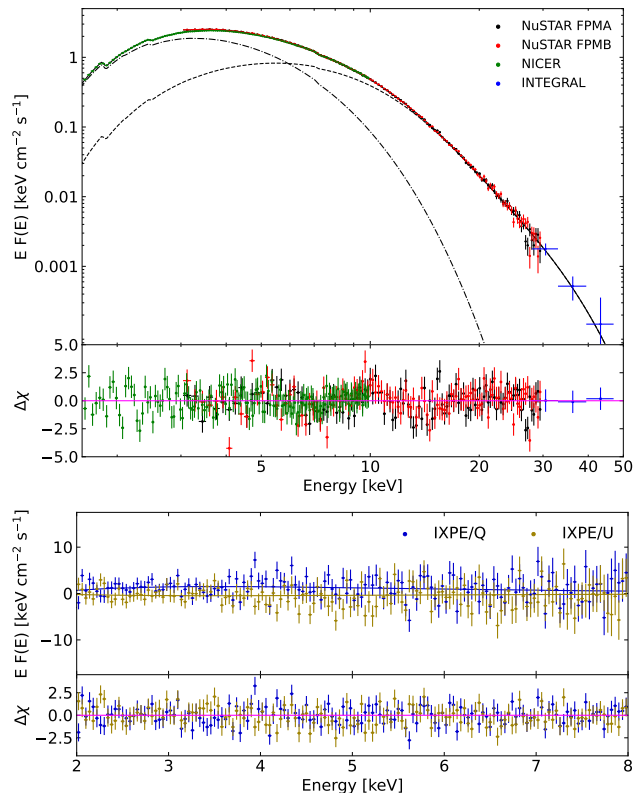


Figure 4.39: Best-fit of the *NuSTAR*, *NICER* and *INTEGRAL* deconvolved *I* spectra (*top panel*) with *IXPE* Stokes *Q* and *U* spectra (*lower panel*) of GX 5–1 (Obs. II). The model includes diskbb (dashed dotted line), thcomp*bbodyrad (dashed line), with residuals in units of σ . The spectral parameters are given in Table 4.17.

FPMB telescopes, *NICER* and *IBIS/ISGRI* are included in the models. During Obs. I when GX 5–1 moves along the HB, the covering fraction of thcomp is > 0.7 with best-fit values equal to 0.99. Therefore, all photons from the boundary/spreading layer are Comptonized. In Obs. II with the GX 5–1 in the NB and FB, only a fraction between 5.9% and 8.7% of seed photons are Comptonized, with a best-fit value of 7.16% (Fabiani et al., 2024). No strong reflection features were detected in both observations. During the first observation, the energy spectrum is harder and a high-energy excess is observed (absent in the second observation). This excess is modelled with an additional hard tail represented by a power-law component with a low-energy exponential roll-off, set equal to the temperature of the bbodyrad component. This parameter link comes from the assumption that the power-law emission originates from the seed distribution of the boundary/spreading layer blackbody. The boundary layer and the inner disk region result to be hotter in Obs. II compared to Obs. I, while the emitting region size of the bbodyrad and the inner disk radius are larger in the first observation. The soft disk component dominates up to ~ 3 keV in Obs. I and up to $\sim 6 - 7$ keV in Obs. II (see Figures 4.38 and 4.39). In the 2–8 keV band, the energy flux in the Comptonized component (including the contribution of the exponentially absorbed power-law) accounts for $\sim 60\%$ of the total in Obs. I and drops to $\sim 25\%$ during Obs. II (Fabiani et al., 2024).

The Stokes parameters of GX 5–1 observed by *IXPE* in the 2–8 keV, 2–4 keV and 4–8 keV energy bands obtained with *IXPEOBSSIM* are reported in Figure 4.40. Polarimetric results show strong (model-independent) variability of the linear PD between the two observations. During Obs. I, an average PD of $3.9\% \pm 0.3\%$ was found, with a slight increasing trend of polarization with energies up to $5.4\% \pm 0.7\%$ in

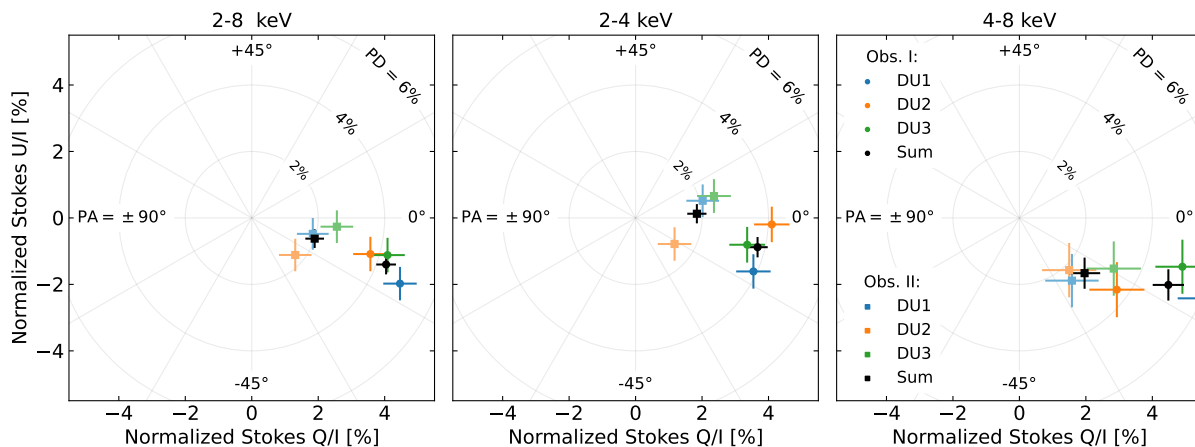


Figure 4.40: Stokes parameters of GX 5–1 in the 2–8 keV, 2–4 keV and 4–8 keV energy bands for DU1 (blue), DU2 (orange), DU3 (green) and by summing all the events of the three DUs (black) for both observations.

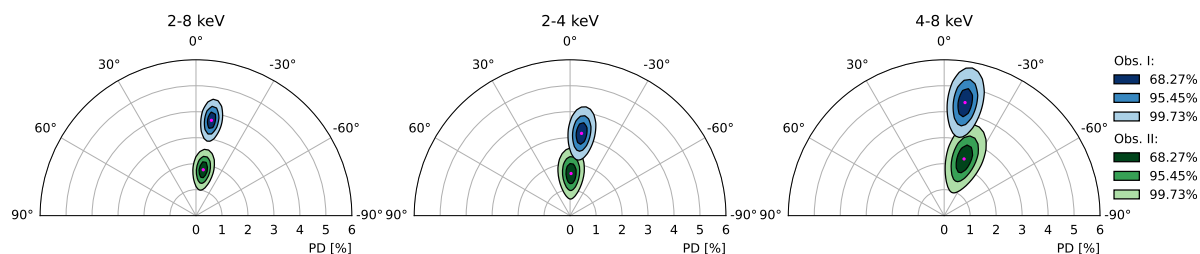


Figure 4.41: Polarization contours for GX 5–1 in the 2–8 keV, 2–4 keV and 4–8 keV energy bands obtained with *xSPEC* for Obs. I (blue) and Obs. II (green). Contours correspond to the 68.27%, 95.45% and 99.73% confidence levels derived using a χ^2 with two degrees of freedom.

the 4–8 keV energy range, while in Obs. II (~ 23 days after the first) the polarization signal in the 2–8 keV band decreases to $1.9\% \pm 0.3\%$ (see also [Fabiani et al. 2024](#)). Also in the second observation, the PD seems to increase with energy, although the increase is quite modest. However, the PA is compatible with being constant between the two observations, whereas it varies from lower to higher energies ($\sim 15 - 20^\circ$ rotation; [Fabiani et al. 2024](#)). As for XTE J1701–462, the polarization is correlated with the position along the Z-track: during Obs. I with GX 5–1 in the HB, the X-ray radiation is more polarized and decreases as it moves along the NB and FB in Obs. II (see also the HID, Figure 4.37). PA does not show any variability along the Z-track. The results are consistent within the errors with those obtained with *xSPEC* (Figure 4.41). Polarization is well constrained in each energy band considered for both observations. Joint spectro-polarimetric analysis of the two observations is performed using the baseline best-fit models obtained with the *NuSTAR*, *NICER*, and *INTEGRAL* spectra and applying to each spectral component a constant polarization through *polconst*. Some significant residuals can be found in the *IXPE* spectra, which are probably due to calibration issues already observed in other sources and NS-LMXBs (e.g. [Taverna et al. 2022](#); [Krawczynski et al. 2022](#); [Marinucci et al. 2022](#)). These problems can be solved by applying a gain shift to the response files of the *IXPE* spectra using the `gain_fit` command in *xSPEC*. The resulting slope is 0.966 ± 0.002 , 0.968 ± 0.002 and 0.990 ± 0.002 keV^{-1} for the three DUs respectively, while the energy offset for each DU is 0.085 ± 0.008 , 0.089 ± 0.007 , 0.053 ± 0.006 keV for Obs. I and 0.966 ± 0.002 , 0.969 ± 0.002 and 0.973 ± 0.002 keV^{-1} with offsets 0.080 ± 0.007 , 0.094 ± 0.006 , 0.085 ± 0.008 keV for Obs. II. All spectral parameters are fixed to their best-fit value.

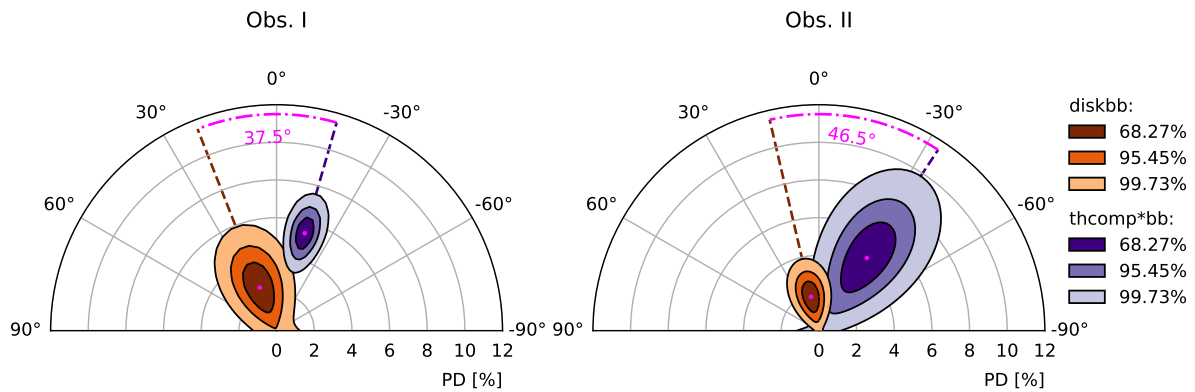


Figure 4.42: Polarization contours for GX 5–1 in the 2–8 keV energy band obtained with `xSPEC` for Obs. I (*left panel*) and Obs. II (*right panel*). The `polconst` polarimetric model is applied separately to the `diskbb` and the hard component. The hard component consists of `thcomp*bbbodyrad` for both observations, the first one includes also the `expabs*powerlaw` component. Contours correspond to the 68.27%, 95.45% and 99.73% confidence levels derived using a χ^2 with two degrees of freedom.

For Obs. I, the same polarization is assigned for the `expabs*powerlaw` and `thcomp*bbbodyrad` components, assuming that the power-law is just a continuation of the boundary/spreading layer component. The polarization of Comptonized+power-law component is well constrained at more than 3σ confidence level with $5.4\% \pm 0.9\%$ PD and $-16.1^\circ \pm 5.2^\circ$ PA, while the polarization of the disk is constrained only at 2σ confidence level with $2.5\% \pm 1.5\%$ PD and $21.4^\circ \pm 19.4^\circ$ PA. The PA of the two components differs by approximately $\sim 37.5^\circ$ (see Figure 4.42, *left panel*). Even considering errors, the soft and hard components seem to be polarized not perpendicularly (as expected theoretically). Fixing the PA of `diskbb` perpendicular to that of `thcomp*bbbodyrad` as for other sources, the fit worsens significantly. In both cases, the high polarization is mainly due to the hard Comptonized component. In Obs. II, the polarization of the `diskbb` and `thcomp*bbbodyrad` components are constrained at 2σ confidence level. The PD of the Comptonized component is $5.0\% \pm 2.6\%$ with $-34.2^\circ \pm 15.4^\circ$ PA, while the disk polarization is $1.8\% \pm 0.9\%$ with $12.4^\circ \pm 14.5^\circ$ PA. Also for this observation, the PAs of the two components are misaligned by $\sim 46^\circ$ and seems to not be perpendicular (see Figure 4.42, *right panel*). Unfortunately, even if the source was bright in the radio band during the observation campaign, it is impossible to compare the direction of the PA with the direction of the radio jet because the radio observations do not have the spatial resolution to resolve it and no information about jet direction is reported in literature. Although disk polarization is compatible with the classical results of a high optical depth scattering atmosphere for a 60° inclination (Chandrasekhar, 1960), the higher PD value of the hard component is difficult to explain by repeated Compton scattering in a high optical depth environment or a boundary layer. Disk reflection is probably the most natural way to explain a PD of 4–5%. Even if not directly detected, the reflection contribution to the spectrum may be low and embedded in the continuum, but nevertheless makes a large contribution to the net polarization signal. To test this assumption, the reflection component is added to the baseline models using `rdblur*rfxconv` (Fabian et al., 1989; Done and Gierliński, 2006; Kolehmainen et al., 2011) applied to the Comptonized radiation. To avoid double convolution, the `thcomp*bbbodyrad` is replaced with the `comptb` model (Farinelli et al., 2008). Since no significant reflection features are observed in the spectrum, some assumptions are required to fit the reflected radiation contribution: due to the absence of a broad emission Fe $K\alpha$ line, a highly ionized disk is considered, with an inclination of 60° , since GX 5–1 is a Cyg X–2-like Z-sources (Homan et al., 2018). The reflection amplitude f is set to a typical value for NS-LMXBs (namely 30%; e.g. Di Salvo et al. 2015; Matranga et al. 2017). In Obs. I,

the reflection component contributes to $\sim 22\%$ of the total flux and $\sim 12\%$ in Obs. II. This contribution to the total emission can easily account for the polarization detected. The fraction of Comptonized photons in Obs. II is significantly smaller with respect to Obs. I, as obtained by applying only the Comptonization model `thcomp`. Adding reflection, the parameter `log A` in `comptb` corresponds to a $\sim 6\%$ of photons upscattered in energy (consistent with $\sim 7\%$ obtained when reflection is not taken into account; see [Fabiani et al. 2024](#)). This confirms the presence of a blackbody component observed through an almost vanished Comptonization medium in Obs. II, even if reflection is included. However, the fraction of Comptonized photons, albeit small, is still sufficient to manifest its presence at high energy. Indeed, neglecting this small fraction of Comptonized photons by considering only a `bbbodyrad` component, the fit results to be unacceptable ($\chi^2 = 3.6$, with a significant excess at high energy due to this small fraction of Comptonized photons).

4.10 Scorpius X–1

Sco X–1 is the first discovered extrasolar X-ray source ([Giacconi et al., 1962](#)) and the brightest persistent X-ray source in the sky. It is located at a distance of $2.13^{+0.21}_{-0.26}$ kpc, as derived with *Gaia* Data Release 2 ([Arnason et al., 2021](#)), similar to the previous estimate obtained by parallax measured with the Very Long Baseline Array (2.8 ± 0.3 kpc; [Bradshaw et al. 1999](#)). Its binary orbit has a low inclination angle to the observer ([Titarchuk et al., 2014](#)), with an orbital period of 0.79 days. This binary system consists of an old, weakly magnetized NS with mass $\sim 1.4 M_{\odot}$ accreting matter via Roche-lobe overflow from an M-class star of $\sim 0.4 M_{\odot}$ ([Steehls and Casares, 2002](#)). Sco X–1 is a prototype of NS-LMXBs, with a peak luminosity close to the Eddington limit for a standard NS (Eq. 2.6; [Titarchuk et al. 2014](#)). The source is classified as a Z-source based on its evolution along the CCD ([Hasinger and van der Klis, 1989](#)). Differently to Cyg X–2-like NS-LMXBs, Sco X–1 the flaring branch is strong and frequent with large increases of X-ray intensity, while the HB is hardly visible. Sco X–1 was also the first X-ray binary for which radio emission was detected ([Andrew and Purton, 1968](#)). VLBI observations spatially resolved a jet at sub-milliarcsecond scales, revealing mildly relativistic motion of components in opposite directions at a position angle of $\sim 54^{\circ}$ and inclination of $44^{\circ} \pm 6^{\circ}$ ([Fomalont et al., 2001a,b](#)).

As the most luminous X-ray source in the sky, apart from the Sun, Sco X–1 was among the first targets for X-ray polarization studies. The OSO-8 satellite spent about 15 days observing Sco X–1, obtaining a low-significance detection at 2.6 keV with PD of $0.4\% \pm 0.2\%$ and PA of $29^{\circ} \pm 10^{\circ}$ and at 5.2 keV with PD of $1.3\% \pm 0.4\%$ and PA of $57^{\circ} \pm 6^{\circ}$ ([Long et al., 1979](#)). Recently, PolarLight ([Feng et al., 2019](#)) observed Sco X–1 for a total of ~ 322 days, obtaining hints for variations of the polarization with the energy and the source flux ([Long et al., 2022](#)). When the flux of Sco X–1 was high, a significant detection (5σ confidence level) was obtained in the 4–8 keV energy band, with $4.3\% \pm 0.8\%$ polarization degree and $53^{\circ} \pm 5^{\circ}$ polarization angle. Although the polarization properties of the NS-LMXBs seem to change significantly with the emission state ([Cocchi et al., 2023](#); [Fabiani et al., 2024](#); [Rankin et al., 2024](#)), this measurement was performed in long exposures, for which the emission state could not be determined.

4.10.1 Observations

IXPE observed Sco X–1 on 2023 August 28 from 16:10:56 UT to 07:35:39 UT (Obs. ID 02002401), for a total net exposure of 24.2 ks per DU. Due to the high X-ray flux of Sco X–1, the *IXPE* observation was performed using a partially opaque absorber, the so-called gray filter, which is already on board in the detector filter and in the calibration wheel ([Ferrazzoli et al., 2020](#); [Weisskopf et al., 2022](#)). The filter is required to reduce the flux to a level compatible with the *IXPE* focal plane detector dead-time. In particular, it allows for a ten-fold reduction of the incident flux at low energies, below 3 keV. Science data were extracted following the procedure described in Section 4.2.1, considering a $120''$ source extraction radius. Due to the high brightness of the source, the background is negligible ([Di Marco et al., 2023b](#)). The daily MAXI light curve is shown in Figure 4.43 (*left panel*) spanning ~ 50 days around *IXPE* observation. The

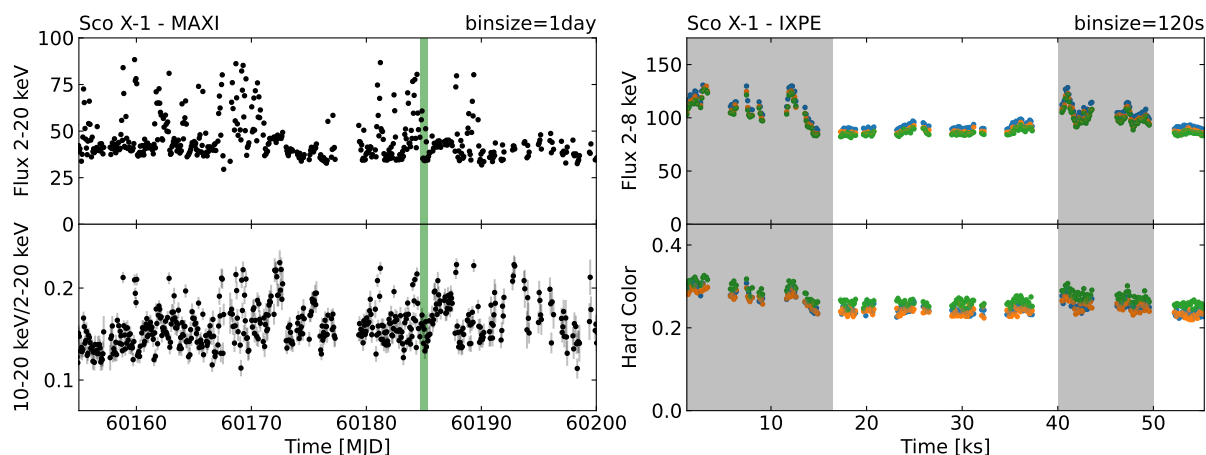


Figure 4.43: *Left panel:* Sco X-1 MAXI 2–20 keV light curve in units of photons $\text{cm}^{-2} \text{s}^{-1}$ (top) and hardness ratio (10–20 keV/2–20 keV, bottom) as function of time in MJD. The green line corresponds to the *IXPE* observation. *Right panel:* Sco X-1 *IXPE* 2–8 keV light curve in units of cps (top) and Hard Color (5–8 keV/3–5 keV, bottom) as a function of observational time. Grey regions correspond to flaring activity. Each bin corresponds to 120 s.

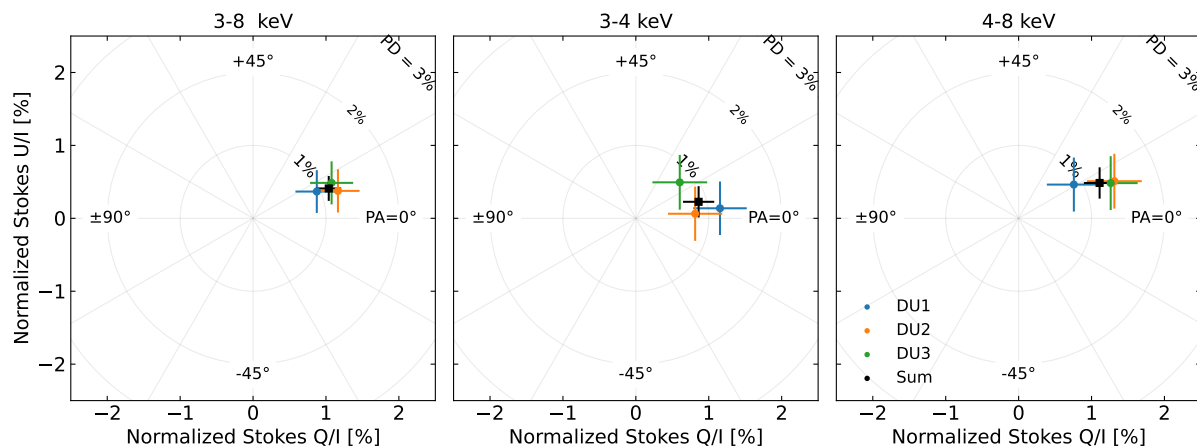


Figure 4.44: Stokes parameters of Sco X-1 in the 3–8 keV, 3–4 keV and 4–8 keV energy bands for DU1 (blue), DU2 (orange), DU3 (green) and by summing all the events of the three DUs (black) for both observations.

X-ray flux exhibits several intensity peaks corresponding to the motion along the flaring branch. The *IXPE* light curves in the 2–8 keV energy band and the hard color (5–8 keV/3–5 keV) are represented in Figure 4.43 (*right panels*) for each DU. During *IXPE* observation, flaring activity is observed (grey regions), causing a simultaneous increase in the count rate of the source for all multi-wavelength telescopes. In particular, during the *IXPE* observation Sco X-1 moved from the FB toward the NB and backward. As the source never entered deeply into the NB, the *IXPE* observation is dominated by the soft apex state (i.e. the apex between the FB and the NB), with short periods in the FB.

4.10.2 Polarimetric Analysis

The Stokes parameters of Sco X-1 observed by *IXPE* in the 3–8 keV, 3–4 keV and 4–8 keV energy bands obtained with *IXPEOBSSIM* are shown in Figure 4.44 for each DU. As reported in the *IXPEOBSSIM*⁸ notes and in [Veledina et al. \(2023\)](#), the polarization obtained with the PCUBE algorithm does not properly account for the telescope response matrices at low energy, when using the gray filter. In particular, an overestimate of

⁸<https://github.com/lucabaldini/ixpeobssim/issues/714>

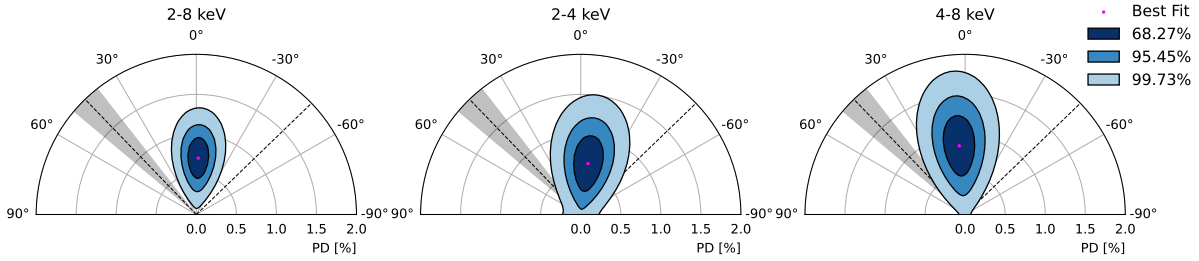


Figure 4.45: Polarization contours for Sco X-1 in the 2–8 keV, 2–4 keV and 4–8 keV energy bands obtained with `xSPEC` by summing the events of the three DUs. Contours correspond to the 68.27%, 95.45% and 99.73% confidence levels derived using a χ^2 with two degrees of freedom. The grey region corresponds to the observed radio jet position angle, consistent with the PA direction observed by *PolarLight* (Long et al., 2022).

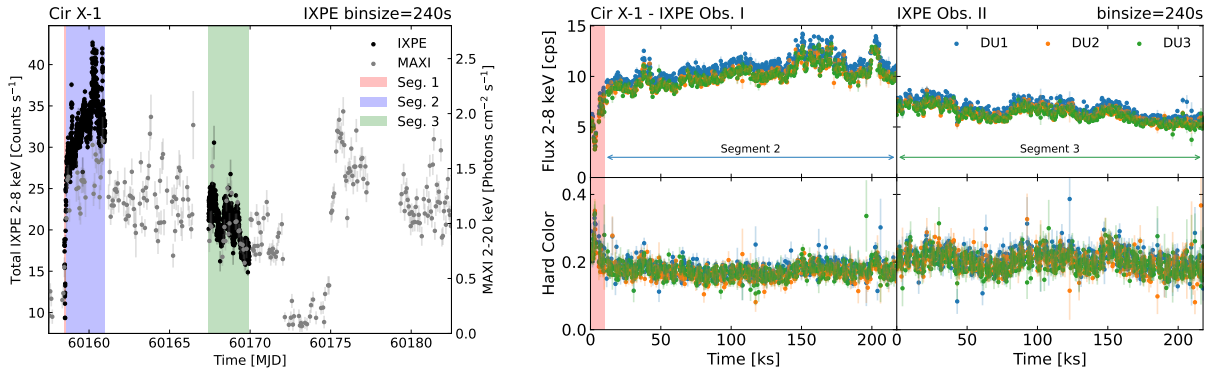


Figure 4.46: *Left panel*: Cir X-1 total *IXPE* and *MAXI* 2–20 keV light curve in units of photons $\text{cm}^{-2} \text{s}^{-1}$. Each segment is highlighted with different colors: the red region corresponds to the transition from the low hard state to the high soft state (Segment 1); the blue region corresponds to the highest flux of the source (Segment 2); the green region covers the entire second *IXPE* observation (Segment 3). *Right panel*: Cir X-1 *IXPE* 2–8 keV light curves in units of cps (*top*) and Hard Color (5–8 keV/3–5 keV, *bottom*) as a function of the observational time for each DUs. Each bin corresponds to 240 s.

the polarization below 3 keV is observed with respect to the one obtained by the more solid `xSPEC` (Arnaud, 1996) spectro-polarimetric analysis, which properly considers the response matrices of the instrument at low energy. Therefore, the `IXPEOBSSIM` procedure is applied only in the 3–8 keV band. The Stokes parameters show no evidence of a PD variation with energy or any rotation of the PA. The polarization is significantly detected at $\sim 7\sigma$ confidence level, with $1.1\% \pm 0.2\%$ polarization degree and $10.8^\circ \pm 2.8^\circ$ polarization angle. By separating the flaring activity (grey regions in Figure 4.43) from the non-flaring state, the polarimetric results are compatible within 90% confidence level, although the PD in the flaring state seems to be slightly higher (La Monaca et al., 2024). The results are consistent within the errors with those obtained with `xSPEC` (Figure 4.45).

4.11 Circinus X-1

Cir X-1 is a weakly magnetized NS X-ray binary characterized by an eccentric ($e \sim 0.45$) orbit with ~ 16.5 days period (Kaluzienski et al., 1976; Schulz et al., 2020), during which its flux and spectrum change significantly, in a very different way from any other known NS-LMXB. Cir X-1 has historically been shown to pass through all the different states for both Z- and Atoll-sources (Schulz et al., 2019),

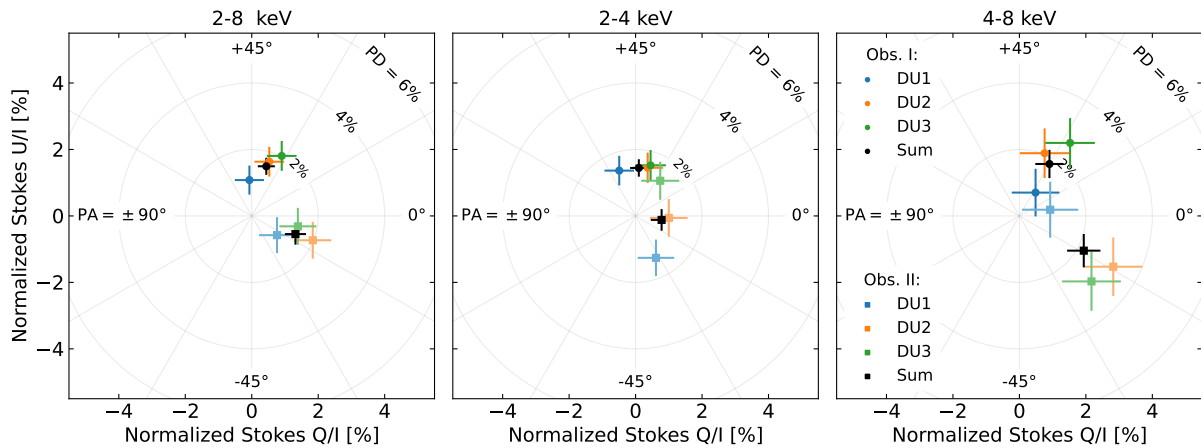


Figure 4.47: Stokes parameters of Cir X–1 in the 2–8 keV, 2–4 keV and 4–8 keV energy bands for DU1 (blue), DU2 (orange), DU3 (green) and by summing all the events of the three DUs (black) for both observations.

similarly to XTE J1701–462 (Homan et al., 2010). Nevertheless, recent studies suggest that Cir X–1 may be a high-mass X-ray binary (with possible Be-star X-ray binary nature; Schulz et al. 2019, 2020), which commonly indicates a young binary system. The discovery of type I X-ray bursts undoubtedly proved that the compact object is a NS (Tennant et al., 1986; Linares et al., 2010). During its orbit, the X-ray flux varies by two orders of magnitude, with more irregular decades-long variation (D’Ài et al., 2012). A dip in the light curve is observed in every orbit, followed by a flaring phase. This dip could be caused by a cold absorber, only if the source is observed at high inclinations (D’Ài et al., 2012). The eccentric orbit causes orbital variations in the mass accretion rate, producing the modulation in the X-ray luminosity (Johnston et al., 1999). An extended emission from a supernova remnant has been found around Cir X–1 (Heinz et al., 2013) with an estimated age of 4600 years, implying that the source is the youngest known NS-XRB. The young age is consistent with both the eccentricity of the orbit and its irregular variations. Another unique characteristic of Cir X–1 is the presence of both radio and – unique case identified so far for NS-XRBs – X-ray jets, indicating the ejection of matter at relativistic speeds. The X-ray jets are clearly visible on both sides of the receding and the approaching radio jet (Heinz et al., 2007; Soleri et al., 2009). The orientation of the radio jets has been reported to change with time either because of the precession of the regions close to the NS from which it is emitted or because of the interaction with interstellar matter (Coriat et al., 2019).

4.11.1 Observations

IXPE observed Cir X–1 in two different pointings (within the same Obs. ID 02002699) to cover two different parts of the orbit, for a total net total exposure time of 263 ks (Rankin et al., 2024). The first segment lasted from 2023 August 02 11:21:55 UT to August 04 23:49:56 UT, while the second observation segment lasted from 2023 August 11 10:15:57 UT to August 13 22:46:56 UT. Science data were extracted following the procedure described in Section 4.2.1 considering a 120'' source extraction radius. Due to the high brightness of the source, the background is negligible (Di Marco et al., 2023b). The *IXPE* light curves in the 2–8 keV energy band and the hard color (5–8 keV/3–5 keV) are reported in Figure 4.46 for each DU, with time bin of 120 s. Both the flux and the hard color vary significantly over time. Based on the hard color, the overall observations are divided into three different segments to study the polarization along the orbit: the first interval corresponds to the transition from the low-flux (hard) state to the high-flux (soft) state, as the source started to come out of the dip; the second interval corresponds to the other part of the first *IXPE* pointing; the third interval covers the entire second *IXPE* observation.

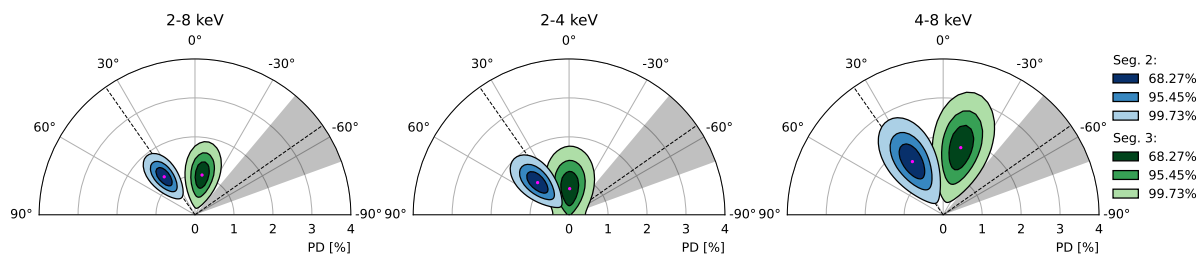


Figure 4.48: Polarization contours for Cir X-1 in the 2–8 keV, 2–4 keV and 4–8 keV energy bands obtained with *xSPEC* for Segment 2 (blue) and Segment 3 (green). Contours correspond to the 68.27%, 95.45% and 99.73% confidence levels derived using a χ^2 with two degrees of freedom. The grey region corresponds to the observed radio jet position angle.

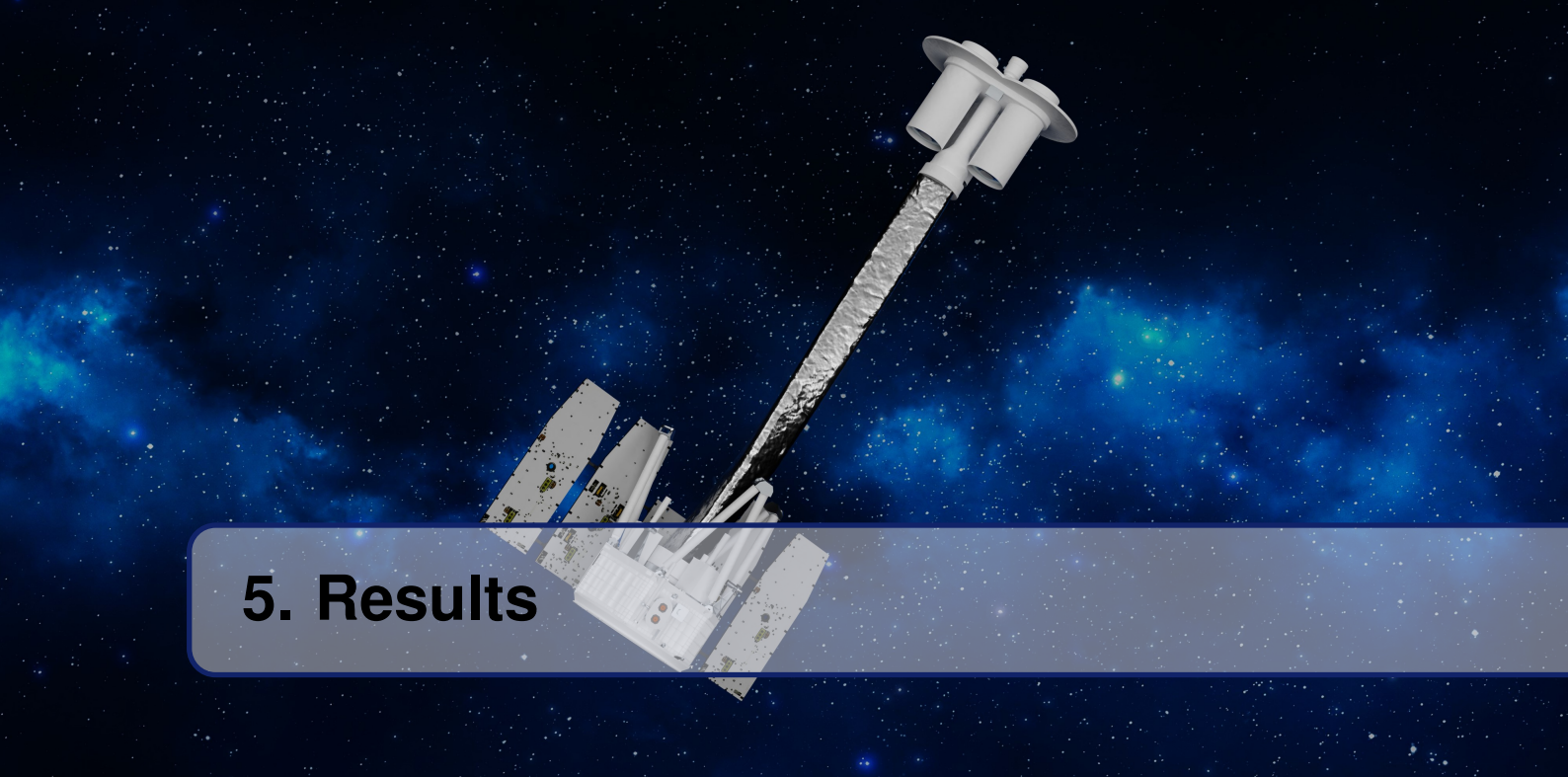
4.11.2 Polarimetric Analysis

The Stokes parameters of Cir X-1 observed by *IXPE* in the 2–8 keV, 2–4 keV and 4–8 keV energy bands obtained with *IXPEOBSIM* are shown in Figure 4.47 for each observation. Due to the low counts and the short exposure of the first interval, the polarization during the transition from the low hard state to the high soft state is unconstrained. Therefore, the first segment is filtered out from the first observation and Figure 4.47 reports only the second and third segments. The polarization in these two intervals is significantly detected at a confidence level higher than 99%, with $1.6\% \pm 0.3\%$ polarization degree and $36.8^\circ \pm 4.5^\circ$ polarization angle in the second segment and $1.4\% \pm 0.3\%$ polarization degree and $-11.3^\circ \pm 2.6^\circ$ polarization angle in the third segment. The polarized signal shows evidence of an increasing trend with energies, up to $1.8\% \pm 0.4\%$ and $2.2\% \pm 0.5\%$ in the high-energy bands for each segment, respectively. The PA exhibits a clear rotation of $\sim 48^\circ \pm 5^\circ$ between the second and third intervals. The results are consistent within the errors with those obtained with *xSPEC* (Figure 4.48).

As the hard color varies during the orbit – even inside each considered segment – the polarization has been studied in different hardness-ratio (HR) states (Rankin et al., 2024):

$$\text{HR}_{\text{IXPE}} = \frac{\text{Counts [4–8 keV]}}{\text{Counts [3–4 keV]}}. \quad (4.7)$$

Given the large uncertainty for each HR value (at a level of ~ 0.05), the average HR in larger time bins (2000 s each) is computed to populate the three HR intervals considered (0.5–0.6, 0.6–0.7 and 0.7–0.8). In the 2–8 keV energy band, the PD is compatible in the three HR intervals, while the PA shows a gradual rotation as the HR changes, with a total rotation by $67^\circ \pm 11^\circ$ between the lowest and the highest HR bins. No evidence for an energy trend at 90% confidence level is observed in any energy band, but there are only hints of an increase of PD with energy.

The image shows the IXPE (Imaging X-ray Polarimetry Explorer) satellite in space. The satellite is white with various instruments and antennas. A prominent feature is a long, silver, cylindrical boom extending from the main body, topped with a complex arrangement of white, cylindrical instruments. The background is a deep blue space filled with stars and nebulae. A semi-transparent blue banner with rounded corners is overlaid on the bottom left of the image, containing the text '5. Results' in white.

5. Results

IXPE has been able to provide for the first time space, energy and time resolved polarimetry of several NS-LMXBs. The spectro-polarimetric analysis has allowed to study and constrain the contribution to the polarization signal of the different spectral components (e.g. the disk emission, the Comptonized radiation and the reflection, if detected). In order to try to understand the nature of the accreting system and the origin of the X-ray polarized radiation, it is necessary to compare the results of the *IXPE* observations with the simulations. *MONK* is able to predict the expected polarization properties of the X-ray radiation coming from the NS-LMXBs, assuming different geometrical configurations for the Comptonizing region.

5.1 Comparison Between Different Geometries

From a theoretical point of view, the total X-ray radiation coming from NS-LMXBs includes the direct blackbody emission of the NS, the direct disk emission modelled with a multicolor blackbody and the Comptonized photons. Comptonized radiation includes both the seed NS and disk photons that are scattered in the hot electron plasma and contributes significantly to the total X-ray polarization in the *IXPE* energy range, along with direct disk radiation (if polarized, see [Chandrasekhar 1960](#)). In Chapter 3, the polarization properties were computed considering the contribution of the NS and disk separately. Maintaining the two components separate is useful for the spectro-polarimetric analysis, as with *XSPEC* the polarization of each spectral component can be decomposed. To find the total X-ray polarization predicted by *MONK*, the Stokes parameters of each component can be summed together. When the contributions of the NS and disk photons are polarized in the same direction, the net polarization can be high. If the two polarization vectors are perpendicular, they partly cancel out and the resulting net polarization will be lower. As for real observations, despite different geometries of the Comptonizing region are considered, the simulated spectra with *MONK* (considering the same set of physical parameters) results to be quite similar to each other. Therefore, X-ray spectroscopy is not able to unambiguously constrain the actual geometrical configuration of the accretion flow surrounding the central NS. However, the X-ray polarization is very sensitive to the choice of the geometry, as scatterings are the main source of the polarized signal.

The main results obtained from *MONK* simulations are reported in Figure 5.1. Different geometries exhibit very different polarimetric properties, both in the PD and PA values and in the behaviour as a function of energy (Figure 5.1, *left panel*). More spherically symmetric configurations (e.g. the spherical

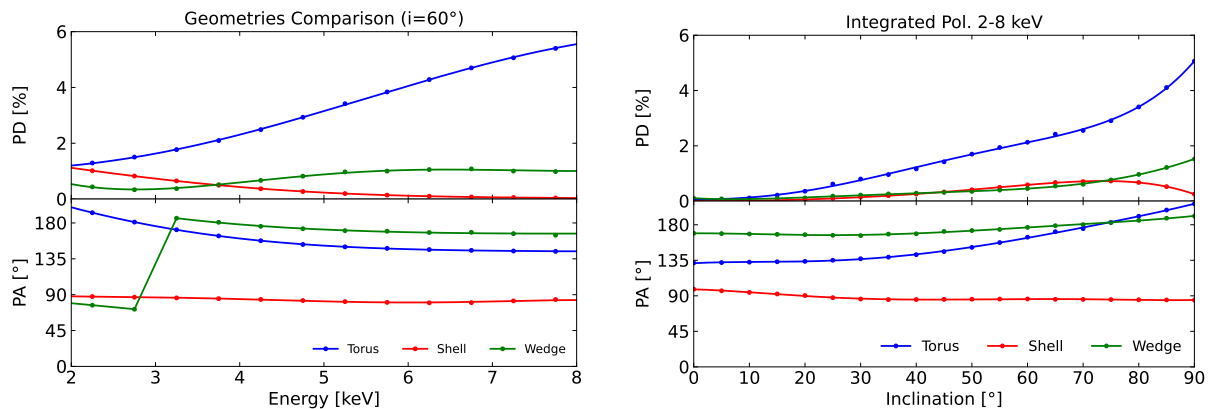


Figure 5.1: Polarization degree and angle as a function of energy for a NS-LMXB in soft state observed at 60° inclination (*left panels*) and integrated in the 2–8 keV band as a function of the system inclination (*right panels*). Different geometries of the hot electron Comptonizing region have been considered: the torus, the spherical shell and the wedge configurations. The PA in `MONK` is measured from the projection of the rotation axis onto the sky plane.

shell, the wedge and the spreading-layer like geometries) result in quite low PD in the 2–8 keV energy range (see also [Gnarini et al. 2022](#); [Ursini et al. 2023a](#)). Despite the fact that these geometries have similar integrated PD values, the behaviour of the polarization is different: the spherical shell is characterized by a PD decreasing with energy, since the main source of polarization is due to the direct disk emission (if polarized; [Chandrasekhar 1960](#)) which dominates at lower energies and is depolarized by the Comptonized radiation, which is almost unpolarized and contributes significantly at higher energies. For the wedge, the Comptonized photons have a non-zero PD; therefore, at lower energies, the disk and NS polarization largely cancel out because they are polarized in orthogonal directions and the total PD is very low. As the energy increases, the disk contribution drops and the polarized signal is related almost only to the NS scattered photons. These behaviours also impact on the PA value: for the shell, the only polarized component is the disk emission and therefore the PA is always parallel to the disk plane. Instead, a 90° rotation is found for the wedge configuration: at lower energies, the PA is parallel to the disk where the direct disk photons dominate the NS-LMXB emission, while at higher energies, the dominant scattered NS photons are polarized orthogonally to the disk, as the wedge corona is (at the zero-order approximation) perpendicular to the accretion disk plane. The torus and thick slab configurations are characterized by higher polarization. In Figure 5.1, only the toroidal configuration is shown, but the thick slab exhibits almost identical polarization, as expected since they are built to be as similar as possible.

The scattered NS photons dominate the polarized signal, with an increasing trend of the PD with energy from $\approx 2\%$ to $\approx 5 - 6\%$. The total PA is almost orthogonal to the accretion disk and exhibits a rotation of $\approx 20^\circ - 30^\circ$ as the energy increases, as a consequence of the Special and General relativistic effects. The disk contribution is significant only in the low-energy part and it lowers the total polarization as the disk photons are polarized perpendicularly to the Comptonized radiation.

The inclination angle between the line of sight of a distant observer and the normal to the plane of the accretion disk plays an important role in the expected X-ray polarization signal (Figure 5.1, *right panel*). A system observed more edge-on (high inclination) presents a different behaviour compared to one observed more face-on (low inclination). In particular, at high inclinations, various effects can significantly alter the expected polarization, besides a higher level of asymmetry: the combination of the strong gravitational field of the NS and the velocity of the electron plasma changes with the viewing inclination, modifying the properties of the emitted photons; moreover, in high-inclined systems the X-ray photons have to pass through a larger column of material in the disk and in the hot electron corona, leading to a larger number of scatterings. The different geometries of the Comptonizing region result in different

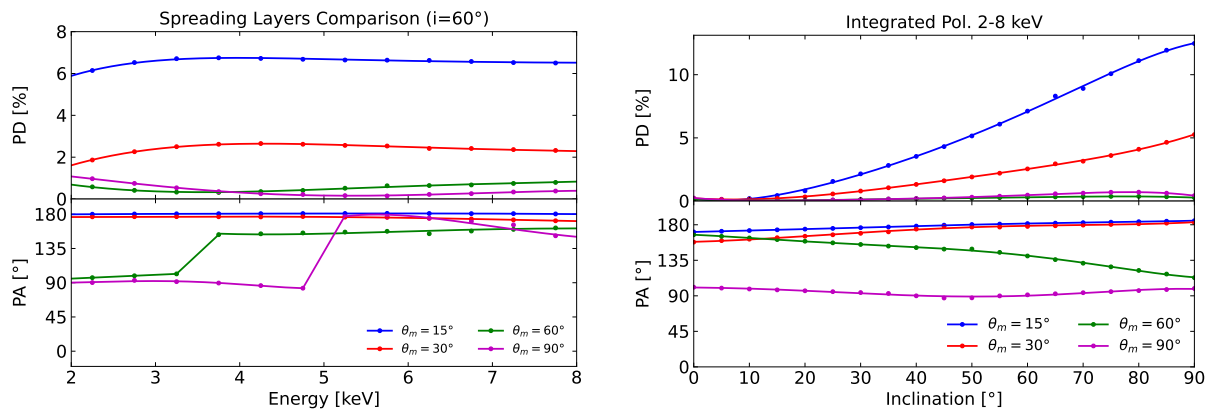


Figure 5.2: Polarization degree and angle as a function of energy for a NS-LMXB in soft state observed at 60° inclination (*left panels*) and integrated in the 2–8 keV band as a function of the system inclination (*right panels*). Different spreading layer-like geometries of the hot electron Comptonizing region have been considered: the maximum opening angle θ_m varies from 15° to 90° as the accretion rate increases, while the inner edge of the disk moves closer to the NS surface. The PA in MONK is measured from the projection of the rotation axis onto the sky plane.

integrated PD and PA in the *IXPE* 2–8 keV energy band: the torus and thick slab configuration exhibit higher polarization with a PA misaligned with respect to both the accretion disk plane and the symmetry axis and tend to rotate toward the normal to the accretion disk as the inclination increases. The wedge and spherical shell geometries produce low polarization in the 2–8 keV range but with orthogonal PA: for the shell, the polarization vector is always along the accretion disk plane (as the disk photons are the only contribution to the polarized signal), while for the wedge the PA is almost perpendicular to the disk as the Comptonizing region is (at the zero order approximation) orthogonal to the accretion plane.

As described in Section 3.7, the radial and latitudinal extensions of the boundary/spreading layer can vary according to the spectral state of the NS-LMXBs, in particular depending on the accretion rate. In order to try to estimate how the polarimetric properties change considering different boundary/spreading layer-like configurations, some numerical simulations are performed with MONK with different radial extension, maximum opening angle θ_m and accretion rates. In particular, the maximum latitudinal extension is assumed to vary from $\theta_m = 15^\circ$ to $\theta_m = 90^\circ$ as the accretion rate increases from $\approx 20\% \dot{M}_{\text{Edd}}$ to $\approx \dot{M}_{\text{Edd}}$. As a consequence, the inner edge of the accretion disk shifts closer to the NS surface as the accretion rate increases. The PD and PA obtained for these configurations are shown in Figure 5.2, as a function of energy and viewing inclination. It can be easily noted how more radially extended boundary layer-like configurations ($\theta_m \lesssim 30^\circ - 35^\circ$) are able to produce a higher PD, almost exactly perpendicular to the accretion disk plane. For these geometries, the disk photons do not contribute significantly to the polarized signal in the 2–8 keV range, as the direct disk emission dominates at lower energies, since its temperature is colder, being truncated further from the NS surface. The high polarization is therefore related mainly to the scattered NS photons, in particular those emitted from the uncovered region of the NS surface and “bouncing” off the boundary layer towards the observer (as a sort of reflection). As the maximum opening angle and the accretion rate increase, the fraction of these photons decreases, producing lower polarization. Moreover, also the PA dependence on energy changes significantly with the maximum latitudinal extension of the spreading layer and with the accretion rate: for higher accretion rates, the direct disk contribution in the 2–8 keV band becomes more important and the polarization vector is therefore aligned with the accretion disk at lower energies and rotates by $\sim 90^\circ$ when the scattered NS photons dominate the emitted flux. For all these kinds of geometries, the scattered NS photons result to be polarized orthogonally to the meridian plane: for high maximum opening angles, the PA is perpendicular to the disk plane, as the Comptonizing region is roughly orthogonal to the disk; for small latitudinal

extension, the majority of the scattered NS are originated in the upper part of the NS surface (uncovered by the Comptonizing region) and hit the hot plasma from above, producing again a PA orthogonal to the disk. The behaviour of the PD and PA with the viewing inclination is consistent with previous results obtained for other geometries: the higher the inclination of the system, the higher the expected PD of the X-ray radiation. The PA remains quite constant with the inclination for each configuration: for small maximum opening angle, the PA is perpendicular to the meridian plane as the scattered NS photons are the main contribution to the polarized signal in the 2–8 keV; when θ_m is close to 90° (i.e. the spreading layer covers almost the entire NS surface), the polarized signal is mainly related to the direct accretion disk emission and therefore is directed along the disk plane. The only exception seems to be the spreading layer with $\theta_m = 60^\circ$, for which the PA rotates from being almost orthogonal to the accretion disk when the system is face-on up to the meridian plane direction. This rotation is due to the combination of Special and General relativistic effects.

Up to now, the disk atmosphere has been modelled as a semi-infinite, plane-parallel, pure scattering atmosphere (Chandrasekhar, 1960), with PA perpendicular to the meridian plane and PD increasing monotonically with the polar emission angle. The disk emission can also be assumed to be isotropic in the local frame, with unpolarized seed photons (in case absorption/emission effects are important). By considering unpolarized disk photons, the expected PD can vary: significant differences arise in the low-energy part of the spectra, as the direct disk emission is the most important contribution. The resulting PD at lower energies is therefore lower by assuming an isotropic and unpolarized disk emission. For the spherical shell case (or for any quasi-spherically symmetric configuration), the direct disk radiation is the main (or the only) contribution to the polarized signal. Therefore, the expected polarization significantly depends on the assumption of initial polarization of the disk photons: if they are unpolarized, the resulting PD will be lower and almost zero (Gnarini et al., 2022).

5.2 Comparison Between Observations

The first two years of *IXPE* observations revealed a scenario more complex than expected. The hard X-ray emission is believed to originate in the boundary or spreading layer around the NS, with the addition of direct disk photons. For a spreading/boundary layer-like geometry, the predicted polarization is quite low, i.e. $< 2\%$. *IXPE* measured an average PD that can reach $\approx 3 - 4\%$ in some Atoll- and Z-sources (Cocchi et al., 2023; Ursini et al., 2023a; Fabiani et al., 2024) and up to $\approx 9 - 10\%$ in 4U 1820–303 in the 7–8 keV energy band (Di Marco et al., 2023a). The Comptonized emission cannot reproduce this highly polarized signal alone, unless some peculiar geometries are considered (e.g. torus; see Sections 3.5 and 5.1). In most of the sources, reflection features are detected. Photons emitted from the spreading layer or from the NS surface can be reflected by the ionized surface of the accretion disk. These reflected photons are highly polarized, up to $\approx 20\%$ (Matt, 1993; Poutanen et al., 1996b; Schnittman and Krolik, 2009). Although the contribution of the reflection to the total flux in the *IXPE* energy band is quite low, these highly polarized photons can contribute significantly to the observed polarization signal.

5.2.1 Atoll-Sources

In Atoll-sources the overall polarization seems to be generally rather weak (less than $1.5 - 2\%$ in the total 2–8 keV energy range) but with a strong energy dependence (see Table 5.1). The first Atoll observed was GS 1826–238 and only a 3σ upper limit of 1.3% was obtained (Capitanio et al., 2023). No reflection features were detected. In the *IXPE* energy range, the disk and the Comptonized radiation contribute almost half of the photon flux each. As the PAs of these two components are expected to be orientated differently, the low-polarized signal can be explained if the two orthogonal contributions have a similar PD. In order to put constraints on the geometry of the accreting system, the *IXPE* polarimetric results can be directly compared with specific MONK simulations using as input parameters the best-fit spectral parameters reported in Table 4.2. Three main configurations were tested to probe the geometry of the

Source	PD(2–4 keV)	PD(4–8 keV)	PD(2–8 keV)
GS 1826–238	< 1.1%	< 1.6%	< 1.1%
GX 9+9	0.8% ± 0.6%	3.1% ± 1.2%	1.6% ± 0.6%
4U 1820–303*	< 1.2%	2.9% ± 0.9%	< 1.1%
4U 1624–49	< 2.5%	4.3% ± 1.6%	3.5% ± 1.2%

* PD(7–8 keV) = 9.6% ± 3.9%.

Notes: The errors are at the 90% confidence level.

Table 5.1: Polarization degree of the Atoll sources observed by *IXPE* during the first two years of observation computed with the model-independent procedure using *IXPEOBSIM* (Baldini et al., 2022).

Comptonizing region:

1. Thick slab (pseudo-toroidal) geometry (Gnarini et al., 2022): a rectangular section torus with similar vertical and horizontal length scales ($2H \sim \Delta R$) corotating with the Keplerian disk. The slab covers only a part of the accretion disk, starting from the inner disk and extending for $\sim 10 R_G$.
2. Spherical shell geometry (Gnarini et al., 2022): a stationary spherical shell surrounding the NS (similar to a spreading layer that extends over the entire surface of the NS). The shell has a thickness of $\sim 2 R_G$. If the radius of the shell is different, the symmetry of the system does not change; consequently, the polarization remains substantially unchanged.
3. Wedge geometry (Capitanio et al., 2023; Ursini et al., 2023a): a spherical shell without polar caps, lying between the NS surface and the disk (roughly mimicking the spreading layer; Popham and Sunyaev 2001). The wedge extends for $\sim 2 R_G$ and rotates with Keplerian velocity.

The net polarization integrated in three different *IXPE* energy bands as a function of the inclination angle is shown in Figure 5.3 for the three configurations of the Comptonizing region. The grey region represents the *IXPE* 3σ upper limit for each energy band. The dotted region corresponds to the inclination values previously derived (Mescheryakov et al., 2011; Johnston et al., 2020). Taking into account this range of inclination, the spherical shell and the wedge geometry are consistent with the upper limit obtained by *IXPE* in each energy band, while the thick slab shows higher PD (Capitanio et al., 2023). Therefore, either GS 1826–238 could have a (quasi) spherical symmetry or its inclination is lower than previously measured. In fact, as a general rule, the polarization fraction decreases with decreasing inclination angle (being null, for symmetry reasons, for a perfectly face-on system; Schnittman and Krolik 2009; Gnarini et al. 2022).

GX 9+9, the second observed Atoll source, shows a polarization of $1.6\% \pm 0.6\%$ in the 2–8 keV band, with an indication of an increasing trend with energy (Ursini et al., 2023a). In this source, a reflection component is detected and the observed polarization can be explained by a combination of Comptonization in a spreading layer plus reflection. Only an upper limit of $\approx 3\%$ can be obtained for the disk polarization, which is consistent with the classical results for a semi-infinite, plane-parallel atmosphere (Chandrasekhar, 1960) but did not allow to ultimately derive tight constraints about the properties of the scattering atmosphere above the disk where the quasi-thermal spectrum is emitted (Shakura and Sunyaev, 1973; Page and Thorne, 1974). Nevertheless, the marginal evidence of a disk PA almost perpendicular to the reflection component could be indicative of the presence of a scattering medium with $\tau \gtrsim 2$ anyway (Sunyaev and Titarchuk, 1985). On the other hand, the polarimetric data are consistent with the Comptonized component being significantly polarized, up to 3–4% depending on the assumptions. As the PD depends on both the shape of the Comptonizing region and on the inclination of the source to the line of sight, the measured polarization can constrain the possible geometries. For GX 9+9, the inclination of the source is known to be less than 70° (Schaefer, 1990; Savolainen et al., 2009). The *relxillNS* model provides values in the range $i \approx 20^\circ - 45^\circ$, consistent with the value

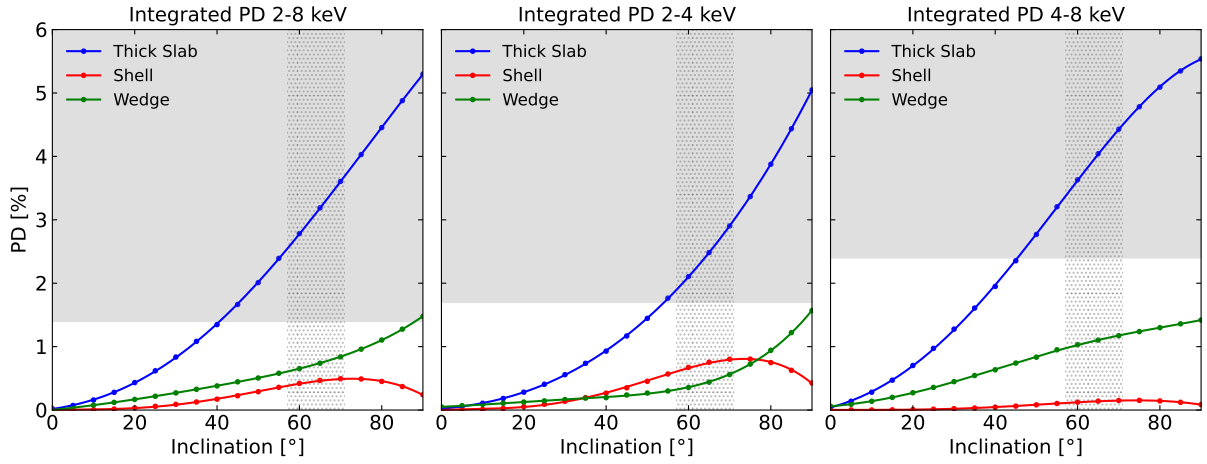


Figure 5.3: *MONK* simulations of the PD for GS 1826–238 integrated over different energy ranges: 2–8 keV (*left panel*), 2–4 keV (*middle panel*) and 4–8 keV (*right panel*) as a function of the inclination angle (Capitanio et al., 2023). The upper grey regions represent the values of the PD excluded by *IXPE* observations (at 99% confidence level), while the vertical dotted regions represent the interval of i found by the previously indirect measurements (Mescheryakov et al., 2011; Johnston et al., 2020).

$i = 40^\circ$ reported by (Iaria et al., 2020). The observed PA of GX 9+9 can not be compared with theoretical expectations, as the orientation of the system is unknown. The *IXPE* results are therefore compared with specific *MONK* simulations using as input parameters the best-fit spectral parameters reported in Table 4.4. As the spectra are well described by a combination of the disk direct emission and the Comptonized radiation coming from the spreading layer, the main configurations of the Comptonizing regions assumed are:

1. Wedge geometry (Ursini et al., 2023a): a spherical shell without polar caps that radially extends from the NS surface up to the inner edge of the accretion disk and it covers the NS up to a latitude of 30° .
2. Spreading layer (Ursini et al., 2023a): the spreading layer configuration is an elliptical shell characterized by a semi-major axis that coincides with the inner disk radius, starting from the NS surface. The shell extends up to 30° latitude and rotates with Keplerian velocity.
3. Torus geometry (Gnarini et al., 2022; Ursini et al., 2023a): the torus has a minor diameter of 10 gravitational radii and covers part of the accretion disk starting from the inner edge. It physically represents a puffed-up inner region of the disk and corotates with the underlying accretion disk.

MONK results are shown in Figure 5.4. The spreading layer-like geometries are characterized by lower polarization in the 2–8 keV band (roughly 1 – 2% for $i = 40^\circ$) than for the torus configuration ($\approx 3 - 4\%$ for $i = 40^\circ$). The PA is approximately 180° for all the three geometries, which corresponds to the polarization being perpendicular to the accretion disk plane and parallel to the symmetry axis. The torus geometry seems to produce a polarization signal consistent with *IXPE* results at higher energies. However, the spreading layer geometry is more realistic if the accretion flow is assumed to extend down to the NS surface, as expected for a source in the Soft state. For the inferred inclination range, both the torus and spreading layer-like configurations are consistent with the observed PD in the 2–8 keV energy band. The observed polarization likely comes from a combination of different components. For example, a wedge- or spreading layer-like geometry could be consistent with the observed polarization if the contribution of the reflected radiation (which is not included in *MONK*) is also taken into account. A small or null PD of the Comptonized component, which would be expected for (quasi)-spherical symmetric configurations (Gnarini et al., 2022; Ursini et al., 2023a), requires a highly polarized reflection component. However, the presence of a further highly ionized reflection component, whose spectral shape would be almost indistinguishable from the primary continuum, cannot be ruled out. For example, a highly

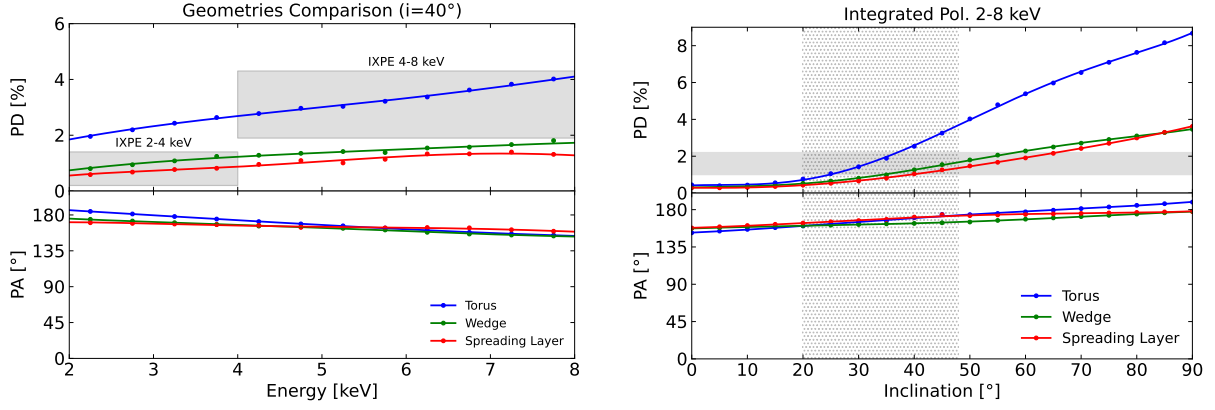


Figure 5.4: MONK simulations of the PD and PA for GX 9+9, as a function of the energy in the 2–8 keV band for 40° inclination (*left panel*; Ursini et al. 2023a) and integrated in the *IXPE* band as a function of the system inclination (*right panel*). The X-ray emission includes the direct NS and accretion disk emission, along with the NS and disk photons scattered in the Comptonizing region. The PA in MONK is measured from the projection of the rotation axis onto the sky plane. The solid grey regions represent the values of the PD obtained by *IXPE*, while the vertical dotted region corresponds to the inferred inclination of the system (Iaria et al., 2020; Ursini et al., 2023a).

ionized disk with $\log \xi = 4$ would produce an essentially featureless reflection component (García et al., 2022). According to the best-fit model, the observed reflection component is not so highly ionized, but the reflecting medium also does not extend down to the ISCO. This leaves open the possibility that part of the reflection is due to a highly ionized innermost region of the disk, extended down to the ISCO. Unfortunately, the present data do not allow to place strong constraints on this component because it is highly degenerate with the primary continuum and with the lower-ionization reflection component, which is – in any case – needed to produce the iron line. If in the best-fit model a further *relxillNS* component with $\log \xi = 4$ and an inner radius equal to the ISCO is included, its contribution to the 2–8 keV photon flux is between zero and 30%. Therefore, the presence of this ionized reflection from the innermost region of the disk cannot be excluded and could significantly contribute to the observed PD.

Reflection is likely to have a significant impact on the polarization signal and can not be included yet in MONK simulations. On the other hand, if the reflection component were the only one to be polarized, it would require a very large PD. The PD of the reflected radiation is not obvious to predict because it depends on the assumed geometry; however, it is not likely to exceed $\approx 20 - 25\%$ (Matt, 1993; Poutanen et al., 1996b; Schnittman and Krolik, 2009). For an accretion disk illuminated by the spreading layer or the full NS surface radiation corresponding to the emission during type I X-ray bursts, the total expected PD of Comptonized plus reflected photons can reach $\approx 5\%$ for the spreading layer over the NS radius-to-height ratio $H/R_{\text{NS}} = 0.1 - 0.2$ (Lapidus and Sunyaev, 1985). As the direct disk emission is not included in Lapidus and Sunyaev (1985) calculation, it can be included with a simple Stokes vectorial analysis. Two polarization pseudo-vectors (here in the form of normalized Stokes parameters) are defined for the spreading layer+reflection and direct disk components:

$$\begin{aligned} q_i &= P_i f_i \cos 2\Psi_i \\ u_i &= P_i f_i \sin 2\Psi_i \end{aligned} \quad (5.1)$$

where P_i and Ψ_i are the PD and PA of the different components, respectively, while f_i is their relative contribution to the total photon flux. Using the values for f_i found for the best-fit model and assuming $P_d = 1\%$, $\Psi_d = 90^\circ$ for the disk (i.e. parallel to the disk plane; see Farinelli et al. 2023) and $P_{c+r} = 5\%$, $\Psi_{c+r} = 0^\circ$ for the spreading layer+reflection, the total polarization is $\text{PD}_{\text{tot}} = (q_{\text{tot}}^2 + u_{\text{tot}}^2)^{1/2} = 1.9\%$ and $\text{PA}_{\text{tot}} = 0^\circ$, compatible with the results obtained with *IXPEOBSSIM* and *XSPEC*. The same calculation in the 2–4 keV and 4–8 keV energy bands yields $\text{PD}_{\text{tot}} = 1.0\%$ and $\text{PD}_{\text{tot}} = 3.7\%$, respectively. To produce

the net total PD, the disk PD can be quite low, which is well consistent with the observed upper limit of 3%. The energy-dependent PD value can be naturally explained by considering that the disk photon flux in the 2–4 keV energy range is about five times higher than that in the 4–8 keV interval, and thus the effect of polarization cancellation by two components polarized at about right angles is less at higher energies. This analysis shows that the accretion geometry of GX 9+9 is consistent with a spreading layer illuminating the ionized surface of the accretion disk, producing polarized reflection as well as the (unpolarized) fluorescent iron line.

The results for 4U 1624–49 are quite similar in many aspects to that of GX 9+9, as it should be expected since the sources are both bright Atolls that remain in the banana state (Lommen et al., 2005). However, the observed polarization of 4U 1624–49 is significantly higher than GX 9+9. This difference can be explained by the different inclinations of the system: while GX 9+9 is observed at $i \approx 20^\circ - 45^\circ$, 4U 1624–49 is observed at higher inclinations ($\gtrsim 60^\circ$; Frank et al. 1987). Differently from GX 9+9, the polarization of the disk component seems to be much higher ($\sim 10\%$) compared to the classical Chandrasekhar result for an inclination of $\approx 70^\circ$ (3.5 – 4%; Chandrasekhar 1960) for all the different scenarios. The reason why such a high value of the PD is needed is that the contribution of disk photons in the 2–8 keV is quite low, therefore a large polarization is required to obtain the measured 3.5%, as the disk emission will be depolarized by the other two (orthogonally polarized) components. Moreover, the disk polarization is very poorly constrained due to its relatively small contribution to the total flux in the 2–8 keV band and the classical Chandrasekhar results are still consistent within error with the observed polarization. There is also marginal evidence for an increase with energy of the PD, as also observed in GX 9+9 and other NS-LMXBs. Therefore, the disk photons cannot be the main contribution to the polarized signal, as the increasing trend with energy is not compatible with this assumption. There is no evidence of rotation of the PA with energy. The Comptonized component results to be polarized up to 3 – 4%, depending on the assumptions. Even though the 4U 1624–49 is observed at high inclination, considering a spreading layer-like or wedge geometry, the expected polarization will be lower than the observed one. However, reflected photons are highly polarized and can contribute significantly to the polarized signal even if their fraction to the total flux is not high. The observed polarization can come from a combination of different components. A spreading layer-like geometry can reproduce the observed polarization if the contribution of reflection is also considered. By assuming a spreading layer with $P_{\text{SL}} = 1\%$, $\Psi_{\text{SL}} = 0^\circ$ (Section 3.6 and 3.7), the direct disk contribution with $P_{\text{disk}} = 2\%$, $\Psi_{\text{disk}} = 90^\circ$, consistent with the classical result for $i \approx 60^\circ$ (Chandrasekhar, 1960), the reflection with $P_{\text{refl}} = 10\%$, $\Psi_{\text{refl}} = 0^\circ$ (Matt, 1993) and considering the values for f_i reported in Table 4.9, the total expected PD is consistent with the results obtained with IXPEOBSSIM and XSPEC and from the spectro-polarimetric analysis. Therefore, the accretion geometry of 4U 1624–49 seems to be consistent with a spreading layer that illuminated the surface of the accretion disk, reflecting photons (and producing the fluorescent iron line) which contribute significantly to the polarized signal.

IXPE results on the X-ray polarization of 4U 1820–303 show a different behaviour with respect to the other Atolls and Z-sources. In particular, although only an upper limit of $< 1.1\%$ is obtained for the average PD in the 2–8 keV band, the polarimetric results show a strong increase in the polarization with energy, up to 9.6% in the 7–8 keV energy band (Di Marco et al., 2023a). At lower energies, no significant polarization is detected ($PD < 1.2\%$), even if there is a hint of a $\sim 0.5\%$ PD at 96% confidence level, with a PA orthogonal to those at higher energies. The rapid increase of the PD appears where in the spectra of 4U 1820–303 the disk contribution drops down to a flux below 10^{-12} erg/s, indicating that the PA of each single component of the spectrum (i.e. disk, Comptonization+reflection) are oriented differently resulting in a decrease in the total PD in the spectral range in which both components are present. Depending on the model, the disk PD ranges between $\approx 2.5 - 4\%$ while Comptonization seems to be low polarized, with no significant detection (always $< 1.5\%$). However, the low polarization can also be produced by two different components polarized (almost) orthogonally, as the disk and the spreading layer photons should be. The disk PD results to be higher compared to the classical result for the inferred inclination

Source	PD(2–4 keV)	PD(4–8 keV)	PD(2–8 keV)
Cyg X–2	1.0% ± 0.4%	2.4% ± 0.8%	1.5% ± 0.4%
XTE J1701–462 (Obs. I)	3.9% ± 0.6%	5.3% ± 1.0%	4.4% ± 0.6%
XTE J1701–462 (Obs. II)	< 1.0%	1.5% ± 0.9%	0.8% ± 0.5%
GX 5–1 (Obs. I)	3.8% ± 0.5%	4.9% ± 0.8%	4.3% ± 0.5%
GX 5–1 (Obs. II)	1.8% ± 0.5%	2.6% ± 0.8%	2.0% ± 0.5%
Cir X–1 (Obs. I)	1.5% ± 0.4%	1.8% ± 0.7%	1.6% ± 0.4%
Cir X–1 (Obs. II)	0.8% ± 0.5%	2.2% ± 0.8%	1.4% ± 0.5%
Sco X–1*	0.9% ± 0.4%	1.2% ± 0.4%	1.1% ± 0.3%

* PD(3–4 keV), PD(4–8 keV), PD(3–8 keV).

Notes: The errors are at the 90% confidence level.

Table 5.2: Polarization degree of the *Z*-sources observed by *IXPE* during the first two years of observation computed with the model-independent procedure using *IXPEOBSSIM* (Baldini et al., 2022).

($\approx 1\%$ for $i \approx 30^\circ - 35^\circ$; Chandrasekhar 1960). As for 4U 1624–49, the inferred PD of the disk is poorly constrained due to its relatively small contribution to the total flux in the 2–8 keV band and the classical Chandrasekhar results are still consistent within error with the observed polarization. The strong increase in the PD is not so easy to achieve. For spreading layer-like geometries, the expected polarization is quite low in the whole *IXPE* band, without strong energy dependence. Therefore, another contribution is required to obtain the high PD observed in the 7–8 keV energy range. As the reflected component is detected in the spectrum, it may contribute significantly to the polarization. However, assuming constant polarization for reflection with $\approx 20 - 30\%$ PD, the high PD value measured in the 7–8 keV bin cannot be achieved considering the relative contribution to the total flux of each spectra component. An alternative (phenomenological) approach is to assume that the PD of the reflected photons is linearly dependent on the energy. Replacing the `polconst` of reflection in the best-fit model with `pollin` (but assuming a constant PA with energy parallel to the PA of Comptonized radiation, i.e. $\psi_{\text{slope}} = 0$ and $\psi_1 = \psi_c$), the fit improves. Depending on the assumption on the polarization of the disk, the PD of reflection can reach $\approx 35 - 45\%$, which is quite high with respect to theoretical expectations (Matt, 1993; Poutanen et al., 1996b).

5.2.2 Z-sources

The *Z*-sources resulted to be the most polarized weakly magnetized NS-LMXBs in the *IXPE* band (Table 5.2). The observed PD seems to be related to the position along the *Z*-track (Cocchi et al., 2023; Fabiani et al., 2024): the X-ray radiation is more polarized along the HB (up to 4–5% for XTE J1701–462 and GX 5–1) and starts decreasing moving towards the NB and FB ($\approx 1 - 2\%$).

Cyg X–2 has been the first *Z*-source observed by *IXPE*, when it moved between the NB and the FB. The most intriguing result is the value of the PA, which is within errors consistent with the direction of the radio-jet, which occurs episodically when the source is in the HB of the *Z*-track (Spencer et al., 2013). The PA obtained from the model-independent analysis performed with *IXPEOBSSIM* (using the `PCUBE` algorithm) is fully consistent within errors with that of the hard (Comptonized) part of the spectrum, as obtained by the two-component fit of the X-ray continuum. The hard component originates in the boundary or spreading layer, covering the NS surface up to some latitude (Inogamov and Sunyaev, 1999; Popham and Sunyaev, 2001; Suleimanov and Poutanen, 2006). To the first approximation, the spreading layer is roughly perpendicular to the disk plane and the PA is expected to be rotated by 90° with respect to that of polarized radiation (if any) emerging from the electron-scattering dominated disk atmosphere

(Chandrasekhar, 1960; Sobolev, 1963). Since the measured PA is consistent with the jet position angle, the possibility that the polarization signal directly comes from the accretion disk or a boundary layer that is coplanar with the disk is excluded. The spectro-polarimetric fit provides only an upper limit of $\approx 3\%$ to the PD value of the disk (and thus is in principle consistent with zero). The opacity in the inner disk is dominated by electron scattering (Shakura and Sunyaev, 1973; Page and Thorne, 1974) and the polarization depends on the inclination of the system and the radial extension of the electron scattering dominated region and the optical depth (Kallman and Bautista, 2001). The classical result (Chandrasekhar, 1960) is valid for initial radiation at the bottom of a scattering medium with $\tau \gg 1$. As shown in (Sunyaev and Titarchuk, 1985), the PD for $\tau \lesssim 2$ can be higher than the corresponding value for the semi-infinite atmosphere with the polarization vector perpendicular to the disk surface. The spectro-polarimetric analysis for Cyg X-2 (see Table 4.11) provides a hint in favour of a disk atmosphere with $\tau > 1$, with PA nearly perpendicular to both the observed radio jet (Spencer et al., 2013) and the PA associated with the Comptonized component. The reflection component can produce a polarized signal with PA aligned to the system symmetry axis and contribute significantly to the polarization even if its fraction to the total flux is small (Iaria et al., 2016; Mondal et al., 2018), as reflected photons are highly polarized. The expected polarization for a geometry where the spreading layer illuminates the accretion disk can reach up to 5 – 6% for X-ray bursters during the phase between bursts (Lapidus and Sunyaev, 1985), not including the direct disk emission which tends to produce a net lower polarization signal. Similarly to previous sources, two polarization pseudo-vectors can be introduced: using the values of the relative photon fluxes to the total flux found for the best-fit model (Table 4.11) and assuming $P_d = 1\%$, $\Psi_d = 90^\circ$ for the disk (i.e. parallel to the disk plane; see Farinelli et al. 2023) and $P_{c+r} = 4.5\%$, $\Psi_{c+r} = 0^\circ$ for the spreading layer+reflection, the total polarization is $PD_{\text{tot}} = 1.6\%$ and $PA_{\text{tot}} = 0$, consistent within errors with the results obtained with *IXPE*BSSIM and *XSPEC*. Therefore, the net total polarized signal is likely a combination of the low-polarized disk direct emission (which is consistent with the observed upper limit), the spreading layer radiation (with typical PD $\approx 1 - 2\%$) and highly polarized photons reflected off the atmosphere above the accretion disk and illuminated by the NS or spreading layer radiation. Both the spreading layer and the reflected emission exhibit PA perpendicular to the accretion disk plane, consistent with the observed PA aligned with the radio-jet.

The results obtained for XTE J1701-462 and GX 5-1 observations are very similar (Cocchi et al., 2023; Fabiani et al., 2024). The multiwavelength observations of both sources allowed to catch them when they were covering most of the Z-track on their CCD/HID (see Sections 4.8 and 4.9). During the first observation of each of them, the sources were on the HB of the Z-track, whereas in the second they moved across to the NB and FB. The measured PD is correlated with the position along the Z-track, being higher in the HB and decreasing by a factor of approximately two in the NB/FB.

From the spectro-polarimetric analysis of XTE J1701-462 *IXPE* data, the disk polarization cannot be well constrained ($< 5 - 6\%$) in both the observations, with a PA misaligned with that of the hard component by $\approx 56^\circ$ in the first and almost perpendicular in the second (at 90% confidence level). Even if in the first observation the two PA appears not to be perpendicular, this cannot be ruled out because of the uncertainty on the polarization of the disk. The polarization of the hard component is significantly higher in the first observation in the HB ($\approx 6 - 7\%$) and drops to $\sim 1\%$ when XTE J1701-462 moves along the NB and FB. This difference could be related to the variation of the fraction of Comptonized photons, which is significantly smaller in the second observation ($f = 0.2$; similarly to GX 5-1, see also Fabiani et al. 2024). Therefore, the blackbody component is not completely Comptonized and this (unpolarized) photons “dilute” the polarization of the Comptonization. Both *IXPE* observations of XTE J1701-462 exhibit a similar trend of the PD with energy: the PD is lower in the low-energy part of the spectrum and increases slightly with energy. This trend of the PD with energy can be explained by the variation of the different contribution of each spectral component. At low energies, where the disk emission contributes significantly to the total photon flux, the polarization results to be lower due to the sum of different polarized components that are orientated differently (i.e. almost orthogonally polarized).

At higher energies, the disk contribution drops and the polarized signal is almost entirely related to the hard component. The average polarization does not show any clear evidence of time variability during each observation and there is no energy dependence for the PA, which is also very similar between the two observations (Cocchi et al., 2023).

The same behaviour is observed in GX 5–1 (Fabiani et al., 2024). The spectro-polarimetric analysis of the *IXPE* data shows that the disk polarization is about 2% in both observations, which is compatible with the classical results of a high optical depth scattering atmosphere at an inclination of 60° (Chandrasekhar, 1960; Sobolev, 1963). The polarization of the Comptonization is well constrained at 3σ confidence level only during the first observation. Both *IXPE* observations show similar behaviour of the PD values: the radiation is less polarized in the 2–4 keV band and increases slightly with energy. The reduction of the PD at lower energies can be explained by the energy dependence of the disk emission: In the low-energy band, the spectrum is dominated by the low-polarized disk emission, whereas at higher energies, the emission of the SL and/or the scattered+reflected component is more visible. Another feature of the observed radiation that needs to be addressed is the variation of the PA with energy (Fabiani et al., 2024). In the spectro-polarimetric analysis, the disk and the Comptonization components show non-orthogonal PAs, differing by $\approx 35^\circ - 50^\circ$ (at 90% confidence level); the variation of the polarization plane of the total emission with energy can be interpreted as the energy-dependent contribution of these two components to the total emission. However, it is well known that both the direct disk and Comptonized emission exhibit the rotation of the polarization plane with energy (Connors and Stark, 1977; Connors et al., 1980; Dovčiak et al., 2008; Loktev et al., 2022; Gnarini et al., 2022). The rotation of the PA with the energy predicted for some configurations of the Comptonizing region, due to special and general relativistic effects, is quite similar to the observed rotation of the PA ($\sim 20 - 30^\circ$). The higher PD value of the hard component cannot be explained by only repeated Compton scattering in high optical depth environment, such as a spreading layer around the NS for which a maximum PD of 1 – 2% is expected (see Sections 3.6 and 3.7; Ursini et al. 2023a). Reflection of soft photons off the disk is probably the most natural way to explain the observed PD of the order 4 – 5% (Lapidus and Sunyaev, 1985). Reflection features have been observed in the XTE J1701–462 spectra (only the iron line is detected in the first observation, since only a short NICER observation was performed simultaneously with *IXPE*). Even if in the GX 5–1 spectra no strong reflection features were observed, the reflection contribution to the spectrum may be low and sometimes embedded in the continuum, but could make a large contribution to the net polarization signal (Schnittman and Krolik, 2009). This may be particularly true if the primary spectrum is not a hard power-law, but a blackbody-like spectrum with a rollover below 30 keV. The presence of a further highly ionized reflection component cannot be completely excluded, as its spectral shape would be very similar to the primary continuum and without particular features (García et al., 2022). Its contribution to the total photon flux in the 2–8 keV band can be $\approx 10 - 20\%$ and can easily account for the net polarization detected.

General Relativistic numerical simulations performed with *MONK* assuming different boundary or spreading layer-like configurations of the hot Comptonizing region have shown a peculiar behaviour of the PD and PA: at lower accretion rates (e.g. along the HB), the boundary layer is expected to extend mainly radially and cover only a small belt around the NS equator (i.e. small maximum opening angle θ_m); when the accretion rate increases (e.g. moving along the NB towards the FB), the spreading layer starts covering most of the NS surface, but with smaller radial extension. In the first case, when the Comptonizing region is a radially extended boundary layer, the expected polarization is significantly higher, as found in the HB for XTE J1701–462 and GX 5–1, and then decreases as the spreading layer extends at high latitudes on the NS surface on the NB or FB. This variation of the radial and latitudinal extension of the boundary/spreading layer seems to be consistent with *IXPE* results, but more detailed simulations specific to each source are necessary. The PA remains quite similar within the two observations, as in both cases the expected PA results to be orthogonal to the accretion disk plane. Although the contribution of reflected photons cannot yet be included in *MONK* simulations (Chapter 3), the fraction of reflected photons to the total flux seems to be quite small for XTE J1701–462 (Section 4.8) while no reflection features are

detected for GX 5–1 at all (Section 4.9).

Another possible mechanism for producing polarization is related to scattering in the wind above the accretion disk: the emission scattered once in a plane (e.g. equatorial wind) can be polarized up to 27% for an inclination $i = 60^\circ$ (Sunyaev and Titarchuk, 1985). This PD is only weakly dependent on the opening angle of the wind. Assuming that $\approx 20\%$ of the source emission is scattered, the observed PD can be achieved. Recently, a similar model was used to explain well the presence of a constant polarized component in the X-ray pulsars RX J9440.9+4431/LS V +44 17 (Doroshenko et al., 2023). Although strong winds are well known to be present in soft state X-ray binaries (Neilsen and Lee, 2009; Ponti et al., 2012, 2014), it should be noted that no wind absorption features were observed in the energy spectra of XTE J1701–462 and GX 5–1, implying that the wind should be completely ionized, if present.

The observations of transient hard tails in the spectra of Z-sources are strictly correlated with HB positions in their CCDs (D’Amico et al., 2001; Di Salvo et al., 2002; Iaria et al., 2004; Farinelli et al., 2005; Paizis et al., 2006) and possibly produced by scattering in a jet-like outflow (Reig and Kylafis, 2016). It is thus tempting to link the HB strong polarimetric signal to the accelerating mechanism (still not fully understood) that produces the jet emission and the possibly jet-related transient hard tails (Reig and Kylafis, 2016). However, the contribution of the hard tail to the flux in the *IXPE* band is not expected to exceed 10% (Paizis et al., 2006) and therefore it is not very likely that this component is responsible for a strong polarized signal, unless the boundary layer photons are single-scattered in the Thomson regime. Furthermore, it is not clear why the PD would then drop at lower energies, unless the hard tail spectrum has a low-energy cut-off around 3–4 keV; however, this can be nevertheless expected because a power-law component without a low-energy cut-off would cause a low-energy fit contamination, which is not observed in the wide band spectra of Z-sources during their transient hard tail spectral phase (Paizis et al., 2006; Farinelli et al., 2009).

Very recently, *IXPE* observed two more Z-sources: Cir X–1 (Rankin et al., 2024) and Sco X–1 (La Monaca et al., 2024). The polarimetric results computed with the model-independent analysis performed with *IXPEOBSSIM* (Baldini et al., 2022) are reported in Table 5.2. Cir X–1 was observed twice during its peculiar eccentric orbit and the measured PD in the 2–8 keV energy band is consistent between the two observations, differently to XTE J1701–462 and GX 5–1, with an hint of an increasing trend with energy. However, differently from previous sources, the PA varies from $\approx 37^\circ$ in the first observation (in the high-flux state, immediately after the flaring state) to $\approx -11^\circ$ in the second observation (when the flux is lower, but not as much as in the low-hard state). This rotation of the PA is consistent within error with that obtained by studying the polarization binned in hardness ratio: between the lowest and highest values of the hardness ratio, the PA rotates by $\approx 67^\circ$ while the PD remains similar (Rankin et al., 2024). The variations along the orbit can be due to the superimposition of two different components contributing in a different way along the phase intervals. The accretion flow (and therefore the hardness ratio) varies significantly along the orbit, with the harder state gradually becoming dominant as the flux decreases after the flaring state at the beginning of the first *IXPE* observation. This is consistent with a model in which the accretion disk changes during the orbit due to its eccentricity (Johnston et al., 1999). In this model, the modulation in the X-ray luminosity is due to orbital variations in the mass accretion rate of the NS. During the periastron passage, the companion star overfills its Roche-lobe and the accretion is perturbed, through both tidal interaction and a sudden surge of material inflow, triggering an X-ray outburst. The variation of the PA can be interpreted as due to two different spectral components: one (i.e. the accretion disk emission) dominating at lower energies and hardness ratio, while the harder one (i.e. Comptonized emission) contributing more significantly at higher energies and hardness ratio. In the intermediate range, the two components are mixed. The PA of the optically thick accretion disk is expected to be along the disk plane (Chandrasekhar, 1960; Sobolev, 1963). Relativistic effects may cause a small decrease (for counterclockwise rotation) of the PA by $\sim 5^\circ - 10^\circ$ (Loktev et al., 2022). The Comptonization component is expected to originate either in the boundary layer (coplanar with the accretion disk) or with the spreading layer surrounding (part of) the NS surface. The PA of the optically thick spreading layer

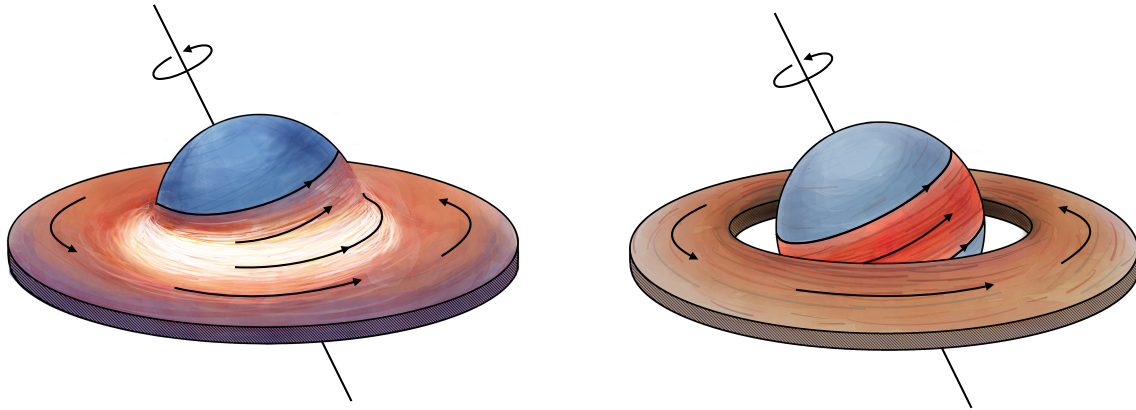


Figure 5.5: Illustration of a possible accretion geometry in Cir X-1. *Left panel:* High accretion-rate case, where the disk touches the NS surface and the boundary layer is emitting (with a polarization almost perpendicular to the symmetry axis of the disk). *Right panel:* Low accretion-rate case, when there is a gap between the disk and the NS surface, and the full spreading layer is developed. (Rankin et al., 2024).

emission is close to the rotation axis (see Sections 3.6 and 3.7). Due to Doppler boosting and General relativistic effects, the emission is expected to be dominated by the part of the spreading layer moving towards the observer, breaking the symmetry of the system and causing a rotation of the PA by $\approx 10^\circ - 20^\circ$ (depending on the parameters). If the spreading layer is optically thin, the polarization may rotate by an additional 90° (Sunyaev and Titarchuk, 1985; Viironen and Poutanen, 2004). Therefore, it is very difficult to explain a rotation in the PA by $50^\circ - 60^\circ$.

The coexistence of two components with such a large difference in the PA may be explained if their symmetry axes are not aligned. This could be related to a misalignment of the NS angular momentum with respect to the orbital axis, causing a shift of the symmetry axis of the Comptonizing region (associated with the spreading layer) with respect to the disk (Abolmasov et al., 2020). Cir X-1 may also not be the only NS-LMXB for which such a misalignment might be present: in XTE J1701-462 and GX 5-1, the PAs of the different components differ by $\approx 40^\circ - 50^\circ$ (Cocchi et al., 2023; Fabiani et al., 2024). X-ray polarimetry also provided evidence of a misalignment in the X-ray pulsar Her X-1 (Doroshenko et al., 2022). Such a misalignment is in fact more likely for Cir X-1 than for other NS-LMXBs, as the system is younger than 4600 years (Heinz et al., 2013): if the newly-formed NS spins out of a plane with respect to the binary system, there was not enough time to come to the alignment of the spinning axes. At the same time, the accretion disk has a lower temperature compared to the Comptonization components (Iaria et al., 2005) and does not contribute significantly in the *IXPE* band. Thus, the only other option for a second component is the boundary layer. At low accretion rates, the disk is truncated at the innermost stable orbit, which is larger than the NS. In this situation, the boundary layer does not form and the matter freefalls on the NS surface, forming the spreading layer. Thus, the PA would correspond to the orientation of the NS rotation axis on the sky (Rankin et al., 2024). At high accretion rates, the thickness of the spreading layer grows, connecting it to the accretion disk through the boundary layer. In this case, the PA would be related to the symmetry axis of the disk (Rankin et al., 2024). As jets are observed both in radio and in X-rays (Fender et al., 1998; Tudose et al., 2008; Sell et al., 2010; Calvelo et al., 2012; Miller-Jones et al., 2012), the PA direction can be directly compared to the orientation of the jet (and of the system). The average jet direction seems to be nearly orthogonal to the direction of the X-ray polarization in the first *IXPE* observation (filtering out the flaring state), which may be related with the radially extended boundary layer emission (with PA aligned with the accretion disk plane; Rankin et al. 2024). However, the X-ray polarization at the highest hardness ratio is neither parallel nor perpendicular to the jet. Associating the observed PA with the spreading layer implies a misalignment of the NS angular momentum from the orbital axis by $\approx 30^\circ$. Because the PA in this case is larger than the jet position angle, the rotation of

the spreading layer (and of the disk) has to be clockwise, corresponding to an inclination exceeding 90° (Rankin et al., 2024).

IXPE observed Sco X–1 mainly in the soft apex state, with short periods in the flaring branch. Only an upper limit of $\approx 3\%$ is obtained for the disk polarization, which did not allow to derive tight constraints on the properties of a scattering atmosphere above the accretion disk (Shakura and Sunyaev, 1973; Page and Thorne, 1974). However, the upper limit is compatible with the classical expectation for an optically thick accretion disk (Chandrasekhar, 1960; Sobolev, 1963), which corresponds to $\approx 1.1\%$ for an inclination of $\approx 44^\circ$ as measured for Sco X–1 (Fomalont et al., 2001a). Although reflection features are observed, the contribution of reflected photons to the total flux in the 2–8 keV band seems to be small. Therefore, even if the reflected photons are highly polarized (Matt, 1993; Poutanen et al., 1996b), the polarization remains quite low ($\approx 1\%$). Considering unpolarized Comptonization component and fixing the PD of the disk to the classical expectation (Chandrasekhar, 1960), the PD of reflected photons is $\approx 14\%$, compatible with the predicted polarization for a Compton-reflected spectrum from cold matter (Matt, 1993; Poutanen et al., 1996b). As Sco X–1 is a bright radio source, where radio-jets are clearly identified (Andrew and Purton, 1968; Bradshaw et al., 1999; Fomalont et al., 2001a), the PA measured by *IXPE* can be compared directly with the direction of the jet, as for Cyg X–2 and Cir X–1 (Farinelli et al., 2023; Rankin et al., 2024). The observed PA, both with the model-independent and the spectro-polarimetric analysis, is not aligned with the direction of the radio-jet. The resulting rotation of the PA with respect to the radio-jet is $\approx 43^\circ$, different from previous observations with OSO-8 and PolarLight (Long et al., 1979; Long et al., 2022). However, none of these X-ray measurements were performed simultaneously with the radio ones. The orientation of the jet in a few sources has been seen to change on short timescales (hours), as in the case of the BH system V404 Cygni (Miller-Jones et al., 2019), probably due to the Lense-Thirring precession of the accretion disk (Stella and Vietri, 1998). Although not yet observed, this can also be expected for NS, and the observed misalignment between the PA measured by *IXPE* and the direction of the radio-jet (Fomalont et al., 2001b) could be consistent with this effect. An alternative scenario that could reproduce the misalignment between the PA and the radio jet direction may be to consider a “tilted” or “warped” accretion disk (Fragile et al., 2001; Krawczynski et al., 2022). If an accretion disk is tilted with respect to a compact rotating object, it will be subject to Lense-Thirring precession (Lense and Thirring, 1918), i.e. local inertial frames are dragged to the rotation of the spacetime. The relativistic Lense-Thirring effect can cause important variation in the geometrically thin accretion disk structure around a spinning Kerr BH, if the disk is not in the equatorial plane with respect to the central object spin axis. In particular, this effect causes a gradual transition of the inner part of such a tilted disk into the equatorial plane of the central object (Bardeen-Petterson effect; Bardeen and Petterson 1975). According to the Bardeen-Petterson effect, the competition between the Lense-Thirring effect and viscous forces divide the accretion disk into three regions: the outer region which remains tilted with respect to the BH/NS spin, the inner part which becomes aligned with the BH/NS spin due to a strong Lense-Thirring effect and a twisted transition region between the above two regions, called “warp” (Fragile et al., 2001). The presence of a tilted region may cause an additional rotation beyond that due to the effects of SR and GR. More detailed analysis, supported also by numerical simulations applied to the NS case (see Abarr and Krawczynski 2020 for numerical simulation for the BH case), are required to test this scenario with Sco X–1 data.

Compared to other previous Z-sources, Sco X–1 was mainly observed in the soft apex state, where the flux is lower (corresponding to the low-flux state in PolarLight results; Long et al. 2022). Other Z-sources exhibit higher polarization when moving along the HB (Cocchi et al., 2023; Fabiani et al., 2024), while the signal is less polarised along the NB and the FB (and thus passing through the soft apex state).



6. Conclusions

Weakly magnetized NS-LMXBs are very bright X-ray sources, ideal for spectro-polarimetric observation in order to study the accreting and radiation processes in the strong gravity regime. According to the pattern they trace in the CCDs/HIDs (Hasinger and van der Klis, 1989; van der Klis, 1989), they are traditionally divided into Atoll- and Z-sources. Atolls are typically less luminous and exhibit lower magnetic fields compared with Z-sources. Moreover, their motion along the CCD is generally slower than the Z-sources, which can trace the three branches of the Z-track in a few days (Hasinger and van der Klis, 1989; van der Klis, 2006; Migliari and Fender, 2006). The X-ray spectrum of weakly magnetized NS-LMXBs is generally well described by a soft thermal component plus a hard Comptonization component, but their physical origin is still uncertain. The soft component could be due either to the accretion disk or to the NS emission, while the hard component could originate in the hot electron plasma corona, in a boundary or spreading layer between the inner edge of the accretion disk and the NS surface (Lapidus and Sunyaev, 1985; Inogamov and Sunyaev, 1999; Popham and Sunyaev, 2001).

With the successful launch of *IXPE* (Weisskopf et al., 2016, 2022) two years ago, a new window has opened for X-ray Astronomy. *IXPE* has been able to provide for the first time space, energy and time resolved spectro-polarimetry for all major kinds of X-ray galactic and extragalactic sources. Being very bright X-ray sources, NS-LMXBs have been perfect targets for polarimetric observations. X-ray polarimetry is the key to understanding the exact nature and physical properties of the X-ray emission of NS-LMXBs. In particular, different geometries of the hot Comptonizing region exhibit significantly different polarization properties (Gnarini et al., 2022): more spherically symmetric configurations (e.g. the spherical shell or the spreading layer geometries) are characterized by lower polarization, differently from the slab-like or toroidal configurations which show very high polarized signal. The polarization angle also depends on the geometry: when the main contribution to the polarized emission is due to the accretion disk, the polarization will be along the meridian plane; otherwise, the expected polarization is generally orthogonal to the accretion disk plane.

Several Atolls and Z-sources were observed by *IXPE* during the first two-year observational campaign. In Atoll-sources (namely GS 1826–238, GX 9+9, 4U 1820–303 and 4U 1624–49), the polarization observed by *IXPE* is generally rather weak ($\lesssim 1 - 2\%$ in the 2–8 keV band; Capitanio et al. 2023; Ursini et al. 2023a; Di Marco et al. 2023a). The only exception is 4U 1624–49 for which the observed PD is 3.5% in the 2–8 keV band. The higher PD with respect to other Atolls can be explained as 4U 1624–49 is the only source observed at very high inclination ($\gtrsim 70^\circ$) and therefore the expected polarization is larger. The observed PD is consistent with resulting from a combination of Comptonization in a boundary or

spreading layer, plus reflection off the accretion disk ionized surface. For most Atoll-sources, the PD is found to increase with energy; in particular, a strong energy dependence is observed for 4U 1820–303 with a polarization degree that also reaches 9 – 10% in the 7–8 keV band. Both the very high PD value and the rapid increase are very difficult to explain by Comptonization alone. For spreading layer-like geometries, the expected PD is quite low and even adding extremely highly-polarized reflected photons considering the relative contribution to the total photon flux of the different spectral components, the measured PD for 4U 1820–303 cannot be reached. A particular shape of the Comptonizing region (e.g. torus-like configurations or an outflowing corona) may be able to reproduce the high polarized signal in the 7–8 keV band. The *Z*-sources exhibit a polarization strongly correlated with the position along the *Z*-track in the CCDs/HIDs (Farinelli et al., 2023; Cocchi et al., 2023; Fabiani et al., 2024): on the horizontal branch, the X-ray radiation is more polarized and the PD starts decreasing as the sources move towards the normal and flaring branches. From spectro-polarimetric analysis, as XTE J1701–462 and GX 5–1 moves along the *Z*-tracks in the CCD, the fraction of Comptonized photons reduces significantly from the HB to the NB/FB producing a lower polarization, due to the presence of an unpolarized blackbody component. The spreading layer-like geometries of the Comptonizing region are not able to produce a polarized signal at 4 – 5%, as observed in XTE J1701–462 and GX 5–1 along the HB. Therefore, reflected photons off the accretion disk seem to be the most natural way to explain the high PD detected, without considering peculiar coronal geometries (e.g. a toroidal geometry). Another intriguing possibility can be related to the evolution of the boundary/spreading layer along the *Z*-track: on the HB, the accretion rate is expected to be lower and starts to increase moving along the NB and FB; therefore, at lower accretion rate, the inner accretion disk radius is further from the NS surface and the Comptonizing region will extend more radially than vertically, forming a geometrically thin boundary layer between the NS and the accretion disk; as the accretion rate increases, the disk inner edge shifts closer to the NS, decreasing the radial extension of the Comptonizing region and the spreading layer will cover a larger area of the NS surface (Inogamov and Sunyaev, 1999). These boundary and spreading layer geometries can produce a polarized signal consistent with the *IXPE* observations of *Z*-sources: the higher PD in the HB can be related to the Comptonized emission in a geometrically thin, radially extended boundary layer, while on the NB and FB when the polarization is lower, the polarized emission may be due to a spreading layer that covers most of the NS surface.

6.1 Future Perspectives

The advent of *IXPE* has inaugurated a new era in the study of NS-LMXBs and more in general of compact objects. In particular, the polarimetric properties of several X-ray sources of various types can be measured and studied for the first time. The advanced polarimetric capabilities of *IXPE* offered unprecedented insights into their complex X-ray emission mechanisms. By combining spectral and polarimetric observations, it has been possible to constrain the physical parameters of the system (e.g. the temperature of the NS and the accretion disk or the properties of the hot electron corona) and to estimate for the first time the polarimetric properties of each spectral component. Even if for both Atolls and *Z*-sources the scenario seems to be more complex than expected, *IXPE* has clearly demonstrated how polarimetric studies offer a very powerful tool to understand the nature and the properties of NS-LMXBs. New spectro-polarimetric observations of both Atolls (e.g. Ser X–1, GX 3+1, GX 9+1 and 4U 1735–44) and *Z*-sources (e.g. GX 17+2, GX 340+0 and GX 349+9) are already planned in order to broaden the sample of observed sources and to try to answer some questions left open by previous observations. For Atoll-sources, it will be interesting to understand whether an increase in the polarization with energy is observed for all these kinds of sources, in particular as the very rapid PD spike up to 9–10% detected in 4U 1820–303. For *Z*-sources, the most important thing would be to see if the behavior of the polarization in the different *Z*-branches is the same in all the sources, similar to what happens for the radio emission or the transient hard X-ray tail above 30 keV. Moreover, it would be interesting to verify whether the

sub-class division between Cyg X–2- and Sco X–1-like sources also affects the polarization or if their properties are the same. Up to now, only one Sco X–1-like was observed by *IXPE* (Sco X–1 itself, observed in the soft apex state, i.e. between the NB and FB) with observed polarization consistent with the results for Cyg X–2-like sources in the same position along the *Z*-track. A larger sample of Sco X–1-like sources is needed to study the X-ray polarization of these two sub-classes along the *Z*-track can provide a new insight into this subdivision, which is still not clear.

As numerical simulations of the expected polarimetric properties of the X-ray emission of NS-LMXBs are the key to distinguishing the different geometries of the Comptonizing region, it is important to build more accurate and realistic models of the hot electron corona. The introduction of the wedge and elliptical shell geometries was a step forward in accurate description of the typical spreading layer, which should form as the disk matter accretes onto the NS. However, the electron plasma velocity profile is still not yet consistent with the standard spreading layer models (Inogamov and Sunyaev, 1999; Popham and Sunyaev, 2001). Including the accurate velocity profile as a function of the radial and latitudinal position would be important to compute the expected PD and PA for this class of geometries and see how the polarization varies considering different sets of geometrical and physical parameters as the considered NS-LMXB moves along the CCD (e.g. the boundary layer extending more radially covering a small belt around the NS equator and with lower accretion rate or the spreading layer which covers most of the NS surface and with higher accretion rate). Up to now, *MONK* is not able to deal with reflection, since when a photon hits the accretion disk it is completely absorbed. However, from spectro-polarimetric observations, reflection seems to be an important contribution to the polarized signal, even if its fraction to the total flux in the 2–8 keV may be small as they are highly polarized (Matt, 1993; Poutanen et al., 1996b). It would therefore be essential to introduce reflection into *MONK* simulations to obtain a proper description of the X-ray polarized emission of NS-LMXBs.

A. Polarization Properties of EM Waves

The amount of energy in EM radiation dE , in a specified frequency interval $(\nu, \nu + d\nu)$, which is transported across an element of area $d\Sigma$ and in directions confined to an element of the solid angle $d\Omega$, during an interval of time dt , is described in terms of the *specific intensity* I by

$$dE = I(x, y, z; l, m, n; t; \nu) \cos \theta \, d\nu \, d\Sigma \, d\Omega \, dt, \quad (\text{A.1})$$

where θ is the angle which the direction considered makes with the outward normal to $d\Sigma$, and (x, y, z) and the direction cosines (l, m, n) define the point and the direction to which I refers (Chandrasekhar, 1960). The net flow of energy in all directions, i.e. the *radiation flux* F is defined as

$$F(x, y, z; t; \nu) = \int_{\Omega} I \cos \theta \, d\Omega \quad (\text{A.2})$$

where the integration is over all solid angles.

A.1 Stokes Parameters

Considering a single EM wave travelling with the speed of light c in the z -direction of a Cartesian coordinate system (t, x, y, z) , a simple solution of Maxwell's equation in vacuum ($\rho = 0$ and $J = 0$)

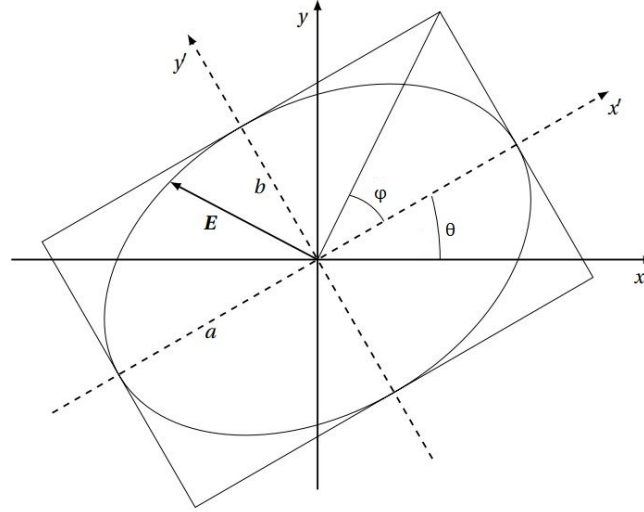
$$\begin{cases} \nabla \cdot \mathbf{E} = 0, & \nabla \times \mathbf{E} = -\frac{1}{c} \frac{\partial \mathbf{B}}{\partial t} \\ \nabla \cdot \mathbf{B} = 0, & \nabla \times \mathbf{B} = \frac{1}{c} \frac{\partial \mathbf{E}}{\partial t}, \end{cases} \quad (\text{A.3})$$

gives two non-trivial components of the electric field vector \mathbf{E}

$$\begin{aligned} E_x(t) &= E_{0,x} \cos(\omega t - \phi_x) \\ E_y(t) &= E_{0,y} \cos(\omega t - \phi_y) \end{aligned} \quad (\text{A.4})$$

where ϕ_x and ϕ_y are the phases. These oscillations combine in such a way that the electric field vector describes an ellipse (Chandrasekhar, 1947; Collett, 1968):

$$\frac{E_x(t)^2}{E_{0,x}^2 \sin^2 \delta} - \frac{2E_x(t)E_y(t) \cos \delta}{E_{0,x}E_{0,y} \sin^2 \delta} - \frac{E_y(t)^2}{E_{0,y}^2 \sin^2 \delta} = 1, \quad (\text{A.5})$$

Figure A.1: Polarization ellipse described by the electric field vector \mathbf{E} .

where $\delta = \phi_y - \phi_x$ is the relative phase between the two components. The \mathbf{E} vector follows an elliptical trajectory in the xy -plane (the *polarisation plane*) depicted in Figure A.1. The special cases of *linear* ($\delta = 0$) and *circular polarization* ($\delta = \pm\pi/2$) correspond to an ellipticity of infinity and unity respectively.

Through the *Stokes parameters* it is possible to give a coherent definition of the polarization properties of an arbitrary beam of radiation and can be defined for light of frequency ν (Stokes, 1852)

$$\begin{aligned}
 I_\nu &\equiv E_{0,x}^2 + E_{0,y}^2 = E_0^2 \\
 Q_\nu &\equiv E_{0,x}^2 - E_{0,y}^2 = E_0^2 \cos 2\psi \cos 2\varphi \\
 U_\nu &\equiv 2E_{0,x}E_{0,y} \cos(\phi_x - \phi_y) = E_0^2 \cos 2\psi \sin 2\varphi \\
 V_\nu &\equiv 2E_{0,x}E_{0,y} \sin(\phi_x - \phi_y) = E_0^2 \sin 2\psi
 \end{aligned} \tag{A.6}$$

where $E_0^2 = E_{0,x}^2 + E_{0,y}^2$. The parameter I_ν represents the total intensity of the EM wave, while U_ν and Q_ν depend on the linear polarization, so they vanish for purely circular polarization. Finally, V_ν is related to circular polarization and becomes null for linear polarization cases. Thanks to additivity, single-photon Stokes parameters can be summed together to obtain the polarization properties of the entire collected radiation.

For individual EM waves the Stokes parameters are related via

$$I^2 = Q^2 + U^2 + V^2 \tag{A.7}$$

reducing the number of free parameters to three, as expected. If we superpose waves with the same polarisation and leave out the unpolarized (randomly polarized) part of a beam, we may rewrite this equation with the total polarized intensity I_P (McMaster, 1954; Chandrasekhar, 1960)

$$I^2 \geq I_P^2 = Q^2 + U^2 + V^2 . \tag{A.8}$$

The Stokes parameters can also be combined into a vector (*Stokes polarization vector*) as

$$\mathbf{S} = \begin{pmatrix} I \\ Q \\ U \\ V \end{pmatrix} = \begin{pmatrix} E_{0,x}^2 + E_{0,y}^2 \\ E_{0,x}^2 - E_{0,y}^2 \\ 2E_{0,x}E_{0,y} \cos(\phi_x - \phi_y) \\ 2E_{0,x}E_{0,y} \sin(\phi_x - \phi_y) \end{pmatrix} \tag{A.9}$$

and it is easy to compute how the Stokes vector varies after a rotation of the (x, y) axes of an angle α (McMaster, 1954)

$$\mathbf{S}' = \begin{pmatrix} I' \\ Q' \\ U' \\ V' \end{pmatrix} = \mathbf{R} \mathbf{S} = \begin{pmatrix} 1 & 0 & 0 & 0 \\ 0 & \cos 2\alpha & \sin 2\alpha & 0 \\ 0 & -\sin 2\alpha & \cos 2\alpha & 0 \\ 0 & 0 & 0 & 1 \end{pmatrix} \begin{pmatrix} I \\ Q \\ U \\ V \end{pmatrix}. \quad (\text{A.10})$$

The polarization properties can also be characterized in terms of the linear polarization degree PD and the polarization angle PA defined as

$$\begin{aligned} \text{PD} &= \frac{\sqrt{Q^2 + U^2}}{I} \\ \text{PA} &= \frac{1}{2} \arctan \frac{U}{Q}. \end{aligned} \quad (\text{A.11})$$

B. X-ray Observatories

Several X-ray facilities performed observations of NS-LMXBs in synergy with IXPE. In particular, timing and spectral information obtained with *NuSTAR*, NICER and *INTEGRAL* are crucial to better understand the polarization properties of the X-ray radiation. The main characteristics and data reduction procedures are described in this Appendix for each of these observatories.

B.1 NuSTAR

The Nuclear Spectroscopic Telescope Array (*NuSTAR*, [Harrison et al. 2013](#)) is a NASA X-ray space telescope operating in the 3–79 keV energy range launched on a Pegasus XL vehicle on 2012 March 21 from Ronald Reagan Ballistic Missile Defense Test Site at Kwajalein Atoll in the Marshall Islands, located in the west central Pacific Ocean.

NuSTAR is equipped with two conical approximation Wolter telescopes with 10.15 m focal length held at the end of a long deployable mast. Each focusing optic consists of 133 concentric shells coated with depth-grated multilayers (alternating atomically thin layers of a high- and low-density material, [Rana et al. 2009](#); [Harrison et al. 2013](#)). To register the image focused by the optics, *NuSTAR* requires high-energy X-ray detectors capable of measuring the position and energy of the incoming X-rays. Each focal-plane detector is manufactured from crystals of cadmium-zinc-telluride ([Rana et al., 2009](#); [Hailey et al., 2010](#); [Kitaguchi et al., 2011](#)), a semiconductor material with the ability to stop high-energy X-rays, surrounded by a caesium iodide anti-coincidence shield.

B.1.1 Data Reduction

All *NuSTAR* unfiltered data were reduced using the latest calibration files (CALDB v.20230718) and the standard `nupipeline` and `nuproducts` tasks of the *NuSTAR* Data Analysis Software (NUSTARDAS v.2.1.2). `nupipeline` is able to calibrate, clean using “good time intervals” (GTIs) and screen for passages through the South Atlantic Anomaly all the data for both Focal Plane Modules (FPMA and FPMB). For bright sources that exceed $100 \text{ counts s}^{-1}$, `statusexpr="(STATUS==b0000xxx00xxxx000) &&(SHIELD==0)"` is included in the `nupipeline` procedure to filter out bad events.

`nuproducts` performed light curves, images and spectra extraction from cleaned event files, covering the full channel and energy range. Analysis of the data from the two similar (but not identical) telescopes is done separately with a joint analysis only at the end during spectral fitting. Source and background

regions were selected from the image of each FPM, using two circular regions sufficiently far from each other. The size of the background region will determine the count rate statistics, but the `nuproducts` `ftool` properly scales the background for the size of the source region via the `backscal` keyword in the source and background spectral files. Spectra are finally rebinned according to the optimal binning scheme by (Kaastra and Bleeker, 2016) using the `ftool` `ftgrouppha`.

B.2 NICER

The Neutron Star Interior Composition ExploreR (NICER, Gendreau et al. 2016) is a NASA telescope on the International Space Station that was launched on 2017 June 3 aboard a SpaceX Falcon 9 rocket. NICER was designed to enable rotation-resolved spectroscopy of the thermal and non-thermal emission of NSs in the soft (0.2–12 keV) X-ray band with unprecedented sensitivity, probing interior structure, the origins of dynamic phenomena, and the mechanisms that underlie the most powerful cosmic particle accelerators known.

At the heart of NICER is the X-ray Timing Instrument (XTI), a co-aligned collection of 56 X-ray concentrator (XRC) optics and associated silicon drift detectors (SDD). Each XRC collects photons over a large ($\sim 50 \text{ cm}^2$) geometric area from a 15 arcmin^2 patch of sky, and focuses them onto a small SDD. The SDDs detect individual X-ray photons, recording their energies and times of arrival to high precision. Together, this assemblage provides a photon counting capability with large effective area, high time resolution, moderate energy resolution, and low background in 0.2–12 keV X-rays. The XRCs “concentrate” X-rays using grazing-incidence reflections. Individual optical elements are truncated conical shells, approximations of ideal mirror figures that are inexpensive to make and provide large throughput. Each XRC consists of 24 nested conical foils, together with a lightweight support structure. X-ray photons can be time-tagged with a precision of less than 300 ns.

B.2.1 Data Reduction

All NICER observations have been reduced and processed using the standard `nicer12` task of the NICER Data Analysis Software (`NICERDAS v.1.1`) in order to apply the recommended calibration processes using the most recent calibration files (`CALDB v.20221001`), as well as standard screening and combining also per-MPU data and filtering. The final spectra and the light curves were then obtained with the `nicer13-spect` and `nicer13-lc` tasks:

- `nicer13-spect` is able to extract the spectrum from cleaned event file and generate a background spectrum using the SCORPEON¹ model. In addition, the redistribution matrix and the effective area for the target are created.
- `nicer13-lc` extracts light curve from the cleaned event file and for the background light curve, automatically normalizing the light curves by the number of enabled and/or selected detectors.

Spectra are finally rebinned according to the optimal binning scheme by (Kaastra and Bleeker, 2016) using the `FTOOL` `ftgrouppha`.

B.3 INTEGRAL

The INTernational Gamma-Ray Astrophysics Laboratory (*INTEGRAL*, Winkler et al. 2003) is an ESA space telescope (with cooperation with NASA and the Russian Space Agency) for observing X-rays and especially gamma rays of energies up to 8 MeV, launched into Earth orbit on 2002 October 17 from the Russian Baikonur spaceport in Kazakhstan. *INTEGRAL* is equipped with two main instruments in the 15 keV to 10 MeV energy range, the SPectrometer aboard *INTEGRAL* (SPI) and the Imager on Board

¹https://heasarc.gsfc.nasa.gov/docs/nicer/analysis_threads/scorpeon-overview/

the *INTEGRAL* Satellite (IBIS, [Ubertini et al. 1999](#); [Lebrun et al. 2003](#)), complemented by two Joint European X-ray Monitors (JEM-X1 and JEM-X2, [Lund et al. \(2003\)](#)) and the Optical Monitoring Camera (OMC).

SPI is ideal for high-resolution spectrometry in the hard X-ray and gamma-ray energy band with a spectral resolution of 3 keV at 1.8 MeV. The main capability of IBIS is imaging in the hard X-ray and gamma-ray energy range, with high angular resolution (12 arcmin FWHM). JEM-X consists of two identical coded-aperture mask telescope, co-aligned with the other *INTEGRAL* instruments. The photon detection system consists of high-pressure imaging Micro-strip Gas Chambers ([Lund et al., 2003](#)). The energy resolution of the JEM-X instruments degraded steadily for the first 10 years of operation, while the temperature sensitivity grew steadily stronger.

B.3.1 Data Reduction

INTEGRAL data were reduced using the latest release of the standard On-line Scientific Analysis (OSA, v.11.2), distributed by the *INTEGRAL* Science Data Centre (ISDC, [Courvoisier et al., 2003](#)) through the multimessenger online data analysis platform (MMODA, [Neronov et al., 2021](#)). The *INTEGRAL* X-ray telescope JEM-X ([Lund et al., 2003](#)) spectra were extracted in the 3–35 keV range with a response matrix with 16 standard channels.

For the imager IBIS ([Ubertini et al., 1999](#)) and the ISGRI detector from 30 to 100 keV ([Lebrun et al., 2003](#)), a mosaicked image of all individuals pointings that constitute the standard dithering strategy of observation has been built for IBIS/ISGRI in the 28–40 keV energy range. These were used to collect the catalogue of detected sources with a S/N larger than 7 and to extract light curves with 1000 s time bins and spectra in 256 standard channels for IBIS/ISGRI, grouped in 10 equally spaced logarithmic channels between 28 and 150 keV. A systematic error of 1.5% was added in quadrature for the spectral analysis for both JEM-X and IBIS/ISGRI data.

C. XSPEC: X-Ray Spectral Fitting Package

All the spectra obtained with the different X-ray observatories are analyzed using the X-ray spectral fitting package XSPEC (v.12.13.0c, [Arnaud 1996](#))¹. XSPEC is an interactive software designed to be detector-independent to use it for any X-ray observatory and included in HEASoft ([Nasa High Energy Astrophysics Science Archive Research Center, 2014](#))².

C.1 Spectral Fitting

The observed spectrum is the photon counts C within specific instrument channels I is related to the actual spectrum of the source $f(E)$ by

$$C(I) = \int f(E)R(I, E)dE \quad (\text{C.1})$$

with $R(I, E)$ the instrumental response, correlated to the probability that an incoming photon of energy E is detected in channel I . In principle, for a given set of $C(I)$, the actual spectrum of the source can be derived by inverting the previous equation. However, in general this is not possible as the inversions tend to be non-unique and unstable to small changes in $C(I)$.

The usual procedure is then to choose a model spectrum $f(E, p_1, p_2, \dots)$ that can be described by several parameters (p_1, p_2, \dots) and fit it into the observational data. The observed data $C(I)$ are then compared with a predicted count spectrum $C_p(I)$ for each model spectrum. The parameters are varied to find the best value that provides the most desirable fit statistic (best-fit parameters). The best-fit model $f_b(E)$ is evaluated using best-fit parameters. The most common fit statistic to determine the best-fit is

$$\chi^2 = \sum \frac{(C(I) - C_p(I))^2}{\sigma(I)^2} \quad (\text{C.2})$$

where $\sigma(I)$ is the (generally unknown) error for channel I . If $C(I)$ are counts, then $\sigma(I)$ is usually estimated by $\sqrt{C(I)}$. The χ^2 statistic can provide a well-known-goodness-of-fit criterion for a given number of degrees of freedom, i.e. the difference between the number of channels and the number of model parameters, and for a given confidence level. If the reduced χ^2 ($\sim \chi^2/\nu$) is much greater than one, the fit is not adequate for $C(I)$, while if the reduced χ^2 is much less than one, the errors have been

¹<https://heasarc.gsfc.nasa.gov/xanadu/xspec/manual/XspecManual.html>

²<https://heasarc.gsfc.nasa.gov/docs/software/heasoft/>

over-estimated. Even if the best-fit model does not pass the goodness-of-fit test, it could be the only acceptable model if the data used in the fit are not particularly good. The confidence interval for a given parameter is calculated by varying the parameter value until the χ^2 increases by a particular amount above the best-fit value. The variation of χ^2 allowed depends on the confidence level required and the number of parameters whose confidence space is computed.

Each observed spectrum is obtained by XSPEC using the data file containing the total photon count detected by the instrument for a given channel and the background file. XSPEC uses the background file to derive the background-subtracted count rate $C(I)$ as

$$C(I) = \frac{D(I)}{a_{D(I)}t_D} - \frac{b_{D(I)}}{b_{B(I)}} \frac{B(I)}{a_{B(I)}t_B} \quad (\text{C.3})$$

where $D(I)$ and $B(I)$ are the data and background counts, t_D and t_B are the exposure time in the data and background files, a_i and b_i are the area and background scaling from the spectrum and background, which together refer the background flux to the same area as the observation as necessary.

XSPEC needs to know the specific characteristics of the instrument in order to proceed with spectral fitting. The detector response $R(I, E)$ is a continuous function of E converted to a discrete function by using a response matrix who defines the energy ranges E_J such that

$$R_D(I, J) = \frac{\int_{E_{J-1}}^{E_J} R(I, E)dE}{E_J - E_{J-1}}. \quad (\text{C.4})$$

An Auxiliary Response File (ARF) designed to represent the efficiency of the detector with the response file representing a normalized Redistribution Matrix Function (RMF) can also be included in XSPEC as follows

$$R_D(I, J) \rightarrow R_D(I, J) \times A_D(J). \quad (\text{C.5})$$

The model spectrum $M(E)$ is computed using the energy ranges by the response file

$$M_D(J) = \int_{E_{J-1}}^{E_J} M(E)dE \quad (\text{C.6})$$

in units of photons/cm²/s. XSPEC allows models consisting of additive components representing X-ray sources (e.g. blackbody, power-law, ...), multiplicative components which modify additive components by an energy-dependent factor (e.g. photoelectric absorption, edges, ...) and convolution and mixing models. Once data, background, RMF and ARF have been read and a model has been defined, XSPEC uses a fitting algorithm to minimize the fit statistic to find the best-fit values of the model parameters. At the end of the fit, XSPEC writes out the best-fit parameters values along with estimated confidence intervals at 1σ , calculated from the second derivatives of the fit statistic with respect to the model parameters at the best-fit.

C.2 Useful Models

All the different models used in the spectro-polarimetric analysis of *IXPE* observations (Chapter 4) are introduced and described here.

C.2.1 Bbodyrad

A blackbody spectrum with normalization proportional to the surface

$$A(E) = \frac{K \times 1.0344 \times 10^{-3} E^2 dE}{e^{E/kT} - 1} \quad (\text{C.7})$$

where the parameters are:

par1 = kT	Temperature (keV)
norm = K	R_{km}^2/D_{10}^2

where R_{km} is the source radius in km and D_{10} is the distance of the source in units of 10 kpc.

C.2.2 CompTT

Analytic model describing Comptonization of soft photons in a hot plasma including relativistic effects, developed by [Titarchuk \(1994\)](#). The approximations used in this model work well for both the optically thin and thick regimes. The Comptonized spectrum is completely determined by the plasma temperature and the so-called β parameter, which is independent of geometry. The optical depth is then determined as a function of β for a given geometry. The soft photon input spectrum is a Wien law x^2e^{-x} because this lends itself to a particularly simple analytical form of the model. The plasma temperature may range from 2–500 keV, but the model is not reasonable for simultaneously low temperatures and low optical depth or for high temperatures and high optical depth. The parameters are:

par1 = z	Redshift
par2 = T_0	Input soft photon temperature (keV)
par3 = kT	Plasma temperature (keV)
par4 = τ	Plasma optical depth
par5 = approx	Geometry switch
norm	Normalization

where par5 switches between spherical (> 1) and disc (≤ 1) geometries and must be frozen. If $\text{par5} \geq 0$, β is obtained from the optical depth using an analytic approximation (e.g. [Titarchuk 1994](#)). If $\text{par5} < 0$ and $0.1 < \tau < 10$, β is obtained by interpolation from a set of accurately calculated pairs of β and τ from [Sunyaev and Titarchuk \(1985\)](#).

C.2.3 Comptb

This model describes the Comptonization spectrum of soft photons by electrons purely thermal or additionally subjected to an inward bulk motion. The spectrum is made up of two components: the direct seed photon blackbody spectrum and the Comptonized spectrum. The latter is obtained as a self-consistent convolution of the seed photon spectrum with the system Green's function. The model is not specific to the bulk Comptonization, but it includes in a coherent way different spectral shapes such as simple blackbody (i.e. neither thermal or bulk Comptonization), thermal Comptonization (equivalent to compTT) and thermal plus bulk Comptonization (see [Farinelli et al. 2008](#)). The parameters are:

par1 = kT_S	Seed photons temperature (keV)
par2 = Γ	Index of the seed photon spectrum
par3 = α	Energy index of the Comptonization spectrum
par4 = δ	Efficiency of bulk over thermal Comptonization
par5 = kT_e	Plasma electrons temperature (keV)
par6 = $\log A$	Log of the illuminating factor parameter
norm	Normalization

The normalization is defined as L_{39}/D_{10}^2 , where L_{39} is the luminosity of the source in units of 10^{39} erg/s and D_{10} is the distance to the source in units of 10 kpc.

C.2.4 Diskbb

Spectrum of an accretion disk consisting of multiple blackbody components (see [Mitsuda et al. 1984](#); [Makishima et al. 1986](#)). The parameters are:

$\text{par1} = kT_{\text{in}}$	Temperature at inner disk radius (keV)
norm	$(R_{\text{in}}/D_{10})^2 \cos \theta$

where R_{in} is an ‘‘apparent’’ inner disk radius in km, D_{10} is the distance to the source in units of 10 kpc and θ is the angle of the disk ($\theta = 0$ is face-on). For the correction factor between the apparent inner disk radius and the realistic radius see [Kubota et al. \(1998\)](#).

C.2.5 ThComp

This model describes spectra from Comptonization by thermal electrons emitted by a spherical source with the sinusoidal-like spatial distribution of the seed photons (as in [Sunyaev and Titarchuk 1980](#)). It is a convolution model and thus it can Comptonize any seed photon distribution, either hard or soft, and it describes both upscattering and downscattering (see e.g. [Zdziarski et al. 2020](#)). In the case of upscattering of some seed photons (e.g. blackbody or disc blackbody), it is a much better description of the continuum shape from thermal Comptonization than an exponential cutoff power law, but has similar corresponding free parameters: the spectral index Γ or the Thomson optical depth τ and the high-energy cutoff parameterized by the electron temperature kT_e , much sharper than an exponential cutoff. The model also provides a correct description of Comptonized spectra at energies comparable to those of seed photons and its normalization follows from that of the seed photons distribution. The parameters are:

$\text{par1} = \tau$	Thomson optical depth
$\text{par2} = kT_e$	Plasma electrons temperature (keV)
$\text{par3} = f$	Covering fraction
$\text{par4} = z$	Redshift

C.2.6 Relxill

The `relxill` model calculates relativistic reflection from the innermost regions of the accretion disk around black hole binaries, neutron stars and active galactic nuclei. The reflection is caused by a primary source irradiating the accretion disk atmosphere. Due to relativistic effects close to the compact object, the reflected spectrum is strongly distorted on its way to the observer. `relxill` models the irradiation of the disk, the intrinsic reflection and the relativistic broadening.

The `relxill` models are distinguished by the assumptions about the primary source. The irradiation of the accretion disk by the primary source is specified by the *emissivity*, which is the radially dependent flux that irradiates the disk. The standard approach until recently was to use an empirical implementation without assuming a geometry or physical location of the primary source. This is done by assuming that the emissivity depends on the radius as a broken power-law, which changes at the break radius R_{br} from $r^{-\text{Index1}}$ to $r^{-\text{Index2}}$. To compute the reprocessed X-ray spectrum out of an illuminated accretion disk around a neutron star, the `relxillNS` model is used ([García et al., 2022](#)). In this case, the illuminating radiation field is changed from the standard power-law spectrum (mostly appropriate for sources in the hard state) to a spectrum described by a blackbody radiation field at given temperature. Most of the X-ray continuum emission is thermal radiation that originates either from the surface of the neutron star (whether that be uniform thermal emission or a hot spot on the surface) or from the boundary layer region

extending between the star and the accretion disk. The parameters of this model are:

par1 = Index1	Emissivity index between R_{in} and R_{br}
par2 = Index2	Emissivity index between R_{br} and R_{out}
par3 = R_{br}	Emissivity break radius
par4 = a	Dimensionless spin of the BH or NS
par5 = i	Inclination angle in degrees with respect to the normal of the disk
par6 = R_{in}	Inner radius of the accretion disk
par7 = R_{out}	Outer radius of the accretion disk
par8 = z	Redshift to the source
par9 = kT_{bb}	Blackbody temperature (in keV) of the primary source spectrum
par10 = $\log \xi$	Ionization of the accretion disk
par11 = A_{Fe}	Iron abundance in Solar units
par12 = $\log N$	Logarithmic value of the density (in cm^{-3})
par13 = r_f	Reflection fraction parameter
norm	Normalization

C.2.7 TBabs

The Tuebingen-Boulder Interstellar Medium (ISM) absorption model calculates the cross section for X-ray absorption due to the gas-phase ISM, the grain-phase ISM and the molecules in the ISM. In the gas-phase ISM, the cross section is the sum of the photoionization cross sections of the different elements, weighted by abundance and taking into account depletion onto grains (Verner et al., 1996). Details of the updated abundances that contribute to the photoionization cross section can be found in Wilms et al. (2000). In the grain-phase ISM, the effect of shielding by the grains is accounted for, but is extremely small. In the molecular contribution, only molecular hydrogen is considered. TBabs allows to vary just the hydrogen column parameter:

$$\text{par1} = nH \quad \text{Equivalent hydrogen column (in units of } 10^{22} \text{ atoms cm}^{-2}\text{)}$$

C.2.8 Polconst

This multiplicative model applies a constant polarization and depends on which Stokes parameter the spectrum is for. The Stokes parameter is determined using XFLTnnnn keyword with values “Stokes:0”, “Stokes:1” or “Stokes:2” for I , Q and U respectively. Given the polarization fraction A and the polarization angle in radians of ψ , then the multiplicative factor is $A \cos(2\psi)$ for Q and $A \sin(2\psi)$ for U . The parameters are:

$$\begin{aligned} \text{par1} &= A && \text{Polarization fraction} \\ \text{par2} &= \psi && \text{Polarization angle (degrees)} \end{aligned}$$

C.2.9 Pollin

This multiplicative model applies a polarization with a linear dependence on energy and depends on which Stokes parameter the spectrum is for. The Stokes parameter is determined using XFLTnnnn keyword with values “Stokes:0”, “Stokes:1” or “Stokes:2” for I , Q and U respectively. The polarization fraction and angle are determined by

$$\begin{aligned} A(E) &= A_1 + (E - 1.0) \times A_{\text{slope}} \\ \psi(E) &= \psi_1 + (E - 1.0) \times \psi_{\text{slope}} . \end{aligned} \tag{C.8}$$

The parameters are:

$\text{par1} = A_1$	Polarization fraction at 1 keV
$\text{par2} = A_{\text{slope}}$	Polarization fraction slope
$\text{par3} = \psi_1$	Polarization angle at 1 keV (degrees)
$\text{par4} = \psi_{\text{slope}}$	Polarization angle slope

References

- Abarr, Q. & Krawczynski, H. The Polarization of X-Rays from Warped Black Hole Accretion Disks. *The Astrophysical Journal*, 889(2):111, Feb. 2020. doi: 10.3847/1538-4357/ab5fdf.
- Abolmasov, P., Nättilä, J., & Poutanen, J. KiloHertz quasi-periodic oscillations from neutron star spreading layers. *Astronomy & Astrophysics*, 638:A142, June 2020. doi: 10.1051/0004-6361/201936958.
- Abramowicz, M. A. & Fragile, P. C. Foundations of Black Hole Accretion Disk Theory. *Living Reviews in Relativity*, 16(1):1, Jan. 2013. doi: 10.12942/lrr-2013-1.
- Abramowicz, M. A., Chen, X. M., Granath, M., & Lasota, J. P. Advection-dominated Accretion Flows around Kerr Black Holes. *The Astrophysical Journal*, 471:762, Nov. 1996. doi: 10.1086/178004.
- Andrew, B. H. & Purton, C. R. Detection of Radio Emission from Scorpio X-1. *Nature*, 218(5144): 855–856, June 1968. doi: 10.1038/218855a0.
- Arnason, R. M., Papei, H., Barmby, P., Bahramian, A., & Gorski, M. D. Distances to Galactic X-ray binaries with Gaia DR2. *Monthly Notices of the Royal Astronomical Society*, 502(4):5455–5470, Apr. 2021. doi: 10.1093/mnras/stab345.
- Arnaud, K. A. XSPEC: The First Ten Years. In Jacoby, G. H. & Barnes, J., editors, *Astronomical Data Analysis Software and Systems V*, volume 101 of *Astronomical Society of the Pacific Conference Series*, page 17, Jan. 1996.
- Asai, K., Mihara, T., & Matsuoka, M. Decades-long variations in NS-LMXBs observed with MAXI/GSC, RXTE/ASM, and Ginga/ASM. *Publications of the Astronomical Society of Japan*, 74(4):974–990, Aug. 2022. doi: 10.1093/pasj/psac049.
- Baade, W. & Zwicky, F. “Remarks on Super-Novae and Cosmic Rays”. *Physical Review*, 46(1):76–77, 1934. doi: 10.1103/PhysRev.46.76.2.
- Baade, W. & Zwicky, F. “Cosmic rays from super-novae”. *Proceedings of the National Academy of Sciences*, 20(5):259–263, 1934a.
- Baade, W. & Zwicky, F. “On Super-Novae”. *Proceedings of the National Academy of Sciences*, 20(5): 254–259, 1934b. ISSN 0027-8424. doi: 10.1073/pnas.20.5.254.
- Baldini, L., Bucciantini, N., Lalla, N. D., et al. ixpeobssim: A simulation and analysis framework for the imaging X-ray polarimetry explorer. *SoftwareX*, 19:101194, July 2022. doi: 10.1016/j.softx.2022.101194.
- Ballantyne, D. R. Reflection spectra from an accretion disc illuminated by a neutron star X-ray burst. *Monthly Notices of the Royal Astronomical Society*, 351(1):57–62, June 2004. doi: 10.1111/j.1365-2966.2004.07767.x.

- Balućńska-Church, M., Gibiec, A., Jackson, N. K., & Church, M. J. On the nature of the Cygnus X-2 like Z-track sources. *Astronomy & Astrophysics*, 512:A9, Mar. 2010. doi: 10.1051/0004-6361/200913199.
- Balućńska-Church, M., Church, M. J., & Gibiec, A. Dipping - versus flaring in Z-track sources: resolving the controversy. *Memorie della Societa Astronomica Italiana*, 83:178, Jan. 2012. doi: 10.48550/arXiv.1110.1266.
- Bardeen, J. M. & Petterson, J. A. The Lense-Thirring Effect and Accretion Disks around Kerr Black Holes. *The Astrophysical Journal Letters*, 195:L65, Jan. 1975. doi: 10.1086/181711.
- Bardeen, J. M., Press, W. H., & Teukolsky, S. A. Rotating Black Holes: Locally Nonrotating Frames, Energy Extraction, and Scalar Synchrotron Radiation. *The Astrophysical Journal*, 178:347–370, Dec. 1972. doi: 10.1086/151796.
- Barret, D. & Olive, J.-F. A Peculiar Spectral State Transition of 4U 1705-44: When an Atoll Looks Like a Z. *The Astrophysical Journal*, 576(1):391–401, Sept. 2002. doi: 10.1086/341626.
- Barret, D., Olive, J. F., Boirin, L., et al. Hard X-Ray Emission from Low-Mass X-Ray Binaries. *The Astrophysical Journal*, 533(1):329–351, Apr. 2000. doi: 10.1086/308651.
- Baumgardt, H. & Vasiliev, E. Accurate distances to Galactic globular clusters through a combination of Gaia EDR3, HST, and literature data. *Monthly Notices of the Royal Astronomical Society*, 505(4): 5957–5977, Aug. 2021. doi: 10.1093/mnras/stab1474.
- Berendsen, S. G. H., Fender, R., Kuulkers, E., Heise, J., & van der Klis, M. Simultaneous radio and X-ray observations of Galactic Centre low-mass X-ray binaries. *Monthly Notices of the Royal Astronomical Society*, 318(2):599–605, Oct. 2000. doi: 10.1046/j.1365-8711.2000.03850.x.
- Berestetskii, V. B., Lifshitz, E. M., & Pitaevskii, V. B. *Relativistic quantum theory. Pt.1.* 1971.
- Bethe, H. A. & Critchfield, C. L. “The Formation of Deuterons by Proton Combination”. *Physical Review*, 54:248–254, Aug 1938. doi: 10.1103/PhysRev.54.248.
- Bondi, H. On spherically symmetrical accretion. *Monthly Notices of the Royal Astronomical Society*, 112: 195, Jan. 1952. doi: 10.1093/mnras/112.2.195.
- Bondi, H. & Hoyle, F. On the mechanism of accretion by stars. *Monthly Notices of the Royal Astronomical Society*, 104:273, Jan. 1944. doi: 10.1093/mnras/104.5.273.
- Bowyer, S., Byram, E. T., Chubb, T. A., & Friedman, H. “Lunar Occultation of X-ray Emission from the Crab Nebula”. *Science*, 146(3646):912–917, 1964. doi: 10.1126/science.146.3646.912.
- Bradshaw, C. F., Fomalont, E. B., & Geldzahler, B. J. High-Resolution Parallax Measurements of Scorpius X-1. *The Astrophysical Journal Letters*, 512(2):L121–L124, Feb. 1999. doi: 10.1086/311889.
- Bradt, H. *Astrophysics Processes*. 2008.
- Bradt, H., Naranan, S., Rappaport, S., & Spada, G. Celestial Positions of X-Ray Sources in Sagittarius. *The Astrophysical Journal*, 152:1005, June 1968. doi: 10.1086/149613.
- Braje, T. M., Romani, R. W., & Rauch, K. P. Light Curves of Rapidly Rotating Neutron Stars. *The Astrophysical Journal*, 531(1):447–452, Mar. 2000. doi: 10.1086/308448.
- Bursa, M. Numerical implementation of equations for photon motion in Kerr spacetime. In *RAGtime 17-19: Workshops on Black Holes and Neutron Stars*, pages 7–21, Dec. 2017.

- Bursa, M. SIM5: Library for ray-tracing and radiation transport in general relativity. *Astrophysics Source Code Library*, record ascl:1811.011, Nov. 2018.
- Byram, E. T., Chubb, T. A., & Friedman, H. Cosmic X-Ray Sources-Galactic and Extragalactic. *The Astronomical Journal*, 71:379, Aug. 1966. doi: 10.1086/109934.
- Calvelo, D. E., Fender, R. P., Tzioumis, A. K., & Broderick, J. W. Millimetre observations of a sub-arcsecond jet from Circinus X-1. *Monthly Notices of the Royal Astronomical Society*, 419(1):L54–L58, Jan. 2012. doi: 10.1111/j.1745-3933.2011.01175.x.
- Canfield, E., Howard, W. M., & Liang, E. P. Inverse Comptonization by one-dimensional relativistic electrons. *The Astrophysical Journal*, 323:565–574, Dec. 1987. doi: 10.1086/165853.
- Capitanio, F., Fabiani, S., Gnani, A., et al. Polarization Properties of the Weakly Magnetized Neutron Star X-Ray Binary GS 1826-238 in the High Soft State. *The Astrophysical Journal*, 943(2):129, Feb. 2023. doi: 10.3847/1538-4357/aca88.
- Carter, B. Global Structure of the Kerr Family of Gravitational Fields. *Physical Review*, 174(5):1559–1571, Oct. 1968. doi: 10.1103/PhysRev.174.1559.
- CASA Team, Bean, B., Bhatnagar, S., et al. CASA, the Common Astronomy Software Applications for Radio Astronomy. *Publications of the Astronomical Society of the Pacific*, 134(1041):114501, Nov. 2022. doi: 10.1088/1538-3873/ac9642.
- Chadwick, J. “Possible Existence of a Neutron”. *Nature*, 129:312, 1932. doi: 10.1038/129312a0.
- Chandra, A. D. Swift/XRT confirms outburst of XTE J1701-462. *The Astronomer’s Telegram*, 15594:1, Sept. 2022.
- Chandrasekhar, S. “The Maximum Mass of Ideal White Dwarfs”. *The Astrophysical Journal*, 74:81, July 1931. doi: 10.1086/143324.
- Chandrasekhar, S. The transfer of radiation in stellar atmospheres. *Bulletin of the American Mathematical Society*, 53(7):641 – 711, 1947.
- Chandrasekhar, S. *Radiative transfer*. 1960.
- Chandrasekhar, S. *The mathematical theory of black holes*. 1983.
- Chen, K. & Eardley, D. M. Polarization Properties of Emission Lines from Relativistic Accretion Disks. *The Astrophysical Journal*, 382:125, Nov. 1991. doi: 10.1086/170701.
- Christian, D. J. & Swank, J. H. The Survey of Low-Mass X-Ray Binaries with the Einstein Observatory Solid-State Spectrometer and Monitor Proportional Counter. *The Astrophysical Journal Supplement*, 109(1):177–224, Mar. 1997. doi: 10.1086/312970.
- Church, M. J., Hali, G. S., & Bałucińska-Church, M. An explanation of the Z-track sources. *Astronomy & Astrophysics*, 460(1):233–244, Dec. 2006. doi: 10.1051/0004-6361:20065035.
- Church, M. J., Gibiec, A., Bałucińska-Church, M., & Jackson, N. K. Spectral investigations of the nature of the Scorpius X-1 like sources. *Astronomy & Astrophysics*, 546:A35, Oct. 2012. doi: 10.1051/0004-6361/201218987.
- Clark, G. W. Monte Carlo Simulation of the X-Ray Halos of GX 5-1 and GX 13+1 to Test Models of Interstellar Dust Grains. *The Astrophysical Journal*, 852(2):121, Jan. 2018. doi: 10.3847/1538-4357/aaaf0.

- Cocchi, M., Bazzano, A., Natalucci, L., et al. Clocked bursts from GS 1826-238. In McConnell, M. L. & Ryan, J. M., editors, *The Fifth Compton Symposium*, volume 510 of *American Institute of Physics Conference Series*, pages 203–207, Apr. 2000. doi: 10.1063/1.1303203.
- Cocchi, M., Farinelli, R., Paizis, A., & Titarchuk, L. Wide band observations of the X-ray burster GS 1826-238. *Astronomy & Astrophysics*, 509:A2, Jan. 2010. doi: 10.1051/0004-6361/200912796.
- Cocchi, M., Farinelli, R., & Paizis, A. BeppoSAX view of the NS-LMXB GS 1826-238. *Astronomy & Astrophysics*, 529:A155, May 2011. doi: 10.1051/0004-6361/201016241.
- Cocchi, M., Gnarini, A., Fabiani, S., et al. Discovery of strongly variable X-ray polarization in the neutron star low-mass X-ray binary transient XTE J1701–462. *Astronomy & Astrophysics*, 674:L10, June 2023. doi: 10.1051/0004-6361/202346275.
- Collett, E. The Description of Polarization in Classical Physics. *American Journal of Physics*, 36(8): 713–725, Aug. 1968. doi: 10.1119/1.1975098.
- Comella, J. M., Craft, H. D., Lovelace, R. V. E., Sutton, J. M., & Tyler, G. L. “Crab nebula pulsar NP 0532”. *Nature*, 221(5179):453–454, 1969.
- Connors, P. A. & Stark, R. F. Observable gravitational effects on polarised radiation coming from near a black hole. *Nature Astronomy*, 269(5624):128–129, Sept. 1977. doi: 10.1038/269128a0.
- Connors, P. A., Piran, T., & Stark, R. F. Polarization features of X-ray radiation emitted near black holes. *The Astrophysical Journal*, 235:224–244, Jan. 1980. doi: 10.1086/157627.
- Coriat, M., Fender, R. P., Tasse, C., et al. The twisted jets of Circinus X-1. *Monthly Notices of the Royal Astronomical Society*, 484(2):1672–1686, Apr. 2019. doi: 10.1093/mnras/stz099.
- Costa, E., Soffitta, P., Bellazzini, R., et al. An efficient photoelectric X-ray polarimeter for the study of black holes and neutron stars. *Nature Astronomy*, 411(6838):662–665, June 2001.
- Courvoisier, T. J. L., Walter, R., Beckmann, V., et al. The INTEGRAL Science Data Centre (ISDC). *Astronomy & Astrophysics*, 411:L53–L57, Nov. 2003. doi: 10.1051/0004-6361:20031172.
- Cromartie, H. T., Fonseca, E., Ransom, S. M., et al. Relativistic Shapiro delay measurements of an extremely massive millisecond pulsar. *Nature Astronomy*, 4:72–76, Jan. 2020. doi: 10.1038/s41550-019-0880-2.
- Cunningham, C. T. The effects of redshifts and focusing on the spectrum of an accretion disk around a Kerr black hole. *The Astrophysical Journal*, 202:788–802, Dec. 1975. doi: 10.1086/154033.
- Curran, P. A., Coriat, M., Miller-Jones, J. C. A., et al. The evolving polarized jet of black hole candidate Swift J1745-26. *Monthly Notices of the Royal Astronomical Society*, 437(4):3265–3273, Feb. 2014. doi: 10.1093/mnras/stt2125.
- D’Ài, A., Iaria, R., Di Salvo, T., Matt, G., & Robba, N. R. Disk Reflection Signatures in the Spectrum of the Bright Z-Source GX 340+0. *The Astrophysical Journal Letters*, 693(1):L1–L5, Mar. 2009. doi: 10.1088/0004-637X/693/1/L1.
- D’Ài, A., Bozzo, E., Papitto, A., et al. A complete X-ray spectral coverage of the 2010 May-June outbursts of Circinus X-1. *Astronomy & Astrophysics*, 543:A20, July 2012. doi: 10.1051/0004-6361/201118577.
- D’Amico, F., Heindl, W. A., Rothschild, R. E., & Gruber, D. E. High-Energy X-Ray Timing Experiment Detections of Hard X-Ray Tails in Scorpius X-1. *The Astrophysical Journal Letters*, 547(2):L147–L150, Feb. 2001. doi: 10.1086/318902.

- Dauser, T., Wilms, J., Reynolds, C. S., & Brenneman, L. W. Broad emission lines for a negatively spinning black hole. *Monthly Notices of the Royal Astronomical Society*, 409(4):1534–1540, Dec. 2010. doi: 10.1111/j.1365-2966.2010.17393.x.
- Dauser, T., Garcia, J., Wilms, J., et al. Irradiation of an accretion disc by a jet: general properties and implications for spin measurements of black holes. *Monthly Notices of the Royal Astronomical Society*, 430(3):1694–1708, Apr. 2013. doi: 10.1093/mnras/sts710.
- Dauser, T., Garcia, J., Parker, M. L., Fabian, A. C., & Wilms, J. The role of the reflection fraction in constraining black hole spin. *Monthly Notices of the Royal Astronomical Society*, 444:L100–L104, Oct. 2014. doi: 10.1093/mnrasl/slu125.
- Dexter, J. & Agol, E. A Fast New Public Code for Computing Photon Orbits in a Kerr Spacetime. *The Astrophysical Journal*, 696(2):1616–1629, May 2009. doi: 10.1088/0004-637X/696/2/1616.
- Di Marco, A., Costa, E., Muleri, F., et al. A Weighted Analysis to Improve the X-Ray Polarization Sensitivity of the Imaging X-ray Polarimetry Explorer. *The Astronomical Journal*, 163(4):170, Apr. 2022. doi: 10.3847/1538-3881/ac51c9.
- Di Marco, A., La Monaca, F., Poutanen, J., et al. First detection of x-ray polarization from the accreting neutron star 4u 1820-303. *The Astrophysical Journal Letters*, 953(2):L22, aug 2023a. doi: 10.3847/2041-8213/acec6e. URL <https://dx.doi.org/10.3847/2041-8213/acec6e>.
- Di Marco, A., Soffitta, P., Costa, E., et al. Handling the Background in IXPE Polarimetric Data. *The Astronomical Journal*, 165(4):143, Apr. 2023b. doi: 10.3847/1538-3881/acba0f.
- Di Salvo, T., Stella, L., Robba, N. R., et al. The Discovery of a State-Dependent Hard Tail in the X-Ray Spectrum of the Luminous Z Source GX 17+2. *The Astrophysical Journal Letters*, 544(2):L119–L122, Dec. 2000. doi: 10.1086/317309.
- Di Salvo, T., Robba, N. R., Iaria, R., et al. Detection of a Hard Tail in the X-Ray Spectrum of the Z Source GX 349+2. *The Astrophysical Journal*, 554(1):49–55, June 2001. doi: 10.1086/321353.
- Di Salvo, T., Farinelli, R., Burderi, L., et al. On the spectral evolution of Cygnus X-2 along its color-color diagram. *Astronomy & Astrophysics*, 386:535–547, May 2002. doi: 10.1051/0004-6361:20020238.
- Di Salvo, T., Iaria, R., Matranga, M., et al. Suzaku broad-band spectrum of 4U 1705-44: probing the reflection component in the hard state. *Monthly Notices of the Royal Astronomical Society*, 449(3): 2794–2802, May 2015. doi: 10.1093/mnras/stv443.
- Díaz Trigo, M., Migliari, S., Miller-Jones, J. C. A., et al. ALMA observations of 4U 1728-34 and 4U 1820-30: first detection of neutron star X-ray binaries at 300 GHz. *Astronomy & Astrophysics*, 600:A8, Apr. 2017. doi: 10.1051/0004-6361/201629472.
- Dolence, J. C., Gammie, C. F., Mościbrodzka, M., & Leung, P. K. grmonty: A Monte Carlo Code for Relativistic Radiative Transport. *The Astrophysical Journal Supplement*, 184(2):387–397, Oct. 2009. doi: 10.1088/0067-0049/184/2/387.
- Done, C. & Gierliński, M. Truncated disc versus extremely broad iron line in XTE J1650-500. *Monthly Notices of the Royal Astronomical Society*, 367(2):659–668, Apr. 2006. doi: 10.1111/j.1365-2966.2005.09968.x.
- Done, C., Gierliński, M., & Kubota, A. Modelling the behaviour of accretion flows in X-ray binaries. Everything you always wanted to know about accretion but were afraid to ask. *Astronomy & Astrophysics Reviews*, 15(1):1–66, Dec. 2007. doi: 10.1007/s00159-007-0006-1.

- Doroshenko, V., Poutanen, J., Tsygankov, S. S., et al. Determination of X-ray pulsar geometry with IXPE polarimetry. *Nature Astronomy*, 6:1433–1443, Dec. 2022. doi: 10.1038/s41550-022-01799-5.
- Doroshenko, V., Poutanen, J., Heyl, J., et al. Complex variations in X-ray polarization in the X-ray pulsar LS V +44 17/RX J0440.9+4431. *Astronomy & Astrophysics*, 677:A57, Sept. 2023. doi: 10.1051/0004-6361/202347088.
- Dovčiak, M., Muleri, F., Goosmann, R. W., Karas, V., & Matt, G. Thermal disc emission from a rotating black hole: X-ray polarization signatures. *Monthly Notices of the Royal Astronomical Society*, 391(1): 32–38, Nov. 2008. doi: 10.1111/j.1365-2966.2008.13872.x.
- Eggleton, P. P. Approximations to the radii of Roche lobes. *The Astrophysical Journal*, 268:368–369, May 1983. doi: 10.1086/160960.
- Einstein, A. Zur allgemeinen Relativitätstheorie. *Sitzungsberichte der Königlich Preussischen Akademie der Wissenschaften*, pages 778–786, Jan. 1915.
- Fabian, A. C., Rees, M. J., Stella, L., & White, N. E. X-ray fluorescence from the inner disc in Cygnus X-1. *Monthly Notices of the Royal Astronomical Society*, 238:729–736, May 1989. doi: 10.1093/mnras/238.3.729.
- Fabian, A. C., Iwasawa, K., Reynolds, C. S., & Young, A. J. Broad Iron Lines in Active Galactic Nuclei. *Publications of the ASP*, 112(775):1145–1161, Sept. 2000. doi: 10.1086/316610.
- Fabiani, S. Instrumentation and Future Missions in the Upcoming Era of X-ray Polarimetry. *Galaxies*, 6 (2):54, May 2018. doi: 10.3390/galaxies6020054.
- Fabiani, S., Capitanio, F., Iaria, R., et al. Discovery of a variable energy-dependent x-ray polarization in the accreting neutron star gx 5-1. *Astronomy & Astrophysics*, 684:A137, 2024. doi: 10.1051/0004-6361/202347374. URL <https://doi.org/10.1051/0004-6361/202347374>.
- Falanga, M., Götz, D., Goldoni, P., et al. The X-ray spectrum of the bursting atoll source 4U 1728-34 observed with INTEGRAL. *Astronomy & Astrophysics*, 458(1):21–29, Oct. 2006. doi: 10.1051/0004-6361:20065297.
- Farinelli, R., Frontera, F., Zdziarski, A. A., et al. The transient hard X-ray tail of GX 17+2: New BeppoSAX results. *Astronomy & Astrophysics*, 434(1):25–34, Apr. 2005. doi: 10.1051/0004-6361:20041567.
- Farinelli, R., Titarchuk, L., Paizis, A., & Frontera, F. A New Comptonization Model for Weakly Magnetized, Accreting Neutron Stars in Low-Mass X-Ray Binaries. *The Astrophysical Journal*, 680(1): 602–614, June 2008. doi: 10.1086/587162.
- Farinelli, R., Paizis, A., Landi, R., & Titarchuk, L. The X-ray spectral evolution of Cygnus X-2 in the framework of bulk Comptonization. *Astronomy & Astrophysics*, 498(2):509–516, May 2009. doi: 10.1051/0004-6361/200810422.
- Farinelli, R., Fabiani, S., Poutanen, J., et al. Accretion geometry of the neutron star low mass X-ray binary Cyg X-2 from X-ray polarization measurements. *Monthly Notices of the Royal Astronomical Society*, 519(3):3681–3690, Mar. 2023. doi: 10.1093/mnras/stac3726.
- Fender, R., Spencer, R., Tzioumis, T., et al. An Asymmetric Arcsecond Radio Jet from Circinus X-1. *The Astrophysical Journal Letters*, 506(2):L121–L125, Oct. 1998. doi: 10.1086/311660.

- Fender, R. P. & Hendry, M. A. The radio luminosity of persistent X-ray binaries. *Monthly Notices of the Royal Astronomical Society*, 317(1):1–8, Sept. 2000. doi: 10.1046/j.1365-8711.2000.03443.x.
- Fender, R. P., Dahlem, M., Homan, J., et al. The variable radio counterpart and possible large-scale jet of the new Z source XTE J1701-462. *Monthly Notices of the Royal Astronomical Society*, 380(1): L25–L29, Sept. 2007. doi: 10.1111/j.1745-3933.2007.00350.x.
- Feng, H., Jiang, W., Minuti, M., et al. PolarLight: a CubeSat X-ray polarimeter based on the gas pixel detector. *Experimental Astronomy*, 47(1-2):225–243, Apr. 2019. doi: 10.1007/s10686-019-09625-z.
- Ferland, G. J., Chatzikos, M., Guzmán, F., et al. The 2017 Release Cloudy. *Revista Mexicana de Astronomía y Astrofísica*, 53:385–438, Oct. 2017. doi: 10.48550/arXiv.1705.10877.
- Ferrazzoli, R., Muleri, F., Lefevre, C., et al. In-flight calibration system of imaging x-ray polarimetry explorer. *Journal of Astronomical Telescopes, Instruments, and Systems*, 6:048002, Oct. 2020. doi: 10.1117/1.JATIS.6.4.048002.
- Fomalont, E. B., Geldzahler, B. J., & Bradshaw, C. F. Scorpius X-1: The Evolution and Nature of the Twin Compact Radio Lobes. *The Astrophysical Journal*, 558(1):283–301, Sept. 2001a. doi: 10.1086/322479.
- Fomalont, E. B., Geldzahler, B. J., & Bradshaw, C. F. Scorpius X-1: Energy Transfer from the Core to the Radio Lobes. *The Astrophysical Journal Letters*, 553(1):L27–L30, May 2001b. doi: 10.1086/320490.
- Fragile, P. C., Mathews, G. J., & Wilson, J. R. Bardeen-Petterson Effect and Quasi-periodic Oscillations in X-Ray Binaries. *The Astrophysical Journal*, 553(2):955–959, June 2001. doi: 10.1086/320990.
- Frank, J., King, A. R., & Lasota, J. P. The light curves of low-mass X-ray binaries. *Astronomy & Astrophysics*, 178:137–142, May 1987.
- Frank, J., King, A., & Raine, D. *Accretion power in astrophysics.*, volume 21. 1992.
- Friend, D. B. & Castor, J. I. Radiation driven winds in X-ray binaries. *The Astrophysical Journal*, 261: 293–300, Oct. 1982. doi: 10.1086/160340.
- García, J., Dauser, T., Lohfink, A., et al. Improved Reflection Models of Black Hole Accretion Disks: Treating the Angular Distribution of X-Rays. *The Astrophysical Journal*, 782(2):76, Feb. 2014. doi: 10.1088/0004-637X/782/2/76.
- García, J. A., Fabian, A. C., Kallman, T. R., et al. The effects of high density on the X-ray spectrum reflected from accretion discs around black holes. *Monthly Notices of the Royal Astronomical Society*, 462(1):751–760, Oct. 2016. doi: 10.1093/mnras/stw1696.
- García, J. A., Dauser, T., Ludlam, R., et al. Relativistic X-Ray Reflection Models for Accreting Neutron Stars. *The Astrophysical Journal*, 926(1):13, Feb. 2022. doi: 10.3847/1538-4357/ac3cb7.
- Gendreau, K. C., Arzoumanian, Z., Adkins, P. W., et al. The Neutron star Interior Composition Explorer (NICER): design and development. In den Herder, J.-W. A., Takahashi, T., & Bautz, M., editors, *Space Telescopes and Instrumentation 2016: Ultraviolet to Gamma Ray*, volume 9905 of *Society of Photo-Optical Instrumentation Engineers (SPIE) Conference Series*, page 99051H, July 2016. doi: 10.1117/12.2231304.
- Geppert, U. & Urpin, V. Accretion-driven magnetic field decay in neutron stars. *Monthly Notices of the Royal Astronomical Society*, 271:490, Nov. 1994. doi: 10.1093/mnras/271.2.490.
- Ghisellini, G. *Radiative Processes in High Energy Astrophysics*, volume 873. 2013. doi: 10.1007/978-3-319-00612-3.

- Giacconi, R., Gursky, H., Paolini, F. R., & Rossi, B. B. “Evidence for X-Rays From Sources Outside the Solar System”. *Physical Review Letters*, 9:439–443, 1962. doi: 10.1103/PhysRevLett.9.439.
- Giacconi, R., Murray, S., Gursky, H., et al. “The Uhuru catalog of X-ray sources”. *The Astrophysical Journal*, 178:281–308, 1972. doi: 10.1086/151790.
- Gilfanov, M., Churazov, E., Sunyaev, R., et al. Three Years of Monitoring GRS 1758-258: an Extremely Hard X-Ray Source near GX 5-1. *The Astrophysical Journal*, 418:844, Dec. 1993. doi: 10.1086/173441.
- Gilfanov, M., Revnivtsev, M., & Molkov, S. Boundary layer, accretion disk and X-ray variability in the luminous LMXBs. *Astronomy & Astrophysics*, 410:217–230, Oct. 2003. doi: 10.1051/0004-6361:20031141.
- Gladstone, J., Done, C., & Gierliński, M. Analysing the atolls: X-ray spectral transitions of accreting neutron stars. *Monthly Notices of the Royal Astronomical Society*, 378(1):13–22, June 2007. doi: 10.1111/j.1365-2966.2007.11675.x.
- Gnarini, A., Ursini, F., Matt, G., et al. Polarization properties of weakly magnetized neutron stars in low-mass X-ray binaries. *Monthly Notices of the Royal Astronomical Society*, 514(2):2561–2567, Aug. 2022. doi: 10.1093/mnras/stac1523.
- Gold, T. “Rotating neutron stars as the origin of the pulsating radio sources”. In *Pulsating Stars*, pages 74–75. Springer, 1968.
- Grindlay, J., Gursky, H., Schnopper, H., et al. Discovery of intense X-ray bursts from the globular cluster NGC 6624. *The Astrophysical Journal Letters*, 205:L127–L130, May 1976. doi: 10.1086/182105.
- Haensel, P., Potekhin, A. Y., & Yakovlev, D. G. *Neutron Stars 1 : Equation of State and Structure*, volume 326. 2007.
- Hailey, C. J., An, H., Blaedel, K. L., et al. The Nuclear Spectroscopic Telescope Array (NuSTAR): optics overview and current status. In Arnaud, M., Murray, S. S., & Takahashi, T., editors, *Space Telescopes and Instrumentation 2010: Ultraviolet to Gamma Ray*, volume 7732 of *Society of Photo-Optical Instrumentation Engineers (SPIE) Conference Series*, page 77320T, July 2010. doi: 10.1117/12.857654.
- Harrison, F. A., Craig, W. W., Christensen, F. E., et al. The Nuclear Spectroscopic Telescope Array (NuSTAR) High-energy X-Ray Mission. *The Astrophysical Journal*, 770(2):103, June 2013. doi: 10.1088/0004-637X/770/2/103.
- Hartle, J. B. & Thorne, K. S. Slowly Rotating Relativistic Stars. II. Models for Neutron Stars and Supermassive Stars. *The Astrophysical Journal*, 153:807, Sept. 1968. doi: 10.1086/149707.
- Hasinger, G. & van der Klis, M. Two patterns of correlated X-ray timing and spectral behaviour in low-mass X-ray binaries. *Astronomy & Astrophysics*, 225:79–96, Nov. 1989.
- Haskell, B., Jones, D. I., & Andersson, N. Mountains on neutron stars: accreted versus non-accreted crusts. *Monthly Notices of the Royal Astronomical Society*, 373(4):1423–1439, Dec. 2006. doi: 10.1111/j.1365-2966.2006.10998.x.
- Heinz, S., Schulz, N. S., Brandt, W. N., & Galloway, D. K. Evidence of a Parsec-Scale X-Ray Jet from the Accreting Neutron Star Circinus X-1. *The Astrophysical Journal Letters*, 663(2):L93–L96, July 2007. doi: 10.1086/519950.
- Heinz, S., Sell, P., Fender, R. P., et al. The Youngest Known X-Ray Binary: Circinus X-1 and Its Natal Supernova Remnant. *The Astrophysical Journal*, 779(2):171, Dec. 2013. doi: 10.1088/0004-637X/779/2/171.

- Hertz, P. & Wood, K. S. Discovery of a 4.2 Hour X-Ray Period in GX 9+9. *The Astrophysical Journal*, 331:764, Aug. 1988. doi: 10.1086/166597.
- Hewish, A., Bell, S. J., Pilkington, J. D. H., Scott, P. F., & Collins, R. A. “Observation of a Rapidly Pulsating Radio Source”. *Nature*, 217(5130):709–713, 1968. doi: 10.1038/217709a0.
- Homan, J., Belloni, T., van der Klis, M., et al. Continuing RXTE observations of XTE J1701-462: a new “Z” in town? *The Astronomer’s Telegram*, 725:1, Feb. 2006.
- Homan, J., Belloni, T., Wijnands, R., et al. First detection of a type-I X-ray burst from the transient Z source XTE J1701-462. *The Astronomer’s Telegram*, 1144:1, July 2007a.
- Homan, J., Wijnands, R., Altamirano, D., & Belloni, T. Rapid decay of the neutron star transient XTE J1701-462. *The Astronomer’s Telegram*, 1165:1, Aug. 2007b.
- Homan, J., van der Klis, M., Fridriksson, J. K., et al. XTE J1701-462 and Its Implications for the Nature of Subclasses in Low-magnetic-field Neutron Star Low-mass X-ray Binaries. *The Astrophysical Journal*, 719(1):201–212, Aug. 2010. doi: 10.1088/0004-637X/719/1/201.
- Homan, J., Steiner, J. F., Lin, D., et al. Absence of Reflection Features in NuSTAR Spectra of the Luminous Neutron Star X-Ray Binary GX 5-1. *The Astrophysical Journal*, 853(2):157, Feb. 2018. doi: 10.3847/1538-4357/aaa439.
- Hoyle, F. & Lyttleton, R. A. The effect of interstellar matter on climatic variation. *Proceedings of the Cambridge Philosophical Society*, 35(3):405, Jan. 1939. doi: 10.1017/S0305004100021150.
- Iaria, R., Di Salvo, T., Robba, N. R., et al. Disappearance of Hard X-Ray Emission in the Last BeppoSAX Observation of the Z Source GX 349+2. *The Astrophysical Journal*, 600(1):358–367, Jan. 2004. doi: 10.1086/379645.
- Iaria, R., Spanò, M., Di Salvo, T., et al. On the Soft Excess in the X-Ray Spectrum of Circinus X-1: Revisitation of the Distance to Circinus X-1. *The Astrophysical Journal*, 619(1):503–516, Jan. 2005. doi: 10.1086/426422.
- Iaria, R., Lavagetto, G., D’Aí, A., di Salvo, T., & Robba, N. R. Chandra observation of the Big Dipper X 1624-490. *Astronomy & Astrophysics*, 463(1):289–295, Feb. 2007. doi: 10.1051/0004-6361/20065862.
- Iaria, R., Di Salvo, T., Del Santo, M., et al. Study of the reflection spectrum of the LMXB 4U 1702-429. *Astronomy & Astrophysics*, 596:A21, Nov. 2016. doi: 10.1051/0004-6361/201628210.
- Iaria, R., Mazzola, S. M., Di Salvo, T., et al. Reflection component in the Bright Atoll Source GX 9+9. *Astronomy & Astrophysics*, 635:A209, Mar. 2020. doi: 10.1051/0004-6361/202037491.
- in ’t Zand, J. J. M., Verbunt, F., Strohmayer, T. E., et al. A new X-ray outburst in the globular cluster NGC 6440: SAX J1748.9-2021. *Astronomy & Astrophysics*, 345:100–108, May 1999. doi: 10.48550/arXiv.astro-ph/9902319.
- Inogamov, N. A. & Sunyaev, R. A. Spread of matter over a neutron-star surface during disk accretion. *Astronomy Letters*, 25(5):269–293, May 1999.
- Ishihara, H., Takahashi, M., & Tomimatsu, A. Gravitational Faraday rotation induced by a Kerr black hole. *Physical Review D*, 38(2):472–477, July 1988. doi: 10.1103/PhysRevD.38.472.
- Iwakiri, W., Serino, M., Negoro, H., et al. MAXI/GSC detection of a new X-ray outburst from XTE J1701-462. *The Astronomer’s Telegram*, 15592:1, Sept. 2022.

- Johnston, H. M., Fender, R., & Wu, K. High-resolution optical and infrared spectroscopic observations of CIR X-1. *Monthly Notices of the Royal Astronomical Society*, 308(2):415–423, Sept. 1999. doi: 10.1046/j.1365-8711.1999.02702.x.
- Johnston, Z., Heger, A., & Galloway, D. K. Multi-epoch X-ray burst modelling: MCMC with large grids of 1D simulations. *Monthly Notices of the Royal Astronomical Society*, 494(3):4576–4589, May 2020. doi: 10.1093/mnras/staa1054.
- Jones, M. H. & Watson, M. G. The X-Ray Dip Source 4U:1624-49. In Hunt, J. & Battrock, B., editors, *Two Topics in X-Ray Astronomy, Volume 1: X Ray Binaries. Volume 2: AGN and the X Ray Background*, volume 1 of *ESA Special Publication*, page 439, Nov. 1989.
- Jonker, P. G., Fender, R. P., Hambly, N. C., & van der Klis, M. The infrared counterpart of the Z source GX 5-1. *Monthly Notices of the Royal Astronomical Society*, 315(4):L57–L60, July 2000. doi: 10.1046/j.1365-8711.2000.03680.x.
- Jonker, P. G., van der Klis, M., Homan, J., et al. Low- and high-frequency variability as a function of spectral properties in the bright X-ray binary GX 5-1. *Monthly Notices of the Royal Astronomical Society*, 333(3):665–678, July 2002. doi: 10.1046/j.1365-8711.2002.05442.x.
- Kaastra, J. S. & Bleeker, J. A. M. Optimal binning of X-ray spectra and response matrix design. *Astronomy & Astrophysics*, 587:A151, Mar. 2016. doi: 10.1051/0004-6361/201527395.
- Kahn, H. Applications of monte carlo. 4 1954. doi: 10.2172/4353680. URL <https://www.osti.gov/biblio/4353680>.
- Kallman, T. & Bautista, M. Photoionization and High-Density Gas. *The Astrophysical Journal Supplement*, 133(1):221–253, Mar. 2001. doi: 10.1086/319184.
- Kaluzienski, L. J., Holt, S. S., Boldt, E. A., & Serlemitsos, P. J. Evidence for a 16.6 day period from Circinus X-1. *The Astrophysical Journal Letters*, 208:L71–L75, Sept. 1976. doi: 10.1086/182235.
- Karzas, W. J. & Latter, R. Electron Radiative Transitions in a Coulomb Field. *The Astrophysical Journal Supplement*, 6:167, May 1961. doi: 10.1086/190063.
- Kaspi, V. M. & Beloborodov, A. M. Magnetars. *Annual Review of Astronomy & Astrophysics*, 55(1): 261–301, Aug. 2017. doi: 10.1146/annurev-astro-081915-023329.
- Kerr, R. P. Gravitational Field of a Spinning Mass as an Example of Algebraically Special Metrics. *Physical Review Letters*, 11(5):237–238, Sept. 1963. doi: 10.1103/PhysRevLett.11.237.
- Kislat, F., Clark, B., Beilicke, M., & Krawczynski, H. Analyzing the data from X-ray polarimeters with Stokes parameters. *Astroparticle Physics*, 68:45–51, Aug. 2015. doi: 10.1016/j.astropartphys.2015.02.007.
- Kitaguchi, T., Grefenstette, B. W., Harrison, F. A., et al. Spectral calibration and modeling of the NuSTAR CdZnTe pixel detectors. In *Society of Photo-Optical Instrumentation Engineers (SPIE) Conference Series*, volume 8145 of *Society of Photo-Optical Instrumentation Engineers (SPIE) Conference Series*, page 814507, Sept. 2011. doi: 10.1117/12.896972.
- Klein, O. & Nishina, T. Über die Streuung von Strahlung durch freie Elektronen nach der neuen relativistischen Quantendynamik von Dirac. *Zeitschrift für Physik*, 52(11-12):853–868, Nov. 1929. doi: 10.1007/BF01366453.

- Kolehmainen, M., Done, C., & Díaz Trigo, M. Modelling the high-mass accretion rate spectra of GX 339-4: black hole spin from reflection? *Monthly Notices of the Royal Astronomical Society*, 416(1): 311–321, Sept. 2011. doi: 10.1111/j.1365-2966.2011.19040.x.
- Kong, A. K. H., Charles, P. A., Homer, L., Kuulkers, E., & O’Donoghue, D. Simultaneous X-ray/optical observations of GX9+9 (4U1728-16). *Monthly Notices of the Royal Astronomical Society*, 368(2): 781–795, May 2006. doi: 10.1111/j.1365-2966.2006.10157.x.
- Kotze, M. M. & Charles, P. A. Very long-term X-ray variations in LMXBs: solar cycle-like variations in the donor? *Monthly Notices of the Royal Astronomical Society*, 402(1):L16–L20, Feb. 2010. doi: 10.1111/j.1745-3933.2009.00790.x.
- Krawczynski, H., Muleri, F., Dovčiak, M., et al. Polarized x-rays constrain the disk-jet geometry in the black hole x-ray binary Cygnus X-1. *Science*, 378(6620):650–654, Nov. 2022. doi: 10.1126/science.add5399.
- Kubota, A., Tanaka, Y., Makishima, K., et al. Evidence for a Black Hole in the X-Ray Transient GRS 1009-45. *Publications of the Astronomical Society of Japan*, 50:667–673, Dec. 1998. doi: 10.1093/pasj/50.6.667.
- Kulkarni, A. K., Penna, R. F., Shcherbakov, R. V., et al. Measuring black hole spin by the continuum-fitting method: effect of deviations from the Novikov-Thorne disc model. *Monthly Notices of the Royal Astronomical Society*, 414(2):1183–1194, June 2011. doi: 10.1111/j.1365-2966.2011.18446.x.
- Kuulkers, E., van der Klis, M., Oosterbroek, T., et al. Spectral and correlated timing behaviour of GX5-1. *Astronomy & Astrophysics*, 289:795–821, Sept. 1994.
- La Monaca, F., Di Marco, A., Poutanen, J., et al. Highly Significant Detection of X-Ray Polarization from the Brightest Accreting Neutron Star Sco X-1. *The Astrophysical Journal Letters*, 960(2):L11, Jan 2024. doi: 10.3847/2041-8213/ad132d.
- Landau, L. “On the theory of stars”. *Phys. Z. Sowjetunion*, 1:285–288, 1932.
- Laor, A. Line Profiles from a Disk around a Rotating Black Hole. *The Astrophysical Journal*, 376:90, July 1991. doi: 10.1086/170257.
- Lapidus, I. I. & Sunyaev, R. A. Angular distribution and polarization of X-ray-burster radiation (during stationary and flash phases). *Monthly Notices of the Royal Astronomical Society*, 217:291–303, Nov. 1985. doi: 10.1093/mnras/217.2.291.
- Lavagetto, G., Iaria, R., di Salvo, T., et al. A BeppoSAX study of the Galactic Z-source GX 340+0. *Nuclear Physics B Proceedings Supplements*, 132:616–619, June 2004. doi: 10.1016/j.nuclphysbps.2004.04.106.
- Lebrun, F., Leray, J. P., Lavocat, P., et al. ISGRI: The INTEGRAL Soft Gamma-Ray Imager. *Astronomy & Astrophysics*, 411:L141–L148, Nov. 2003. doi: 10.1051/0004-6361:20031367.
- Lense, J. & Thirring, H. Über den Einfluß der Eigenrotation der Zentralkörper auf die Bewegung der Planeten und Monde nach der Einsteinschen Gravitationstheorie. *Physikalische Zeitschrift*, 19:156, Jan. 1918.
- Li, L.-X., Zimmerman, E. R., Narayan, R., & McClintock, J. E. Multitemperature Blackbody Spectrum of a Thin Accretion Disk around a Kerr Black Hole: Model Computations and Comparison with Observations. *The Astrophysical Journal Supplement*, 157(2):335–370, Apr. 2005. doi: 10.1086/428089.

- Li, L.-X., Narayan, R., & McClintock, J. E. Inferring the Inclination of a Black Hole Accretion Disk from Observations of its Polarized Continuum Radiation. *The Astrophysical Journal*, 691(1):847–865, Jan. 2009. doi: 10.1088/0004-637X/691/1/847.
- Lin, D., Altamirano, D., Homan, J., et al. Type i x-RAY BURSTS FROM THE NEUTRON-STAR TRANSIENT XTE j1701-462. *The Astrophysical Journal*, 699(1):60–65, jun 2009a.
- Lin, D., Remillard, R. A., & Homan, J. Spectral states of xte j1701-462: Link between z and atoll sources. *The Astrophysical Journal*, 696(2):1257–1277, apr 2009b.
- Linares, M., Watts, A., Altamirano, D., et al. The Return of the Bursts: Thermonuclear Flashes from Circinus X-1. *The Astrophysical Journal Letters*, 719(1):L84–L89, Aug. 2010. doi: 10.1088/2041-8205/719/1/L84.
- Liu, Q. Z., van Paradijs, J., & van den Heuvel, E. P. J. A catalogue of low-mass X-ray binaries in the Galaxy, LMC, and SMC (Fourth edition). *Astronomy & Astrophysics*, 469(2):807–810, July 2007. doi: 10.1051/0004-6361:20077303.
- Loktev, V., Veledina, A., & Poutanen, J. Analytical techniques for polarimetric imaging of accretion flows in the Schwarzschild metric. *Astronomy & Astrophysics*, 660:A25, Apr. 2022. doi: 10.1051/0004-6361/202142360.
- Lommen, D., van Straaten, S., van der Klis, M., & Anthonisse, B. RXTE observations of the dipping low-mass X-ray binary 4U 1624-49. *Astronomy & Astrophysics*, 435(3):1005–1011, June 2005. doi: 10.1051/0004-6361:20040405.
- Long, K. S., Chanan, G. A., Ku, W. H. M., & Novick, R. The linear X-ray polarization of Scorpius X-1. *The Astrophysical Journal Letters*, 232:L107–L110, Sept. 1979. doi: 10.1086/183045.
- Long, X., Feng, H., Li, H., et al. A significant detection of x-ray polarization in sco x-1 with PolarLight and constraints on the corona geometry. *The Astrophysical Journal Letters*, 924(1):L13, jan 2022.
- Longair, M. S. *High Energy Astrophysics*. 2011.
- Ludlam, R. M., Miller, J. M., Barret, D., et al. NuSTAR Observations of the Accreting Atolls GX 3+1, 4U 1702-429, 4U 0614+091, and 4U 1746-371. *The Astrophysical Journal*, 873(1):99, Mar. 2019. doi: 10.3847/1538-4357/ab0414.
- Ludlam, R. M., Cackett, E. M., García, J. A., et al. Radius constraints from reflection modeling of cygnus x-2 with NuSTAR and NICER. *The Astrophysical Journal*, 927(1):112, mar 2022.
- Lund, N., Budtz-Jørgensen, C., Westergaard, N. J., et al. JEM-X: The X-ray monitor aboard INTEGRAL. *Astronomy & Astrophysics*, 411:L231–L238, Nov. 2003. doi: 10.1051/0004-6361:20031358.
- Maier, D., Tenzer, C., & Santangelo, A. Point and Interval Estimation on the Degree and the Angle of Polarization: A Bayesian Approach. *Publications of the Astronomical Society of the Pacific*, 126(939): 459, May 2014. doi: 10.1086/676820.
- Makino, F. GS 1826-24. *IAU Circulars*, 4653:2, Sept. 1988.
- Makishima, K., Maejima, Y., Mitsuda, K., et al. Simultaneous X-Ray and Optical Observations of GX 339-4 in an X-Ray High State. *The Astrophysical Journal*, 308:635, Sept. 1986. doi: 10.1086/164534.
- Manchester, R. N., Hobbs, G. B., Teoh, A., & Hobbs, M. The Australia Telescope National Facility Pulsar Catalogue. *The Astronomical Journal*, 129(4):1993–2006, Apr. 2005. doi: 10.1086/428488.

- Marinucci, A., Muleri, F., Dovciak, M., et al. Polarization constraints on the X-ray corona in Seyfert Galaxies: MCG-05-23-16. *Monthly Notices of the Royal Astronomical Society*, 516(4):5907–5913, Nov. 2022. doi: 10.1093/mnras/stac2634.
- Matranga, M., Papitto, A., Di Salvo, T., et al. XMM-Newton and INTEGRAL view of the hard state of EXO 1745-248 during its 2015 outburst. *Astronomy & Astrophysics*, 603:A39, July 2017. doi: 10.1051/0004-6361/201629731.
- Matsuoka, M., Kawasaki, K., Ueno, S., et al. The MAXI Mission on the ISS: Science and Instruments for Monitoring All-Sky X-Ray Images. *Publications of the Astronomical Society of Japan*, 61:999, Oct. 2009. doi: 10.1093/pasj/61.5.999.
- Matt, G. X-ray polarization properties of a centrally illuminated accretion disc. *Monthly Notices of the Royal Astronomical Society*, 260:663–674, Feb. 1993. doi: 10.1093/mnras/260.3.663.
- Matt, G. & Perola, G. C. The iron K-alpha response in an X-ray illuminated relativistic disc and a black hole mass estimate. *Monthly Notices of the Royal Astronomical Society*, 259:433–436, Dec. 1992. doi: 10.1093/mnras/259.3.433.
- Matt, G., Perola, G. C., Piro, L., & Stella, L. Iron K-alpha line from X-ray illuminated relativistic disks. *Astronomy & Astrophysics*, 257:63–68, Apr. 1992.
- Matt, G., Fabian, A. C., & Ross, R. R. Iron K-alpha lines from X-ray photoionized accretion discs. *Monthly Notices of the Royal Astronomical Society*, 262:179–186, May 1993. doi: 10.1093/mnras/262.1.179.
- Matt, G., Fabian, A. C., & Reynolds, C. S. Geometrical and chemical dependence of K-shell X-ray features. *Monthly Notices of the Royal Astronomical Society*, 289(1):175–184, July 1997. doi: 10.1093/mnras/289.1.175.
- McLaughlin, M. A., Lyne, A. G., Lorimer, D. R., et al. Transient radio bursts from rotating neutron stars. *Nature*, 439(7078):817–820, Feb. 2006. doi: 10.1038/nature04440.
- McMaster, W. H. Polarization and the Stokes Parameters. *American Journal of Physics*, 22(6):351–362, Sept. 1954. doi: 10.1119/1.1933744.
- Mereghetti, S. X-ray emission from isolated neutron stars. In *High-Energy Emission from Pulsars and their Systems*, volume 21 of *Astrophysics and Space Science Proceedings*, page 345, Jan. 2011. doi: 10.1007/978-3-642-17251-9_29.
- Merloni, A., Fabian, A. C., & Ross, R. R. On the interpretation of the multicolour disc model for black hole candidates. *Monthly Notices of the Royal Astronomical Society*, 313(1):193–197, Mar. 2000. doi: 10.1046/j.1365-8711.2000.03226.x.
- Mescheryakov, A. V., Revnivtsev, M. G., & Filippova, E. V. Parameters of irradiated accretion disks from optical and X-ray observations of GS 1826-238. *Astronomy Letters*, 37(12):826–844, Dec. 2011. doi: 10.1134/S1063773711120073.
- Migliari, S. & Fender, R. P. Jets in neutron star X-ray binaries: a comparison with black holes. *Monthly Notices of the Royal Astronomical Society*, 366(1):79–91, Feb. 2006. doi: 10.1111/j.1365-2966.2005.09777.x.
- Migliari, S., Fender, R. P., Rupen, M., et al. Radio detections of the neutron star X-ray binaries 4U 1820 - 30 and Ser X-1 in soft X-ray states. *Monthly Notices of the Royal Astronomical Society*, 351(1): 186–192, June 2004. doi: 10.1111/j.1365-2966.2004.07768.x.

- Migliari, S., Miller-Jones, J. C. A., Fender, R. P., et al. Linking Jet Emission, X-Ray States, and Hard X-Ray Tails in the Neutron Star X-Ray Binary GX 17+2. *The Astrophysical Journal*, 671(1):706–712, Dec. 2007. doi: 10.1086/522516.
- Mihara, T., Tsunemi, H., & Negoro, H. *MAXI: Monitor of All-Sky X-Ray Image*, pages 1–25. Springer Nature Singapore, Singapore, 2022. ISBN 978-981-16-4544-0. doi: 10.1007/978-981-16-4544-0_38-1. URL https://doi.org/10.1007/978-981-16-4544-0_38-1.
- Miller, J. M., Gendreau, K., Ludlam, R. M., et al. A NICER Spectrum of MAXI J1535-571: Near-maximal Black Hole Spin and Potential Disk Warping. *The Astrophysical Journal Letters*, 860(2):L28, June 2018. doi: 10.3847/2041-8213/aacc61.
- Miller-Jones, J. C. A., Moin, A., Tingay, S. J., et al. The first resolved imaging of milliarcsecond-scale jets in Circinus X-1. *Monthly Notices of the Royal Astronomical Society*, 419(1):L49–L53, Jan. 2012. doi: 10.1111/j.1745-3933.2011.01176.x.
- Miller-Jones, J. C. A., Tetarenko, A. J., Sivakoff, G. R., et al. A rapidly changing jet orientation in the stellar-mass black-hole system V404 Cygni. *Nature*, 569(7756):374–377, Apr. 2019. doi: 10.1038/s41586-019-1152-0.
- Misner, C. W., Thorne, K. S., & Wheeler, J. A. *Gravitation*. 1973.
- Mitsuda, K., Inoue, H., Koyama, K., et al. Energy spectra of low-mass binary X-ray sources observed from Tenma. *Publications of the ASJ*, 36:741–759, Jan. 1984.
- Mitsuda, K., Inoue, H., Nakamura, N., & Tanaka, Y. Luminosity-related changes of the energy spectrum of X 1608-522. *Publications of the ASJ*, 41:97–111, Jan. 1989.
- Mitton, S. *The Cambridge encyclopaedia of astronomy*. 1977.
- Mondal, A. S., Dewangan, G. C., Pahari, M., & Raychaudhuri, B. NuSTAR view of the Z-type neutron star low-mass X-ray binary Cygnus X-2. *Monthly Notices of the Royal Astronomical Society*, 474(2): 2064–2072, Feb. 2018. doi: 10.1093/mnras/stx2931.
- Motta, S. E., Rouco Escorial, A., Kuulkers, E., Muñoz-Darias, T., & Sanna, A. Links between quasi-periodic oscillations and accretion states in neutron star low-mass X-ray binaries. *Monthly Notices of the Royal Astronomical Society*, 468(2):2311–2324, June 2017. doi: 10.1093/mnras/stx570.
- Muñoz-Darias, T., Fender, R. P., Motta, S. E., & Belloni, T. M. Black hole-like hysteresis and accretion states in neutron star low-mass X-ray binaries. *Monthly Notices of the Royal Astronomical Society*, 443(4):3270–3283, Oct. 2014. doi: 10.1093/mnras/stu1334.
- Muleri, F. Analysis of the Data from Photoelectric Gas Polarimeters. In *Handbook of X-ray and Gamma-ray Astrophysics*, page 6. 2022. doi: 10.1007/978-981-16-4544-0_143-1.
- Muleri, F., Lefevre, C., Piazzolla, R., et al. Calibration of the IXPE instrument. In den Herder, J.-W. A., Nikzad, S., & Nakazawa, K., editors, *Space Telescopes and Instrumentation 2018: Ultraviolet to Gamma Ray*, volume 10699 of *Society of Photo-Optical Instrumentation Engineers (SPIE) Conference Series*, page 106995C, July 2018. doi: 10.1117/12.2312203.
- Nasa High Energy Astrophysics Science Archive Research Center. HEASoft: Unified Release of FTOOLS and XANADU. Astrophysics Source Code Library, record ascl:1408.004, Aug. 2014.
- Neilsen, J. & Lee, J. C. Accretion disk winds as the jet suppression mechanism in the microquasar GRS 1915+105. *Nature*, 458(7237):481–484, Mar. 2009. doi: 10.1038/nature07680.

- Neronov, A., Savchenko, V., Tramacere, A., et al. Online data analysis system of the INTEGRAL telescope. *Astronomy & Astrophysics*, 651:A97, July 2021. doi: 10.1051/0004-6361/202037850.
- Novikov, I. D. & Thorne, K. S. Astrophysics of black holes. In *Black Holes (Les Astres Occlus)*, pages 343–450, Jan. 1973.
- Oppenheimer, J. R. & Volkoff, G. M. “On Massive Neutron Cores”. *Physical Review*, 55(4):374–381, 1939. doi: 10.1103/PhysRev.55.374.
- Pacini, F. Energy Emission from a Neutron Star. *Nature*, 216(5115):567–568, Nov. 1967. doi: 10.1038/216567a0.
- Page, D. N. & Thorne, K. S. Disk-Accretion onto a Black Hole. Time-Averaged Structure of Accretion Disk. *The Astrophysical Journal*, 191:499–506, July 1974. doi: 10.1086/152990.
- Paizis, A., Farinelli, R., Titarchuk, L., et al. Average hard X-ray emission from NS LMXBs: observational evidence of different spectral states in NS LMXBs. *Astronomy & Astrophysics*, 459(1):187–197, Nov. 2006. doi: 10.1051/0004-6361:20065792.
- Patruno, A. & Watts, A. L. Accreting Millisecond X-ray Pulsars. In Belloni, T. M., Méndez, M., & Zhang, C., editors, *Timing Neutron Stars: Pulsations, Oscillations and Explosions*, volume 461 of *Astrophysics and Space Science Library*, pages 143–208, Jan. 2021. doi: 10.1007/978-3-662-62110-3_4.
- Patruno, A., Haskell, B., & Andersson, N. The Spin Distribution of Fast-spinning Neutron Stars in Low-mass X-Ray Binaries: Evidence for Two Subpopulations. *The Astrophysical Journal*, 850(1):106, Nov. 2017. doi: 10.3847/1538-4357/aa927a.
- Peterson, L. E. & Jacobson, A. S. The Spectrum of Scorpius XR-1 to 50 KEV. *The Astrophysical Journal*, 145:962, Sept. 1966. doi: 10.1086/148848.
- Piconcelli, E., Jimenez-Bailón, E., Guainazzi, M., et al. Evidence for a multizone warm absorber in the XMM-Newton spectrum of Markarian 304. *Monthly Notices of the Royal Astronomical Society*, 351(1): 161–168, June 2004. doi: 10.1111/j.1365-2966.2004.07764.x.
- Podgorný, J., Dovčiak, M., Marin, F., Goosmann, R., & Róžańska, A. Spectral and polarization properties of reflected X-ray emission from black hole accretion discs. *Monthly Notices of the Royal Astronomical Society*, 510(4):4723–4735, Mar. 2022. doi: 10.1093/mnras/stab3714.
- Ponti, G., Fender, R. P., Begelman, M. C., et al. Ubiquitous equatorial accretion disc winds in black hole soft states. *Monthly Notices of the Royal Astronomical Society*, 422(1):L11–L15, May 2012. doi: 10.1111/j.1745-3933.2012.01224.x.
- Ponti, G., Muñoz-Darias, T., & Fender, R. P. A connection between accretion state and Fe K absorption in an accreting neutron star: black hole-like soft-state winds? *Monthly Notices of the Royal Astronomical Society*, 444(2):1829–1834, Oct. 2014. doi: 10.1093/mnras/stu1742.
- Popham, R. & Sunyaev, R. Accretion Disk Boundary Layers around Neutron Stars: X-Ray Production in Low-Mass X-Ray Binaries. *The Astrophysical Journal*, 547(1):355–383, Jan. 2001. doi: 10.1086/318336.
- Porter, J. M. & Rivinius, T. Classical Be Stars. *The Publications of the Astronomical Society of the Pacific*, 115(812):1153–1170, Oct. 2003. doi: 10.1086/378307.
- Poutanen, J., Nagendra, K. N., & Svensson, R. Green’s matrix for Compton reflection of polarized radiation from cold matter. *Monthly Notices of the Royal Astronomical Society*, 283(3):892–904, Dec. 1996a. doi: 10.1093/mnras/283.3.892.

- Poutanen, J., Nagendra, K. N., & Svensson, R. Green's matrix for Compton reflection of polarized radiation from cold matter. *Monthly Notices of the Royal Astronomical Society*, 283(3):892–904, Dec. 1996b. doi: 10.1093/mnras/283.3.892.
- Poutanen, J., Veledina, A., & Zdziarski, A. A. Doughnut strikes sandwich: the geometry of hot medium in accreting black hole X-ray binaries. *Astronomy & Astrophysics*, 614:A79, June 2018. doi: 10.1051/0004-6361/201732345.
- Pozdnyakov, L. A., Sobol, I. M., & Syunyaev, R. A. Comptonization and the shaping of X-ray source spectra - Monte Carlo calculations. *Astrophysics Space Physics Research*, 2:189–331, Jan. 1983.
- Rana, V. R., Cook, Walter R., I., Harrison, F. A., Mao, P. H., & Miyasaka, H. Development of focal plane detectors for the Nuclear Spectroscopic Telescope Array (NuSTAR) mission. In Siegmund, O. H., editor, *UV, X-Ray, and Gamma-Ray Space Instrumentation for Astronomy XVI*, volume 7435 of *Society of Photo-Optical Instrumentation Engineers (SPIE) Conference Series*, page 743503, Aug. 2009. doi: 10.1117/12.825418.
- Rankin, J., Muleri, F., Tennant, A. F., et al. An Algorithm to Calibrate and Correct the Response to Unpolarized Radiation of the X-Ray Polarimeter Onboard IXPE. *The Astronomical Journal*, 163(2):39, Feb. 2022. doi: 10.3847/1538-3881/ac397f.
- Rankin, J., Monaca, F. L., Marco, A. D., et al. X-ray polarized view of the accretion geometry in the x-ray binary circinus x-1. *The Astrophysical Journal Letters*, 961(1):L8, jan 2024. doi: 10.3847/2041-8213/ad1832.
- Rappaport, S., Nelson, L. A., Ma, C. P., & Joss, P. C. The Evolutionary Status of 4U 1820-30. *The Astrophysical Journal*, 322:842, Nov. 1987. doi: 10.1086/165778.
- Rauch, K. P. & Blandford, R. D. Optical Caustics in a Kerr Spacetime and the Origin of Rapid X-Ray Variability in Active Galactic Nuclei. *The Astrophysical Journal*, 421:46, Jan. 1994. doi: 10.1086/173625.
- Reig, P. & Kylafis, N. The origin of the hard X-ray tail in neutron-star X-ray binaries. *Astronomy & Astrophysics*, 591:A24, June 2016. doi: 10.1051/0004-6361/201628294.
- Remillard, R. A., Lin, D., ASM Team at MIT, & NASA/GSFC. New X-ray Transient, XTE J1701-462. *The Astronomer's Telegram*, 696:1, Jan. 2006.
- Revnitvsev, M. G. & Gilfanov, M. R. Boundary layer emission and z-track in the color-color diagram of luminous lmxbs. *Astronomy & Astrophysics*, 453(1):253–259, 2006. doi: 10.1051/0004-6361:20053964.
- Revnitvsev, M. G., Suleimanov, V. F., & Poutanen, J. On the spreading layer emission in luminous accreting neutron stars. *Monthly Notices of the Royal Astronomical Society*, 434(3):2355–2361, 07 2013. ISSN 0035-8711. doi: 10.1093/mnras/stt1179. URL <https://doi.org/10.1093/mnras/stt1179>.
- Reynolds, C. S. An X-ray spectral study of 24 type 1 active galactic nuclei. *Monthly Notices of the Royal Astronomical Society*, 286(3):513–537, Apr. 1997. doi: 10.1093/mnras/286.3.513.
- Reynolds, C. S. & Nowak, M. A. Fluorescent iron lines as a probe of astrophysical black hole systems. *Physics Reports*, 377(6):389–466, Apr. 2003. doi: 10.1016/S0370-1573(02)00584-7.
- Rosenfeld, L. *Astrophysics and Gravitation: Proceedings of the Sixteenth Solvay Conference on Physics at the University of Brussels*. Editions de l'Université, 1974. ISBN 9782800405964.

- Russell, T. D., Degenaar, N., van den Eijnden, J., et al. The evolving radio jet from the neutron star X-ray binary 4U 1820-30. *Monthly Notices of the Royal Astronomical Society*, 508(1):L6–L11, Nov. 2021. doi: 10.1093/mnras/rlab087.
- Rybicki, G. B. & Lightman, A. P. *Radiative processes in astrophysics*. 1979.
- Saavedra, E. A., García, F., Fogantini, F. A., et al. Relativistic X-ray reflection and photoionized absorption in the neutron star low-mass X-ray binary GX 13+1. *Monthly Notices of the Royal Astronomical Society*, 522(3):3367–3377, July 2023. doi: 10.1093/mnras/stad1157.
- Sánchez-Fernández, C., Kajava, J. J. E., Poutanen, J., Kuulkers, E., & Suleimanov, V. F. Burst-induced coronal cooling in GS 1826-24. The clock wagging its tail. *Astronomy & Astrophysics*, 634:A58, Feb. 2020. doi: 10.1051/0004-6361/201936599.
- Sanna, A., Méndez, M., Altamirano, D., et al. The kilohertz quasi-periodic oscillations during the Z and atoll phases of the unique transient XTE J1701-462. *Monthly Notices of the Royal Astronomical Society*, 408(1):622–630, 08 2010. ISSN 0035-8711. doi: 10.1111/j.1365-2966.2010.17145.x.
- Savolainen, P., Hannikainen, D. C., Vilhu, O., et al. Exploring the spreading layer of GX 9+9 using RXTE and INTEGRAL. *Monthly Notices of the Royal Astronomical Society*, 393(2):569–578, Feb. 2009. doi: 10.1111/j.1365-2966.2008.14201.x.
- Schaefer, B. E. The Optical Light Curve of the Low-Mass X-Ray Binary GX 9+9. *The Astrophysical Journal*, 354:720, May 1990. doi: 10.1086/168728.
- Schnittman, J. D. & Krolik, J. H. X-ray Polarization from Accreting Black Holes: The Thermal State. *The Astrophysical Journal*, 701(2):1175–1187, Aug. 2009. doi: 10.1088/0004-637X/701/2/1175.
- Schnittman, J. D. & Krolik, J. H. A Monte Carlo Code for Relativistic Radiation Transport around Kerr Black Holes. *The Astrophysical Journal*, 777(1):11, Nov. 2013. doi: 10.1088/0004-637X/777/1/11.
- Schulz, N. S., Kallman, T. E., Heinz, S., et al. The young Be-star binary Circinus X-1. *IAU Symposium*, 346:125–130, Dec. 2019. doi: 10.1017/S1743921319002497.
- Schulz, N. S., Kallman, T. E., Heinz, S., et al. Origins of X-Ray Line Emissions in Circinus X-1 at Very Low X-Ray Flux. *The Astrophysical Journal*, 891(2):150, Mar. 2020. doi: 10.3847/1538-4357/ab6dc8.
- Sell, P. H., Heinz, S., Calvelo, D. E., et al. Parsec-scale Bipolar X-ray Shocks Produced by Powerful Jets from the Neutron Star Circinus X-1. *The Astrophysical Journal Letters*, 719(2):L194–L198, Aug. 2010. doi: 10.1088/2041-8205/719/2/L194.
- Shakura, N. I. & Sunyaev, R. A. Black holes in binary systems. Observational appearance. *Astronomy & Astrophysics*, 24:337–355, Jan. 1973.
- Shaposhnikov, N. & Titarchuk, L. On the Nature of the Flux Variability during an Expansion Stage of a Type I X-Ray Burst: Constraints on Neutron Star Parameters for 4U 1820-30. *The Astrophysical Journal Letters*, 606(1):L57–L60, May 2004. doi: 10.1086/421015.
- Shimura, T. & Takahara, F. On the Spectral Hardening Factor of the X-Ray Emission from Accretion Disks in Black Hole Candidates. *The Astrophysical Journal*, 445:780, June 1995. doi: 10.1086/175740.
- Shklovsky, I. S. On the Nature of the Source of X-Ray Emission of Sco XR-1. *The Astrophysical Journal Letters*, 148:L1, Apr. 1967. doi: 10.1086/180001.
- Sądowski, A., Abramowicz, M., Bursa, M., et al. Relativistic slim disks with vertical structure. *Astronomy & Astrophysics*, 527:A17, Mar. 2011. doi: 10.1051/0004-6361/201015256.

- Smale, A. P. A Type I Burst with Radius Expansion Observed from Cygnus X-2 with the Rossi X-Ray Timing Explorer. *The Astrophysical Journal Letters*, 498(2):L141–L145, May 1998. doi: 10.1086/311319.
- Smale, A. P., Zhang, W., & White, N. E. Discovery of Kilohertz Quasi-periodic Oscillations from 4U 1820-303 with Rossi X-Ray Timing Explorer. *The Astrophysical Journal Letters*, 483(2):L119–L122, July 1997. doi: 10.1086/310749.
- Smale, A. P., Church, M. J., & Bałucińska-Church, M. The Ephemeris and Dipping Spectral Behavior of 4U 1624-49. *The Astrophysical Journal*, 550(2):962–969, Apr. 2001. doi: 10.1086/319800.
- Smith, R. K., Dame, T. M., Costantini, E., & Predehl, P. The X-Ray Halo of GX 5-1. *The Astrophysical Journal*, 648(1):452–460, Sept. 2006. doi: 10.1086/505650.
- Sobolev, V. V. *A treatise on radiative transfer*. 1963.
- Soleri, P., Heinz, S., Fender, R., et al. A parsec scale X-ray extended structure from the X-ray binary Circinus X-1. *Monthly Notices of the Royal Astronomical Society*, 397(1):L1–L5, July 2009. doi: 10.1111/j.1745-3933.2008.00574.x.
- Spencer, R. E., Rushton, A. P., Bałucińska-Church, M., et al. Radio and X-ray observations of jet ejection in Cygnus X-2. *Monthly Notices of the Royal Astronomical Society*, 435(1):L48–L52, Oct. 2013. doi: 10.1093/mnras/slt090.
- Steeghs, D. & Casares, J. The Mass Donor of Scorpius X-1 Revealed. *The Astrophysical Journal*, 568(1): 273–278, Mar. 2002. doi: 10.1086/339224.
- Stella, L. & Vietri, M. Lense-Thirring Precession and Quasi-periodic Oscillations in Low-Mass X-Ray Binaries. *The Astrophysical Journal Letters*, 492(1):L59–L62, Jan. 1998. doi: 10.1086/311075.
- Stella, L., Priedhorsky, W., & White, N. E. The Discovery of a Second Orbital Period from the X-Ray Source 4U 1820-30 in the Globular Cluster NGC 6624. *The Astrophysical Journal Letters*, 312:L17, Jan. 1987. doi: 10.1086/184811.
- Stokes, G. G. On the Change of Refrangibility of Light. *Philosophical Transactions of the Royal Society of London Series I*, 142:463–562, Jan. 1852.
- Strohmer, T. E. & Kallman, T. R. On the Statistical Analysis of X-Ray Polarization Measurements. *The Astrophysical Journal*, 773(2):103, Aug. 2013. doi: 10.1088/0004-637X/773/2/103.
- Strohmer, T. E., Gendreau, K. C., Altamirano, D., et al. NICER Discovers mHz Oscillations in the “Clocked” Burster GS 1826-238. *The Astrophysical Journal*, 865(1):63, Sept. 2018. doi: 10.3847/1538-4357/aada14.
- Suleimanov, V. & Poutanen, J. Spectra of the spreading layers on the neutron star surface and constraints on the neutron star equation of state. *Monthly Notices of the Royal Astronomical Society*, 369(4): 2036–2048, 07 2006. ISSN 0035-8711. doi: 10.1111/j.1365-2966.2006.10454.x.
- Sunyaev, R., Churazov, E., Gilfanov, M., et al. Two hard X-ray sources in 100 square degrees around the Galactic Center. *Astronomy & Astrophysics*, 247:L29–L32, July 1991.
- Sunyaev, R. A. & Titarchuk, L. G. Comptonization of X-Rays in Plasma Clouds - Typical Radiation Spectra. *Astronomy & Astrophysics*, 86:121, June 1980.
- Sunyaev, R. A. & Titarchuk, L. G. Comptonization of low-frequency radiation in accretion disks Angular distribution and polarization of hard radiation. *Astronomy & Astrophysics*, 143(2):374–388, Feb. 1985.

- Tamborra, F., Matt, G., Bianchi, S., & Dovčiak, M. MoCA: A Monte Carlo code for Comptonisation in Astrophysics. I. Description of the code and first results. *Astronomy & Astrophysics*, 619:A105, Nov. 2018. doi: 10.1051/0004-6361/201732023.
- Taverna, R., Turolla, R., Muleri, F., et al. Polarized x-rays from a magnetar. *Science*, 378(6620):646–650, Nov. 2022. doi: 10.1126/science.add0080.
- Tennant, A. F., Fabian, A. C., & Shafer, R. A. Observations of type I X-ray bursts from CIR X-1. *Monthly Notices of the Royal Astronomical Society*, 221:27P–31, July 1986. doi: 10.1093/mnras/221.1.27P.
- Titarchuk, L. Generalized Comptonization Models and Application to the Recent High-Energy Observations. *The Astrophysical Journal*, 434:570, Oct. 1994. doi: 10.1086/174760.
- Titarchuk, L., Seifina, E., & Shrader, C. X-Ray Spectral and Timing Behavior of Scorpius X-1. Spectral Hardening during the Flaring Branch. *The Astrophysical Journal*, 789(2):98, July 2014. doi: 10.1088/0004-637X/789/2/98.
- Tolman, R. C. “Static Solutions of Einstein’s Field Equations for Spheres of Fluid”. *Physical Review*, 55: 364–373, 1939. doi: 10.1103/PhysRev.55.364.
- Tsuruta, S. & Cameron, A. G. W. Cooling and detectability of neutron stars. *Canadian Journal of Physics*, 44:1863, Jan. 1966. doi: 10.1139/p66-156.
- Tudose, V., Fender, R. P., Tzioumis, A. K., Spencer, R. E., & van der Klis, M. A decade of radio imaging the relativistic outflow in the peculiar X-ray binary CircinusX-1. *Monthly Notices of the Royal Astronomical Society*, 390(1):447–464, Oct. 2008. doi: 10.1111/j.1365-2966.2008.13788.x.
- Turolla, R. Isolated Neutron Stars: The Challenge of Simplicity. In Becker, W., editor, *Astrophysics and Space Science Library*, volume 357 of *Astrophysics and Space Science Library*, page 141, Jan. 2009. doi: 10.1007/978-3-540-76965-1_7.
- Turolla, R., Zane, S., & Watts, A. L. Magnetars: the physics behind observations. A review. *Reports on Progress in Physics*, 78(11):116901, Nov. 2015. doi: 10.1088/0034-4885/78/11/116901.
- Ubertini, P., Bazzano, A., Cocchi, M., et al. Bursts from GS 1826-238: A Clocked Thermonuclear Flashes Generator. *The Astrophysical Journal Letters*, 514(1):L27–L30, Mar. 1999. doi: 10.1086/311933.
- Ursini, F., Matt, G., Bianchi, S., et al. Prospects for differentiating extended coronal geometries in AGNs with the IXPE mission. *Monthly Notices of the Royal Astronomical Society*, 510(3):3674–3687, Mar. 2022. doi: 10.1093/mnras/stab3745.
- Ursini, F., Farinelli, R., Gnarini, A., et al. X-ray polarimetry and spectroscopy of the neutron star low-mass x-ray binary gx 9+9: An in-depth study with ixpe and nustar. *Astronomy & Astrophysics*, 676: A20, 2023a. doi: 10.1051/0004-6361/202346541. URL <https://doi.org/10.1051/0004-6361/202346541>.
- Ursini, F., Marinucci, A., Matt, G., et al. Mapping the circumnuclear regions of the Circinus galaxy with the Imaging X-ray Polarimetry Explorer. *Monthly Notices of the Royal Astronomical Society*, 519(1): 50–58, Feb. 2023b. doi: 10.1093/mnras/stac3189.
- van der Klis, M. Quasi-periodic oscillations and noise in low-mass X-ray binaries. *Annual Review of Astronomy & Astrophysics*, 27:517–553, Jan. 1989. doi: 10.1146/annurev.aa.27.090189.002505.
- van der Klis, M. *Rapid X-ray variability*, page 39–112. Cambridge Astrophysics. Cambridge University Press, 2006. doi: 10.1017/CBO9780511536281.003.

- van der Klis, M., Hasinger, G., Damen, E., et al. Correlation of X-Ray Burst Properties with Source State in the “Atoll” Source 4U/MXB 1636-53. *The Astrophysical Journal Letters*, 360:L19, Sept. 1990. doi: 10.1086/185802.
- Veledina, A., Muleri, F., Dovčiak, M., et al. Discovery of X-Ray Polarization from the Black Hole Transient Swift J1727.8-1613. *The Astrophysical Journal Letters*, 958(1):L16, Nov. 2023. doi: 10.3847/2041-8213/ad0781.
- Verner, D. A., Ferland, G. J., Korista, K. T., & Yakovlev, D. G. Atomic Data for Astrophysics. II. New Analytic FITS for Photoionization Cross Sections of Atoms and Ions. *The Astrophysical Journal*, 465: 487, July 1996. doi: 10.1086/177435.
- Viironen, K. & Poutanen, J. Light curves and polarization of accretion- and nuclear-powered millisecond pulsars. *Astronomy & Astrophysics*, 426:985–997, Nov. 2004. doi: 10.1051/0004-6361:20041084.
- Walker, M. & Penrose, R. On quadratic first integrals of the geodesic equations for type { 22 } spacetimes. *Communications in Mathematical Physics*, 18(4):265–274, Dec. 1970. doi: 10.1007/BF01649445.
- Watson, M. G., Willingale, R., King, A. R., Grindlay, J. E., & Halpern, J. The Big Dipper - 4U1624-49. *Space Science Reviews*, 40(1-2):195–200, Feb. 1985. doi: 10.1007/BF00212884.
- Weisskopf, M. C., Elsner, R. F., & O’Dell, S. L. On understanding the figures of merit for detection and measurement of x-ray polarization. In Arnaud, M., Murray, S. S., & Takahashi, T., editors, *Space Telescopes and Instrumentation 2010: Ultraviolet to Gamma Ray*, volume 7732 of *Society of Photo-Optical Instrumentation Engineers (SPIE) Conference Series*, page 77320E, July 2010. doi: 10.1117/12.857357.
- Weisskopf, M. C., Ramsey, B. D., O’Dell, S. L., et al. The imaging x-ray polarimetry explorer (ixpe). *SPIE Proceedings*, 6:1179–1180, July 2016. doi: 10.1117/12.2235240.
- Weisskopf, M. C., Soffitta, P., Baldini, L., et al. Imaging x-ray polarimetry explorer: prelaunch. *Journal of Astronomical Telescopes, Instruments, and Systems*, 8(2):1 – 28, 2022. doi: 10.1117/1.JATIS.8.2.026002. URL <https://doi.org/10.1117/1.JATIS.8.2.026002>.
- White, N. E. & Swank, J. H. The periodic absorption events from 4U 1915-05. *The Astrophysical Journal Letters*, 253:L61–L66, Feb. 1982. doi: 10.1086/183737.
- White, N. E., Stella, L., & Parmar, A. N. The X-Ray Spectral Properties of Accretion Disks in X-Ray Binaries. *The Astrophysical Journal*, 324:363, Jan. 1988. doi: 10.1086/165901.
- Wijnands, R., Homan, J., van der Klis, M., et al. Discovery of kHz Quasi-periodic Oscillations in the Z Source Cygnus X-2. *The Astrophysical Journal Letters*, 493(2):L87–L90, Feb. 1998. doi: 10.1086/311138.
- Wilkins, D. R. On the illumination of neutron star accretion discs. *Monthly Notices of the Royal Astronomical Society*, 475(1):748–756, Mar. 2018. doi: 10.1093/mnras/stx3167.
- Wilkins, D. R. & Fabian, A. C. Understanding X-ray reflection emissivity profiles in AGN: locating the X-ray source. *Monthly Notices of the Royal Astronomical Society*, 424(2):1284–1296, Aug. 2012. doi: 10.1111/j.1365-2966.2012.21308.x.
- Will, C. M. “The binary pulsar, gravitational waves, and the Nobel prize”. *Physics-Uspekhi*, 37(7): 697–703, 1994.

- Wilms, J., Allen, A., & McCray, R. On the absorption of x-rays in the interstellar medium. *The Astrophysical Journal*, 542(2):914, oct 2000. doi: 10.1086/317016. URL <https://dx.doi.org/10.1086/317016>.
- Winkler, C., Courvoisier, T. J. L., Di Cocco, G., et al. The INTEGRAL mission. *Astronomy & Astrophysics*, 411:L1–L6, Nov. 2003. doi: 10.1051/0004-6361:20031288.
- Xiang, J., Lee, J. C., Nowak, M. A., Wilms, J., & Schulz, N. S. The Accretion Disk Corona and Disk Atmosphere of 4U 1624-490 as Viewed by the Chandra-High Energy Transmission Grating Spectrometer. *The Astrophysical Journal*, 701(2):984–993, Aug. 2009. doi: 10.1088/0004-637X/701/2/984.
- Yakovlev, D. G., Levenfish, K. P., & Shibano, Y. A. REVIEWS OF TOPICAL PROBLEMS: Cooling of neutron stars and superfluidity in their cores. *Physics Uspekhi*, 42(8):737–778, Aug. 1999. doi: 10.1070/PU1999v042n08ABEH000556.
- Yakovlev, D. G., Gnedin, O. Y., Gusakov, M. E., et al. Neutron star cooling. *Nuclear Physics A*, 752: 590–599, Apr. 2005. doi: 10.1016/j.nuclphysa.2005.02.061.
- Yakovlev, D. G., Haensel, P., Baym, G., & Pethick, C. Lev Landau and the concept of neutron stars. *Physics Uspekhi*, 56(3):289-295, Mar. 2013. doi: 10.3367/UFNe.0183.201303f.0307.
- Younsi, Z., Wu, K., & Fuerst, S. V. General relativistic radiative transfer: formulation and emission from structured tori around black holes. *Astronomy & Astrophysics*, 545:A13, Sept. 2012. doi: 10.1051/0004-6361/201219599.
- Zamfir, M., Cumming, A., & Galloway, D. K. Constraints on Neutron Star Mass and Radius in GS 1826-24 from Sub-Eddington X-Ray Bursts. *The Astrophysical Journal*, 749(1):69, Apr. 2012. doi: 10.1088/0004-637X/749/1/69.
- Zdziarski, A. A. Thermal Comptonization in compact sources and the cosmic X-ray background. *Monthly Notices of the Royal Astronomical Society*, 233:739–758, Aug. 1988. doi: 10.1093/mnras/233.4.739.
- Zdziarski, A. A., Johnson, W. N., & Magdziarz, P. Broad-band γ -ray and X-ray spectra of NGC 4151 and their implications for physical processes and geometry. *Monthly Notices of the Royal Astronomical Society*, 283(1):193–206, Nov. 1996. doi: 10.1093/mnras/283.1.193.
- Zdziarski, A. A., Gierliński, M., Wen, L., & Kostrzewa, Z. Dependence of the orbital modulation of X-rays from 4U 1820-303 on the accretion rate. *Monthly Notices of the Royal Astronomical Society*, 377(3):1017–1023, May 2007. doi: 10.1111/j.1365-2966.2007.11688.x.
- Zdziarski, A. A., Szanecki, M., Poutanen, J., Gierliński, M., & Biernacki, P. Spectral and temporal properties of Compton scattering by mildly relativistic thermal electrons. *Monthly Notices of the Royal Astronomical Society*, 492(4):5234–5246, Mar. 2020. doi: 10.1093/mnras/staa159.
- Zhang, W., Dovčiak, M., & Bursa, M. Constraining the Size of the Corona with Fully Relativistic Calculations of Spectra of Extended Coronae. I. The Monte Carlo Radiative Transfer Code. *The Astrophysical Journal*, 875(2):148, Apr. 2019. doi: 10.3847/1538-4357/ab1261.
- Życki, P. T., Done, C., & Smith, D. A. The 1989 May outburst of the soft X-ray transient GS 2023+338 (V404 Cyg). *Monthly Notices of the Royal Astronomical Society*, 309(3):561–575, Nov. 1999. doi: 10.1046/j.1365-8711.1999.02885.x.

YOU'RE GONNA CARRY THAT WEIGHT.

